

VALIDATING THE METHOD OF PRESSURE SENSING TO OPTIMIZE
FLAPPING FOIL ENERGY EXTRACTION
BY
AMANDA J. PERSICHETTI

A THESIS SUBMITTED IN PARTIAL FULFILLMENT OF THE
REQUIREMENTS FOR THE DEGREE OF
MASTER OF SCIENCE
IN
OCEAN ENGINEERING

UNIVERSITY OF RHODE ISLAND
2013

UMI Number: 1545427

All rights reserved

INFORMATION TO ALL USERS

The quality of this reproduction is dependent upon the quality of the copy submitted.

In the unlikely event that the author did not send a complete manuscript and there are missing pages, these will be noted. Also, if material had to be removed, a note will indicate the deletion.



UMI 1545427

Published by ProQuest LLC (2013). Copyright in the Dissertation held by the Author.

Microform Edition © ProQuest LLC.

All rights reserved. This work is protected against unauthorized copying under Title 17, United States Code



ProQuest LLC.
789 East Eisenhower Parkway
P.O. Box 1346
Ann Arbor, MI 48106 - 1346

MASTER OF SCIENCE THESIS
OF
AMANDA J. PERSICHETTI

APPROVED:

Thesis Committee:

Major Professor Dr. Jason Dahl

Dr. Stephen Licht

Dr. Richard Vaccaro

Dr. Nasser Zawia

DEAN OF THE GRADUATE SCHOOL

UNIVERSITY OF RHODE ISLAND

2013

ABSTRACT

Renewable energy resources are in high demand due to a world-wide desire for cleaner energy production. Flapping foil tidal driven systems have begun being tested and implemented at prototype scales. These prototype systems use limited control to maximize energy production. This thesis uses biological inspiration from the sensory system in fish to enhance the efficiency of these energy harnessing systems with the use of surface mounted pressure sensing. Eight pressure sensors were found to be a good balance for quantity with respect to cost and accuracy. Optimal locations around the foil were determined from application of a Random Search algorithm and a fluid moment approximation. A 2-D numerical code was created to simulate a NACA0015 flapping foil in uniform flow. A wide parameter space of sinusoidal heave and pitch motions was run and a database of force, pressure, and efficiency values along with flow visualization was built. A maximum efficiency of 0.43 was reached for the trajectory of motion with a pitch amplitude of 90°, heave amplitude of 1.25 and a Strouhal number of 0.5.

A control platform dependent on pressure measurements at the eight sensor locations was created in the 2-D numerical code. By implementing basic control, motion trajectories converge to the optimal motion based on pressure comparisons around the foil to pressure traces from the motion with highest efficiency. In addition, a laboratory for experimental testing and validation was set-up. The motion control system was connected and tested for a tow tank set-up. Motion programs were written for the same parameter space modeled in this thesis. Through numerical modeling, pressure sensing was found to be an effective method to enhancing the efficiency of a flapping foil energy extraction system.

ACKNOWLEDGMENTS

I wish to express my extreme gratitude to everyone who supported me throughout my graduate studies. My adviser, Dr. Jason Dahl, always had his door open, ready and willing to answer any questions I may have had, intelligent or lack thereof. More importantly, he shared with me his passion for Ocean Engineering and constantly turned my frustrations around into constructive optimism. The members of my committee also deserve great thanks. Dr. Stephen Licht enthusiastically welcomed all quests for abbreviated lessons from his first day with the department. Dr. Richard Vaccaro, from the Electrical Engineering Department, is an amazing professor who gave me different points of view on the engineering world with every lecture I attended.

I am especially grateful for the love and support from my fiance, Jeff. Regardless of how overwhelmed I became, he continuously reminded me of my strengths and power of mind. It was a pleasure to attend the entire six years of my college career with him by my side, books open, and constantly bouncing ideas and concepts off of one another.

Much appreciation is extended to my friends and family who unintentionally have carried me through this experience. Thank you Michelle, Mary, Jenn, and Regina, for listening to my rants on my research and TA duties. Without you all, I would have run out of caffeine and not been my cheerful self.

I am dedicating this thesis to my parents, Rita and Stephen. Since the day I was born, they encouraged my love for learning and experiencing new things. They always made me feel like I could change the world and were a constant reminder that along with them, God was always by my side.

TABLE OF CONTENTS

ABSTRACT	ii
ACKNOWLEDGMENTS	iii
TABLE OF CONTENTS	iv
LIST OF TABLES	vii
LIST OF FIGURES	viii
CHAPTER	
1 Introduction	1
1.1 Biological Inspiration	2
1.1.1 Lateral Line System	3
1.2 Previous Research	4
1.2.1 Artificial Lateral Line Sensing	4
1.2.2 Flapping Foil Energy Harvester Academic Work	6
1.2.3 Commercial Flapping Foil Devices	7
1.3 Limitations	9
1.4 Organization of Thesis	11
2 Kinematic Set-Up	12
2.1 Equations of Motions	12
2.2 Relevant Parameters	13
2.3 Simulation Set-Up	15
3 Sensor Array Optimization	17

	Page
3.1 Numerical Source Code	17
3.2 Fluid Moment Approximation	18
3.3 Sensor Optimization	20
3.3.1 Random Search	22
3.4 Results	24
3.5 Discussion	26
4 Database	28
4.1 Parameter Space	29
4.2 Power Extraction	29
4.3 Results	30
4.3.1 Model Validation	30
4.3.2 Motion Efficiency	31
4.3.3 Pressure and Velocity Traces	39
4.4 Discussion	39
5 Control	45
5.1 Method	45
5.2 Results	46
5.2.1 Reacting Heave Attempt	48
5.2.2 LQR Optimal Control Attempt	49
5.3 Discussion	50
6 Experimental Setup	51
7 Conclusion	54

	Page
LIST OF REFERENCES	57
 APPENDIX	
A Appendix A	60
B Appendix B	63
B.1 $h_0/c = 0.05$	64
B.2 $h_0/c = 0.75$	68
B.3 $h_0/c = 1.0$	74
B.4 $h_0/c = 1.25$	81
C Wake Patterns	88
D Database	149
E Laboratory Set-up	153
E.1 MATLAB Motion Program Writer	153
E.2 Example Motion Program	163
BIBLIOGRAPHY	177

LIST OF TABLES

Table		Page
1	Simulation parameter space	29
2	Efficiency change with control for each cycle N.	48
A.3	Efficiency values for $\frac{h_0}{c} = 0.5$	61
A.4	Efficiency values for $\frac{h_0}{c} = 0.75$	61
A.5	Efficiency values for $\frac{h_0}{c} = 1.0$	62
A.6	Efficiency values for $\frac{h_0}{c} = 1.25$	62
D.7	Simulation Parameter Space	149
D.8	Text files store extracted data for every timestep in the sixth cycle of motion.	151

LIST OF FIGURES

Figure		Page
1	Schematic of canal neuromast (each ciliary bundle represented by a single line). [1]	3
2	Schematic showing different types of neuromast receptor organs in fish. [2]	3
3	Lateral view of canals that contain neuromasts in a Goldfish. [3]	4
4	Definitions of motion for an oscillating foil in two degrees of freedom in which U is the free stream velocity, $\dot{h}(t)$ is the heave velocity, $\alpha(t)$ is the nominal angle of attack, and $\theta(t)$ is the pitching position.	12
5	Schematic representing the computational domain and fluid flow orientation of simulations where U is the uniform fluid flow.	15
6	Example of 18 equally spaced sensors around the foil. Red circles symbolize $q=18$ sensors and the blue lines mark the bounds of the corresponding segment lengths.	19
7	Example of 8 randomly spaced sensors around the foil. Red circles symbolize $q=8$ sensors and the blue lines mark the bounds of the corresponding segment lengths. Notice here that the sensors locations are necessarily centered in their segment, but the segment boundaries are centered between corresponding sensors.	19
8	Plot showing error in approximate fluid moment calculation for various numbers of equally spaced sensor locations. A number of 8 sensors is chosen due to the large increase in error for fewer sensors. At 200 sensors, minimal error is due to rounding segment lengths l_i to significant digits.	21
9	Representation of the pressure gradient around a NACA foil created by [4].	21
10	Flow chart representing steps in random search algorithm used for finding the optimal locations for pressure sensors on a hydrofoil.	23

Figure	Page
11 Results from Random Search method after (a) 69 populations and (b) 236 populations. These plots include the sensor locations for each of the best 100 members and scales the circle at the location based on how many members had that location in its array. The axis are coordinates in relation to global coordinate grid in LilyPad 2D Simulations.	25
12 Results from Random Search method after 2396 populations. Best 100 arrays of sensors locations plotted.	26
13 Snapshot from simulation for $h_0 = 1.0$, $\theta_0 = 50^\circ$, and $St = 0.1$. Colorbar shows non-dimensional vorticity.	28
14 Comparison between (a) efficiency output from 2-D model with (b) Zhu [5] efficiency outputs for $h_0 = 1$	31
15 Efficiency Contour and Sample Force value plots for $h_0 = 0.5$ simulations. In force plots, blue represents the coefficient of lift force, green the heave velocity, red the coefficient of moment scaled by 10^{-1} , teal the pitch amplitude scaled by 10^{-1} , and magenta the coefficient of power. (15b) $\eta = 0.29$ and (15c) $\eta = -0.07$	32
16 Sample wake patterns for $h_0 = 0.5$ simulations with efficiency values $\eta = 0.29$ (16a) and $\eta = -0.07$ (16b)	33
17 Efficiency Contour and Sample Force value plots for $h_0 = 0.75$ simulations. In force plots, blue represents the coefficient of lift force, green the heave velocity, red the coefficient of moment scaled by 10^{-1} , teal the pitch amplitude scaled by 10^{-1} , and magenta the coefficient of power. (17b) $\eta = 0.376$ and (17c) $\eta = -0.386$	35
18 Sample wake patterns for $h_0 = 0.75$ simulations with efficiency values $\eta = 0.376$ (18a) and $\eta = -0.386$ (18b)	36
19 Efficiency Contour and Sample Force value plots for $h_0 = 1.0$ simulations. In force plots, blue represents the coefficient of lift force, green the heave velocity, red the coefficient of moment scaled by 10^{-1} , teal the pitch amplitude scaled by 10^{-1} , and magenta the coefficient of power. (19b) $\eta = 0.394$ and (19c) $\eta = -0.042$	37

Figure	Page
20 Sample wake patterns for $h_0 = 1.0$ simulations with efficiency values $\eta = 0.394$ (20a) and $\eta = -0.042$ (20b)	38
21 Efficiency Contour and Sample Force value plots for $h_0 = 1.25$ simulations. In force plots, blue represents the coefficient of lift force, green the heave velocity, red the coefficient of moment scaled by 10^{-1} , teal the pitch amplitude scaled by 10^{-1} , and magenta the coefficient of power. (21b) $\eta = 0.43$ and (21c) $\eta = -0.44$	40
22 Sample wake patterns for $h_0 = 1.25$ simulations with efficiency values $\eta = 0.43$ (22a) and $\eta = -0.44$ (22b)	41
23 Flow visualization and non-dimensional force data from $h_0/c = 1.0$, $St = 0.4$, $\theta_0 = 90^\circ$. In the force plot, the x axis represents degrees in phase, blue represents the coefficient of lift force, green the heave velocity, red the coefficient of moment scaled by 10^{-1} , teal the pitch amplitude scaled by 10^{-1} , and magenta the coefficient of power.	43
24 Flow visualization and non-dimensional force data from $h_0/c = 0.75$, $St = 0.3$, $\theta_0 = 30^\circ$. In the force plot, the x axis represents degrees in phase, blue represents the coefficient of lift force, green the heave velocity, red the coefficient of moment scaled by 10^{-1} , teal the pitch amplitude scaled by 10^{-1} , and magenta the coefficient of power.	44
25 Simple control algorithm implemented in new control platform.	46
26 Convergence of (a) RMSE calculation and (b) Pitch Amplitude, θ_0 per each half cycle.	47
27 Picture of tow tank in experimental lab.	51
28 Picture of the carriage holding two of the linear motors and a rotational motor to induce pitch motion with a force sensor and foil extended from it.	52
29 Picture of taken of the control set-up mounted on the wall near the tow tank.	53

Figure	Page
B.30 In the force plots throughout this Appendix, blue represents the coefficient of lift force, green the heave velocity, red the coefficient of moment scaled by 10^{-1} , teal the pitch amplitude scaled by 10^{-1} , and magenta the coefficient of power.	63
C.31 Points in phase throughout a half cycle in which screenshots were taken.	88
C.32 $h_0/c = 0.5, St = 0.1, \theta_0 = 30^\circ$	89
C.33 $h_0/c = 0.5, St = 0.1, \theta_0 = 60^\circ$	90
C.34 $h_0/c = 0.5, St = 0.1, \theta_0 = 90^\circ$	91
C.35 $h_0/c = 0.5, St = 0.2, \theta_0 = 30^\circ$	92
C.36 $h_0/c = 0.5, St = 0.2, \theta_0 = 60^\circ$	93
C.37 $h_0/c = 0.5, St = 0.2, \theta_0 = 90^\circ$	94
C.38 $h_0/c = 0.5, St = 0.3, \theta_0 = 30^\circ$	95
C.39 $h_0/c = 0.5, St = 0.3, \theta_0 = 60^\circ$	96
C.40 $h_0/c = 0.5, St = 0.3, \theta_0 = 90^\circ$	97
C.41 $h_0/c = 0.75, St = 0.1, \theta_0 = 30^\circ$	98
C.42 $h_0/c = 0.75, St = 0.1, \theta_0 = 60^\circ$	99
C.43 $h_0/c = 0.75, St = 0.1, \theta_0 = 90^\circ$	100
C.44 $h_0/c = 0.75, St = 0.2, \theta_0 = 30^\circ$	101
C.45 $h_0/c = 0.75, St = 0.2, \theta_0 = 60^\circ$	102
C.46 $h_0/c = 0.75, St = 0.2, \theta_0 = 90^\circ$	103
C.47 $h_0/c = 0.75, St = 0.3, \theta_0 = 30^\circ$	104
C.48 $h_0/c = 0.75, St = 0.3, \theta_0 = 60^\circ$	105
C.49 $h_0/c = 0.75, St = 0.3, \theta_0 = 90^\circ$	106
C.50 $h_0/c = 0.75, St = 0.4, \theta_0 = 30^\circ$	107

Figure		Page
C.51	$h_0/c = 0.75, St = 0.4, \theta_0 = 60^\circ$	108
C.52	$h_0/c = 0.75, St = 0.4, \theta_0 = 90^\circ$	109
C.53	$h_0/c = 0.75, St = 0.5, \theta_0 = 30^\circ$	110
C.54	$h_0/c = 0.75, St = 0.5, \theta_0 = 60^\circ$	111
C.55	$h_0/c = 0.75, St = 0.5, \theta_0 = 90^\circ$	112
C.56	$h_0/c = 1.0, St = 0.1, \theta_0 = 30^\circ$	113
C.57	$h_0/c = 1.0, St = 0.1, \theta_0 = 60^\circ$	114
C.58	$h_0/c = 1.0, St = 0.1, \theta_0 = 90^\circ$	115
C.59	$h_0/c = 1.0, St = 0.2, \theta_0 = 30^\circ$	116
C.60	$h_0/c = 1.0, St = 0.2, \theta_0 = 60^\circ$	117
C.61	$h_0/c = 1.0, St = 0.2, \theta_0 = 90^\circ$	118
C.62	$h_0/c = 1.0, St = 0.3, \theta_0 = 30^\circ$	119
C.63	$h_0/c = 1.0, St = 0.3, \theta_0 = 60^\circ$	120
C.64	$h_0/c = 1.0, St = 0.3, \theta_0 = 90^\circ$	121
C.65	$h_0/c = 1.0, St = 0.4, \theta_0 = 30^\circ$	122
C.66	$h_0/c = 1.0, St = 0.4, \theta_0 = 60^\circ$	123
C.67	$h_0/c = 1.0, St = 0.4, \theta_0 = 90^\circ$	124
C.68	$h_0/c = 1.0, St = 0.5, \theta_0 = 30^\circ$	125
C.69	$h_0/c = 1.0, St = 0.5, \theta_0 = 60^\circ$	126
C.70	$h_0/c = 1.0, St = 0.5, \theta_0 = 90^\circ$	127
C.71	$h_0/c = 1.0, St = 0.6, \theta_0 = 30^\circ$	128
C.72	$h_0/c = 1.0, St = 0.6, \theta_0 = 60^\circ$	129
C.73	$h_0/c = 1.0, St = 0.6, \theta_0 = 90^\circ$	130

Figure		Page
C.74	$h_0/c = 1.25, St = 0.1, \theta_0 = 30^\circ$	131
C.75	$h_0/c = 1.25, St = 0.1, \theta_0 = 60^\circ$	132
C.76	$h_0/c = 1.25, St = 0.1, \theta_0 = 90^\circ$	133
C.77	$h_0/c = 1.25, St = 0.2, \theta_0 = 30^\circ$	134
C.78	$h_0/c = 1.25, St = 0.2, \theta_0 = 60^\circ$	135
C.79	$h_0/c = 1.25, St = 0.2, \theta_0 = 90^\circ$	136
C.80	$h_0/c = 1.25, St = 0.3, \theta_0 = 30^\circ$	137
C.81	$h_0/c = 1.25, St = 0.3, \theta_0 = 60^\circ$	138
C.82	$h_0/c = 1.25, St = 0.3, \theta_0 = 90^\circ$	139
C.83	$h_0/c = 1.25, St = 0.4, \theta_0 = 30^\circ$	140
C.84	$h_0/c = 1.25, St = 0.4, \theta_0 = 60^\circ$	141
C.85	$h_0/c = 1.25, St = 0.4, \theta_0 = 90^\circ$	142
C.86	$h_0/c = 1.25, St = 0.5, \theta_0 = 30^\circ$	143
C.87	$h_0/c = 1.25, St = 0.5, \theta_0 = 60^\circ$	144
C.88	$h_0/c = 1.25, St = 0.5, \theta_0 = 90^\circ$	145
C.89	$h_0/c = 1.25, St = 0.6, \theta_0 = 30^\circ$	146
C.90	$h_0/c = 1.25, St = 0.6, \theta_0 = 60^\circ$	147
C.91	$h_0/c = 1.25, St = 0.6, \theta_0 = 90^\circ$	148
D.92	Matrix format of pressure and velocity fields ".mat" files.	150

CHAPTER 1

Introduction

Energy demand around the world is expected to continue increasing over the upcoming decades [6]. Energy projections from BP state that increase in energy demand is mainly due to population and income growth [6]. Since 1900 the population has more than quadrupled and primary energy consumption has increased by a factor of 22.5. Similar energy consumption trends are expected to occur over the next 20 years [6]. With such an expected increase in demand, the interest in research related to discovering improved methods of harnessing energy has blossomed. Wind energy (increased by 20% in 2011) and solar energy (increased by 80% in 2011) have been identified as effective renewable energy sources for years [7]. Ocean energy sources such as wave energy harnessing, have emerged more recently (Aguadoura wave farm in 2008, north of Portugal) [8]. Aside from waves as an energy source, harnessing energy from tidal driven currents has been an area of interest due to the fairly high kinetic energy density in a current [9], [10], [11], [12], [13], [14]. One difficulty that is faced with this energy source is the constant change in tidal direction throughout a 24 hour period. It would be ideal to construct energy extraction systems to react like biological systems that adapt to their environment by using environmental sensing.

Tidal driven energy extraction systems that utilize oscillating foils are currently being implemented around the world, [10], [11], [12], and [13]. A few of these systems are described in detail in the Previous Research section to follow. The ultimate goal of any energy extraction device is to reduce the cost per kW-hour. This can be done by making the device more efficient or by reducing its manufacturing and maintenance costs. Increasing the overall efficiency of these

flapping foil systems was examined. This motivated the idea to study in more detail, the mechanisms that fish utilize to improve their motion. Conclusions from this research can be immediately implemented by multiple projects to upgrade the performances of flapping foils.

1.1 Biological Inspiration

System designs inspired by nature have been used in science and engineering fields for hundreds of years. Since organisms must adapt to different environments, some believe that evolution has produced the most efficient systems. It can be recognized that prior to the first successfully flown airplane design from the Wright Brothers, they indulged in a fascination and study of birds. Application of biologically inspired phenomena is commonly known as Biomimetics. Biomimetics and Bio-Inspiration have played a very important role in many Ocean Engineering advances as well. Specifically, the propulsion of ocean animals have led to implementation of fin shaped thrusters on autonomous underwater vehicles, [15], [16], [17], [18]. Even observations of how ocean mammals used these fins to propel are implemented in the specific motion of the vehicle thrusters [19]. This thesis project is inspired by the energy extraction and conservation that fish embody. For example, salmon swim several hundred miles upstream without stopping to feed [20]. Trout exploit eddies and turbulence in the water to utilize similar excellent energy extraction abilities [21]. This ability for fish is due to their streamlined, foil-shaped bodies as well as their sensory capabilities. Recent renewable energy systems that implement streamlined shaped bodies, similar to those of fish, will be reviewed and discussed.

1.1.1 Lateral Line System

All fish have pressure sensing arrays along their bodies that make up their lateral line system [3]. The system is composed of a spatial array of pressure sensors known as neuromast receptor organs. These neuromasts are located along the head, trunk, and tail of fish as in Figure 1. Neuromasts are small epithelial receptor organs made up of hundreds to thousands of sensory hair cells oriented 180° to one another. The ciliary bundles of hair cells are covered by a gelatinous cupula that serves as the biomechanical interface between the flow and sensors [1].

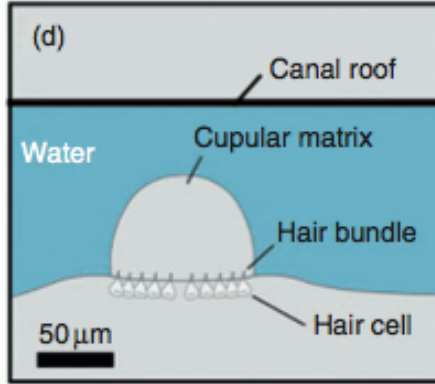


Figure 1: Schematic of canal neuromast (each ciliary bundle represented by a single line). [1]

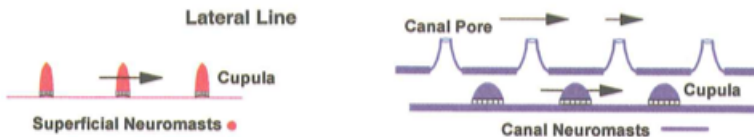


Figure 2: Schematic showing different types of neuromast receptor organs in fish. [2]

Neuromasts come in two forms: superficial neuromasts, which are distributed on the skin surface, and canal neuromasts (Figure 2). Inspiration for this project comes from the canal neuromasts due to their functionality. These head canals run along the body (Figure 3) and have pores opening the canal to external fluid flow

(Figure 2). When there is a pressure gradient between two adjacent pores, fluid in the canal is disturbed, bending the cupula, and the ciliary bundles contained in it. This generates a stimulus, which is dependent on the direction that the neuromast is bent, that is transmitted to the brain [1]. By sensing changes in pressure that signify changes in flow with these receptor organs, fish are able to make minor adjustments in their body position at little to no effort to them for large gains in energy [21]. This thesis investigates the effectiveness of bio-inspired pressure sensor arrays in enhancing efficiency of a flapping foil energy harnessing system.

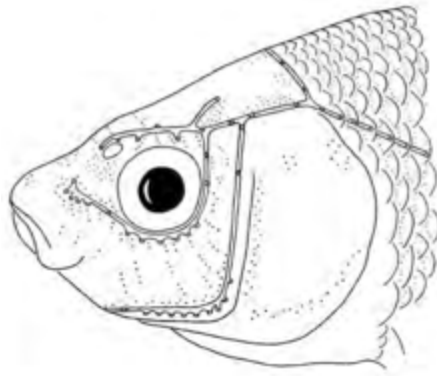


Figure 3: Lateral view of canals that contain neuromasts in a Goldfish. [3]

1.2 Previous Research

Alternative energy resources have been researched for decades as the demand for more energy has continually increased. Such systems that study the characteristics and use of flapping foils have been reviewed for this project. In addition, applications of pressure sensing arrays similar to the lateral line system were studied.

1.2.1 Artificial Lateral Line Sensing

Multiple engineers have worked to reproduce the positive effects of the sensory lateral line system. Cheng [22] and Yang [23] took an approach to mimicking the physical design of the neuromasts. A cantilevered arm attached to a strain gauge

was used within a canal in order to obtain a pressure gradient along the body in question. Fernandez et al [24] took the more biologically inspired approach to implement this sensor system in a more space efficient way. Their research used a linear array of off-the-shelf pressure sensors along with an analytic model of fluid flow in order to detect nearby objects. They were able to demonstrate that with the use of as little as four pressure sensors paired with the use of a potential flow model, the problem can be inverted in order to locate the position of an object and identify the existence of a vortex. Fernandez et al [24] successfully distinguished shapes and sizes of nearby objects through active and passive pressure sensing.

Xu et al tested the use of pressure sensor arrays for feedforward data to assist in underwater vehicle control [25]. They constructed an AUV model based on the prototype CephaloBot that was developed by the group [17]. Pressure measurements were recorded at fixed locations on the body, and by using curve fitting techniques, the pressure distribution over the vehicle's elliptic profile was reconstructed. Hydrodynamic force estimations on the AUV were calculated without considering added mass and viscous damping. Xu et al [25] conclude that their pressure feedforward design may serve as important guidance for maneuvers due to observed improvement in control performance.

Similarly, at Michigan State University, Abdulsadda and Tan implemented an artificial lateral line system using ionic polymer-metal composite (IPMC) sensor arrays [26]. This artificial lateral line array was tested and proposed for underwater vehicle navigation. Validation experiments were run in the localization of a vibrating sphere (dipole source) underwater. Experiments showed that only a few sensor elements were needed for the IPMC-based lateral line to be able to localize sources approximately 1 to 2 body lengths away. With implementation of larger scaling, Abdulsadda and Tan's research [26] could lead to the improvement

of underwater vehicle navigation efficiency.

1.2.2 Flapping Foil Energy Harvester Academic Work

McKinney and DeLaurier investigate the idea of flapping foils being utilized for energy extraction [27]. In 1981, they constructed what they called the "wingmill" in a wind tunnel that was put under harmonic pitch and heave motions variably out of phase with one another. A symmetric NACA 0012 airfoil was used in these experiments and power output was measured when oscillating. McKinney and DeLaurier were able to conclude from their research that this wingmill could be a good competition for the more commonly known windmill for power generation. They realized that theoretical results underestimated possible power outputs in which they observed a maximum of 9 Watts for a 110° maximum angle of attack.

Both Isshiki [16] and Grue [15] applied the idea of the wingmill but submerged it in flow for propulsion mechanisms. They attached the wing to the bottom of a boat and oscillated it. They analytically and experimentally verified that the hydrofoil-boat combination successfully propelled the body. The heaving of the ship was translated to the foil which as a result, generated vortices similar to a jet. Zhu and Peng conducted research of submerged flapping foils for the purpose of harnessing energy from flow, specifically in their case for low Reynolds numbers [28]. Their results showed that the phasing between the formation of leading edge vortices contributed greatly to overall energy output. They concluded that leading edge vortices, if timed correctly, can contribute to the pitching motion of the foil, allowing more energy to be transferred back into the system. Zhu and Peng's discovery has sparked the notion of detecting leading edge vortices as an approach to optimize our energy extraction system.

Simpson [9], examined the hydrodynamic performance of flapping foils to extract energy in a two dimensional flow. He observed the effects that the various

hydrodynamic parameters had on the efficiency of harnessing energy with a symmetric NACA 0012 flapping foil. The foil was forced in pitch and heave motion for various heave to chord ratios. Energy extraction efficiencies of up to $\eta = 0.45$ were found within a small region for small oscillation amplitudes. In comparison, broader regions of substantial efficiency, to $\eta = 0.20$, were observed at large oscillation amplitudes. Simpson also studied the types of vortex shedding for different energy extraction efficiency. The highest efficiency trials seemed to exhibit the same formation of vortex shedding (2P mode).

Inspiration from fish rose from research done by Liao et al on the efficiency of trout locomotion in a wake [21]. Their research used a combination of flow visualization and observation of electrical activity produced by skeletal muscles. They concluded that when a euthanized trout was exposed to a vortex street, it would adopt a mode of locomotion to slalom in between these vortices. It is shown that fish have a body shape that doesn't require muscle to act as a self-correcting hydrofoil when caught in a vortex street. Liao et al [21] shows that the choice to use a foil shape similar to that of fish is valid for current driven energy extraction devices.

1.2.3 Commercial Flapping Foil Devices

The Engineering Business Ltd. had previously began work on a tidal stream generator in 1997 known as the Stingray [12]. The project made it through three phases before being put on hold for lack of funding. Phase one of the project included a technical and commercial feasibility study in which an outline machine design was developed. The Stingray is a wing-like hydroplane attached to a seabed mounted supporting frame by a pivot arm. As current passes over the plane, lift and drag forces cause the plane (and arm) to lift. This actuates cylinders at the arm pivot point which turn a hydraulic motor that in turn drives an electric

generator. Hydraulically powered cylinders are used to alter the apparent angle of attack of the hydrofoil relative to the current. The angle of attack will be programmed to remain at the optimal apparent angle. When the hydro-plane reaches its maximum and minimum height limits, the angle of the foil is reversed and the arm is driven in the opposite direction. During 2002 in phase two of the project, the Stingray was built and installed in Yell Sound, Shetland Islands. It was proven that the concept had considerable potential but underwent modifications in 2003 during phase three. A suspected unit energy cost for a pre-commercial MW demonstration farm was projected at 6.7 pounds per kWh [12]. More modifications and implementation are awaited.

A company known as BioPower Systems based out of Sydney Australia is currently developing a technology known as bioSTREAM. The design includes a whale's tale shaped fin attached to a pivoting arm mounted on a supporting frame on the seafloor. The fin oscillates in moving water to extract energy from sites that have peak current speeds of 2.5 m/s [10]. The angle of attack is continually adjusted by an on-board computer in order to simulate a swimming motion for the fin. Currently, a 250kW bioSTREAM demonstration project is in development to be deployed.

In the UK, Pulse Tidal is in the stages of beginning work developing a fully commercial, 1MW tidal-energy generator [13]. The system is made up of dual hydrofoils that move up and down in tidal streams to drive a generator. Pulse Tidal installed a test rig off Immingham in the Humber Estuary from 2009 until 2012. Working at full capacity, 100kW were produced by the machine and fed directly into Immingham Chemical company. This was enough to power 70 houses in the area. The project successfully demonstrated that hydrofoils can be used to capture energy from tidal flows with comparable efficiency to those of rotary

devices.

At the University of Laval, the research group of Guy Dumas in the Mechanical Engineering Department is embracing the concept of oscillating hydrofoils in flow as well. They are developing the "Oscillating-foils Hydrokinetic Turbine (HAO)". The results from a field test conducted in 2009 confirmed the potential of HAO with performances that are competitive to those of rotating blade technologies [11]. In 2012 to 2014, the second generation systems of the oscillating-foil turbine will be put into place.

1.3 Limitations

There are limitations on the amount of energy that can be extracted from any system. Albert Betz, a German Physicist, derived a law in 1919 that determined the maximum percentage of Kinetic energy that could be extracted from wind based on conservation of mass and momentum. The Betz limit states that only 59.4% of the available kinetic energy in a wind/water system can be harvested. On average, a wind turbine can achieve at peak, 75% of the Betz limit or efficiency values of approximately 0.4. The goal is to push these limits and get as close to Betz limit as possible.

In addition to the Betz limit, the amount of energy available from a source dictates the energy that can be harvested. Available energy from a source can be measured by a relationship to its mass density, Equation (1).

$$Power_{Available} = \frac{1}{2}\rho U^3 A \quad (1)$$

Here, ρ is the fluid density, U is the fluid flow velocity and A is the cross-sectional area being observed. Using this expression along with the densities of air, $1.225 \frac{kg}{m^3}$, it is calculated that a cubic meter of wind moving at $1 \frac{m}{s}$, the available power is $0.6125 \frac{J}{s}$. In water with a density of $1000 \frac{kg}{m^3}$, for the same flow speed and

volume, $500\frac{J}{s}$ is available. Clearly, in terms of the available power for harvesting, ocean energy is a competitive choice.

Another limitation that affects the cost per kWh of a system is taking into account the manufacturing and maintenance costs. Since the energy available in a specified volume is orders of magnitude higher in water than air, energy extraction systems in water can be much smaller than the giant size of wind turbines. This saves on manufacturing costs. However, maintenance may require more in the water due to the possibility of corrosion. The choice of ocean source over wind source energy is validated here due to water's higher energy density. This thesis will explore motions that will push closer to the Betz limit for percentage of energy harvested.

1.4 Organization of Thesis

Chapter Two begins with a brief overview of relevant parameters from hydrodynamics that are used to describe the characteristics of a flapping foil and its motion. Equations of motions that will be applied throughout the model will be introduced.

Chapter Three introduces the first step to utilizing pressure sensing by discussing the optimization of the number of pressure sensors needed for control. Optimal locations for these sensors are determined in order to provide an acceptable representation of the pressure gradient around the foil.

Chapter Four discusses the experimental database of forced foil motions and the parameter space it covered. This chapter presents efficiency and force results from these simulations.

Chapter Five introduces a platform built for motion control of the foil based on pressure measurements. A simple control algorithm is described and applied to the platform.

Chapter Six discusses the laboratory set-up for future validation experiments and implementation of control on flapping foil motion. The lab is described along with pictures of the set-up.

Chapter Seven contains a conclusion of the findings of the thesis. Future work for the project is proposed and recommendations are made.

Many plots and tables displaying results are presented in the Appendices at the end of this thesis.

CHAPTER 2

Kinematic Set-Up

2.1 Equations of Motions

For 2-D motion of the foil, two of the possible three axes of motion are considered to describe the oscillating foil kinematics. Heave and pitch are used to define the movement of the foil, but surge is not considered. Heave, $h(t)$, is the transverse or vertical displacement of the foil with respect to the free stream velocity direction. Pitch motion, $\theta(t)$, is the rotation about the pitching point located a distance from the nose on the cross section of the foil. When these motions are combined, an angle of attack, $\alpha(t)$, and a combined velocity angle, $\beta(t)$, results as depicted in Figure 4 below.

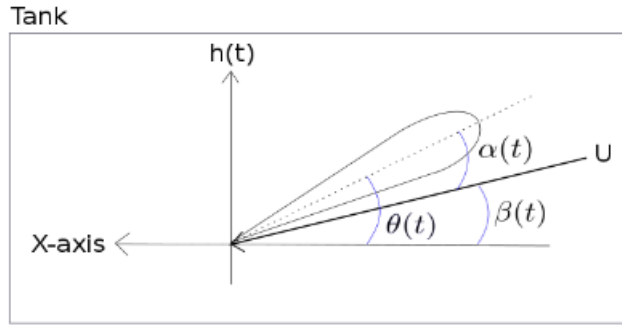


Figure 4: Definitions of motion for an oscillating foil in two degrees of freedom in which U is the free stream velocity, $h(t)$ is the heave velocity, $\alpha(t)$ is the nominal angle of attack, and $\theta(t)$ is the pitching position.

In this system, we have more variables than degrees of freedom. In order to be able to solve for the motion of the foil, a clear definition of which variables are independent and which are dependent must be made. In learning from previous research [28], [9], a similar assumption that the motion of oscillating foils can be represented sinusoidal will be made. Heave, pitch, and angle of attack will be the three motions that will be driven in the flapping foil system. If we take a look at

Figure 4 again, we can determine the relationship of dependence each motion has on one another.

The pitch motion, $\theta(t)$, is made up of the sum of the angle of attack, $\alpha(t)$ and the combined velocity angle, $\beta(t)$. If we use basic trigonometry rules to solve for β , we get an equation to describe how the directions of motion are related:

$$\theta(t) = \alpha(t) + \beta(t) = \alpha(t) + \arctan\left(\frac{\dot{h}(t)}{U}\right) \quad (2)$$

In order to avoid an over-determined system, only two of the motions can be forced while the third must react. In our flapping foil system, heave and pitch motion will be defined as forced harmonic functions and angle of attack will react to the fluid forces produced from the $h(t)$ and $\theta(t)$ motions. Angle of attack was not chosen to be the dependent variable because of the specific control algorithm to be used for this system. Control will be applied to the pitch motion based on measurable heave velocity values. Therefore, heave and pitch must be the independent variables. Heave and pitch are represented as

$$\theta(t) = \theta_0 \sin(\omega t + \Psi) \quad (3)$$

$$h(t) = h_0 \sin(\omega t) \quad (4)$$

where θ_0 is the maximum pitch amplitude in radians, ω is the frequency of oscillation in radians per second, t is time in seconds, and Ψ is the phase angle between the heave and pitch motions in radians. For the ability to compare to previous work from Zhu [5] and Simpson [9], a phase shift of $\frac{\pi}{2}$ is used for Ψ in Equation (3).

2.2 Relevant Parameters

With heave and pitch defined, there are important non-dimensional parameters that are associated with these motions. Commonly referred to and dependent

upon is the non-dimensional heave amplitude, h_0 , which is also known as the heave to chord ratio. Heave amplitude signifies the magnitude of the sweeping motion that the flapping foil undergoes in relation to fractions of the chord length. This is evident in the equation defining the heave motion above in Equation (4).

Harmonic heave and pitch motions result in a certain frequency of the foil's oscillation in time. Different frequencies of flapping motion will be a big contribution to the efficiency of energy extraction. A certain frequency in motion also results in a frequency related to the vortex shedding. A common dimensionless parameter used to characterize such shedding of vortices is known as the Strouhal number, St . The Strouhal number describes the oscillation of flow about the foil and is determined by the frequency of the heave motion, f , the characteristic length, L , and the free stream velocity, U .

$$St = \frac{fL}{U} \quad (5)$$

The characteristic length for flapping foils is commonly measured as the total heave excursion, h_T , which is equal to double the heave amplitude, h_0 .

$$St = \frac{fh_T}{U} = \frac{f2h_0}{U} \quad (6)$$

The ratio of inertial to viscous forces, Re , is an important parameter of flow known as the Reynolds number (7). It is defined below where U is the free stream velocity, L is the characteristic length and ν is the kinematic viscosity of the fluid. In these experiments, L is defined as the chord length of the foil.

$$Re = \frac{UL}{\nu} \quad (7)$$

The characteristics of the flow around the submerged object deviate with changes in Reynolds number.

2.3 Simulation Set-Up

Simulations are 2-Dimensional of a body submerged in a uniform fluid flow. A NACA0015 foil is the streamlined body modeled. NACA foils are a standardized shape for the cross section of the foil developed by the National Advisory Committee for Aeronautics. The "00" denotes that the foil is symmetric. If this was anything other than zeros, the foil would bend or camber would not be even on top and bottom. The second sequence of numbers, "15" in this case, signifies the maximum thickness of the foil. This is a percentage in relation to the chord length, meaning the maximum thickness point of the foil is 15% of the chord length.

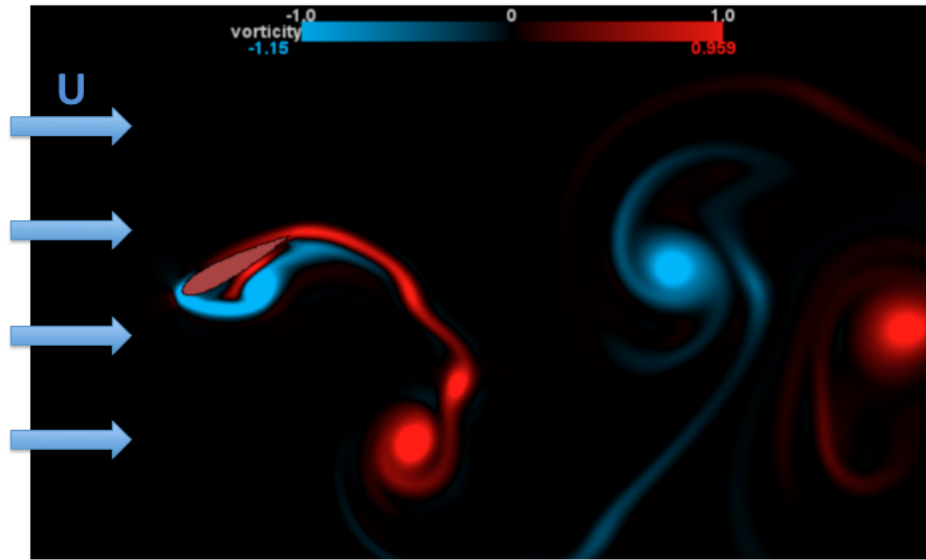


Figure 5: Schematic representing the computational domain and fluid flow orientation of simulations where U is the uniform fluid flow.

The simulated flow will be oriented head on to the nose of the foil as seen in a cross-sectional view in Figure (5). Uniform flow is implemented for the velocity field approaching the foil. The full computational domain is approximately 1 chord length upstream from the foil and 5 chord lengths down stream. About 5 chord lengths cover the overall height of the computational domain with the

body approximately at the center.

CHAPTER 3

Sensor Array Optimization

The motion control of a flapping foil energy extraction systems requires a source to communicate to the controller. Pressure will be measured and used to inform the controller. Therefore, the overall project begins with a determination of the quantity of pressure sensors to be implemented on the NACA foil. A compromise between the minimal space available on the foil, the cost of pressure sensors, and the accuracy of the pressure field representation must be attained. A random search algorithm is defined for determining this minimum number of sensors and their locations. This algorithm requires a computational fluid dynamics simulation for testing various sensors and positions.

3.1 Numerical Source Code

A 2-D numerical simulation of the energy harvesting foil was performed using the open source software LilyPad [29]. A library of various different functions that compile into Lilypad are available in an accessible cloud online. This allows for updates to be made to the functions and new functions to be added at anytime. Open source allows for multiple people to manipulate functions and capabilities of the flow simulation software. This open source software was chosen for its simplified calculation methods, allowing real time simulation for fast processing with good solutions of pressure.

LilyPad is a computer model that implements a 2-D flow simulation using a Boundary Data Immersion Method (BDIM). This is an accurate Cartesian-grid system written for the immersion of solid bodies in a fluid with general boundary conditions [29]. BDIM is derived based on a general integration kernel formulation which analytically combines the field equations of each domain (fluid and object)

and the interfacial conditions. The resulting governing equation for the system preserves the behavior of the system in a Cartesian-grid method, including stable and accurate pressure values on the solid boundary, which are of most interest to this project.

A 2-D model was created in Lilypad to simulate a NACA0015 symmetric foil in BDIM flow with forced sinusoidal pitch motion. Pressure is evaluated at 200 locations around the foil. Measurements of foil movements based on the coordinate system are recorded as well. The forces and moments exerted on the foil are evaluated based on an integral of these pressure measurements around the foil. Using these force values, a function to allow heave motion to react to this force was formulated. This can be computed for every time-step using a first order Euler integration method. Along with the option of heave reacting to the pressure force on the foil, there is also the option to force the heave motion along with the pitch. Viscous stresses are neglected in determining the force on the body since the pressure-based forces dominate in this type of unsteady flow. The resolution of the simulation window is 32 bits per chord length.

3.2 Fluid Moment Approximation

Using all pressure values p_i for $i = 1 : 200$, and segment lengths on the body, l_i , that each pressure measurement is centered at, the fluid moment is calculated by

$$M = \sum_{i=1:200} p_i * l_i * [n_y(x_i - x_{cen}) - n_x(y_i - y_{cen})] \quad (8)$$

where $n_{x/y}$ are the normal projections at each point i around the foil, x_i and y_i are the coordinates of p_i , and x_{cen} and y_{cen} are the coordinates of the centroid of the body. Using all available pressure locations on the body, this computation gives the actual moment exerted on the body by the fluid. Lower order approximations may be made using fewer pressure measurements.

Similarly, the fluid force on the foil is calculated with respect to the pressure around the foil as well with the following integral,

$$F = \sum_{i=1:200} p_i * l_i * n_x, \sum_{i=1:200} p_i * l_i * n_y) \quad (9)$$

For q number of locations around the foil, pressure measurements, p_i for $i = 1 : q$, will be used to calculate a fluid moment. This will simulate the idea of putting pressure sensors at those q locations. Each p_i will be scaled by the segment length that it is centered at. The segment length corresponding to a pressure point is defined as the distance from the midpoint between p_{i-1} and p_i to the midpoint between p_i and p_{i+1} as seen in Figure 6 below. The same calculation as equation (8) above is made in which $i = 1 : q$ for the set of q sensors with pressure measurements p_i .

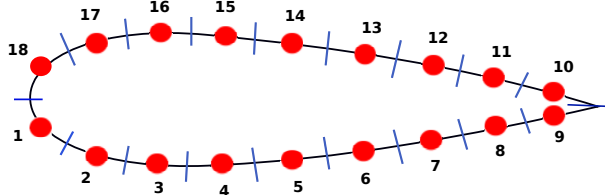


Figure 6: Example of 18 equally spaced sensors around the foil. Red circles symbolize $q=18$ sensors and the blue lines mark the bounds of the corresponding segment lengths.

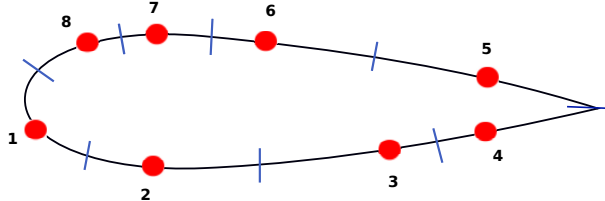


Figure 7: Example of 8 randomly spaced sensors around the foil. Red circles symbolize $q=8$ sensors and the blue lines mark the bounds of the corresponding segment lengths. Notice here that the sensors locations are necessarily centered in their segment, but the segment boundaries are centered between corresponding sensors.

The calculation of segment length was kept general allowing for sensor loca-

tions to be completely random, rather than limiting them to being equally spaced. Since the pressure segment boundaries are defined as midpoints between two corresponding sensors, the locations themselves can vary as seen in Figure 7.

Error of the approximate fluid moment calculation is determined by a comparison with the fluid moment calculation made in the 2-D simulation using all available pressure measurements. This error will be the cost function when applying optimization methods to determine the best pressure sensor locations that can still produce a reasonable fluid moment approximation. The error between the actual fluid moment and the approximated fluid moment of equally spaced locations was used to determine a good choice for the minimum number of sensors that can be placed on the foil.

3.3 Sensor Optimization

Initially, equally spaced sensor locations were assumed around the body. The approximate fluid moment was calculated and compared to the actual fluid moment. The total number of sensors for the calculations were varied from as high as 200 sensors to 4 sensors. Errors in the fluid moment calculation are shown in Figure 8. A total of 8 sensors were chosen and implemented throughout the rest of this thesis project. This number was chosen because of its location before a significant increase in error which is clear to see in the plot in Figure 8.

Placement of the sensors is crucial to the accuracy of the fluid moment approximation on the foil as the gradient of the pressure field on a flapping foil can be very extreme between respective locations. Represented in Figure 9 below, a small angle of attack produce a fan like distribution of the pressure on the foil. Thus, putting sensors on the nose of the foil would provide drastically different results from placing sensors on the tail of the foil. The goal is to place the pressure sensors strategically in order to produce an accurate approximation of the pressure

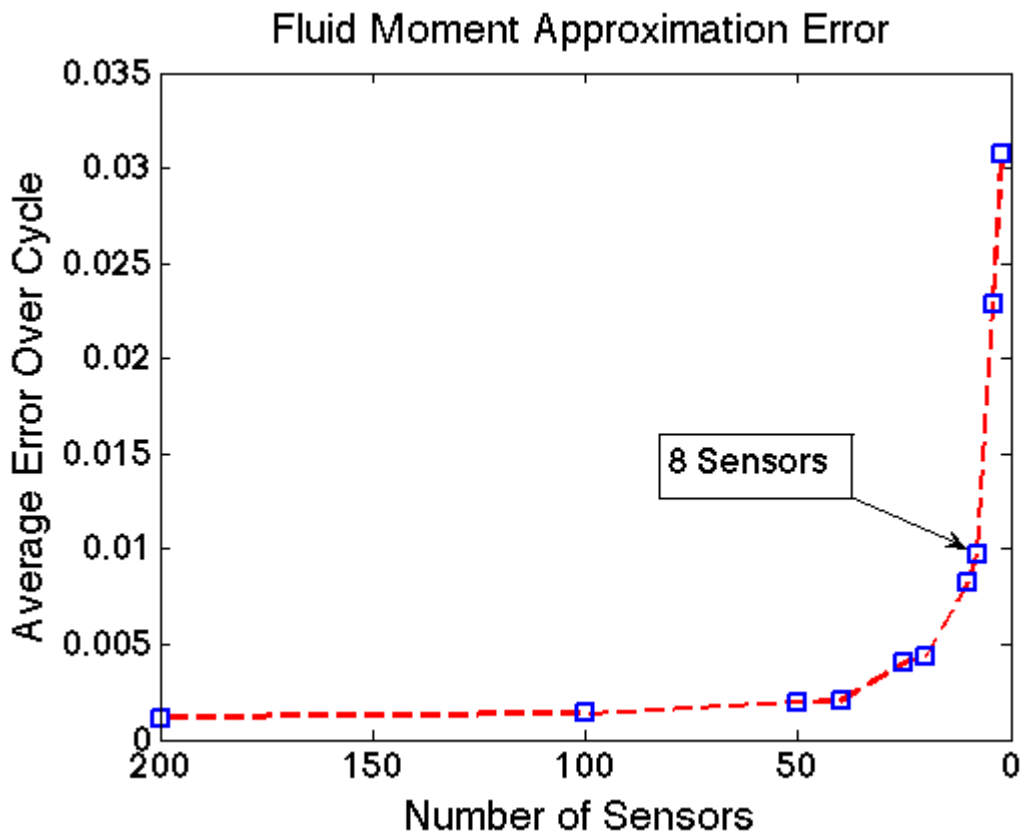


Figure 8: Plot showing error in approximate fluid moment calculation for various numbers of equally spaced sensor locations. A number of 8 sensors is chosen due to the large increase in error for fewer sensors. At 200 sensors, minimal error is due to rounding segment lengths l_i to significant digits.

field around the foil.

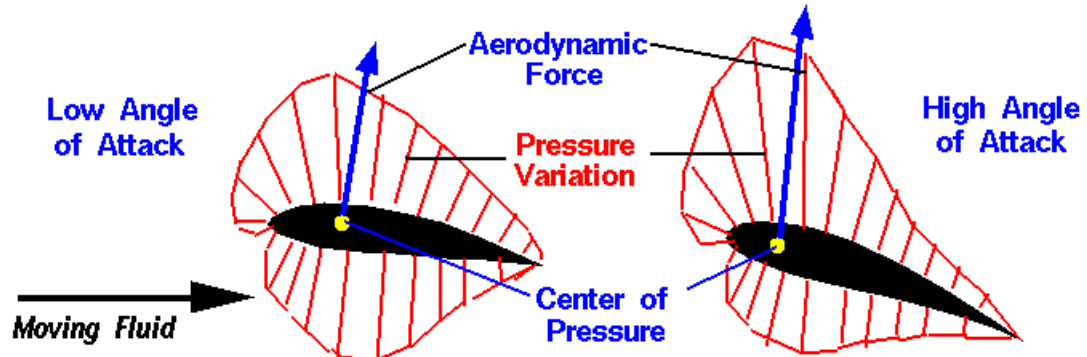


Figure 9: Representation of the pressure gradient around a NACA foil created by [4].

An optimization method was implemented in order to choose and verify the best eight locations to place the pressure sensors. A constraint was enforced that the sensor locations on the top would mirror the locations on the bottom. This rule was chosen based on the idea that the foil is moving in heave in both directions. Therefore, pressure sensors would have to be located on both the top and bottom of the foil in order to properly measure the pressure gradient around the foil. The mirrored locations on both sides is expected to be the best approach since the heave motion will be similar in both directions and this placement of measurements will improve the approximated integral calculation. Therefore, four locations will be optimized based on the rule that the other four will be mirrored about the chord line. For each of the eight segments along the foil, the pressure is assumed to be constant over that length.

3.3.1 Random Search

A random search is used to find best pressure sensor locations based on matching the fluid moment. A Random Search algorithm specific to determining sensor locations for the flapping foil system was compiled and can be seen below in Figure 10. The algorithm begins by choosing a population made up of arrays of 8 different sensor locations. A set of 1000 arrays of sensor locations ("members" of the "population") was originally generated. The members were randomly selected and subjected to constraints that: (i) no sensor location could show up more than once in each array/member and (ii) that sensors 5 through 8 mirrored sensor locations 1 through 4 that were randomly selected. Once the population of 1000 members was generated, pressure values were taken at the sensor locations for each member, and an approximate moment was calculated (Equation (8)). This calculation was done for time steps of data over a whole cycle of the foil's motion.

Each solution per time-step is evaluated using an error metric. The error was

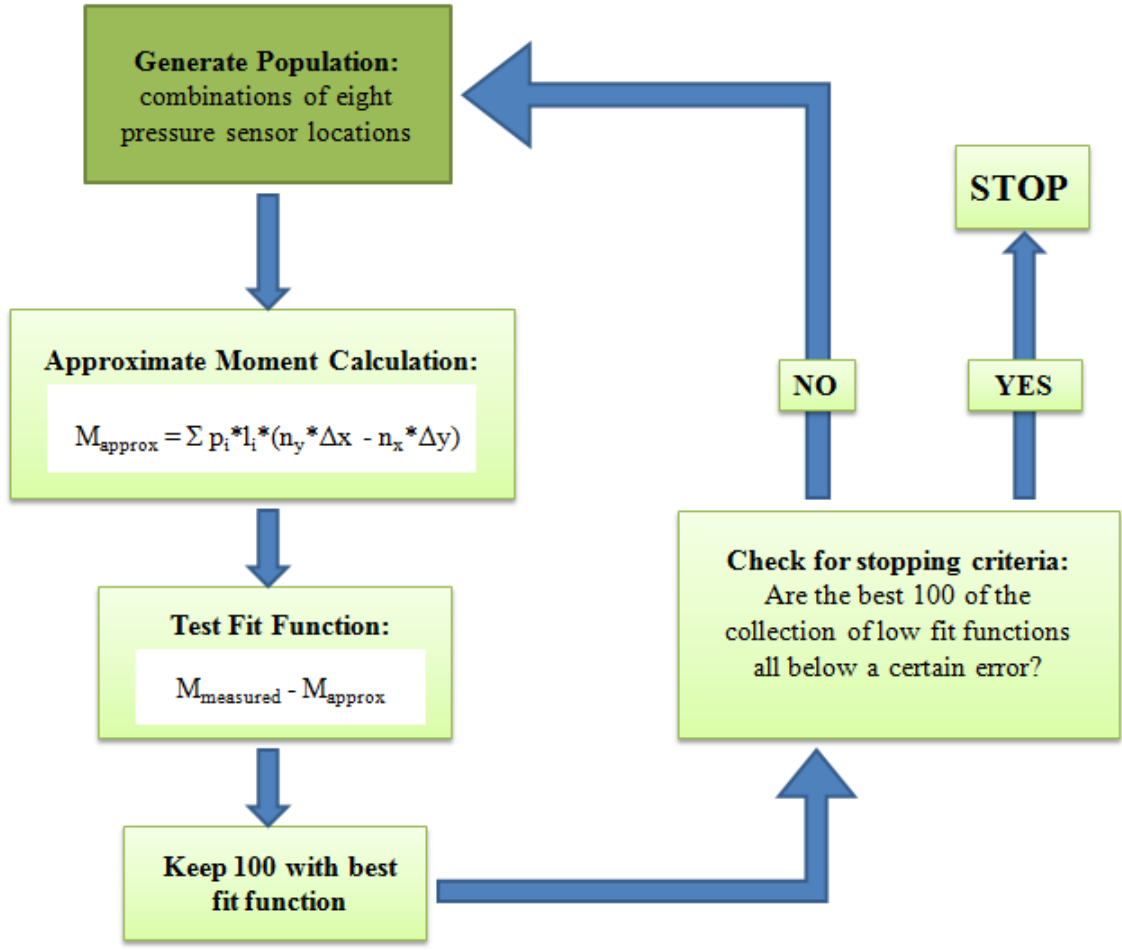


Figure 10: Flow chart representing steps in random search algorithm used for finding the optimal locations for pressure sensors on a hydrofoil.

defined as the difference between the actual fluid moment calculation generated from LilyPad and the approximate moment calculated with the 8 sensor locations in each array. These error calculations were averaged over the cycle for each member in the population, and were compared. The fit function of error can be seen in Equation (10) below, where n is the number of time steps. The 100 members with the lowest errors were stored.

$$\eta = \frac{\sum_n (M_{actual} - M_{approx})}{n} \quad (10)$$

The random search continued to run and create new populations until a certain cut-off criteria of error is met. Once the best 100 of all the good members stored have errors below a chosen value, the control algorithm ends. Solutions for various cut-off errors are shown in the Results section in Figures 11a and 12. For an infinite amount of time, a random search method will always converge to the best solution for your parameter space. However, the method is computationally expensive since the error must be calculated for every random model generated. Reaching a good solution is very dependent on what the cut-off criteria is and increases the probability of reaching an optimal solution by a large sample number.

The fluid moment can be used to determine the optimal sensor location due to its dependence on pressure and its importance in the future power calculations. It is calculated based on an integrated pressure. Using a term based on an integrated pressure allows us to compare if the pressure locations chosen to put sensors at will give a reasonable interpretation of the pressure gradient around the foil. The fluid moment shows up in the power term due to torque that quantifies the required power input due to the desired motion of the system. So if we can monitor and minimize the fluid moment on the foil, less power will be needed to achieve the desired motion resulting in power to be harvested.

3.4 Results

With increasingly smaller margins of error set in the cut off criteria, larger numbers of populations were tested against the fit function. In Figure 11a, the outcomes of 100 sensor location arrays with the lowest fit function are plotted on the foil shape. The dots are scaled by the number of array that include that specific location. In Figure 11, (a) is plotted after 69 populations (each with 1000 possible sensor array locations) were tested and (b) is after 236 populations. The axis in these figures are consistent with the specific coordinate system used in the

2-D simulations. Looking at 11a, there are sensors located in various locations around the foil with six wide, prominent locations. After more populations tested in 11b, we can see the 8 prominent location areas. This is already showing a good approximation of where the 8 sensors can be attached around the foil.

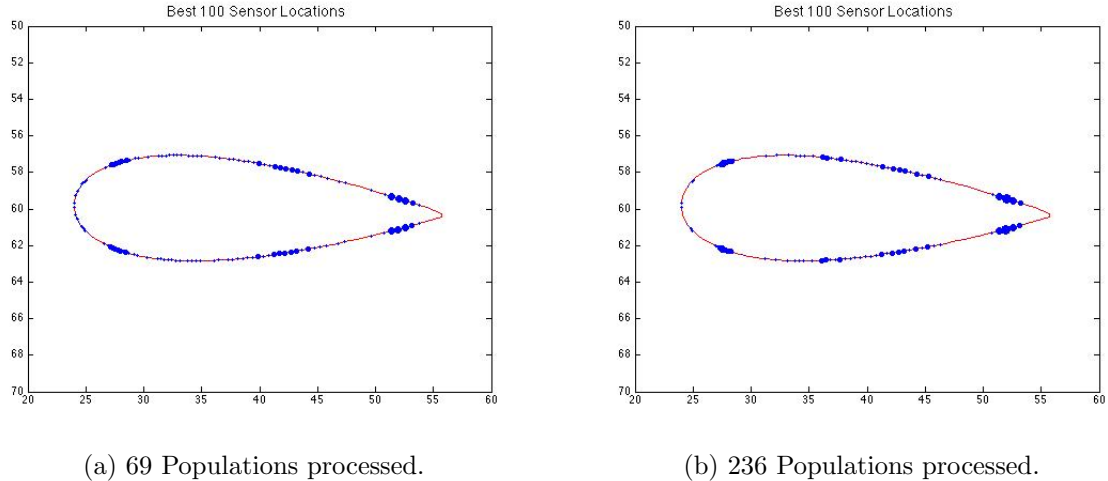


Figure 11: Results from Random Search method after (a) 69 populations and (b) 236 populations. These plots include the sensor locations for each of the best 100 members and scales the circle at the location based on how many members had that location in its array. The axis are coordinates in relation to global coordinate grid in LilyPad 2D Simulations.

After applying a lower error for the cut-off criteria that ends the algorithm, 2396 populations were created and tested to result in the locations specified in Figure 12 below. Four of the locations are very prominent for sensor locations. The other four have become more dense areas than in plot 11b. When the data points are examined, there are clear pairings between two corresponding locations. If you choose a specific spot in one of the clusters, then there is a consistent paired location in the adjacent cluster. This set of locations in Figure 12 provides a clear guideline for sensor array placement on a symmetrical NACA foil.

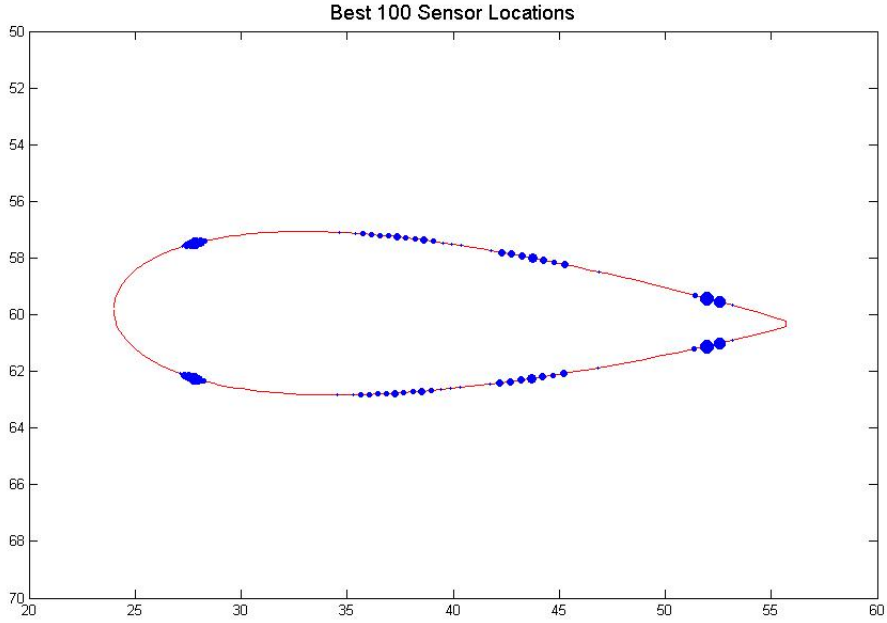


Figure 12: Results from Random Search method after 2396 populations. Best 100 arrays of sensors locations plotted.

3.5 Discussion

The optimal location of the eight pressure sensors around the foil are described in relation to the distance along the chord starting from the nose. The optimal locations of four sensors on the top and four on the bottom of the foil are $0.3325 * c$, $0.6225 * c$, $0.7872 * c$, and $0.9407 * c$. These locations correspond to specific spots in the eight dense areas from Figure 12.

It is important to observe that this sensor optimization was applied to a specific motion trajectory of the foil. Pitch amplitude reached 60° with a maximum heave amplitude to chord length of 1.0. It was not tested whether these locations would deviate if applied to smaller or larger amplitudes of motion. It is anticipated that not much change would occur with respect to the sensor locations. The pressure gradient would be expected to be different in magnitude, but would scale between location regions. Further optimization tests are necessary to validate these

sensor locations over the total possible trajectories of the foil.

CHAPTER 4

Database

A database of output data from flapping foil motions will benefit related research in the future. A model was successfully written in the open source program, LilyPad, to simulate the NACA0015 flapping foil in uniform flow at a specified Reynolds number (Re). For the simulations depicted in the Appendices, Re was set to 1000 for a direct comparison to [5]. A clear depiction of the wake is observed in the computational domain downstream from the foil. An example of this is shown in Figure 13 for $h_0 = 1.0$, $\theta_0 = 50^\circ$, and $St = 0.1$.

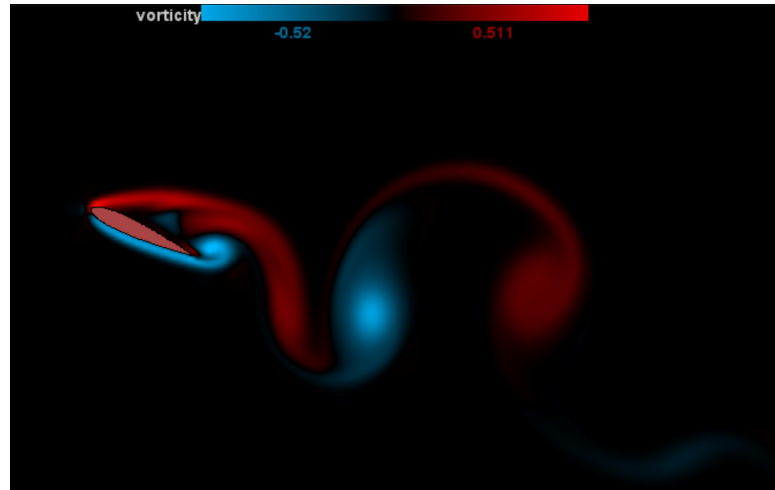


Figure 13: Snapshot from simulation for $h_0 = 1.0$, $\theta_0 = 50^\circ$, and $St = 0.1$. Colorbar shows non-dimensional vorticity.

Simulations measured pressure around the foil and output force and moment vectors. A power relationship is defined and calculated based on these measurements and efficiency values can be determined for each scenario. With such a clear visual of the oscillating vortices in the wake of the foil as shown in Figure 13, patterns can be related to positive/negative efficiencies.

4.1 Parameter Space

The parameter space tested with the 2-D simulations were with respect to heave amplitude (heave to chord ratio, $\frac{h_0}{c}$), pitch amplitude (θ_0), and non-dimensional oscillation frequency (Strouhal Number, St). Combinations of St and θ_0 were simulated for various $\frac{h_0}{c}$ amplitudes. Table 1 below summarizes the parameter space.

Parameter	Values
$\frac{h_0}{c}$	0.5, 0.75, 1.0, 1.25
θ_0	$30^\circ, 40^\circ, 50^\circ, 60^\circ, 70^\circ, 80^\circ, 90^\circ$
St	0.1, 0.2, 0.3, 0.4, 0.5, 0.6

Table 1: Simulation parameter space

4.2 Power Extraction

The fluid moment exerted on the foil plays a big role in the power required to be put into the system. Calculations for power output estimations were implemented in the model. An equation to quantify this is defined below in Equation (11).

$$P(t) = P_L(t) + P_\theta(t) = F_T \dot{h}(t) + M \dot{\theta}(t) \quad (11)$$

It is observed that the time varying power, $P(t)$, is the sum of the power due to the heave motion, $P_L(t)$, and the power due to torque about the centroid of the body, $P_\theta(t)$. The first term, $P_L(t)$ represents the power that can be extracted from the motion of the system where F_T is the transverse hydrodynamic force on the foil and $\dot{h}(t)$ is the heave velocity. The second term, $P_\theta(t)$ quantifies the power output in pitch for the desired motion of the system where M is the fluid moment mentioned above (8), and $\dot{\theta}(t)$ is the angular velocity of the foil. In the actual device, pitch must be controlled. Thus, this term combined with the rotational

inertia has a negative impact on power production.

Improving the efficiency of the system is the primary focus of this thesis project. It will be defined as the average of the time varying power, $P(t)$ over one cycle of the foil's motion, divided by the total potential power of the flow that the pitching point of the foil sweep through.

$$\eta = \frac{\bar{P}}{\frac{1}{2}\rho U^3 2h_0 s} \quad (12)$$

In equation (12) above, ρ is the density of the fluid, U is the free stream velocity, h_0 is the heave amplitude, and s is the span of the foil. Since this is a 2-D model specific to the chord length and thickness of the foil, span will be assumed to be 1.

4.3 Results

4.3.1 Model Validation

The 2D flow simulation model built in this thesis was validated against Zhu [5]. Simulations were run with motions to mimic those outlined in [5] and the same calculations of efficiency were implemented. One scenario is highlighted here in Figure 14 to present validation. Both plots are efficiency contour plots with respect to a heave amplitude of 1, a chosen pitch amplitude and frequency of oscillation for each simulation. Contour (a) is a plot generated from data resulting from the 2-D model described in Section 4.2, and contour (b) comes directly from [5].

Consistently when comparing all contour plots for the various heave amplitudes, the efficiency pattern is very similar. In all plots, the efficiency is higher in the simulations from this program than those from Zhu [5]. In addition, the peak efficiency scenarios is shifted to the next highest frequency in the results from this program than Zhu. These differences are not drastic but a very consistent pattern

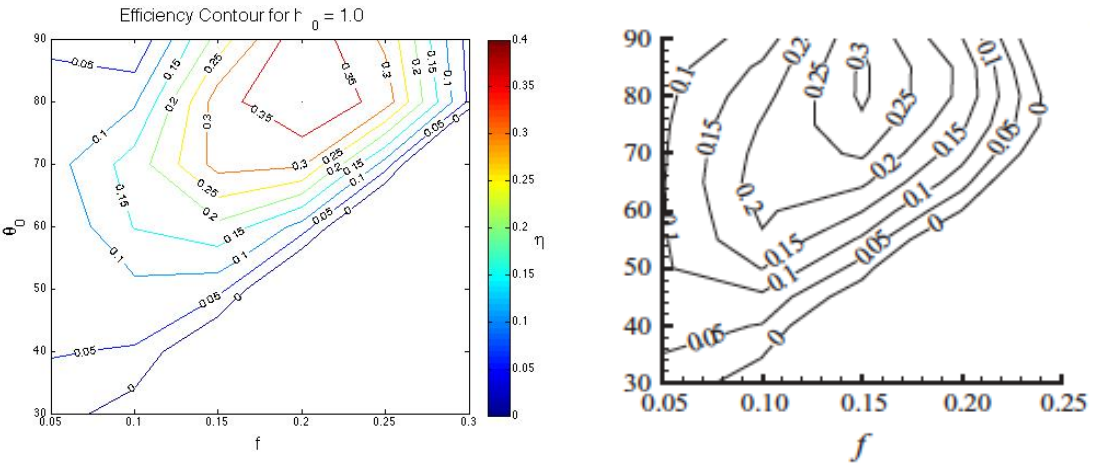


Figure 14: Comparison between (a) efficiency output from 2-D model with (b) Zhu [5] efficiency outputs for $h_0 = 1$.

for all heave amplitude contours.

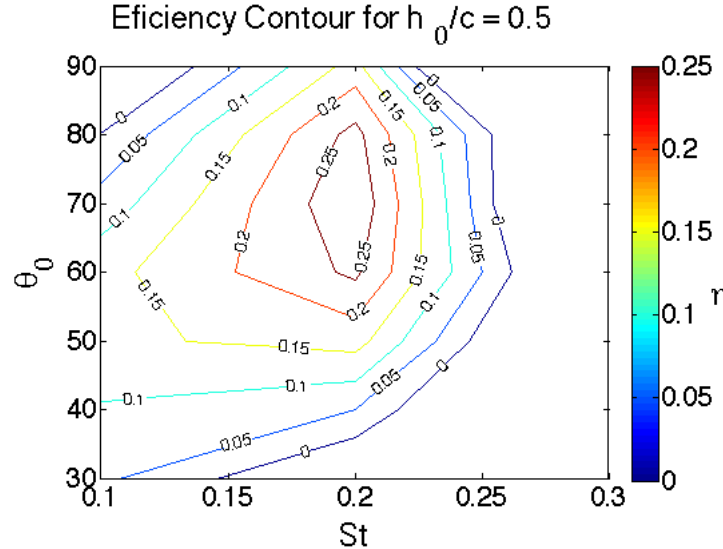
4.3.2 Motion Efficiency

The highest efficiency of $\eta = 0.43$ occurred for the scenario with harmonic heave and pitch motion with amplitudes 1.25 and 90° respectively. This occurred at Strouhal Number 0.5 corresponding to an oscillation frequency of 0.2. The heave amplitude with a relatively high efficiency occurring over the widest range of St and θ° was $\frac{h_0}{c} = 0.5$. The contour plots representing the efficiency values from simulations over the parameter space depicted in Table 1 can be found in Figures 15a - 21a. A breakdown of the efficiency values for the entire parameter space can be found in Tables A.3 - A.6 in the Appendix.

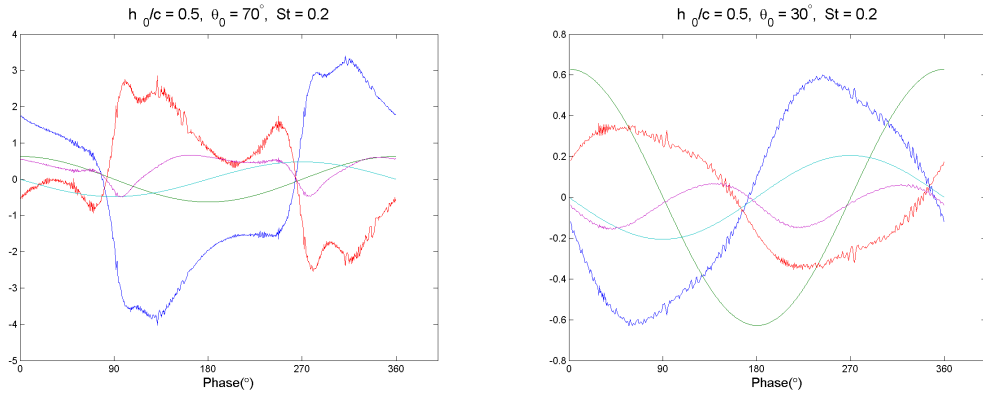
$$h_0/c = 0.5$$

For the entire parameter space where $h_0/c = 0.5$, the highest efficiency of $\eta = 0.26$ occurred at $St = 0.2$ and $\theta_0 = 70^\circ$, as seen in Figure 15a. The range of non-dimensional oscillation frequency in which the system is extracting energy is only from $St = 0.1 - 0.25$. This is not much of a wide range compared to the other heave amplitudes to follow. The efficiency values for each θ_0 , St combination for

$h_0 = 0.5$ can be found summarized in Table A.3.



(a) Energy Extraction Efficiency for $h_0 = 0.5$.

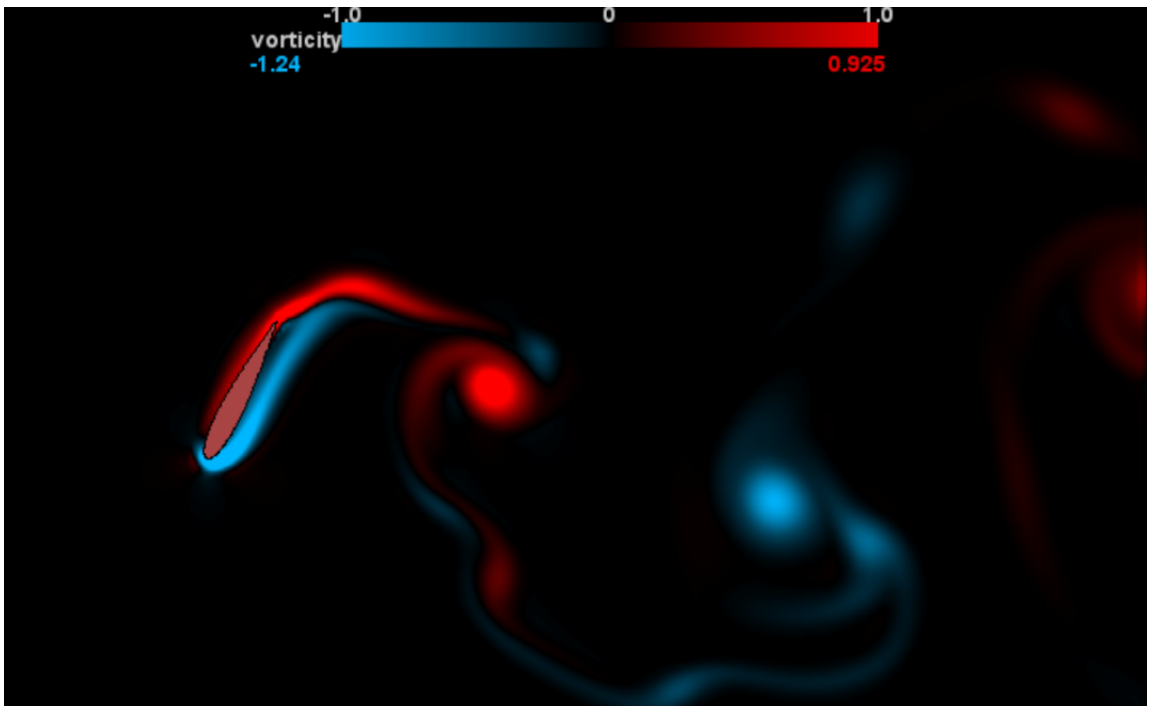


(b) Positive Efficiency Example Forces

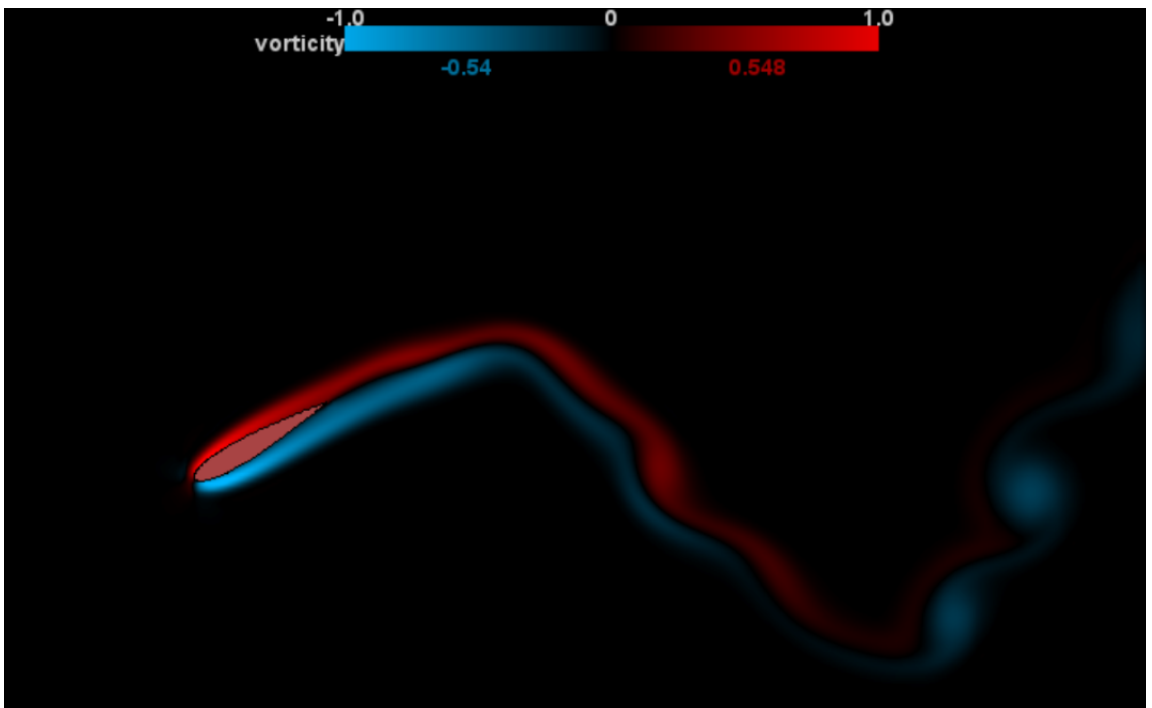
(c) Negative Efficiency Example Forces

Figure 15: Efficiency Contour and Sample Force value plots for $h_0 = 0.5$ simulations. In force plots, blue represents the coefficient of lift force, green the heave velocity, red the coefficient of moment scaled by 10^{-1} , teal the pitch amplitude scaled by 10^{-1} , and magenta the coefficient of power. (15b) $\eta = 0.29$ and (15c) $\eta = -0.07$

Positive efficiency corresponds to forces and their supplemental velocities being in phase with one another. From Equation (11) defining power extracted from the system per time step, it was concluded that the transverse force, F_Y and the heave velocity, \dot{h} should be in phase for positive available power. Similarly, how



(a) Positive Efficiency Wake



(b) Negative Efficiency Wake

Figure 16: Sample wake patterns for $h_0 = 0.5$ simulations with efficiency values $\eta = 0.29$ (16a) and $\eta = -0.07$ (16b)

much the moment, M and the angular velocity, $\dot{\theta}$ are in phase dictates whether there is a positive or negative impact on energy harvesting in pitch.

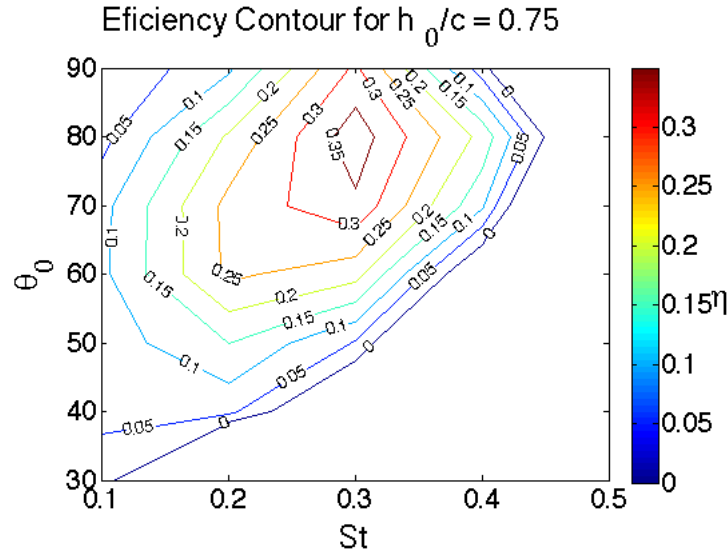
Here we compare plots of these four variables for the highest efficiency case, $\eta = 0.297$ in Figure 15b and a negative efficiency case, $\eta = -0.068$ in Figure 15c. For the positive, high energy extraction efficiency in Figure 15b, the heave velocity in green is completely in phase with the transverse force coefficient in blue. In the case where there was negative efficiency in Figure 15c, the transverse force and heave velocity are precisely 90° out of phase from one another.

Observing the wake patterns for these example simulations in Figure 16, there is a clear extreme difference. The motion producing negative energy extraction efficiency produced little separation on the foil. Figure 16b shows a wake comparable to a shear layer. However, the positive energy extraction efficiency case produces a strong alternating vortex street.

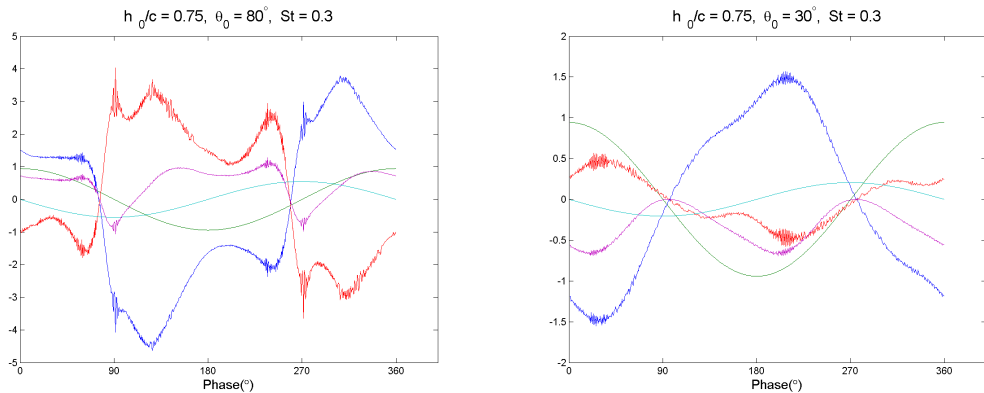
$$h_0/c = 0.75$$

The simulations performed for $h_0/c = 0.75$ resulted in a higher possible energy extraction efficiency that occurred at $St = 0.3$. Here, $\eta = 0.376$ for a pitch amplitude of $\theta_0 = 80^\circ$. This Strouhal number corresponds to a frequency of oscillation of 0.2. For the parameter space simulated with $h_0/c = 0.75$, the non-dimensional frequency range in which energy is being extracted is much broader than in the previous section with $h_0/c = 0.5$. Positive efficiency values occur from approximately $St = 0.2 - 0.4$ and are summarized in the Appendix A in Table A.4. It is noted that for this heave amplitude, the range of energy extraction is also very wide in reference to the pitch amplitude ($30^\circ - 90^\circ$).

A similar pattern to the plots with the power terms occurs in this heave amplitude as $h_0/c = 0.5$. In Figure 17b where $\eta = 0.376$, $\theta_0 = 80^\circ$ and $St = 0.3$, the blue line for F_Y is in phase with the green curve for h_0 . The heave amplitude



(a) Energy Extraction Efficiency

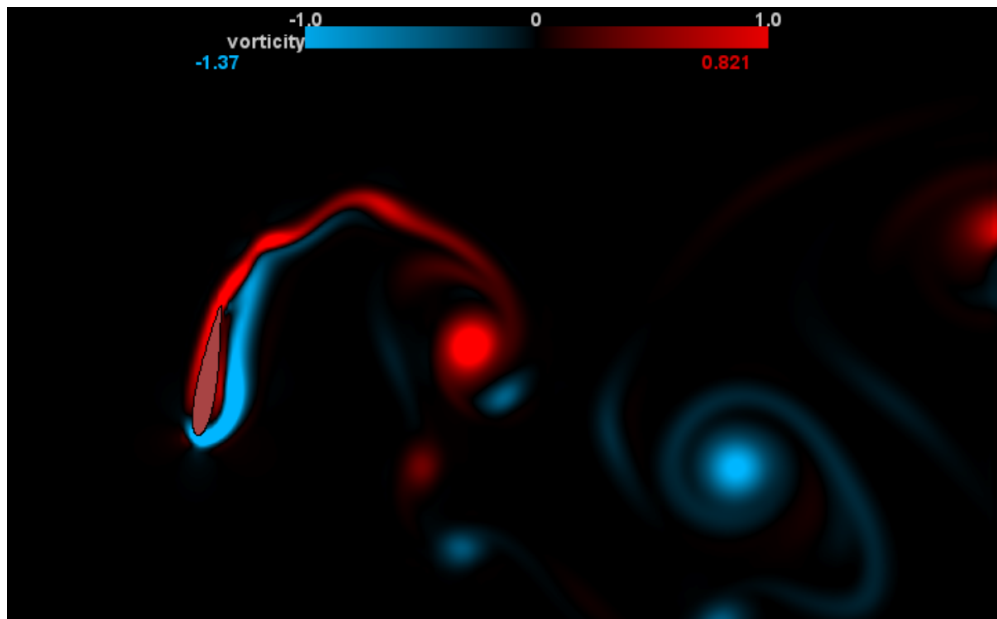


(b) Positive Efficiency Example Forces

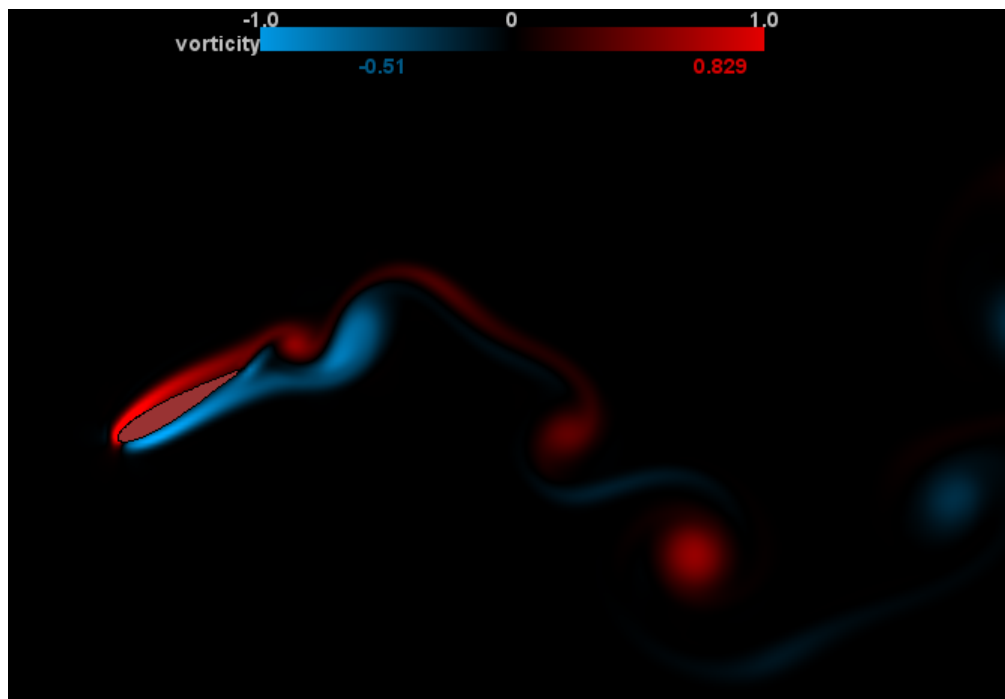
(c) Negative Efficiency Example Forces

Figure 17: Efficiency Contour and Sample Force value plots for $h_0 = 0.75$ simulations. In force plots, blue represents the coefficient of lift force, green the heave velocity, red the coefficient of moment scaled by 10^{-1} , teal the pitch amplitude scaled by 10^{-1} , and magenta the coefficient of power. (17b) $\eta = 0.376$ and (17c) $\eta = -0.386$

is larger than $h_0/c = 0.5$ which increases the available power term, P_L in Equation (11). In Figure 17c where $\eta = -0.386$, $\theta_0 = 30^\circ$ and $St = 0.3$ again it is observed that the transverse force in blue and the heave velocity in green are about 90° out of phase.



(a) Positive Efficiency Wake



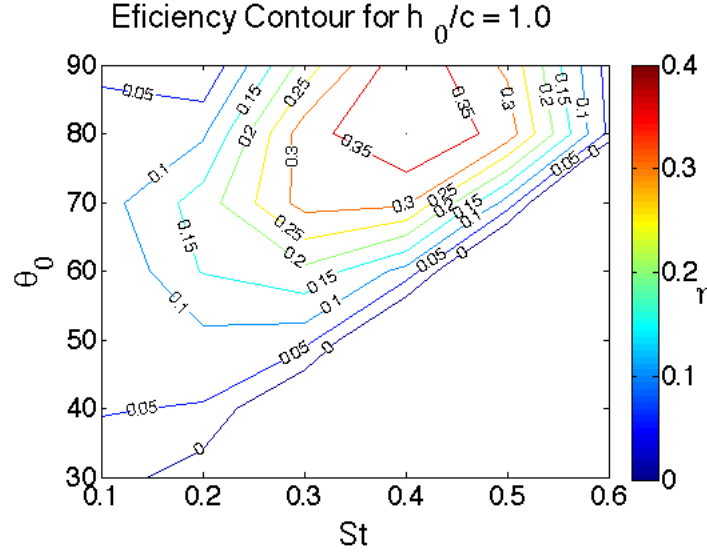
(b) Negative Efficiency Wake

Figure 18: Sample wake patterns for $h_0 = 0.75$ simulations with efficiency values $\eta = 0.376$ (18a) and $\eta = -0.386$ (18b)

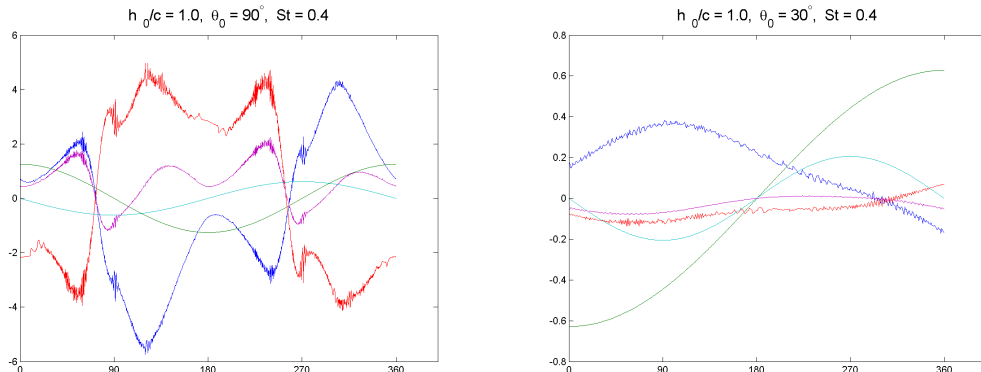
$$h_0/c = 1.0$$

The second highest efficiency calculated, $\eta = 0.394$, occurred for $h_0/c = 1.0$ with $\theta_0 = 90^\circ$ and $St = 0.4$. This Strouhal number corresponds to a flapping

frequency of 0.2. Energy extraction occurs for this heave amplitude over a wide range of Strouhal numbers (approximately $St = 0.1 - 0.6$) but not as wide a range of pitch amplitudes as the $h_0/c = 0.75$ parameter space. Efficiency values are shown in Figure 19a and summarized in Table A.5 in Appendix A.



(a) Energy Extraction Efficiency Plot

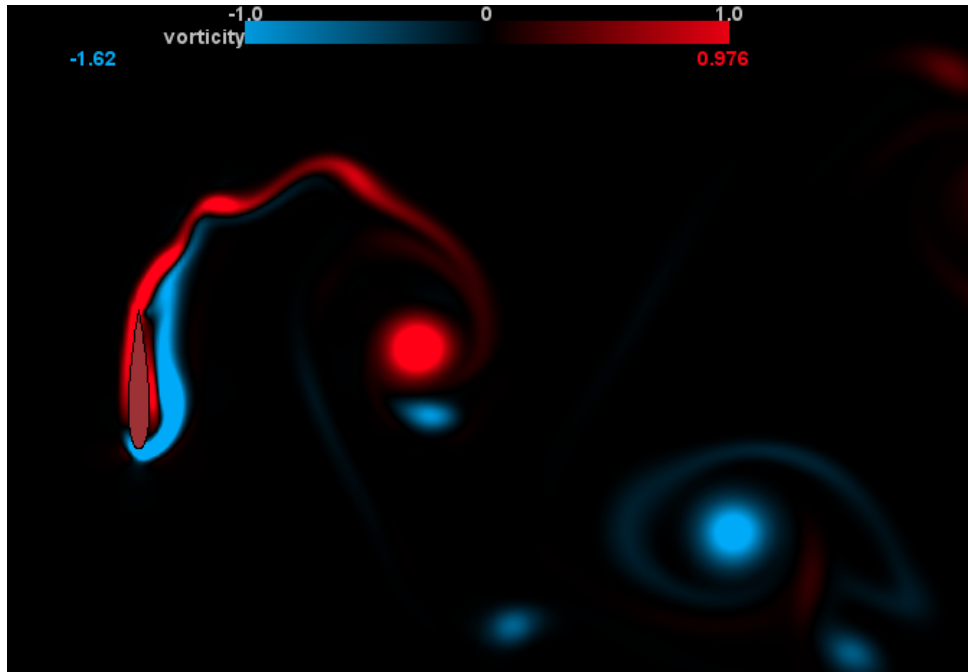


(b) Positive Efficiency Forces

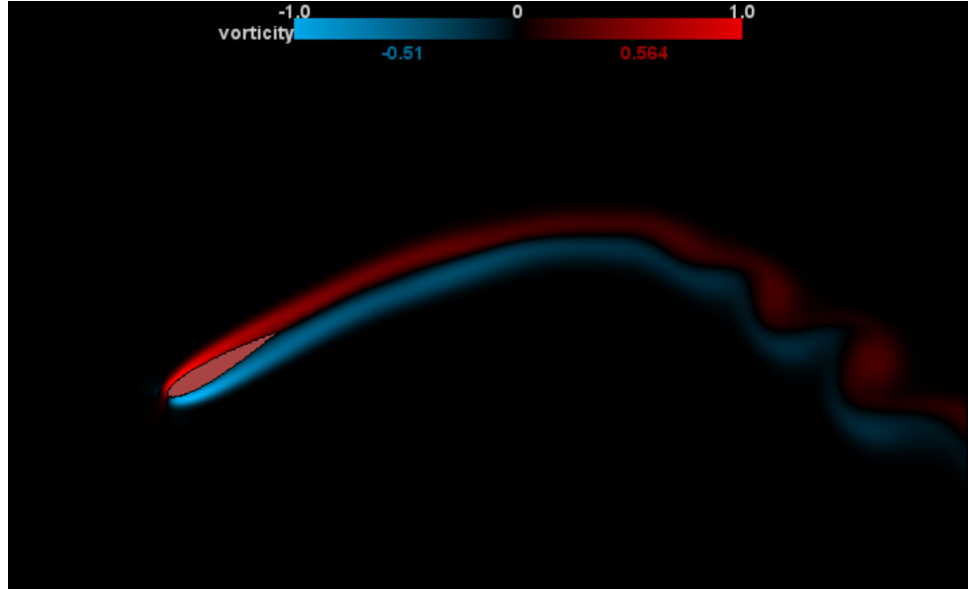
(c) Negative Efficiency Forces

Figure 19: Efficiency Contour and Sample Force value plots for $h_0 = 1.0$ simulations. In force plots, blue represents the coefficient of lift force, green the heave velocity, red the coefficient of moment scaled by 10^{-1} , teal the pitch amplitude scaled by 10^{-1} , and magenta the coefficient of power. (19b) $\eta = 0.394$ and (19c) $\eta = -0.042$

Patterns in Figures 19b and 19c are similar to the previous plots of the power



(a) Positive Efficiency Wake



(b) Negative Efficiency Wake

Figure 20: Sample wake patterns for $h_0 = 1.0$ simulations with efficiency values $\eta = 0.394$ (20a) and $\eta = -0.042$ (20b)

terms. However, in the plot of the negative efficiency, $\eta = -0.042$ seen in Figure 19c, the transverse force and heave velocity are 180° out of phase. This is 90° more out of phase than the previous h_0/c parameter spaces. It is also a much higher

magnitude of negative efficiency. Again, minimal separation occurs on the foil for the negative efficiency example in Figure 20b, while the positive efficiency example shows both positive and negative alternating vortices in the wake.

$$h_0/c = 1.25$$

The highest efficiency value reached, $\eta = 0.43$ was calculated for $h_0/c = 1.25$ and can be seen in Figure 21a for $\theta_0 = 90^\circ$ and $St = 0.5$. This is only largest by 0.036 compared to the high efficiency discussed for $h_0/c = 1.0$. In comparison to all the other contour plots in Figures 15a, 17a, and 19a, the peak efficiency occurred at the maximum tested pitch amplitude.

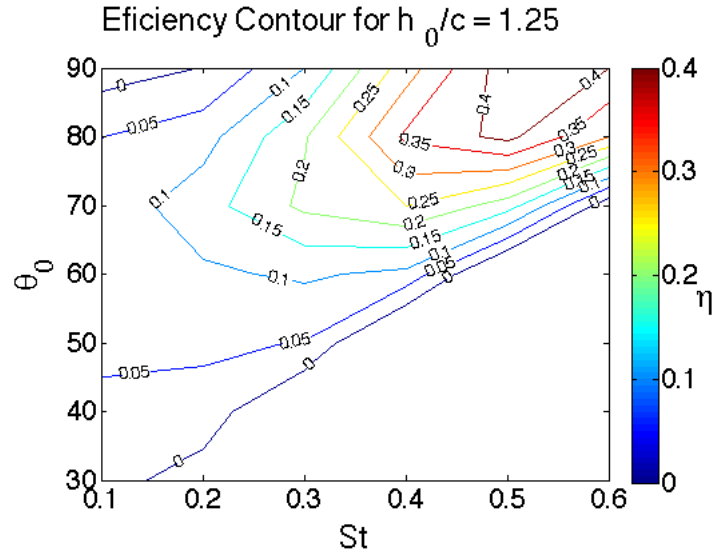
Transverse force in green, F_Y in Figure 21b reaches a higher maximum than in Figures 15b, 17b, and 19b. A high F_Y contributes to this simulation having the highest efficiency observed. Patterns in phase shift between heave velocity and transverse pressure force on the body are similar to Figures 15b, 15c, 17b, 17c, in which they are in phase for the high efficiencies and 90° out of phase for the negative efficiencies.

4.3.3 Pressure and Velocity Traces

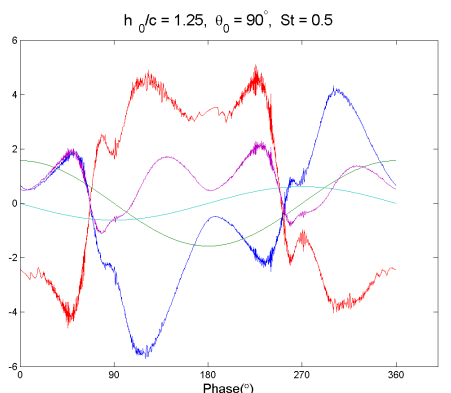
For use in motion control, pressure values at each grid point in the project space were recorded at every time step during the simulations. They were ensemble averaged with respect to phase, resulting in the average pressure values of the grid over one cycle of motion. Similarly, this was also done for the horizontal and vertical components of the fluid velocity.

4.4 Discussion

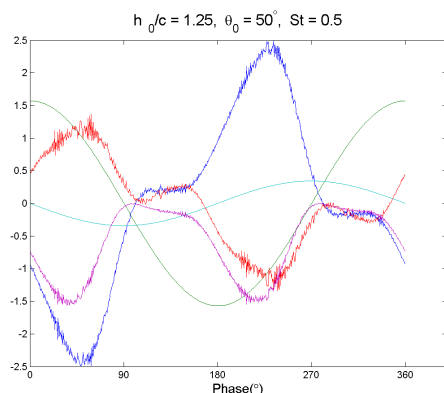
Observing the wake visualization for these motions provides much reasoning to their positive or negative energy extraction efficiencies. Observing the positive efficiency case ($\eta = 0.394$) in Figure 20a, two vortices of opposing sign are generated



(a) Energy Extraction Efficiency Plot



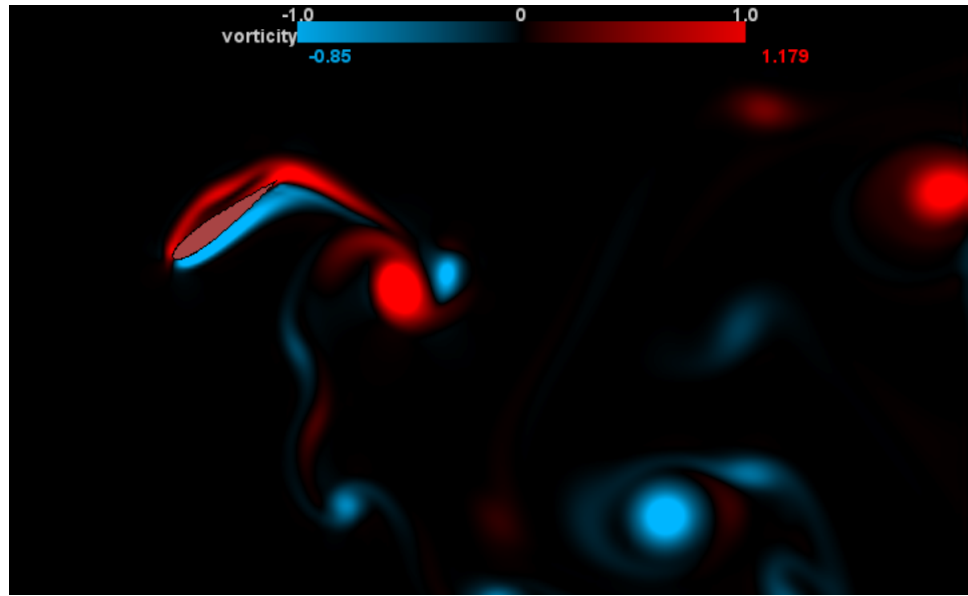
(b) Positive Efficiency Example Forces



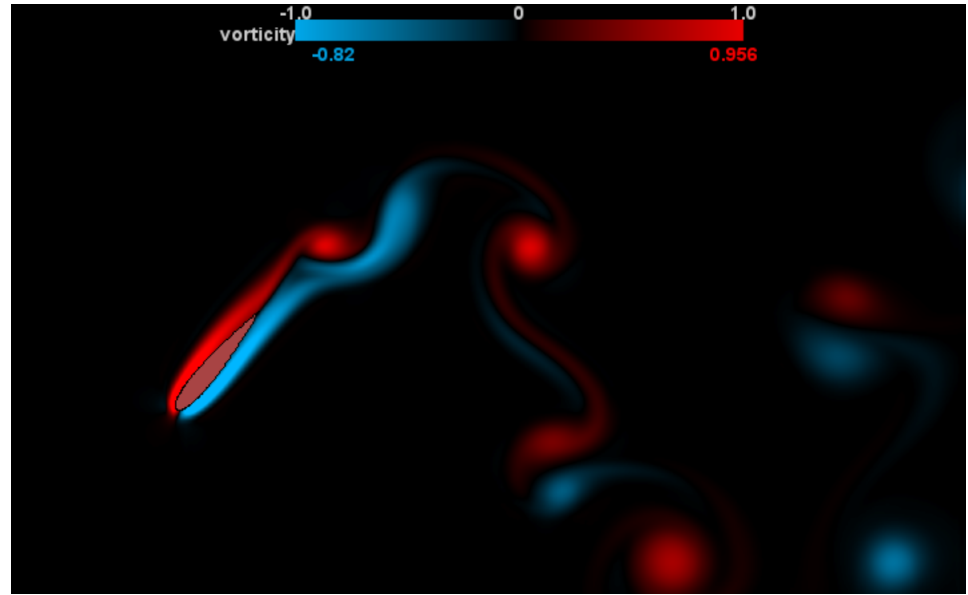
(c) Negative Efficiency Example Forces

Figure 21: Efficiency Contour and Sample Force value plots for $h_0 = 1.25$ simulations. In force plots, blue represents the coefficient of lift force, green the heave velocity, red the coefficient of moment scaled by 10^{-1} , teal the pitch amplitude scaled by 10^{-1} , and magenta the coefficient of power. (21b) $\eta = 0.43$ and (21c) $\eta = -0.44$

every half cycle. Below in Figure 23 this wake pattern is displayed in a bit more detail and coupled with the force plot for the first half of the cycle. It can be seen here that a large negative vortex is positioned behind the pitching point. This imparts coupled pressure force and moment forces in the same direction (shown in the plot as the blue and magenta curves) as rotation. This motion is transferring



(a) Positive Efficiency Wake



(b) Negative Efficiency Wake

Figure 22: Sample wake patterns for $h_0 = 1.25$ simulations with efficiency values $\eta = 0.43$ (22a) and $\eta = -0.44$ (22b)

the energy back into the foil resulting in the positive efficiency.

Taking a deeper look at a negative efficiency simulation ($\eta = -0.386$) introduced in Figure 18b shows us a much different wake pattern in Figure 24. Two same sign vortices are created every half cycle which cause different moments on

the foil. Looking at the force plot it is a bit hard to see, but the pitch velocity (teal) is never in phase with the moment (magenta). Thus, the moments are always opposing the motion of the foil which requires external energy input to move the foil resulting in the negative efficiency.

The maximum efficiency value occurs not only at the highest pitch amplitude, but also the highest heave amplitude. It is expected that the maximum efficiency would occur for lower heave amplitudes because the available power is less for lower heave amplitude to chord length ratios. A possible explanation for these results could be an effect from the Lilypad simulation boundaries onto the forces on the foil. The top and bottom boundaries may be exerting an additional lift on the foil as it gets closer to the boundaries. A computational domain sensitivity test could be simulated to test the severity of the boundary effects on the foil. A select few specific motion trajectories may be run for various computational domain sizes and the calculations made can be compared.

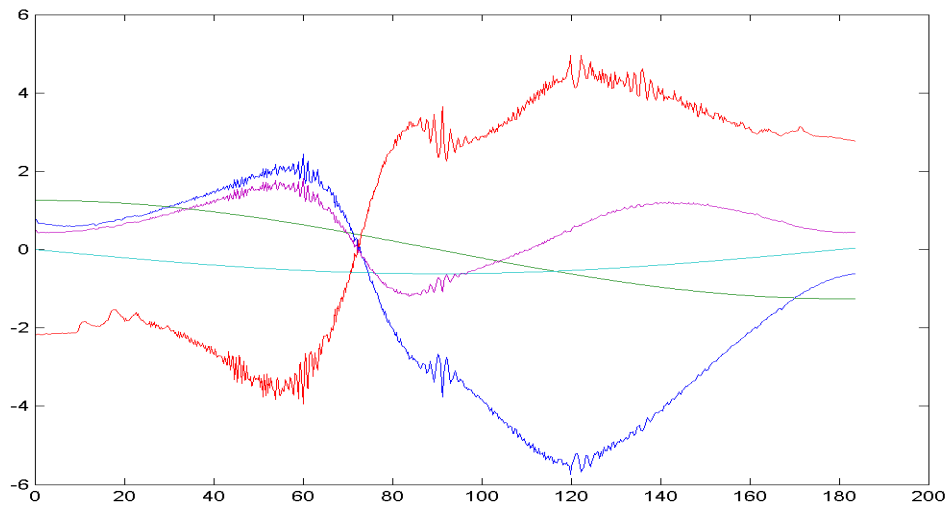
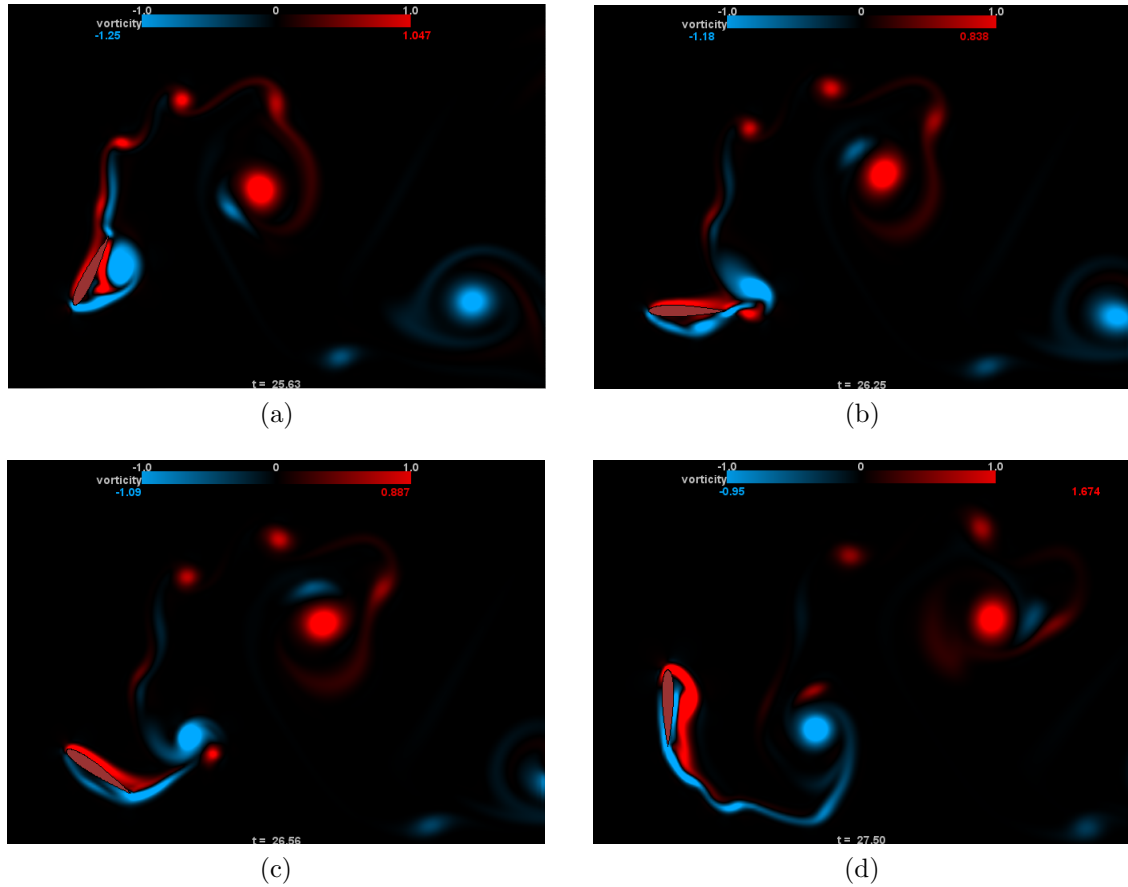


Figure 23: Flow visualization and non-dimensional force data from $h_0/c = 1.0$, $St = 0.4$, $\theta_0 = 90^\circ$. In the force plot, the x axis represents degrees in phase, blue represents the coefficient of lift force, green the heave velocity, red the coefficient of moment scaled by 10^{-1} , teal the pitch amplitude scaled by 10^{-1} , and magenta the coefficient of power.

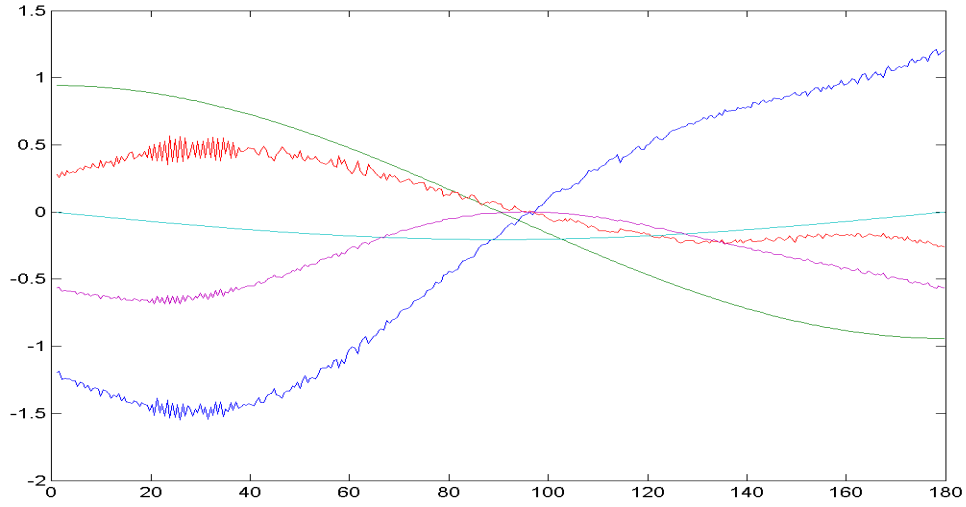
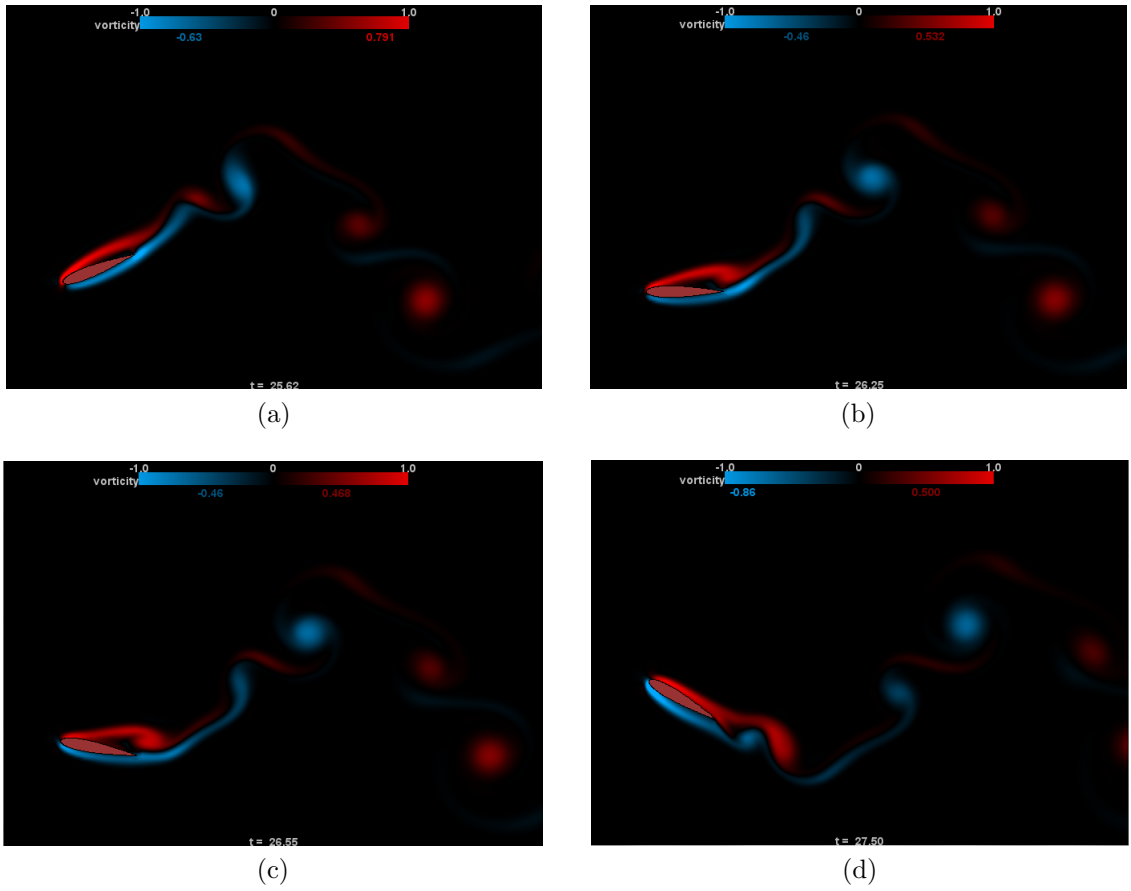


Figure 24: Flow visualization and non-dimensional force data from $h_0/c = 0.75$, $St = 0.3$, $\theta_0 = 30^\circ$. In the force plot, the x axis represents degrees in phase, blue represents the coefficient of lift force, green the heave velocity, red the coefficient of moment scaled by 10^{-1} , teal the pitch amplitude scaled by 10^{-1} , and magenta the coefficient of power.

CHAPTER 5

Control

With use of the results from the flapping foil motion database, a platform for control was created in Lilypad. This platform provides a mechanism for applying motion changes based on pressure measurements. The format implemented for control allows additions of more complex control guidelines. Control may be based on achieving a specific power output, or control can be set to converge to an optimal motion profile.

5.1 Method

The Random Search method from Chapter 3 determined the optimal location for 8 pressure sensors on the foil. From the Database in Chapter 4, the simulation that produced the highest efficiency was chosen as an optimal motion. From here on, this simulation is labeled the optimal motion for the foil to undergo in energy extraction. The pressure traces at the eight sensor locations for this optimal motion are considered to be the optimal pressure traced. The goal is to apply control to the pitching motion of the foil in any motion trajectory within this parameter space in order to achieve the optimal pressure trace.

From the optimal motion trajectory, the pressure trace at each of the sensor locations is ensemble averaged over ten cycles. When a simulation is run, the pressure measurements at the sensor locations are compared to those of the optimal. After the trajectory reaches steady state over several cycles, control is applied to drive the system to the optimal state. A summation of root mean square errors from each sensor is calculated as shown in Equation (26a) below where N is the number of time steps within the half cycle. While this value is below a certain threshold, the pitch motion is adjusted after every cycle of motion in order to

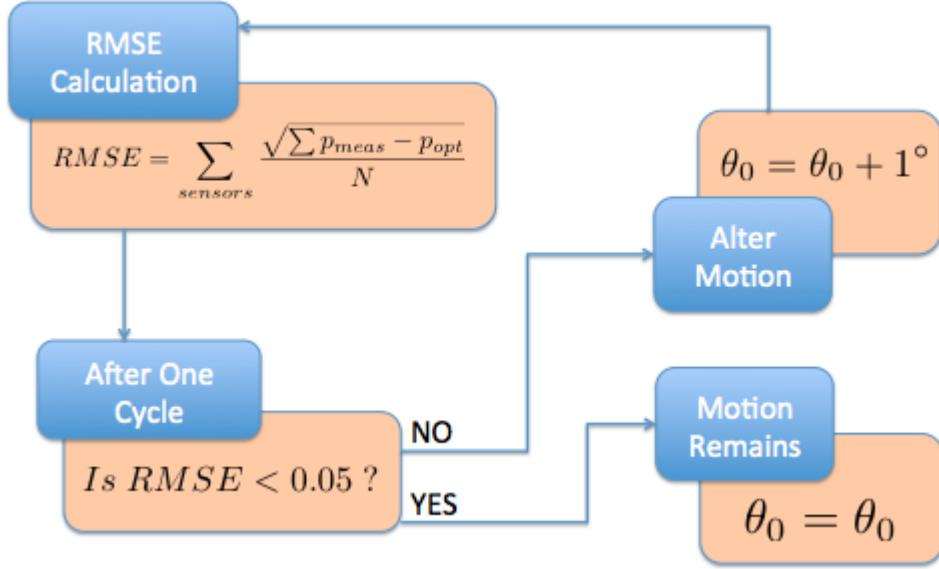


Figure 25: Simple control algorithm implemented in new control platform.

converge to the optimal motion.

$$RMSE = \sum_{sensors} \frac{\sqrt{\sum_N (P_{opt} - P_{meas})}}{N} \quad (13)$$

A basic example of control is implemented on the designed control platform. Pitch is increased with every cycle when the RMSE value is above the threshold. The implemented alteration to pitch motion is recorded along with the pressure measurements at each sensor. As the pitch motion converges to that of the optimal, its pressure trace does the same. Once error minimizes past a threshold, the control is stopped and the foil continues following its final trajectory close to that of the optimal. This simple algorithm of the example control is represented in the schematic below in Figure 25

5.2 Results

With the database, the optimal motion was chosen as the most efficient simulation where $\eta = 0.43$, $h_0 = 1.25$, $\theta = 90^\circ$, and $St = 0.5$. The pressure trace at sensor locations were extracted and ensemble averaged. These pressure values for

each degree in phase throughout the trajectory were used for control. After two cycles of motion during a simulation, the control described above was implemented based on the pressure measurements at the sensor locations, causing the motion to converge to that of the optimal.

We can see this convergence by looking at the change in the pressure measurements and the pitch motion in comparison to those from the optimal motion simulation. An example of control is displayed below in Figure 26. The original trajectory at the beginning has $\theta_0 = 60^\circ$, $St = 0.3$, and $\frac{h_0}{c} = 1.0$. When run at this trajectory past steady state, it has an efficiency of $\eta = 0.06$. After one full cycle of this prescribed motion, control is implemented. The pressure trace, pitch motion, and efficiency converges to that of the optimal motion. Figures 26a and 26b, and Table 2 show the convergence with respect to each cycle of the RMSE value, pitch amplitude, and efficiency respectively.

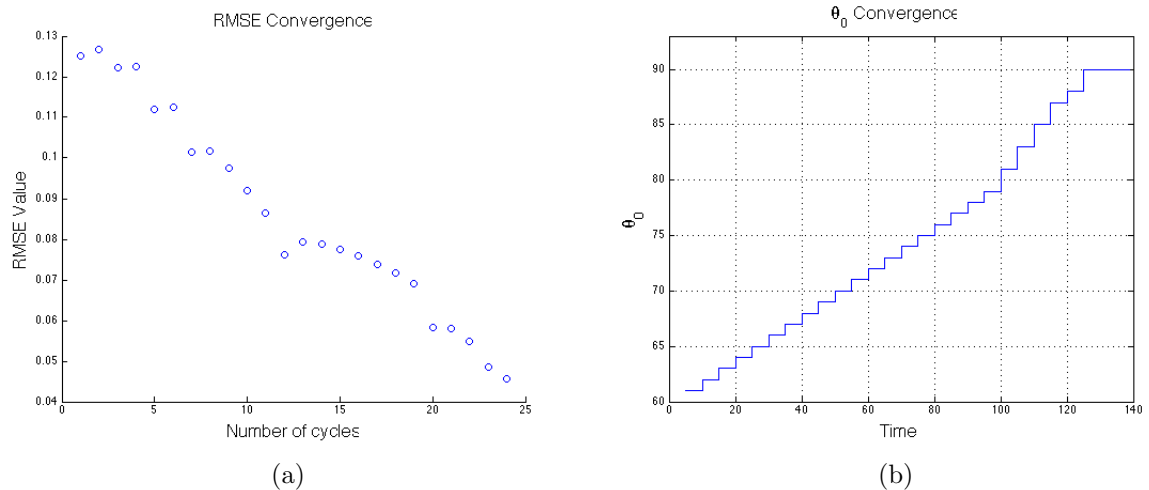


Figure 26: Convergence of (a) RMSE calculation and (b) Pitch Amplitude, θ_0 per each half cycle.

N	Efficiency	N	Efficiency
1	0.076	16	0.395
2	0.088	17	0.410
3	0.102	18	0.421
4	0.123	19	0.431
5	0.148	20	0.434
6	0.172	21	0.444
7	0.196	22	0.448
8	0.223	23	0.455
9	0.251	24	0.456
10	0.279	25	0.454
11	0.306	26	0.454
12	0.333	27	0.449
13	0.348	28	0.448
14	0.366	29	0.442
15	0.379	30	0.434

Table 2: Efficiency change with control for each cycle N.

5.2.1 Reacting Heave Attempt

After implementing a simple example of control to test the platform, more sophisticated approaches were begun for implementing control based on the same pressure measurement comparison technique. For the first cycle of motion, the same pitch and heave sinusoidal motions were forced on the foil. Then, after that cycle, heave was turned off and free to react due to integrated pressure forces on the foil. Control in the pitch motion was turned on for the simple algorithm of increasing the pitch amplitude by one degree each cycle in the presence of a RMSE between the measured pressure and optimal pressure trace. With the heave motion reacting to this, a higher heave to chord ratio was reached than the optimal case. The foil would heave almost to the extremes of the computational domain. This suggests that the pressure trace may not be unique to that specific Strouhal number, heave to chord ratio, and pitch amplitude set of parameters. Eventually,

after a few cycles, the simulation would become unstable.

5.2.2 LQR Optimal Control Attempt

Optimal control was attempted by implementing a Linear Quadratic Regulator. A relationship between pressure and pitch had to be derived for this approach. To begin, the definition of Lift force is used, Equation (14), and 2-D potential flow lift theory is applied setting C_L to $2\pi\alpha$. In this representation of lift, U_α is the flow velocity apparent to the angle of attack. This term can be represented in terms of heave velocity and total uniform incoming flow by the square-root of the sum of the squares, as shown in Equation (15). Since the lift force on a wing can be examined in terms of pressure difference, L was replaced with pA , therefore dropping the planform area A from both sides of the equation.

$$L = \frac{1}{2}\rho U_\alpha^2 A C_L \quad (14)$$

$$p = \pi\rho\{\dot{h(t)}^2 + U(t)^2\}\{\theta(t) - \arctan(\frac{\dot{h(t)}}{U})\} \quad (15)$$

After inputting the equations defining alpha, differentiating, and rearranging the terms, the relationship for control of theta is expressed as Equation (16). Notably, the gain that will change in the pitch motion is dependent on the heave velocity and uniform flow velocity. There is no dependence on previous pressure values at the sensors. This is ideal, allowing application of linear control.

$$\Delta\dot{p} = \pi\rho\{2\dot{h(t)}\frac{\delta\dot{h(t)}}{\delta t} + (\dot{h(t)}^2 + U(t)^2)\}\Delta\theta(t) \quad (16)$$

The optimal control described was implemented in the simulations after 3 cycles of forced sinusoidal pitch and heave motion were run. The magnitude of the change in pitch motion was dependent upon the difference between the pressure

measurements at the sensor locations and those of the optimal pressure trace. This led to abrupt changes in the pitch motion from the beginning of control causing instability in the foil motion, ending the simulation. In the current open source code calculations, the level of detail necessary in the pressure field for control is not quite achieved. It is anticipated that reduced time steps are necessary to resolve the pressure field with the applied control. Additionally, the applied control may require hard limits on acceleration of the foil when implemented with the real time flow simulation.

5.3 Discussion

Observing the most efficient motion trajectory, the pitch amplitude achieved was the highest tested, $\theta_0 = 90^\circ$. Looking back on the flapping foil energy extraction devices discussed in Chapter 1, it doesn't appear that a 90° pitch amplitude would be physically achievable. From the results of this research, some of the prototypes may have to alter the design of their flapping foil system. It is possible that these high pitch amplitude might not be the most efficient case for motions that deviate from sinusoidal pitch and heave. Deviating from sinusoidal trajectories would be a good step to explore for control.

CHAPTER 6

Experimental Setup

A very important next step for this research is the experimental validation of the simulations and their efficiency and force outputs. The University of Rhode Island has a recently built towing for such experimental research related to flapping foil energy harvesting as well as many other projects. This towing tank is 14 feet long by 3 feet wide by 2.5 feet deep and is depicted below in a photograph in Figure 28. Between computational modeling and simulation runs, I was able to assemble a motion control system and write the motion programs to run the sinusoidal motion trajectories of a foil outlined in Chapter 2.

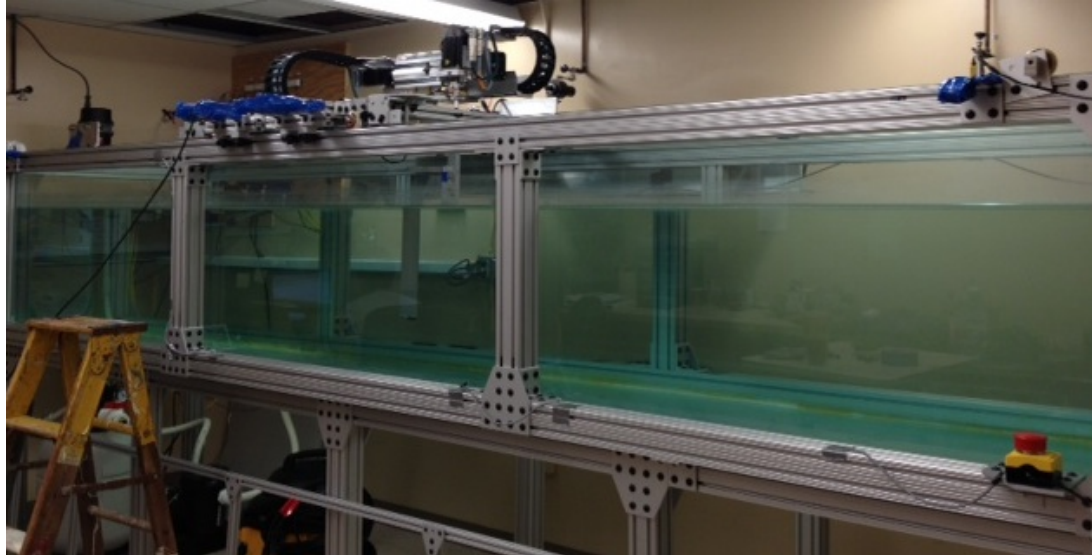


Figure 27: Picture of tow tank in experimental lab.

Resting at the top of the tank is an aluminum carriage mounted on wheels. This carriage holds three of the control motors that dictate the motion of the towed object. Two are linear motors prescribe the heave (Y motor) and inline (X motor) motion of the object. For the motion required by the parameter space defined

in this thesis, only the Y motor is used to achieve heave. The third motor is a rotational (Z rotation motor) motor for controlling the pitching motion of the foil. On the back side of the tank, a tow motor is mounted with a chain belt running the length of the tank and is attached to the carriage.

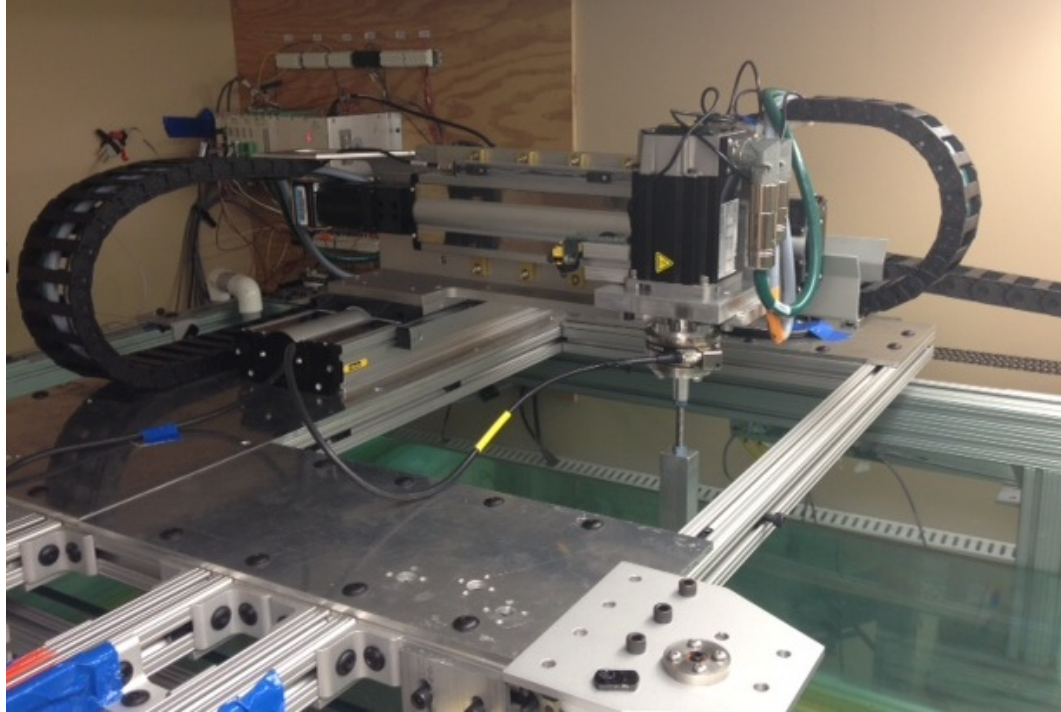


Figure 28: Picture of the carriage holding two of the linear motors and a rotational motor to induce pitch motion with a force sensor and foil extended from it.

Attached to the Z-axis rotational motor is a 6-axis force sensor that measures the x and y components of the force exerted on the foil as well as the torque. Below the sensor the foil is mounted with a threaded rod and submerges vertically in the water. The foils span extends almost to the bottom of the tank without touching.

The motion of the foil is prescribed by a program written in PMAC 2 control software on the lab computer. The computer writes the commands for the discrete motions of each of the motors to the PMAC controller card from Delta Tau Data Systems represented by (A) in Figure 29 below. The signals are then amplified to the levels required by the motors with (B) XENUS XTL amplifiers. The Delta Tau

and XENUS devices are powered by a +25V external power supply. The motion is carried out by the motors and the resulting forces are measured and converted to the computer by a National Instruments DAQ board.

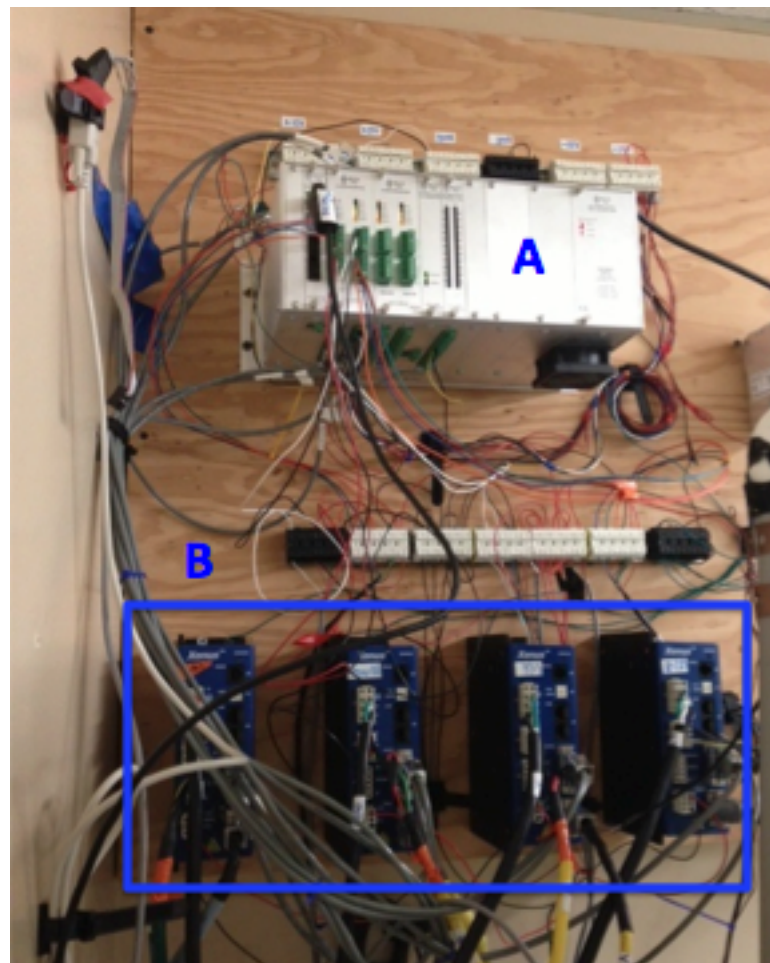


Figure 29: Picture of taken of the control set-up mounted on the wall near the tow tank.

CHAPTER 7

Conclusion

Analysis of the efficiency results from simulations over the parameter space outlined in Table 1 was performed. The highest efficiency achieved was $\eta = 0.43$ for parameters $h_0/c = 1.25$, $\theta_0 = 90^\circ$, and $St = 0.5$ (or $f = 0.2$). From this simulation, the highest transverse force, F_Y was also observed. Energy extraction occurred for a reasonable small range of pitch amplitudes in this $h_0/c = 1.25$ section of simulations (mostly between $\theta_0 = 70^\circ - 90^\circ$). Heave amplitudes of $h_0/c = 0.5$ and 0.75 extracted energy for the entire range of pitch amplitudes tested ($\theta_0 = 30^\circ - 90^\circ$). However, the frequencies of oscillation in which energy is extracted in these cases is between approximately 0.75 and 0.3 and very similar to the higher heave amplitudes, $h_0/c = 1.0$ and 1.25 .

A reasonably consistent pattern was observed between the phase difference from the transverse force to the heave velocity and the values of calculated efficiencies. Positive, high efficiencies occurred when F_Y and \dot{h} were completely in phase with one another. Negative efficiencies occurred when F_Y and \dot{h} were 90° or more out of phase with one another. The greater the two were out of phase, the lower the efficiency value. This validates the discussion of the Power equation, (11), discussed in the Methods Chapter.

In comparison to results from Zhu [5], the efficiency values from these simulations were higher. Additionally, although the patterns of efficiency were very similar to [5], the peak efficiency areas were shifted to the next highest frequency. These differences may be attributed to the lack of consideration of viscous forces in the simulations performed. Zhu's model calculated and included both pressure and viscous related forces. The simulations resulting from the model implemented

in LilyPad ignored viscous forces and only considered the force and moments resulting from the pressure field around the foil. Since the efficiency plots were very similar to Zhu, it can be concluded that using this model is a good approximation of energy extraction efficiency of a flapping foil system. Since only pressure forces are considered, it is assumed that computational time may be less for this model used.

Optimal pressure sensor locations in an array along the symmetrical NACA foil were determined and mapped out in Section 3.4. These outcomes fall under the restriction that the top spacing of the sensor array mirrors that of the bottom. This assumption is assumed to be valid due to the need for a proper representation of the pressure gradient. Also, sensors are located on the top and bottom of the foil rather than trying to mount them on one side only. This is necessary since the foil is oscillating with motion in both transverse directions. Therefore, the pressure gradient will fluctuate from being dominant on the top to being dominant on the bottom depending on if the foil is in positive or negative heave motion and positive or negative pitch motion. The optimal sensors locations include distances $0.3325 * c$, $0.6225 * c$, $0.7872 * c$, and $0.9407 * c$ away from the nose both on top and bottom of the symmetrical foil.

With these pressure sensors in place, it has been validated that control may be applied based on the pressure measurements taken at these locations. Pressure measurements can be compared to the pressure trace at each sensor from the optimal motion trajectory. This comparison can be used to control the pitch motion of the foil in order to converge to the optimal trajectory and improve energy extraction. This validates that pressure sensors constructed in an array along the hydrofoil's chord can contribute to enhancing the efficiency of a flapping foil energy harnessing system.

Several Suggestions are made in regards to future work related to this project. Knowing that pressure sensing can be used to contribute to controlling the motion of a flapping foil energy extraction system, more detailed control can be considered in more detail. Implementing approaches discussed in Sections 5.2.1 and 5.2.2 with a more detailed pressure field calculation would be extremely beneficial. In the open source code used, the system became unstable too easily. This should be investigated more in the future.

Implementation of the motion trajectories outlined in the parameter space in Table 1, in an experimental setting would be beneficial. This would allow for comparison with the force and efficiency data both from these simulations and those outlined in [5]. The laboratory was set-up and its functionality was tested to be ready for these experiments. In addition to the motion trajectories, mounting an array of pressure sensors along the chord length of a NACA foil and implementing mechanical control to the motion based on the sensor readings can be performed.

LIST OF REFERENCES

- [1] J. Webb, *Encyclopedia of Fish Physiology: From Genome to Environment*, 1st ed., A. P. Farrell, Ed. Academic Press, July 2011.
- [2] S. Coombs and S. Netten, *Fish Biomechanics*, G. R.E. Shadwick, Ed. Academic Press, January 2006, vol. 23.
- [3] J. Webb, “Morphological diversity, development, and evolution of the mechanosensory lateral line system,” 2012.
- [4] NASA. “Center of pressure.” [Online]. Available: <http://www.grc.nasa.gov/WWW/k-12/airplane/cp.html>
- [5] Q. Zhu, “Optimal frequency for flow energy harvesting of a flapping foil,” *Journal of Fluid Mechanics*, vol. 675, pp. 495–517, March 2011.
- [6] BP, “Bp energy outlook 2030,” <http://www.bp.com/>, January 2012.
- [7] “Bp statistical review of world energy,” June 2012. [Online]. Available: <http://www.bp.com/statisticalreview>
- [8] A. Jha. “Making waves: Uk firm harnesses power of the sea ... in portugal.”
- [9] B. J. Simpson, “Experimental studies of flapping foils for energy extraction,” Master’s thesis, Massachusetts Institute of Technology, Cambridge, MA, September 2009.
- [10] G. Kloos, C. Gonzalez, and T. Finnigan, “The biostream tidal current energy converter,” in *Proceedings of the 8th European Wave and Tidal Energy Conference*. Uppsala, Sweden: BioPower Systems Pty Ltd, 2009, pp. 426 – 434.
- [11] T. Kinsey, G. Dumas, G. Lalande, J. Ruel, A. Mehut, P. Viarouge, J. Lemay, and Y. Jean, “Prototype testing of hydrokinetic turbine based on oscillating hydrofoils,” *Renewable Energy*, vol. 36, pp. 1710–1718, November 2011.
- [12] Department of Trade and Industry, “Stingray tidal stream energy device - phase 3,” Engineering Business LTD, UK, Tech. Rep. T/06/00230/00/REP URN 05/864, 2005.
- [13] M. Paish, “Can 1mw tidal systems compete with off-shore wind?: An analysis of the opportunities and challenges associated with scaling up,” in *4th International Conference on Ocean Energy*. Dublin: Pulse Tidal ltd; The Electric Works, October 2012.

- [14] M. Bernitsas, “Vivace: A new concept in generation of clean and renewable energy from fluid flow,” *Journal of Offshore Mechanics and Arctic Engineering*, vol. 130, no. 041101, November 2008.
- [15] J. Grue, A. Mo, and E. Palm, “Propulsion of a foil moving in water waves,” *Journal of Fluid Mechanics Digital Archive*, vol. 186, pp. 393–417, 2006.
- [16] H. Isshiki and M. Murakami, “A theory of wave devouring propulsion. iv: a comparison between theory and experiment in case of a passive-type hydrofoil propulsor.” *Journal of Society of Naval Architects of Japan*, vol. 156, pp. 102–114, 1984.
- [17] M. Krieg, P. Klein, R. Hodgkinson, and K. Mohseni, “A hybrid class underwater vehicle: Bioinspired propulsion, embedded system, and acoustic communication and localization system,” *Marine Technology Society Journal*, vol. 45, no. 4, pp. 153–164, Jul/Aug 2011.
- [18] S. Licht, F. Hover, and M. Triantafyllou, “Design of a flapping foil underwater vehicle.”
- [19] S. Licht, M. Wibawa, F. Hover, and M. Triantafyllou, “In-line motion causes high thrust and efficiency in flapping foils that use power downstroke,” *The Journal of Experimental Biology*, vol. 613, pp. 63–71, September 2009.
- [20] C. Groot and L. Margolis, *Pacific salmon life histories*. UBC Press, 1991.
- [21] J. C. Liao, D. N. Beal, G. V. Lauder, and M. S. Triantafyllou, “Fish exploiting vortices decrease muscle activity,” *Science*, vol. 302, pp. 1566–1569, November 2003.
- [22] J. Chen, J. Engel, N. Chen, S. Pandya, S. Coombs, and C. Liu, “Artificial lateral line and hydrodynamic object tracking,” *Micro Electro Mechanical Systems*, pp. 694–697, 2006.
- [23] Y. Yang, N. Chen, C. Tucker, S. Pandya, D. Jones, and C. Liu, “Biomimetic flow sensing using artificial lateral lines,” *ASME Conference Proceedings*, vol. 43025, pp. 1331–1338, 2007.
- [24] V. I. Fernandez, A. Maertens, F. M. Yaul, J. Dahl, J. H. Lang, and M. S. Triantafyllou, “Lateral-line inspired sensor arrays for navigation and object identification,” *Marine Technology Society Journal*, vol. 45, no. 4, pp. 130–146, July/August 2011.
- [25] Y. Xu, Z. Ren, and K. Mohseni, “Lateral line inspired pressure feedforward for autonomous underwater vehicle control,” ser. Workshop on Robotics for Environmental Monitoring, August 2012.

- [26] A. Abdulsadda and X. Tan, “An artificial lateral line system using ipmc sensor arrays,” *International Journal of Smart and Nano Materials*, vol. 3, no. 3, September 2012.
- [27] W. McKinney and J. DeLaurier, “The wingmill: An oscillating-wing windmill,” *Journal of Energy*, vol. 5, pp. 109–115, 1981.
- [28] Q. Zhu and Z. Peng, “Mode coupling and flow energy harvesting by a flapping foil,” *Physics of Fluids*, vol. 21, no. 033601, 2009.
- [29] G. Weymouth and D. K. Yue, “Boundary data immersion method for cartesian-grid simulations of fluid-body interaction problems,” *Journal of Computational Physics*, vol. 230, pp. 6233–6247, April 2011.

APPENDIX A

Appendix A

This Appendix is comprised of tables for each heave to chord ratio ($\frac{h_0}{c} = 0.5, 0.75, 1.0, 1.25$). Each table includes efficiency calculations based on the forces and moments measured in the 2-D simulations. Pitch amplitude and Strouhal number combinations were only simulated if the pattern of efficiencies suggested to be remaining positive.

	0.1	0.2	0.3	0.4	0.5	0.6
30°	0.059	-0.07	-0.33	N/A	N/A	N/A
40°	0.095	0.05	-0.24	N/A	N/A	N/A
50°	0.14	0.17	-0.21	N/A	N/A	N/A
60°	0.133	0.26	-0.16	N/A	N/A	N/A
70°	0.07	0.29	-0.24	N/A	N/A	N/A
80°	0.001	0.27	-0.23	N/A	N/A	N/A
90°	-0.1	0.17	-0.55	N/A	N/A	N/A

Table A.3: Efficiency values for $\frac{h_0}{c} = 0.5$

	0.1	0.2	0.3	0.4	0.5	0.6
30°	0.038	-0.34	-0.386	-1.03	-1.99	N/A
40°	0.056	0.065	-0.125	-0.52	-1.38	N/A
50°	0.071	0.15	0.046	-0.27	-0.84	N/A
60°	0.089	0.257	0.216	-0.085	-0.57	N/A
70°	0.084	0.265	0.34	-0.11	-0.41	N/A
80°	0.032	0.205	0.376	0.185	-0.187	N/A
90°	0.002	0.09	0.31	0.025	-0.42	N/A

Table A.4: Efficiency values for $\frac{h_0}{c} = 0.75$

	0.1	0.2	0.3	0.4	0.5	0.6
30°	0.027	-0.032	-0.3	-0.042	-1.55	-2.84
40°	0.053	0.046	-0.09	-0.46	-1.07	-1.93
50°	0.059	0.086	0.071	-0.14	-0.53	-1.23
60°	0.051	0.153	0.189	0.081	-0.18	-0.65
70°	0.078	0.174	0.32	0.311	0.08	-0.3
80°	0.075	0.092	0.33	0.4	0.33	0.04
90°	0.038	0.002	0.22	0.39	0.29	0.03

Table A.5: Efficiency values for $\frac{h_0}{c} = 1.0$

	0.1	0.2	0.3	0.4	0.5	0.6
30°	0.02	-0.026	-0.21	-0.7	-1.3	-2.275
40°	0.044	0.032	-0.075	-0.39	-0.85	-1.54
50°	0.056	0.059	0.048	-0.11	-0.44	-1.0
60°	0.06	0.092	0.108	0.086	-0.09	-0.414
70°	0.07	0.128	0.212	0.25	0.174	-0.037
80°	0.049	0.08	0.194	0.363	0.415	0.30
90°	-0.025	0.001	0.1	0.277	0.43	0.405

Table A.6: Efficiency values for $\frac{h_0}{c} = 1.25$

APPENDIX B

Appendix B

For each simulation of various heave amplitudes, pitch amplitudes, and Strouhal numbers represented in the tables in Appendix A, force plots were produced. Each plot includes the coefficient of lift force, C_L , heave velocity, \dot{h} , pitch velocity scaled by a factor of 10, $\dot{\theta}$, and the coefficient of fluid moment scaled by a factor of $10^{-1}, C_M$. The equations for C_L and C_M are listed below where M and F_Y are output force measurements scaled by a length.

$$C_L = \frac{F_Y}{\frac{1}{2}\rho U^2 c} \quad (\text{B.17})$$

$$C_M = \frac{M}{\frac{1}{2}\rho U^2 c} \quad (\text{B.18})$$

In the following plots, the legend depicted in Figure B.30 applies.

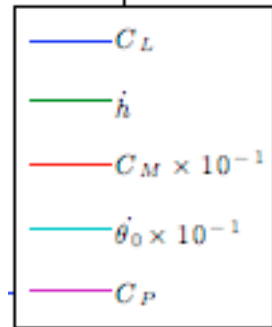
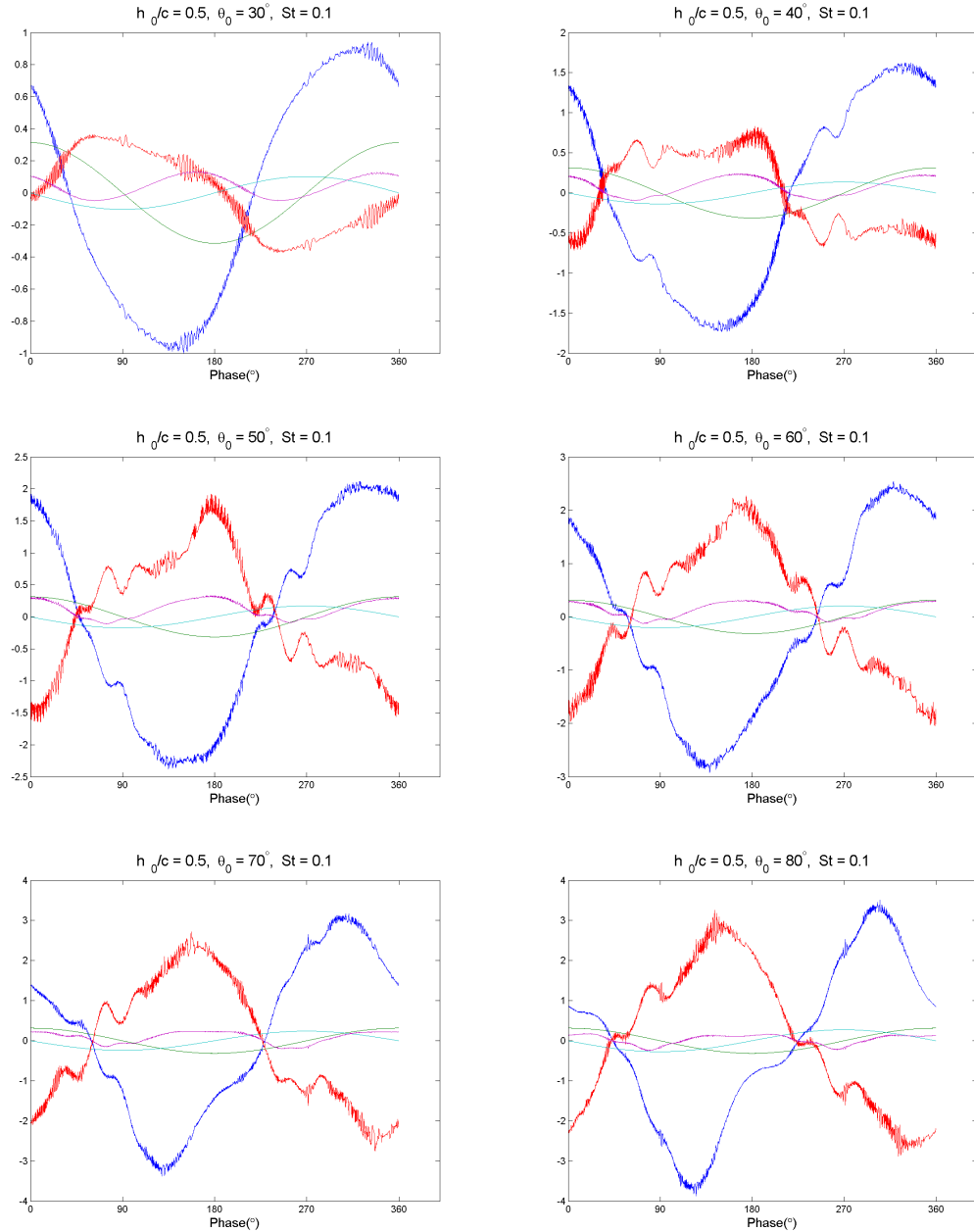
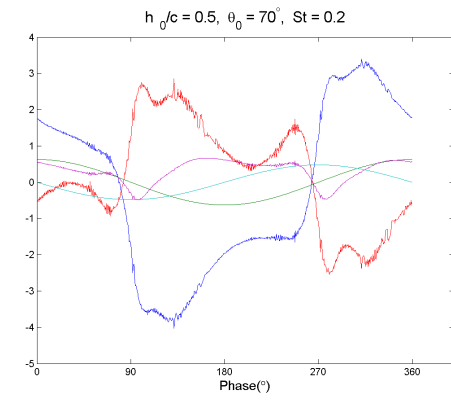
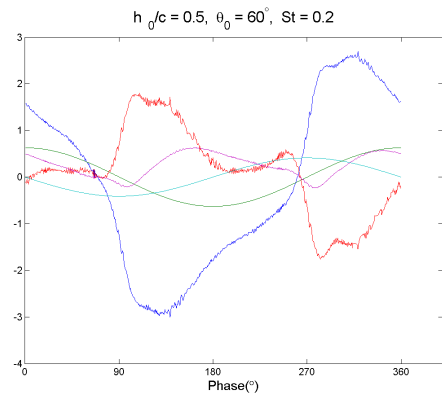
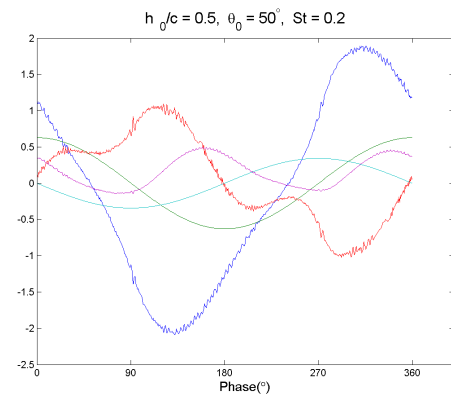
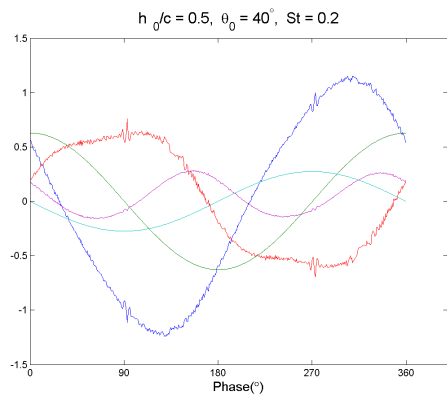
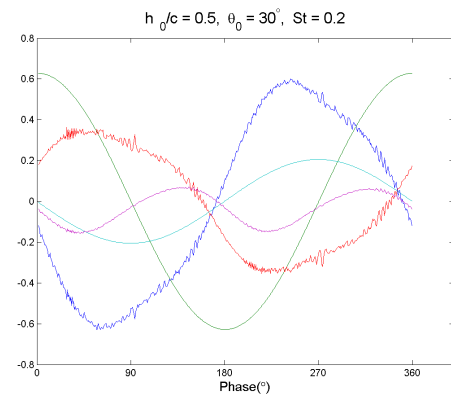
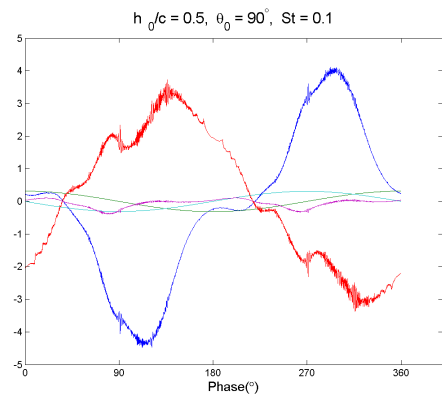
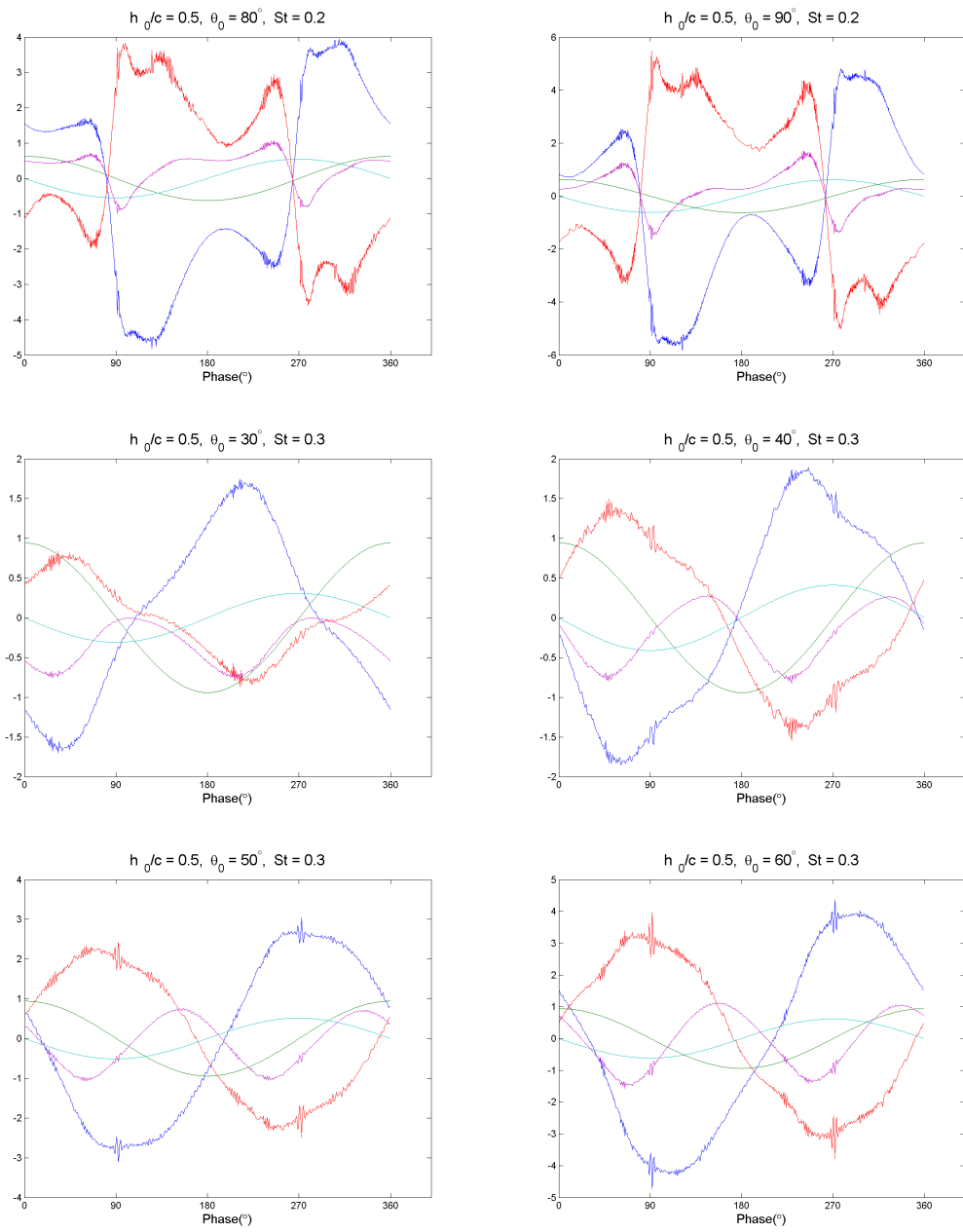


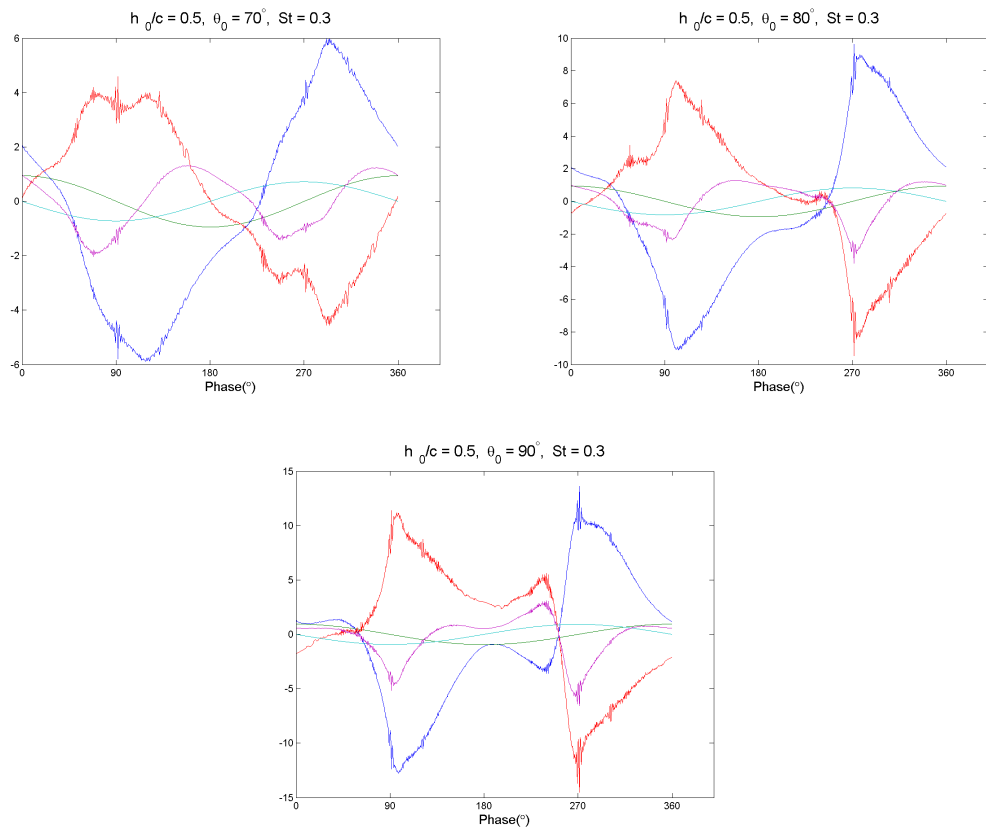
Figure B.30: In the force plots throughout this Appendix, blue represents the coefficient of lift force, green the heave velocity, red the coefficient of moment scaled by 10^{-1} , teal the pitch amplitude scaled by 10^{-1} , and magenta the coefficient of power.

B.1 $h_0/c = 0.05$

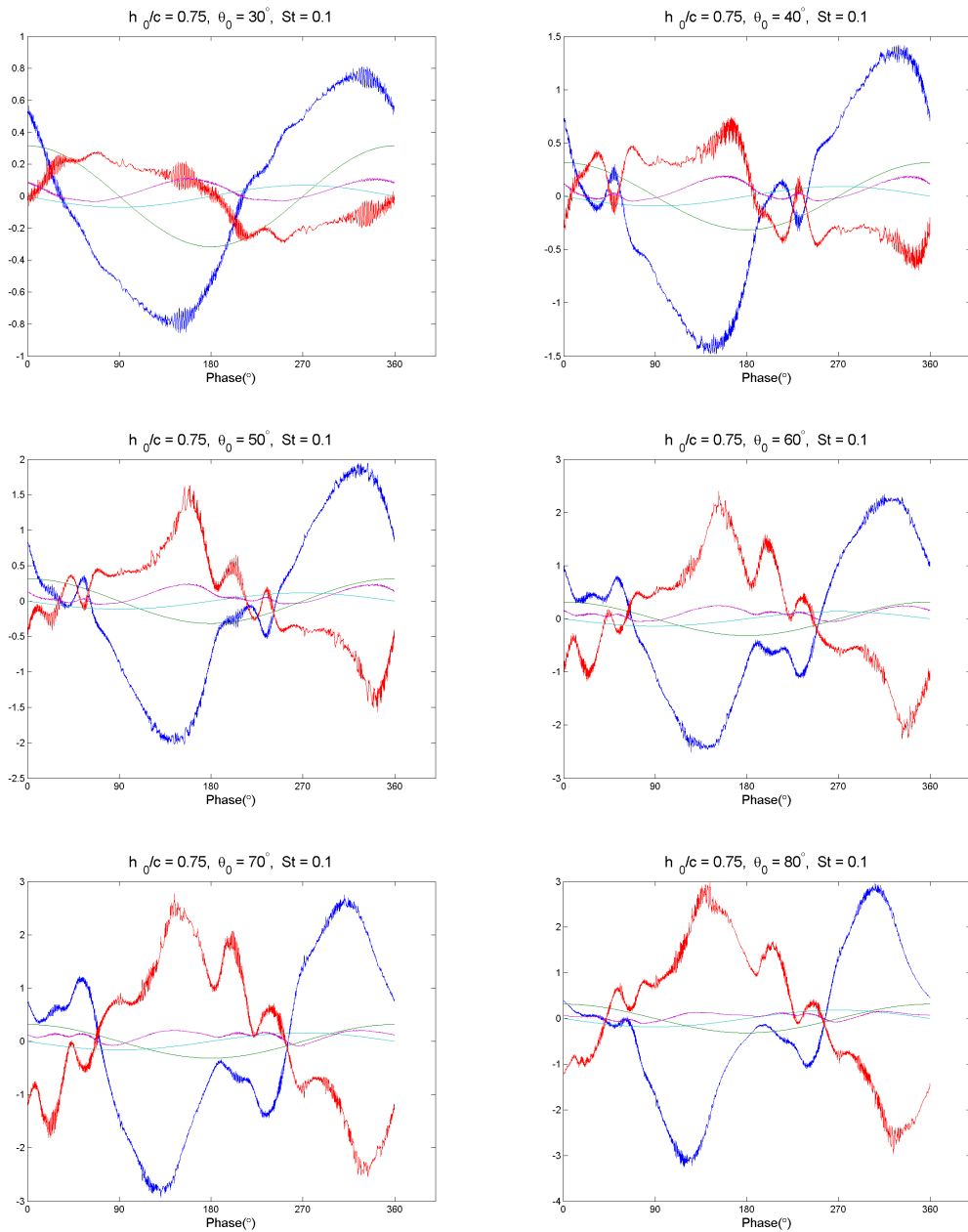


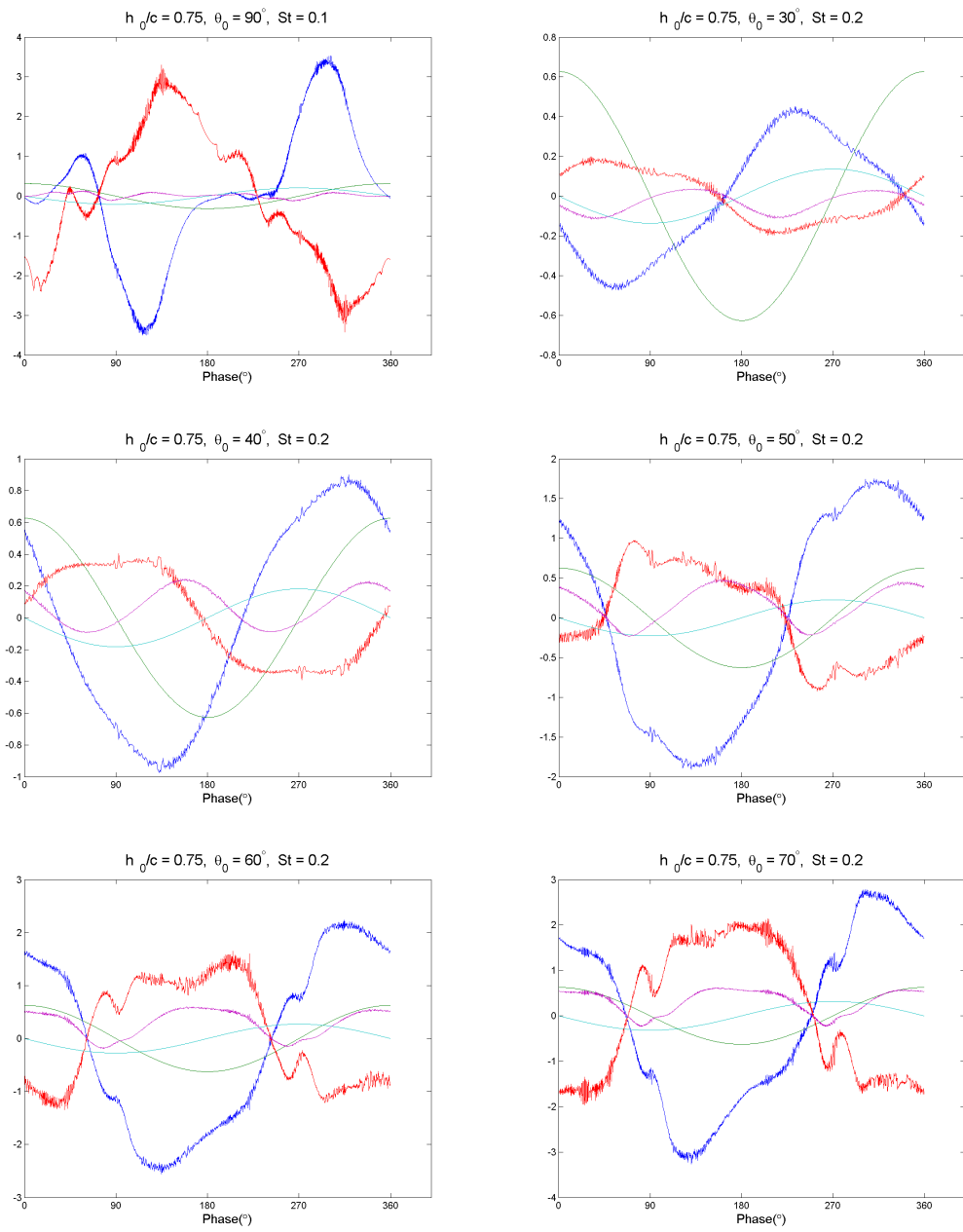


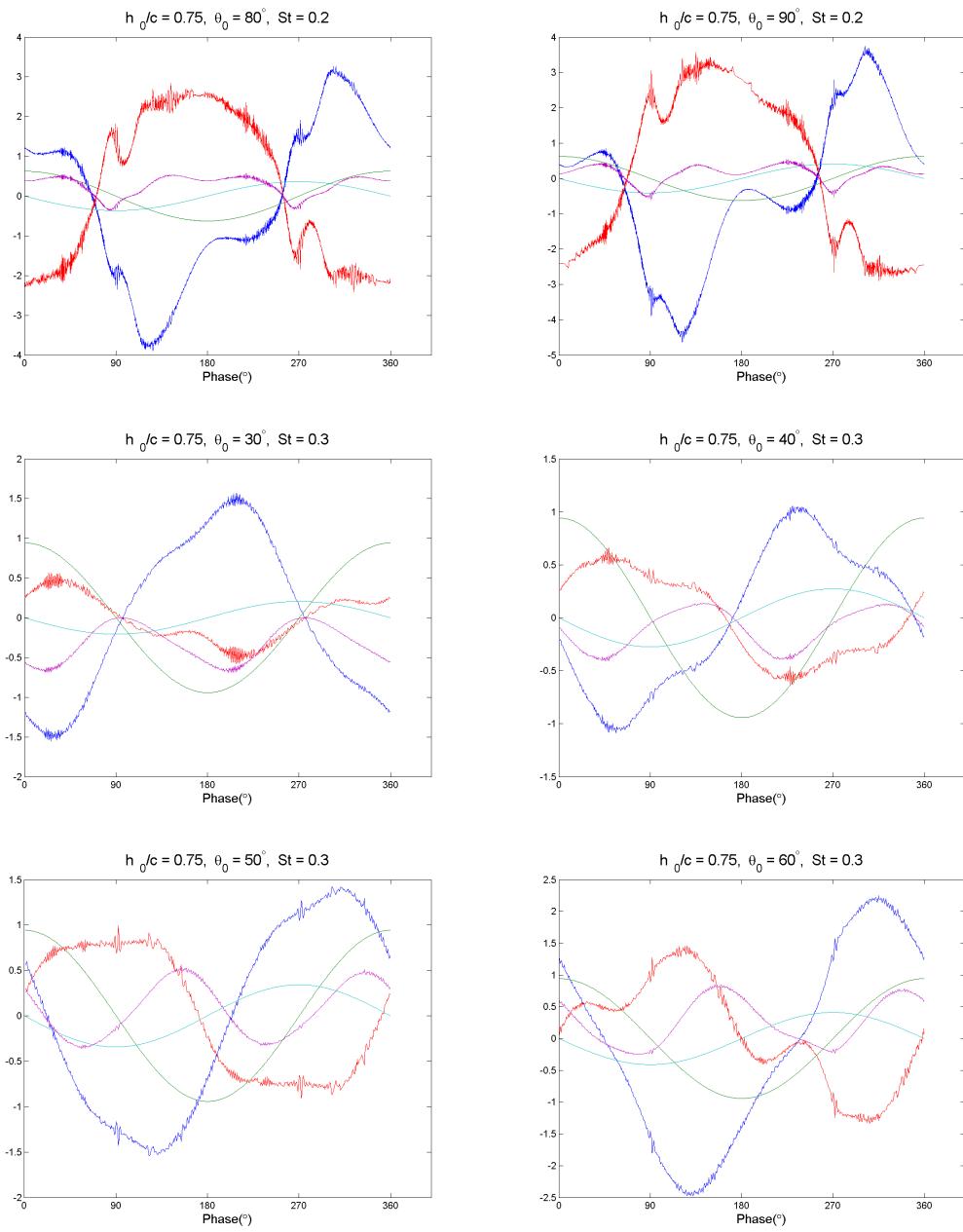


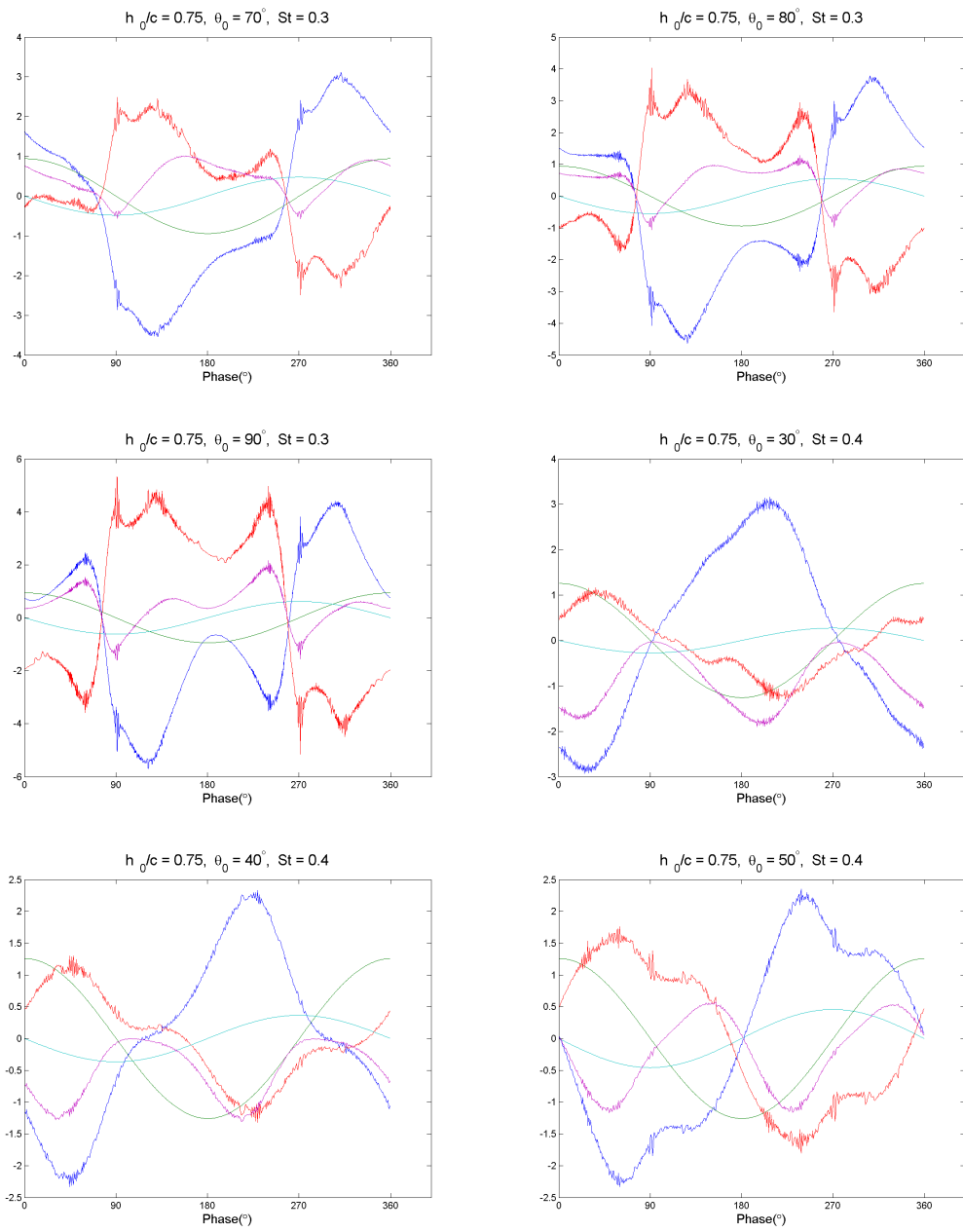


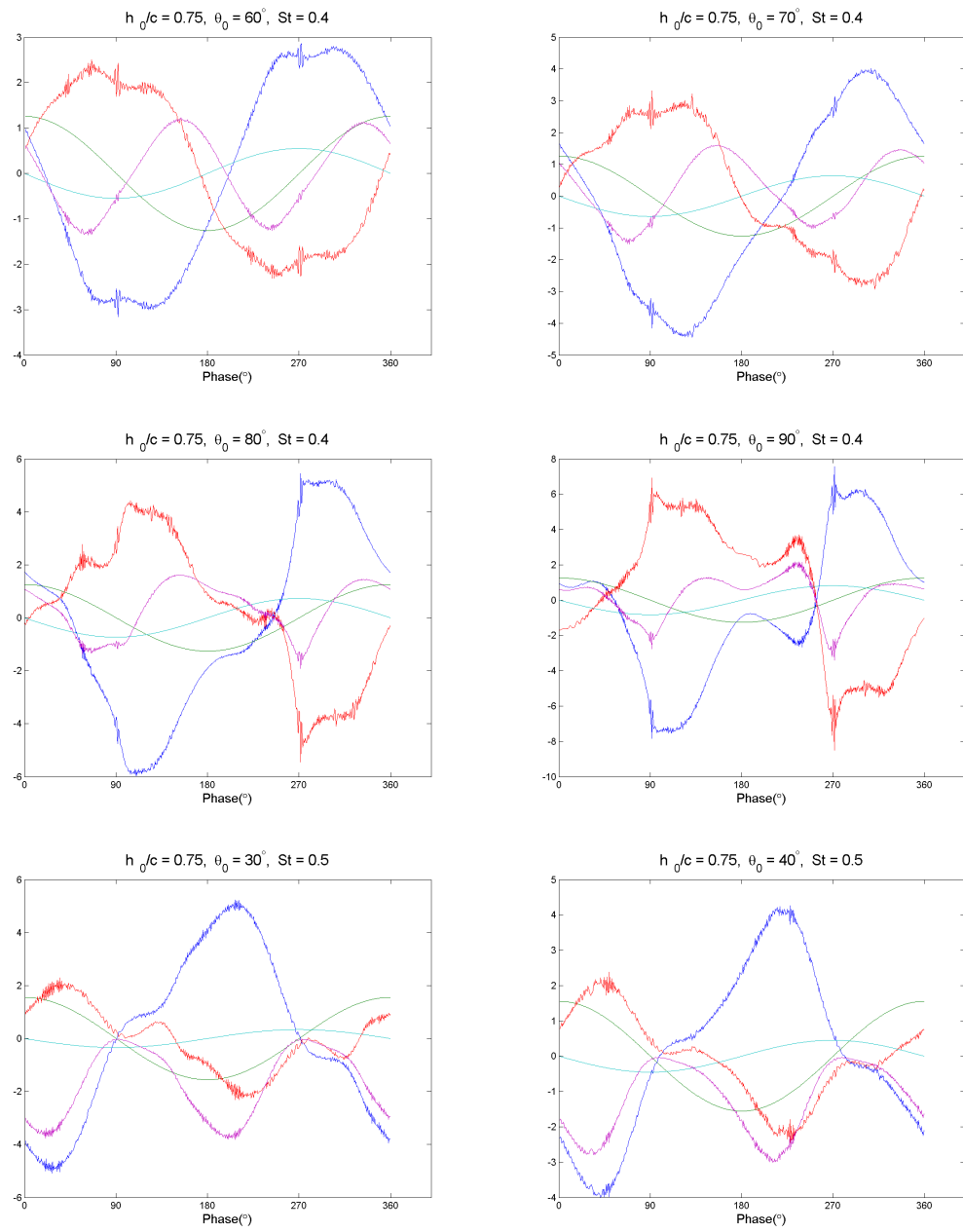
B.2 $h_0/c = 0.75$

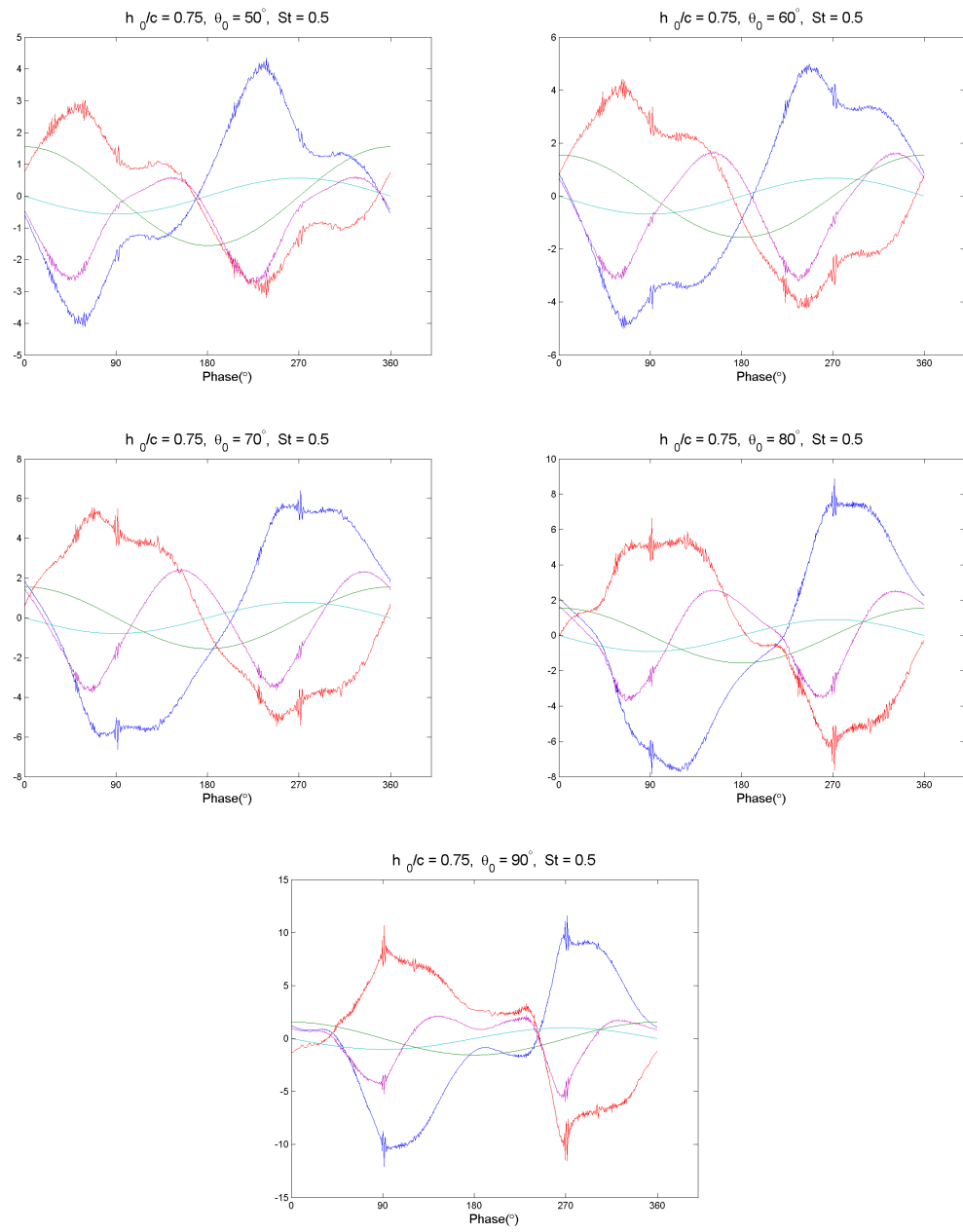




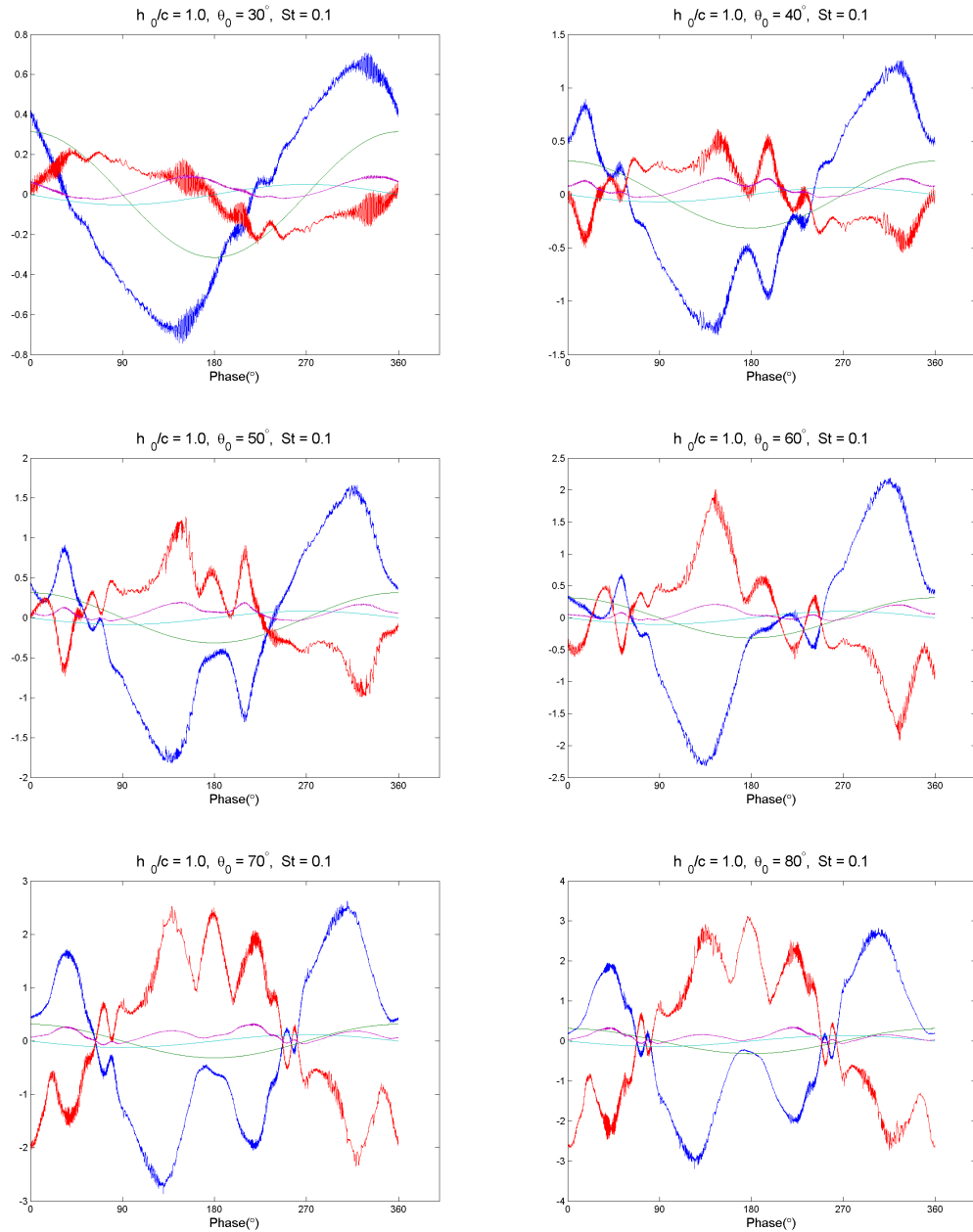


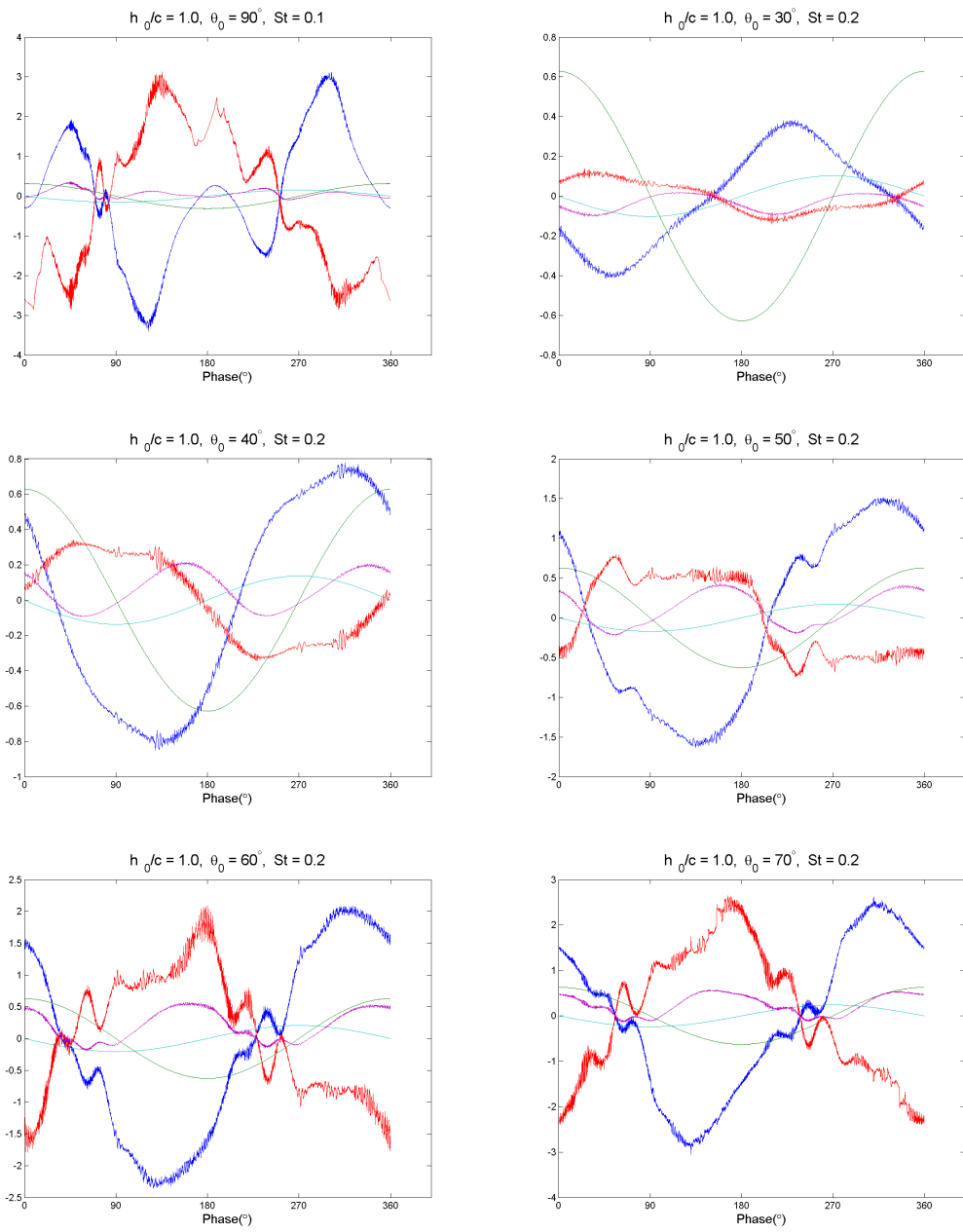


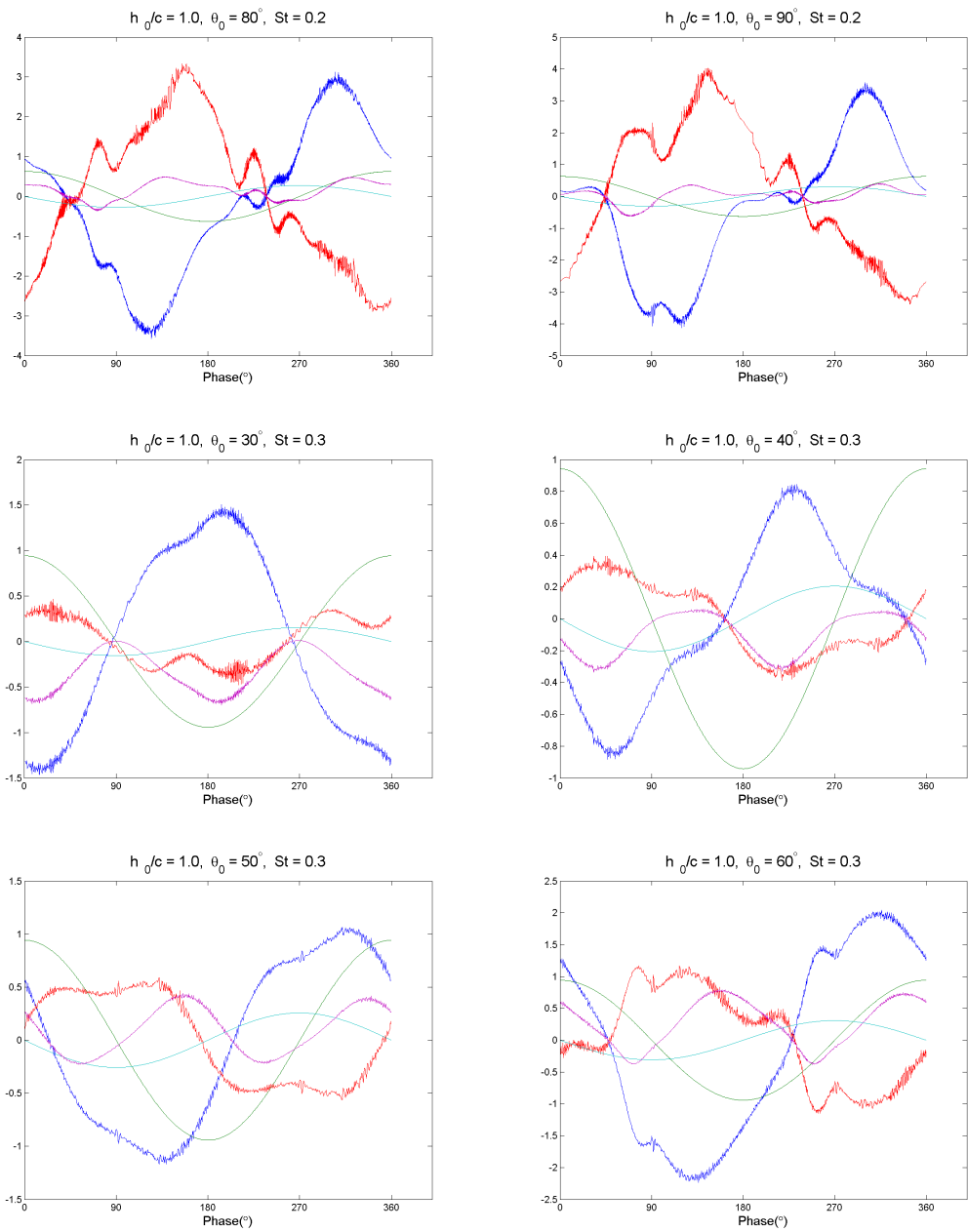


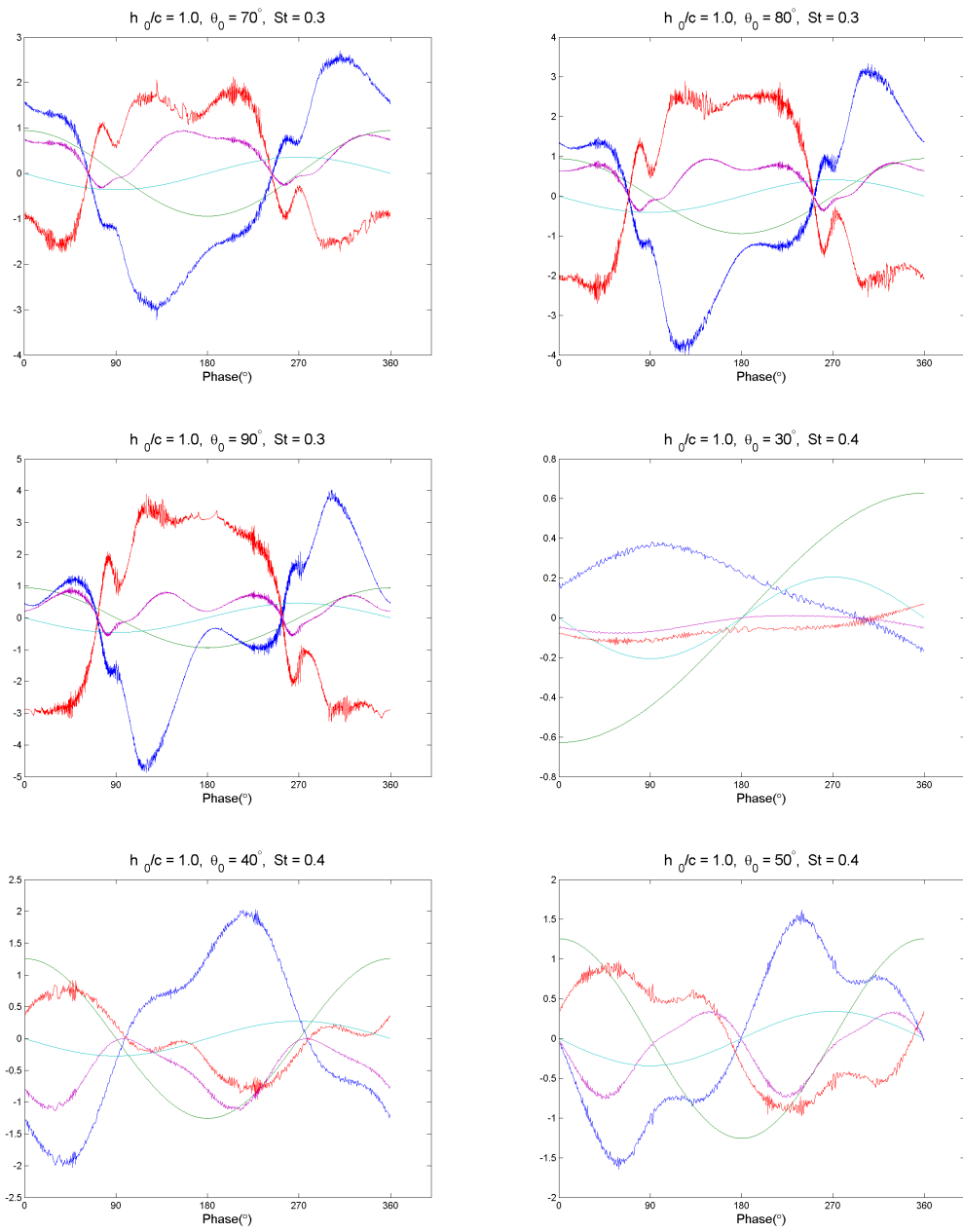


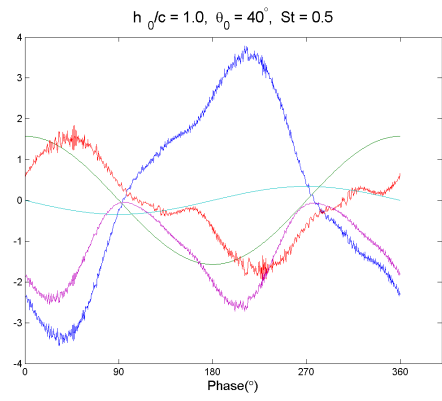
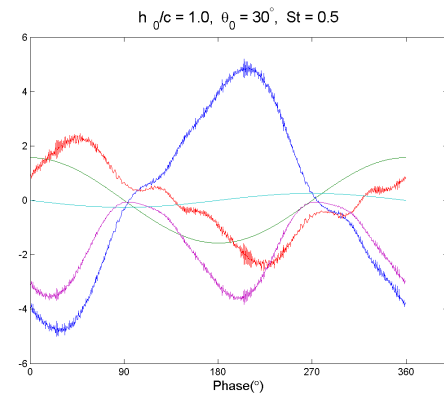
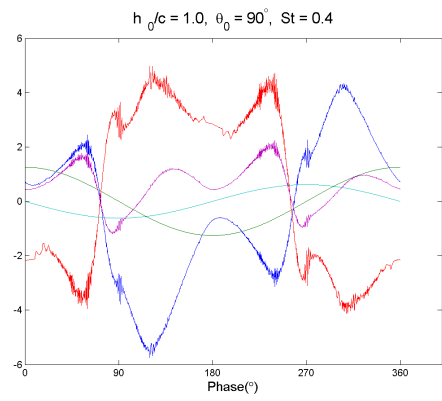
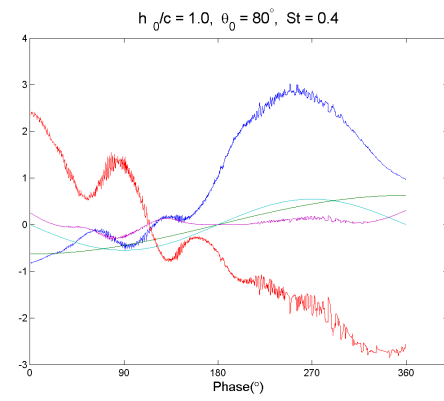
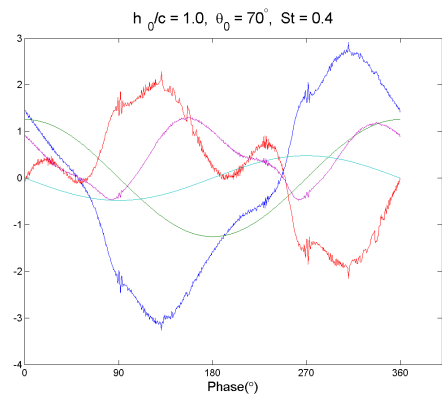
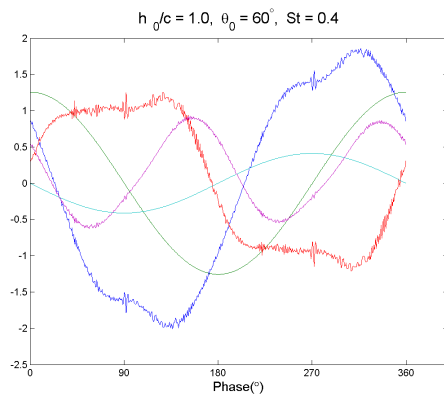
B.3 $h_0/c = 1.0$

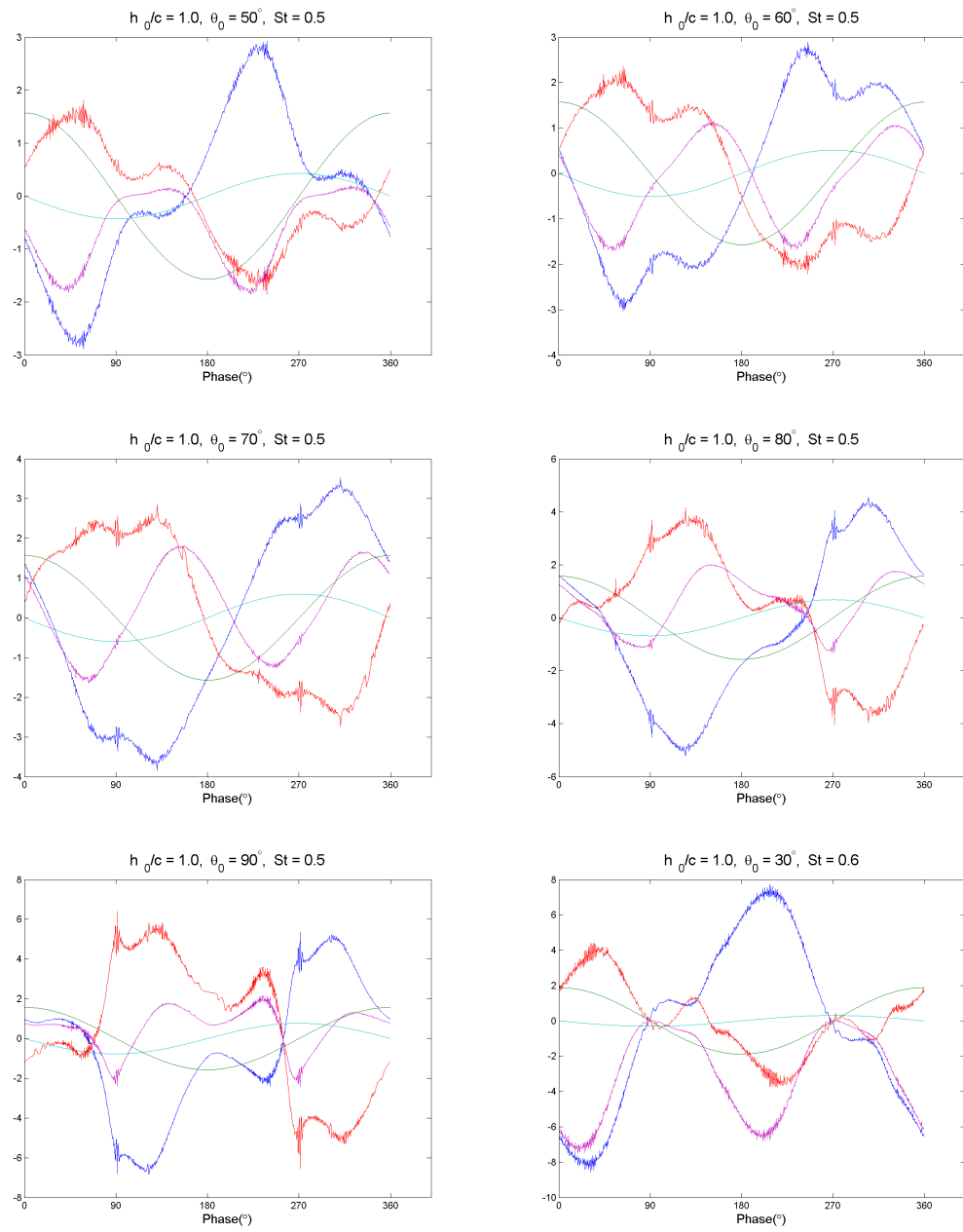


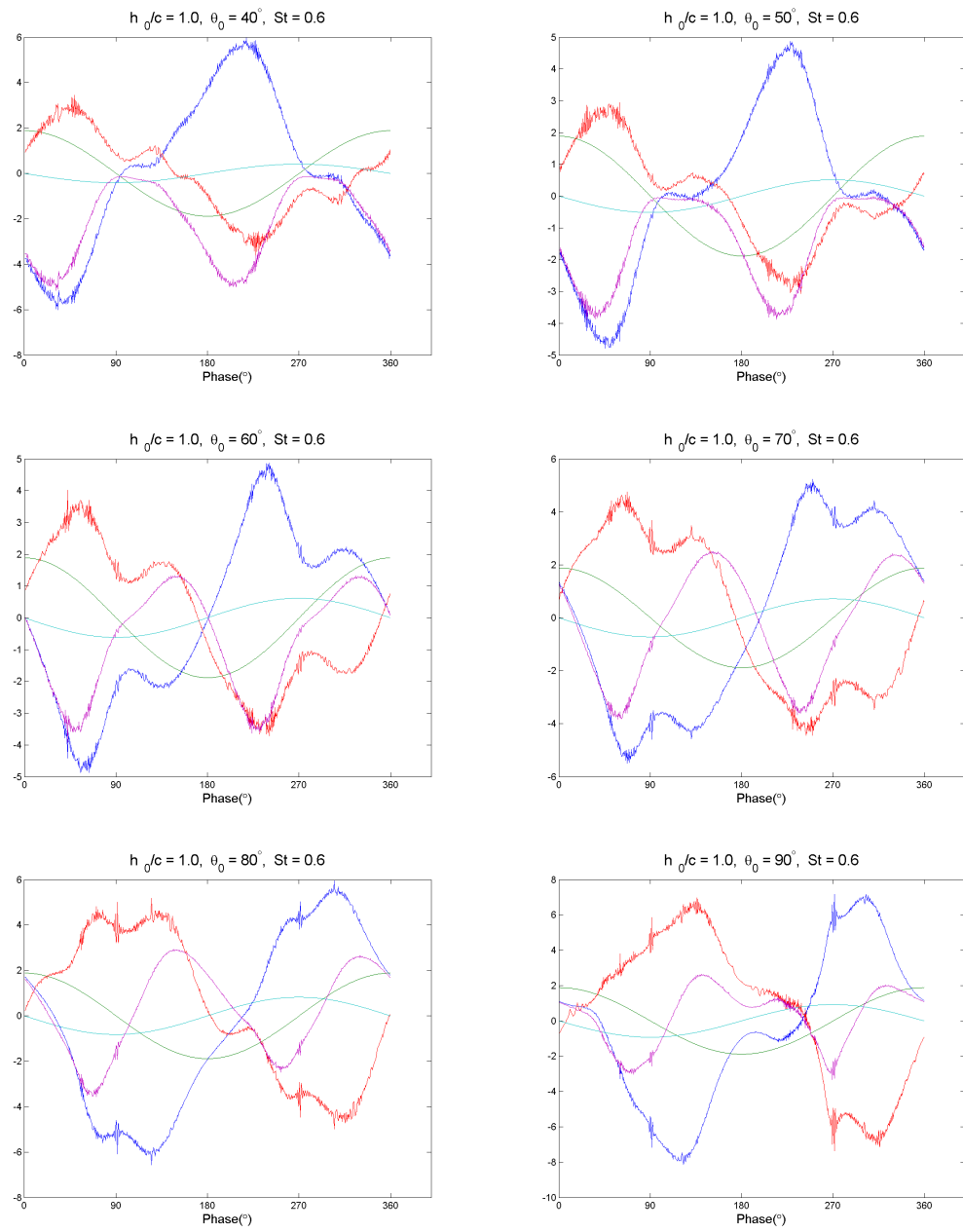




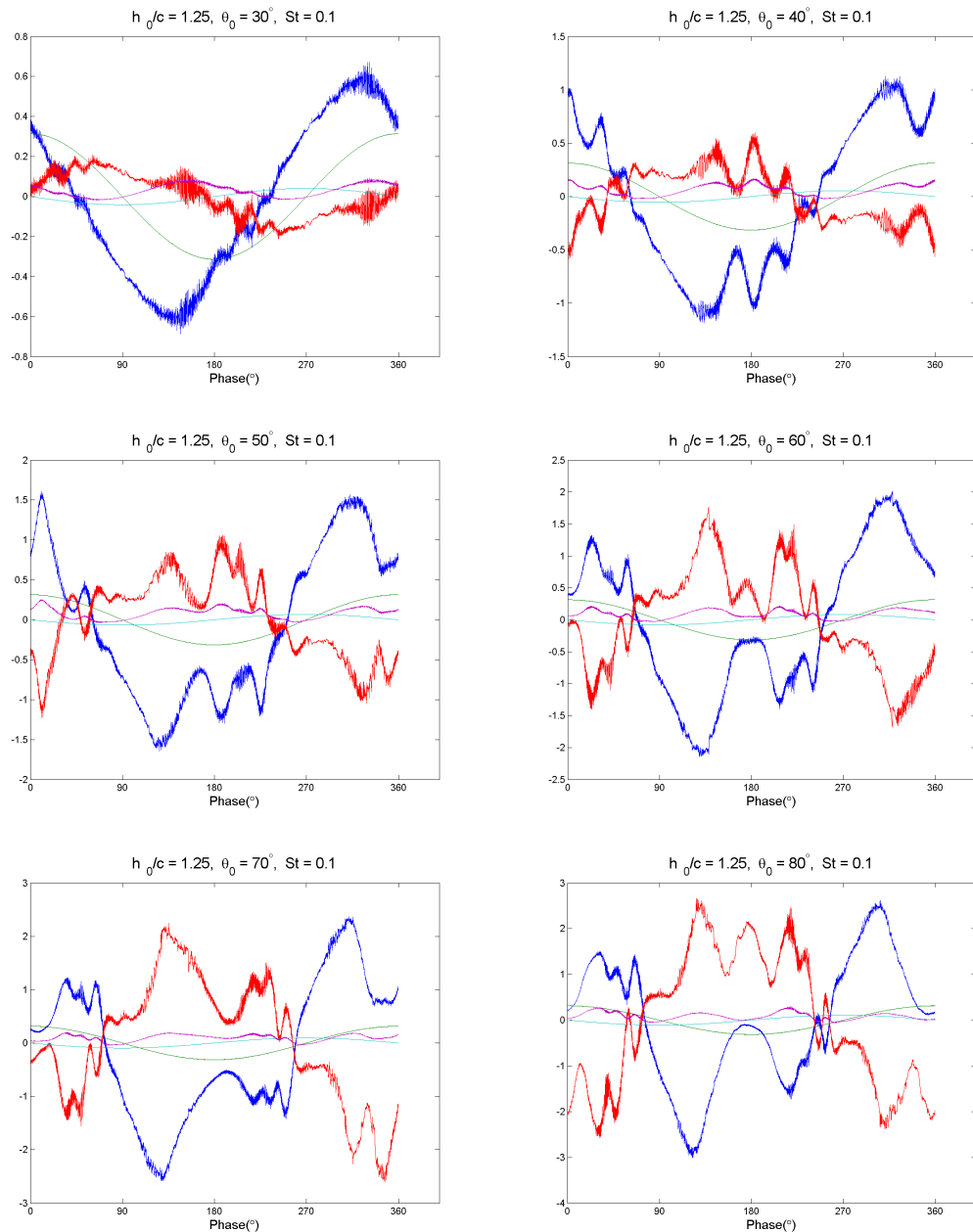


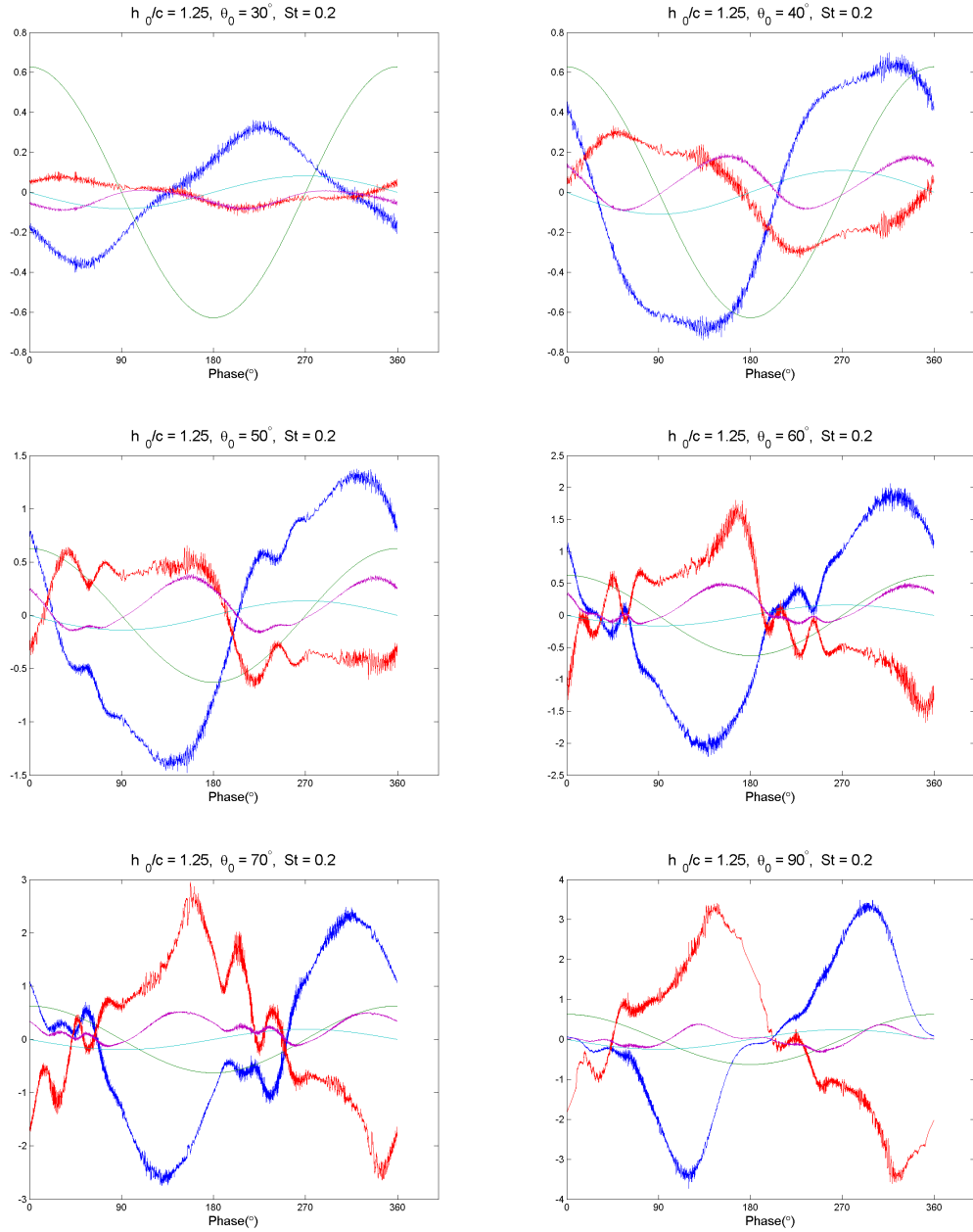


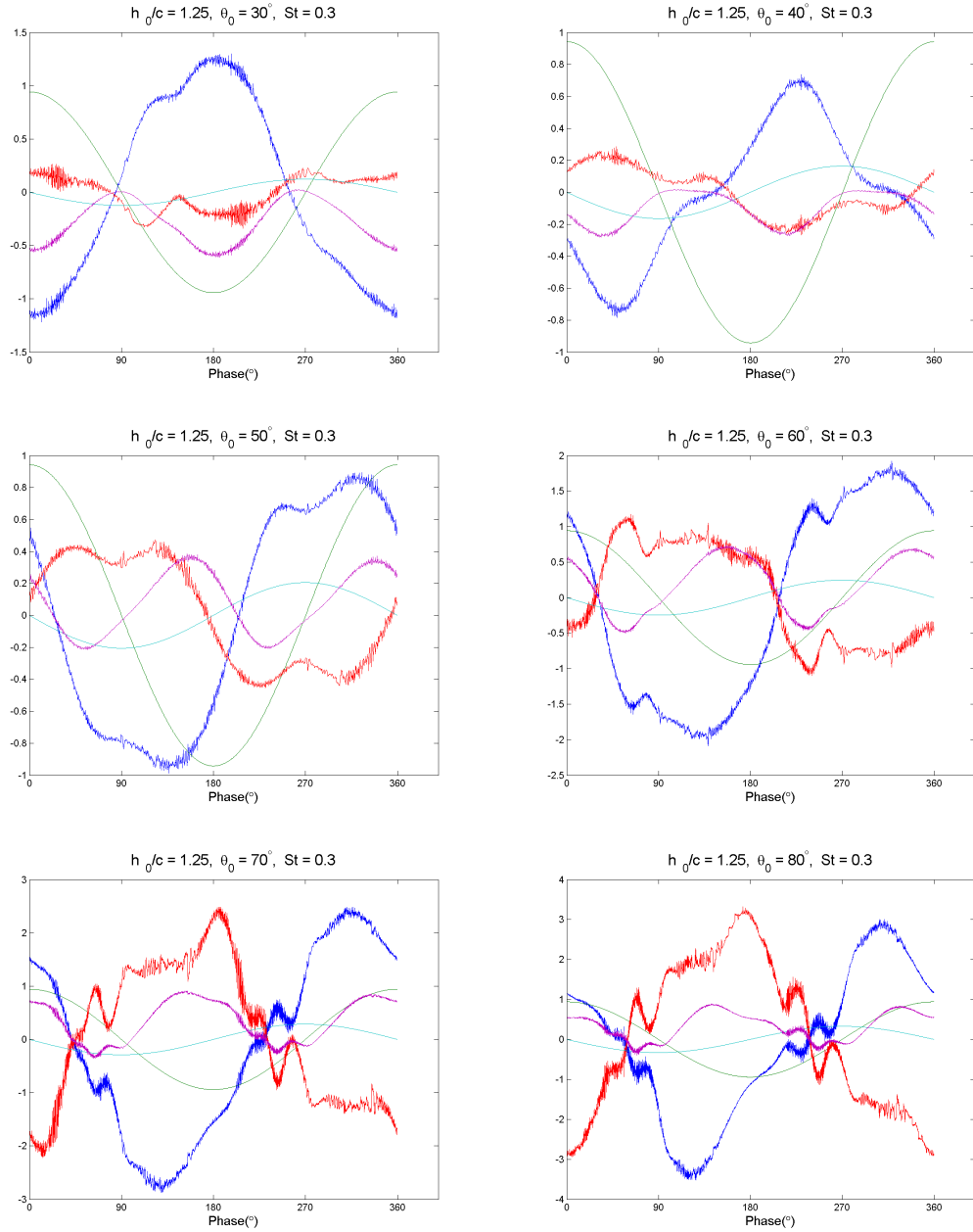


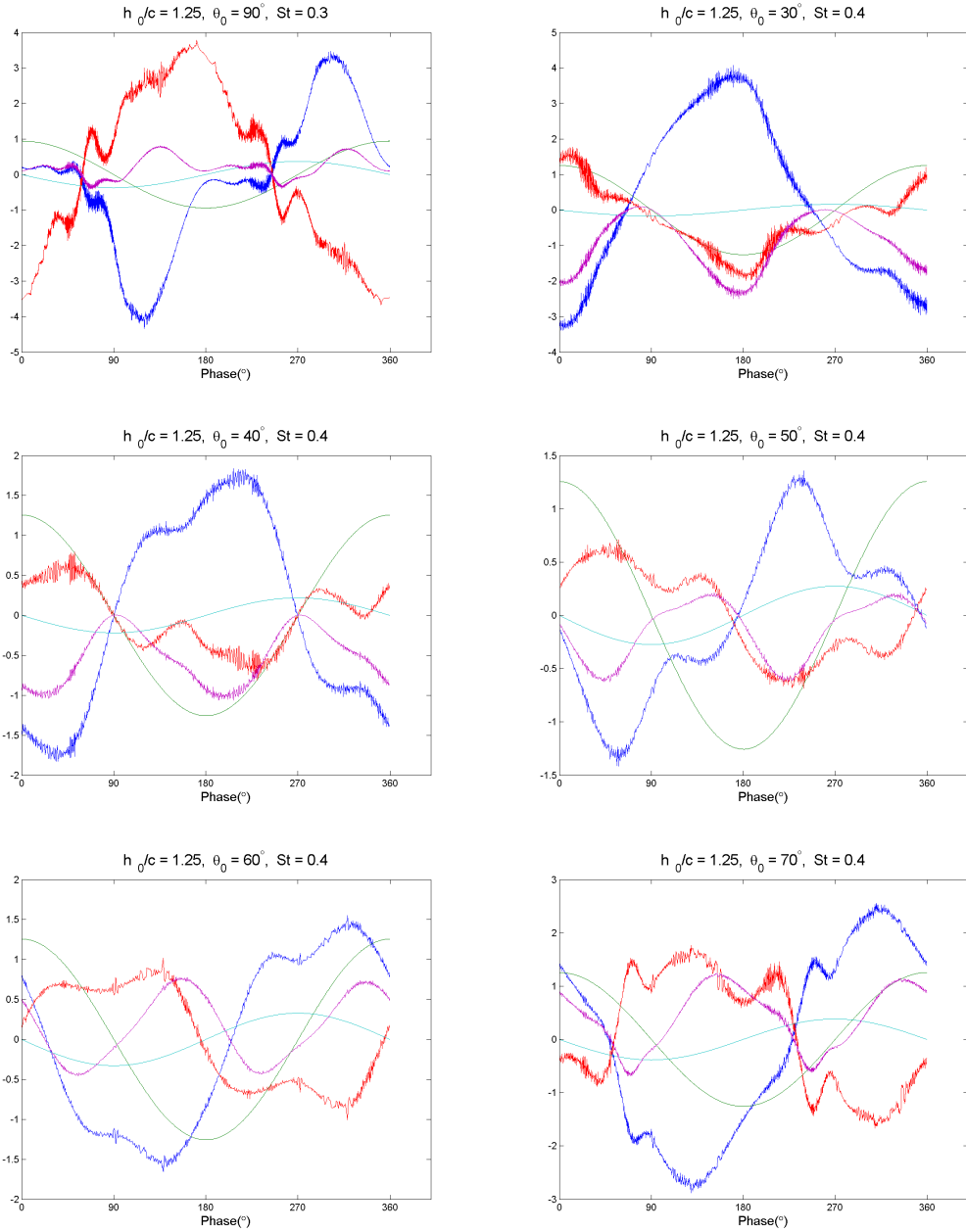


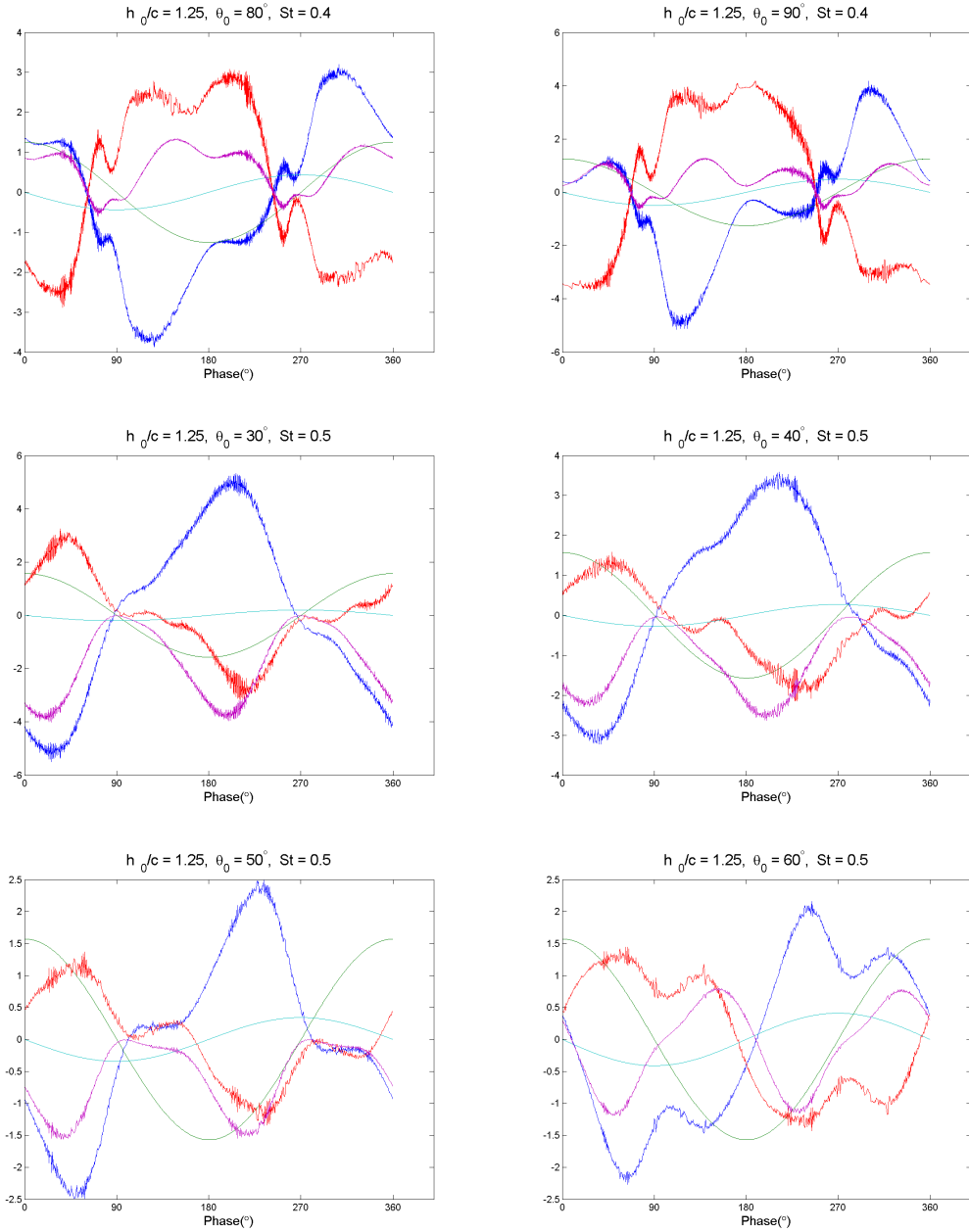
B.4 $h_0/c = 1.25$

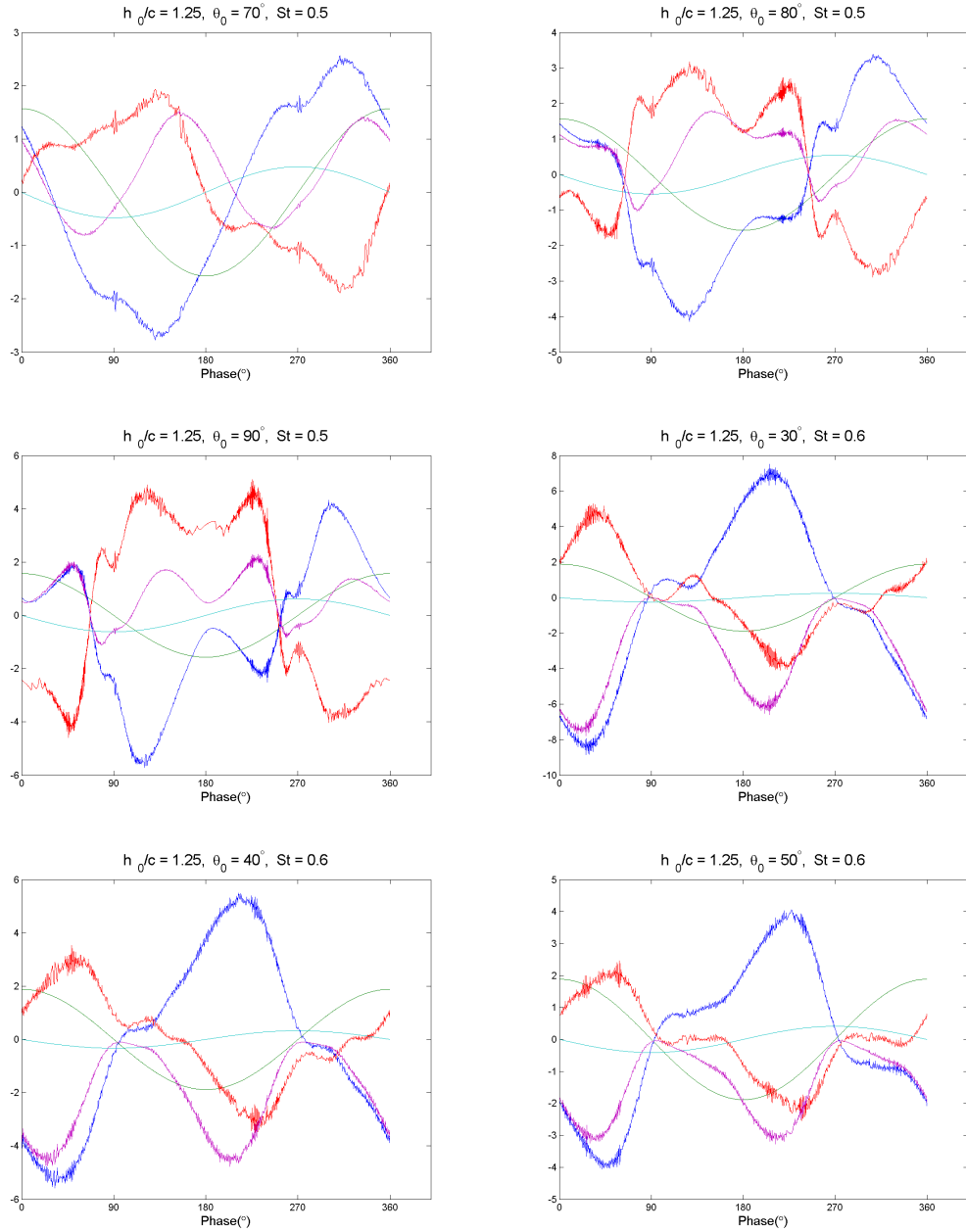


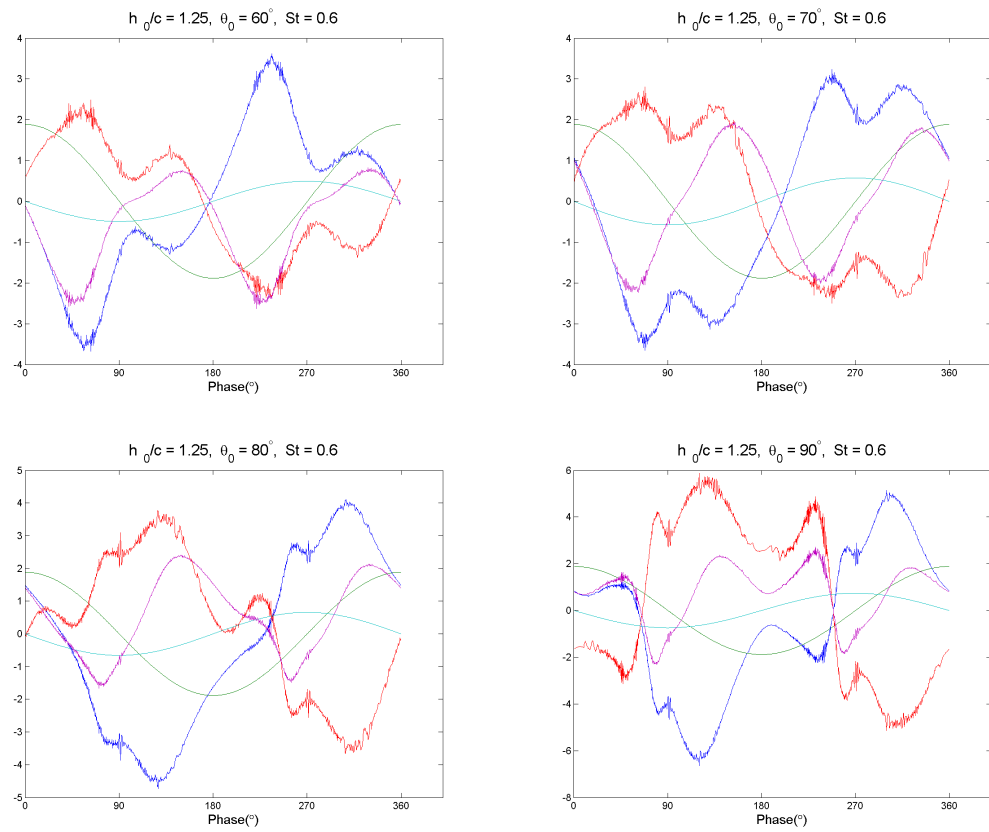












APPENDIX C

Wake Patterns

As a part of the database, the 6th cycle of the foil's sinusoidal motion is recorded in a video for wake visualization. From this video, screenshots of the wake pattern were extracted at four points throughout a half cycle of motion, depicted in Figure C.31. Screenshots from the entire cycle would be unnecessary due to the fact that the wake pattern is mirrored in the second half of the cycle. Displayed below these screenshots for convenience is the force data from the previous Appendix for the corresponding half cycle. Colors and axis reflect those from the force plots in Appendix B.

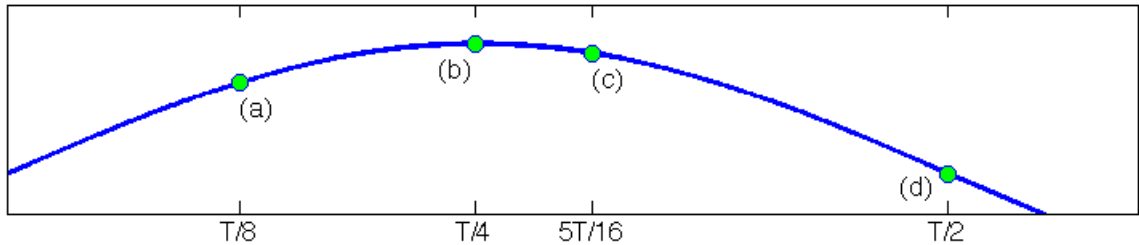


Figure C.31: Points in phase throughout a half cycle in which screenshots were taken.

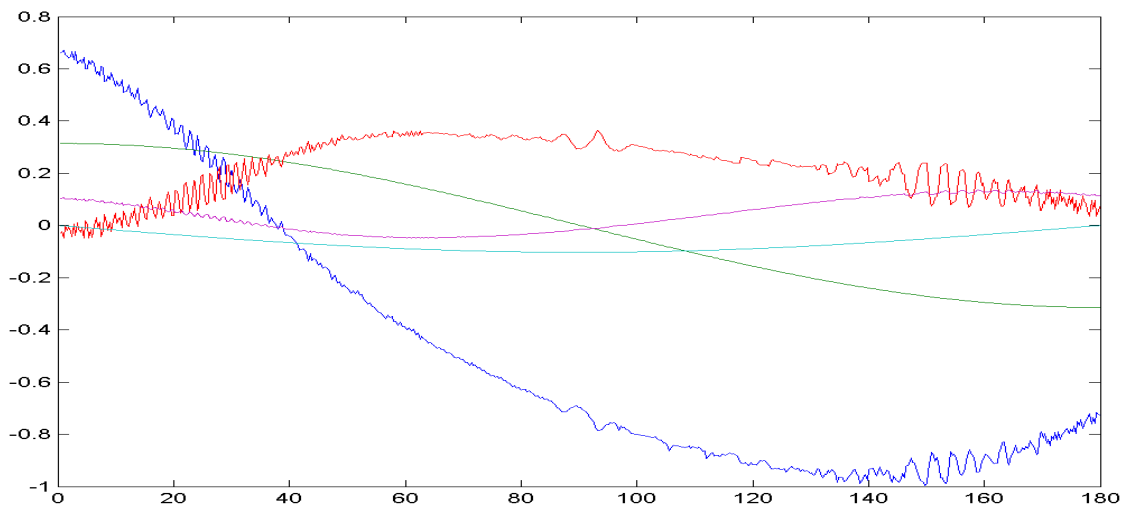
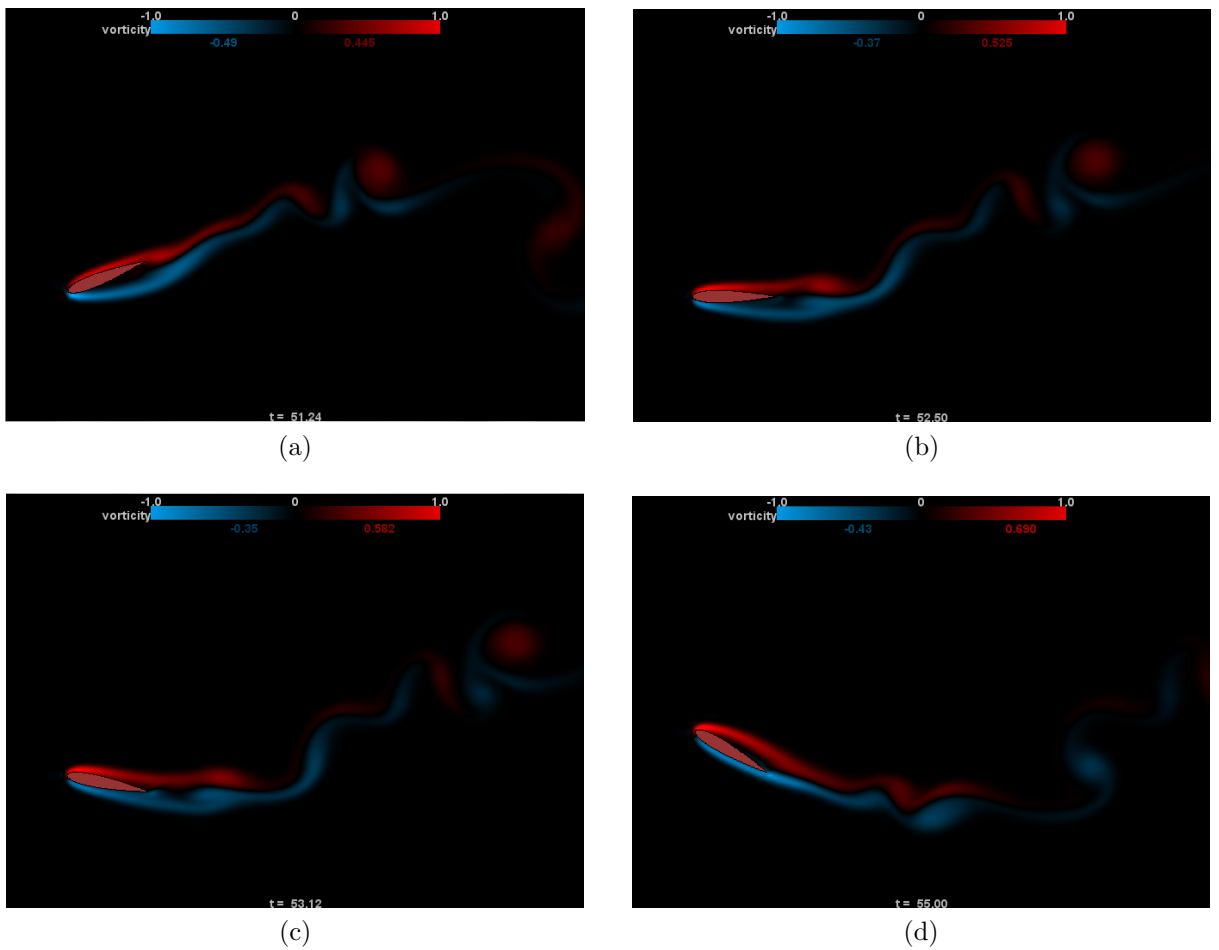


Figure C.32: $h_0/c = 0.5$, $St = 0.1$, $\theta_0 = 30^\circ$

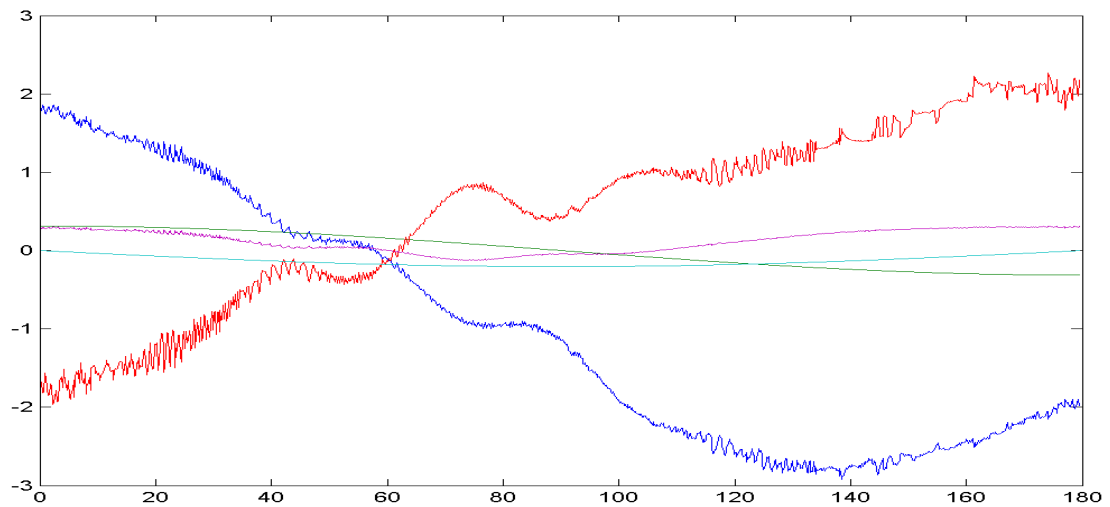
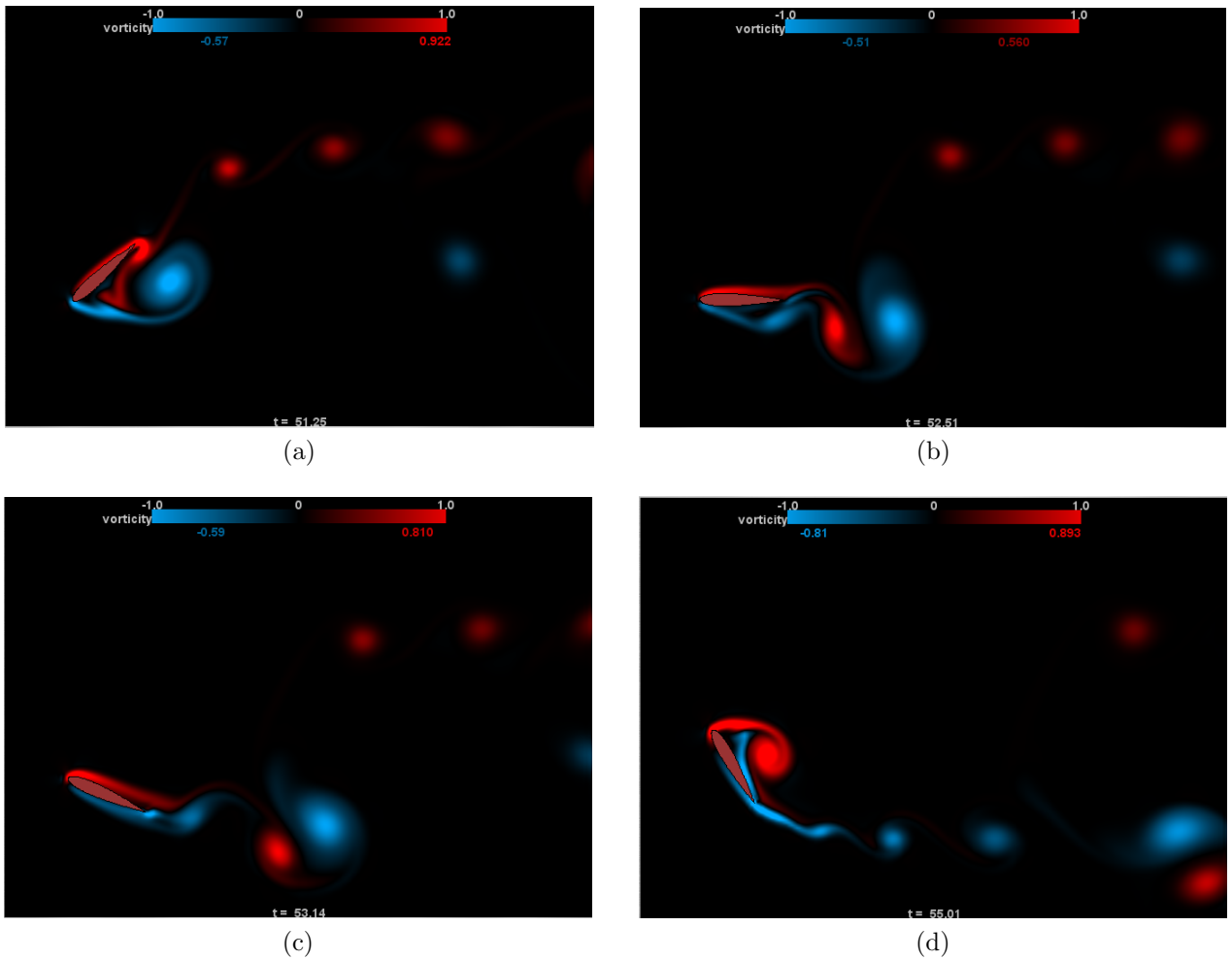


Figure C.33: $h_0/c = 0.5$, $St = 0.1$, $\theta_0 = 60^\circ$

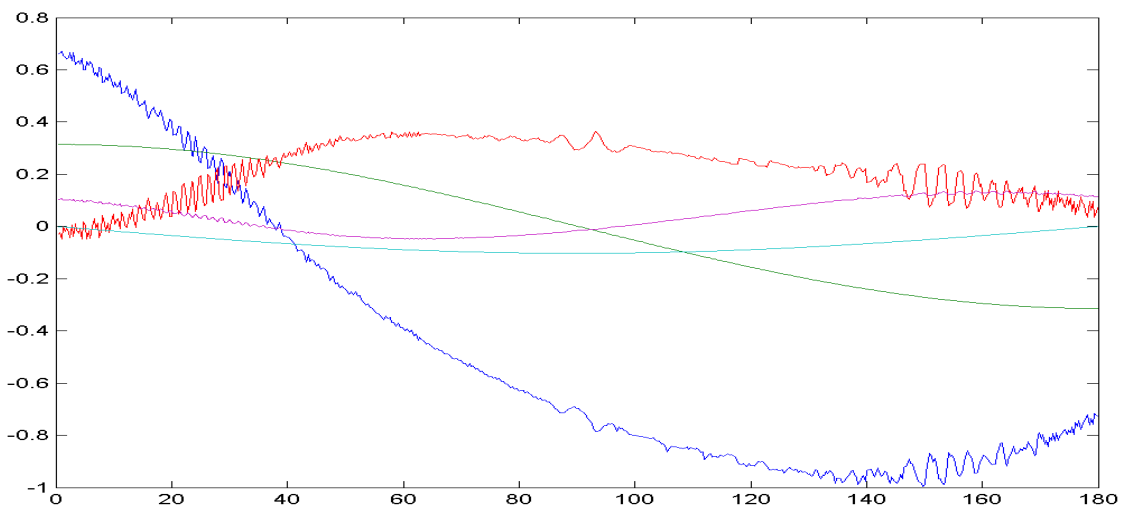
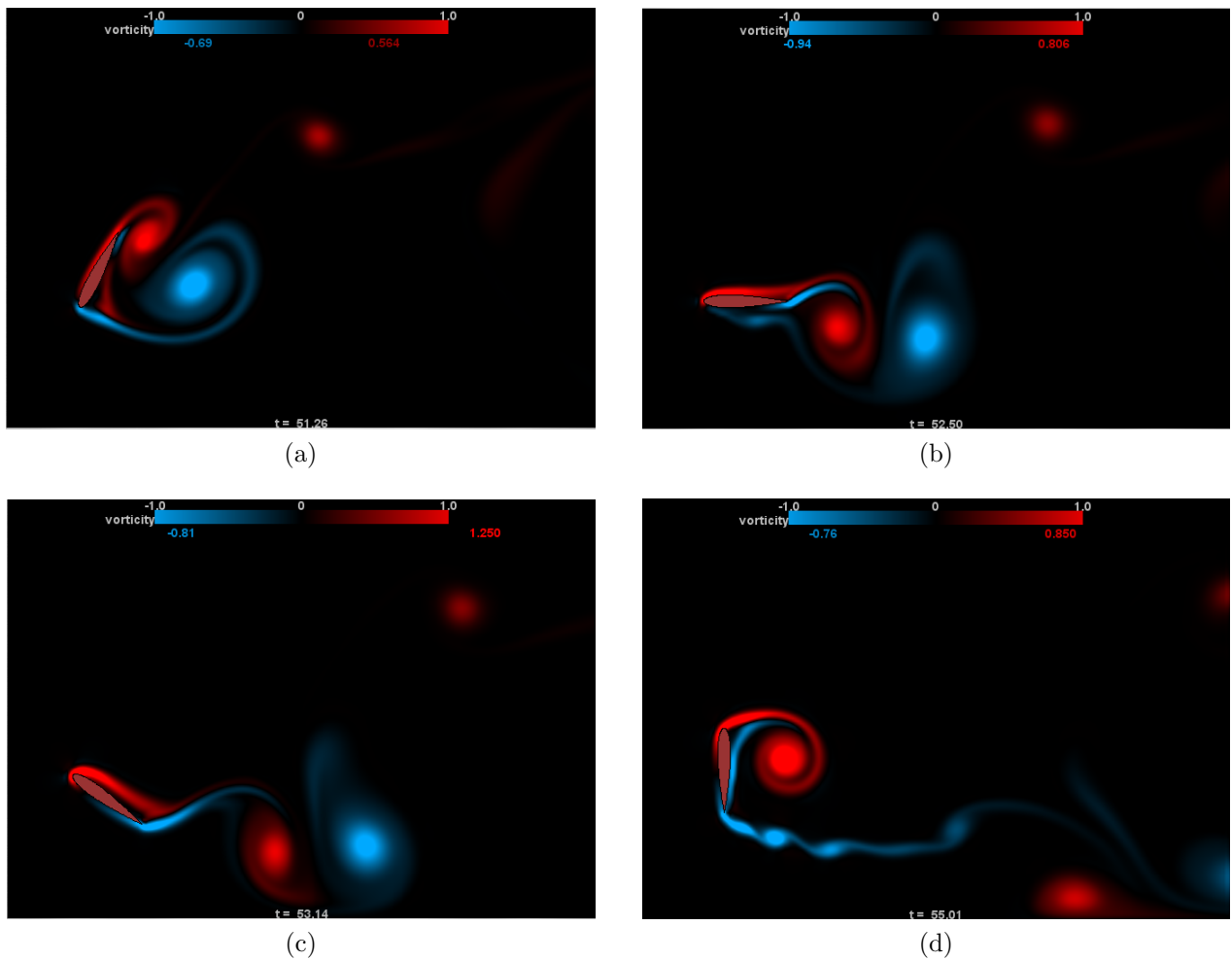


Figure C.34: $h_0/c = 0.5$, $St = 0.1$, $\theta_0 = 90^\circ$

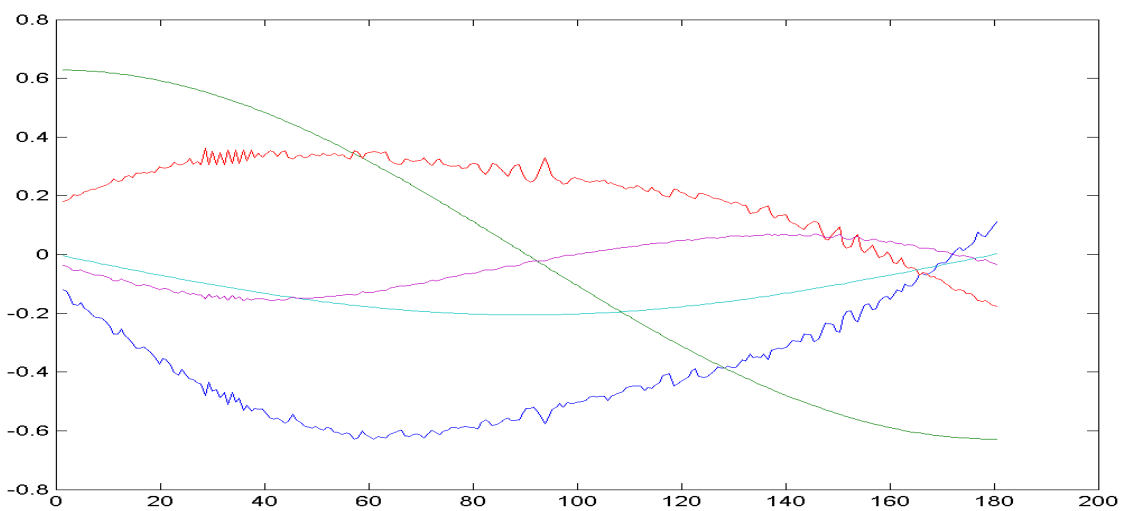
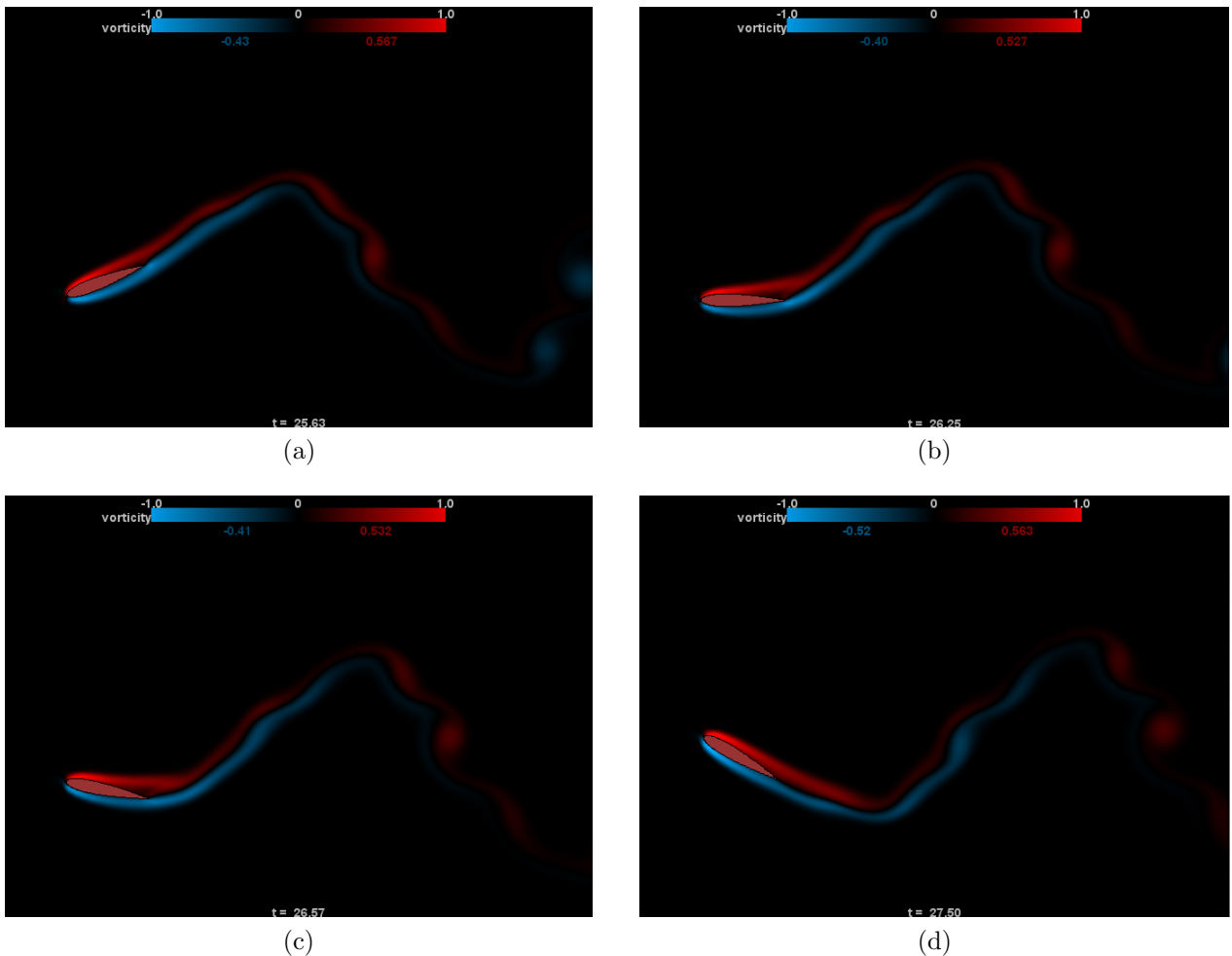


Figure C.35: $h_0/c = 0.5$, $St = 0.2$, $\theta_0 = 30^\circ$

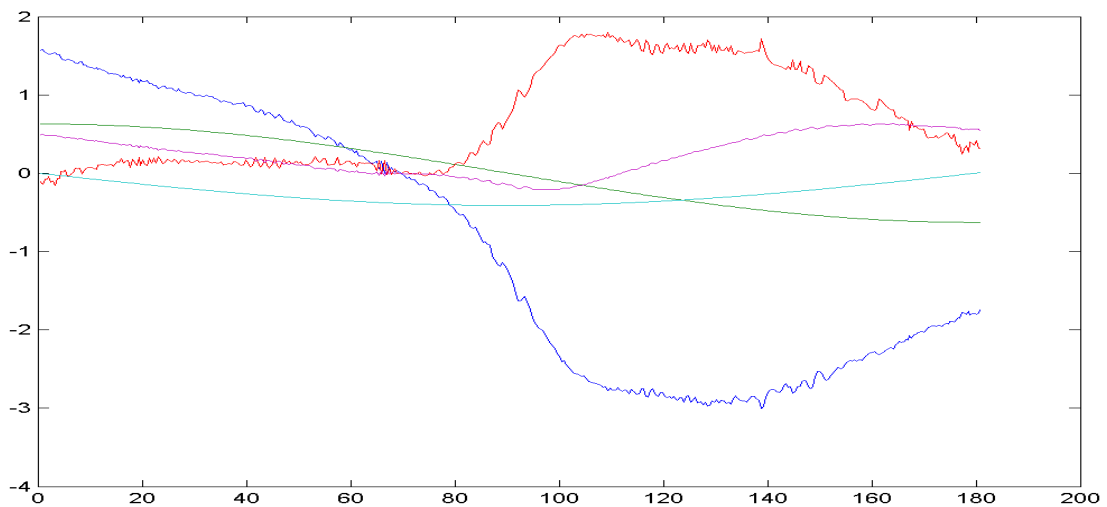
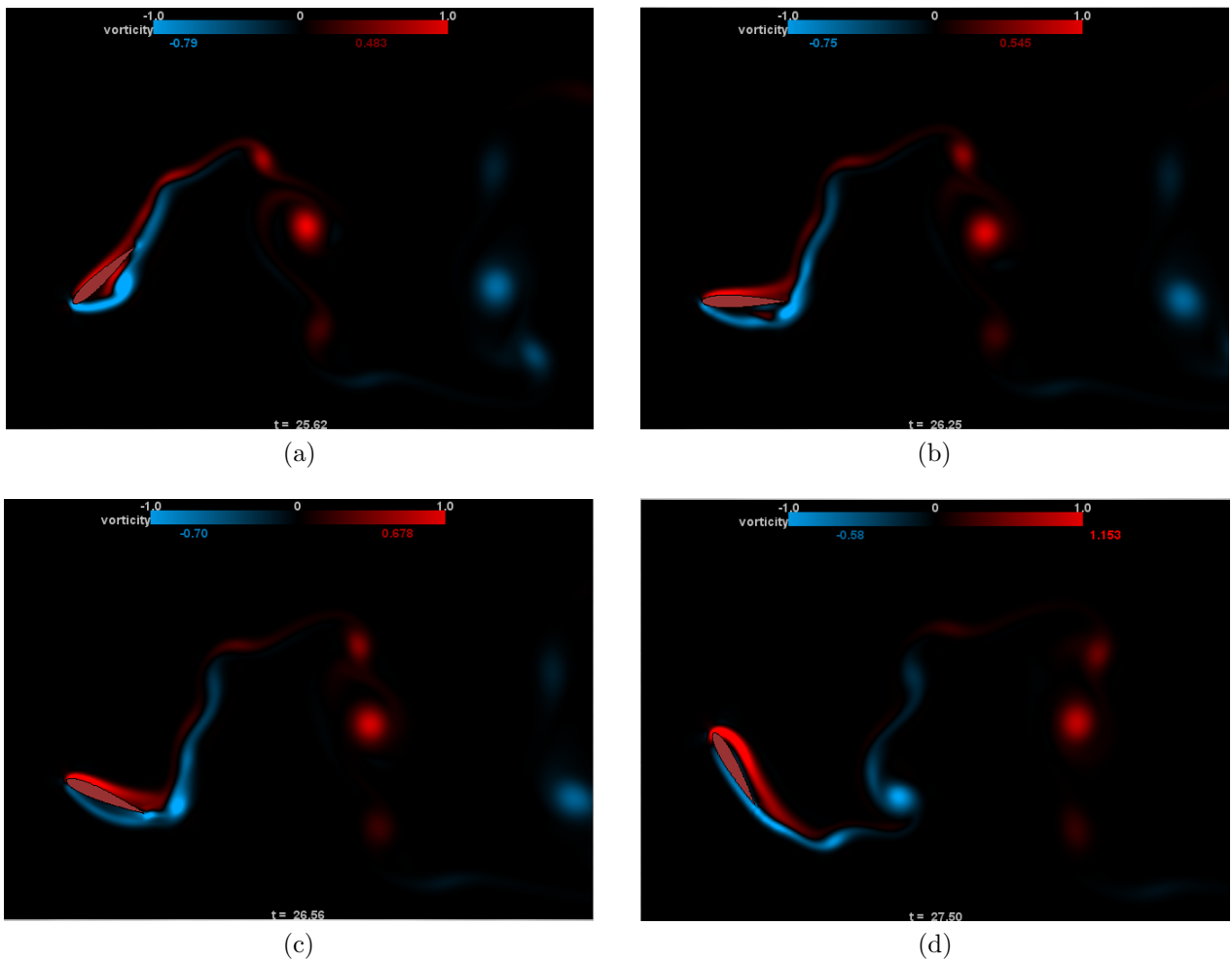


Figure C.36: $h_0/c = 0.5$, $St = 0.2$, $\theta_0 = 60^\circ$

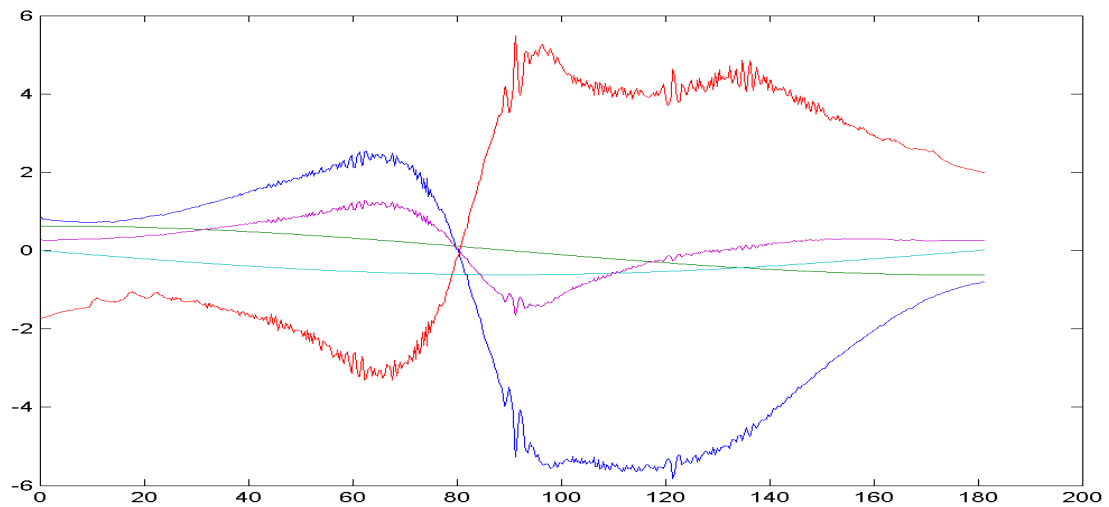
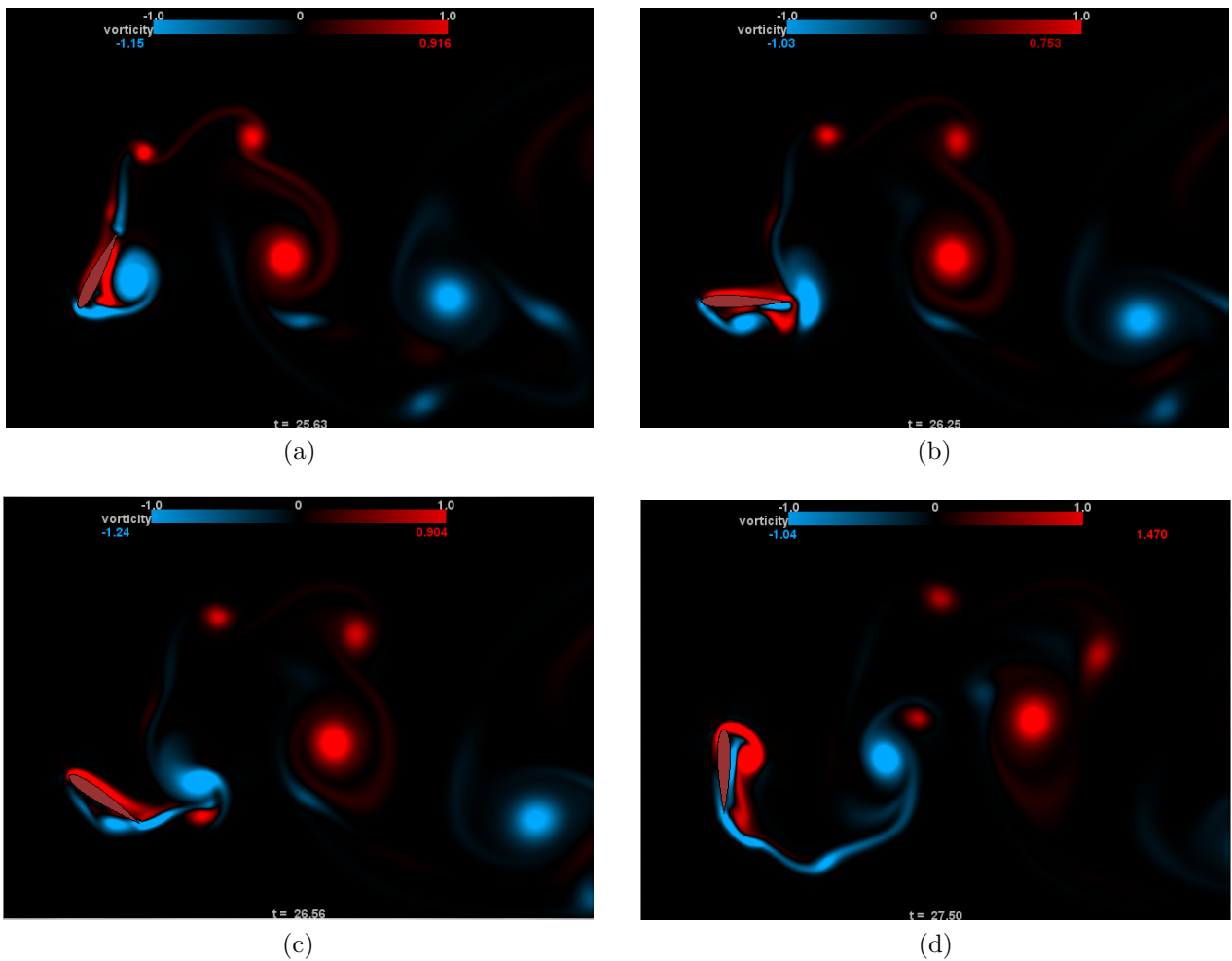


Figure C.37: $h_0/c = 0.5$, $St = 0.2$, $\theta_0 = 90^\circ$

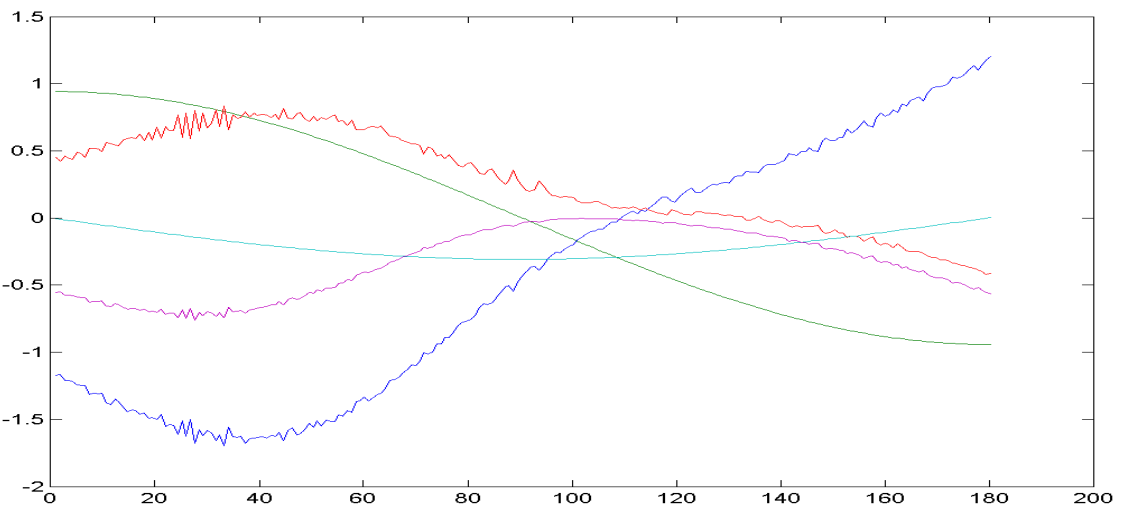
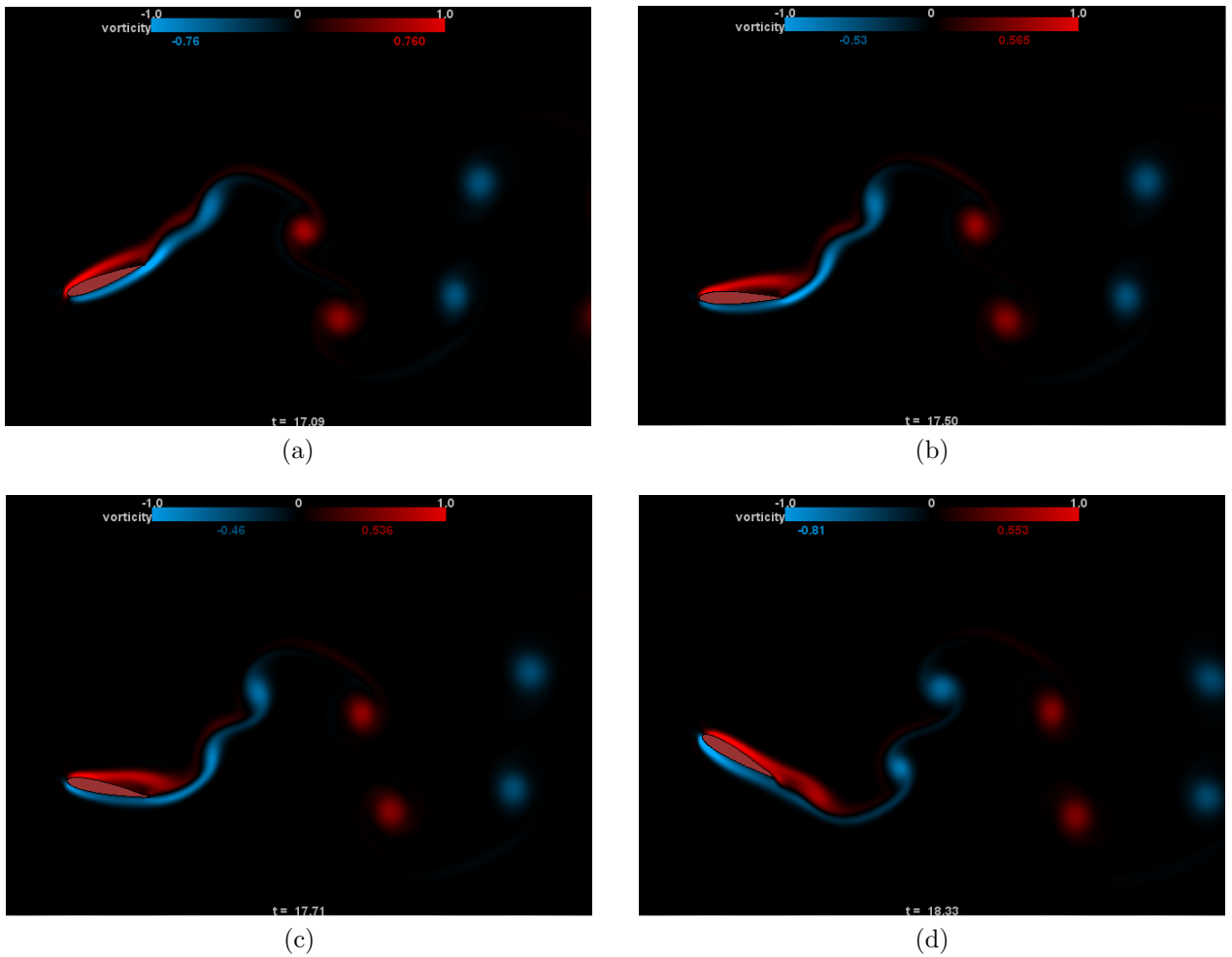


Figure C.38: $h_0/c = 0.5$, $St = 0.3$, $\theta_0 = 30^\circ$

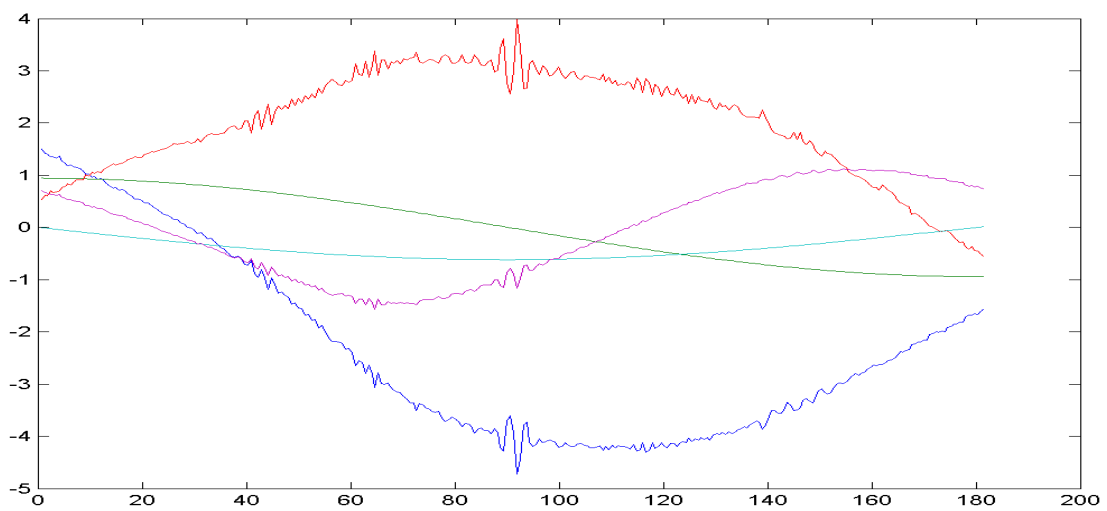
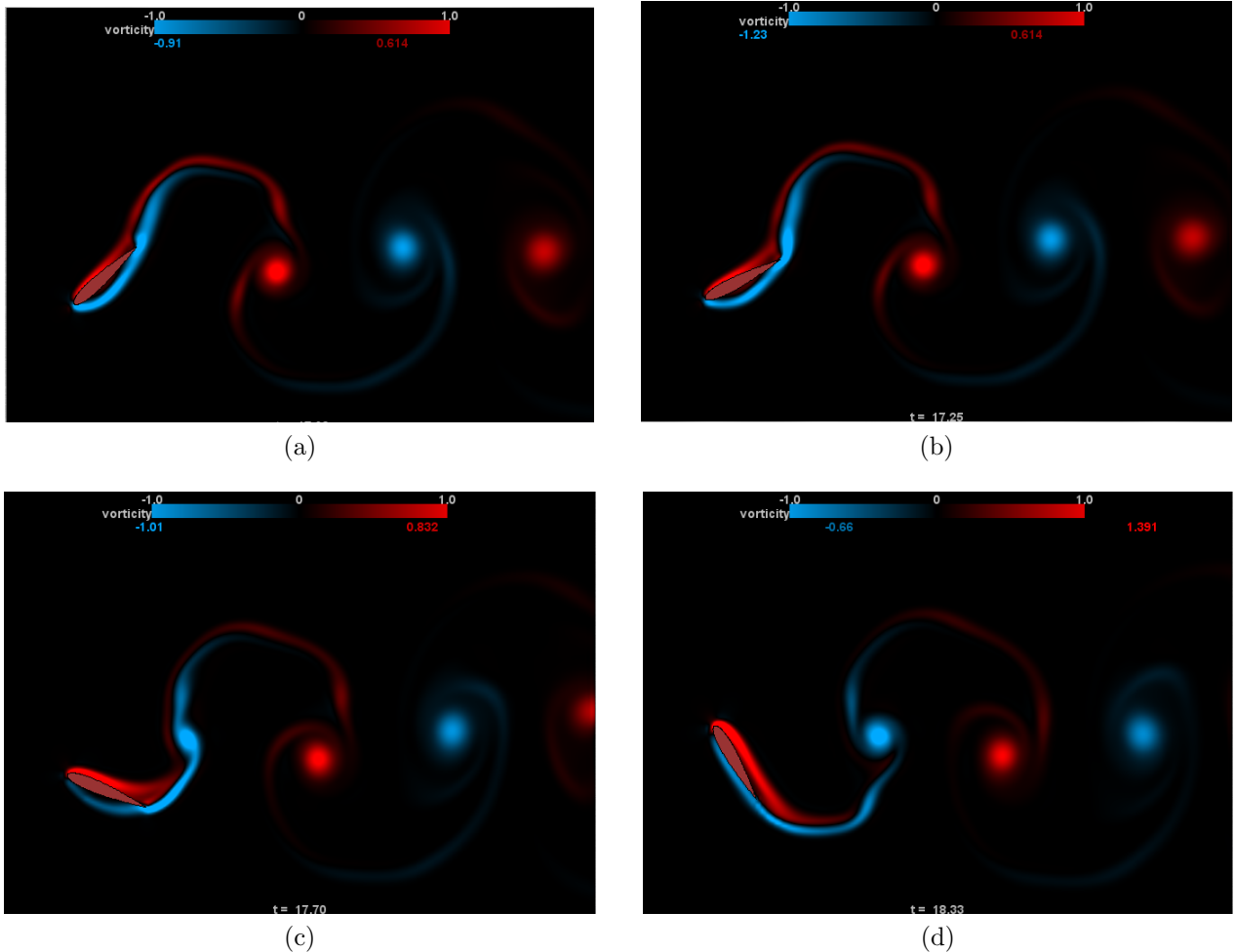


Figure C.39: $h_0/c = 0.5$, $St = 0.3$, $\theta_0 = 60^\circ$

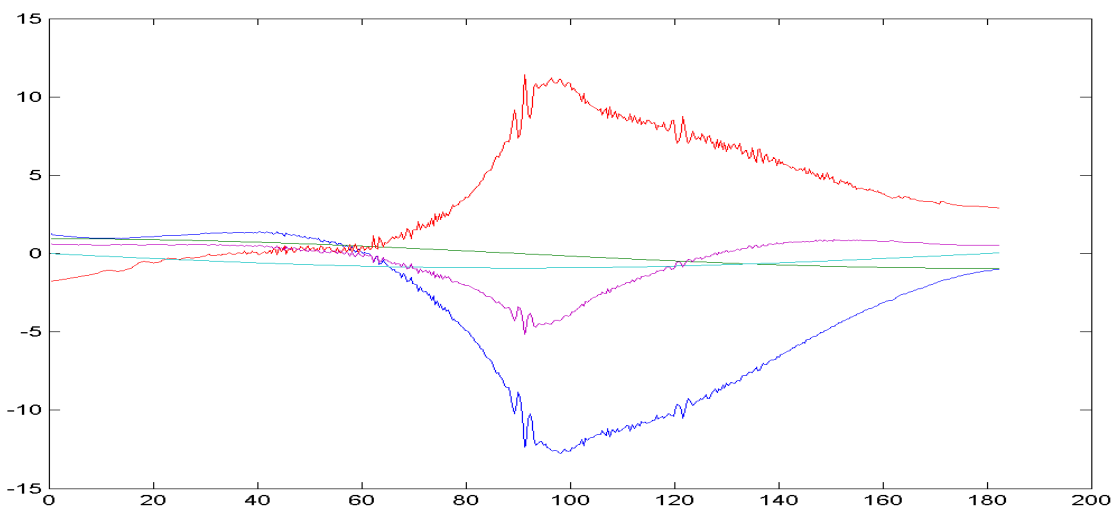
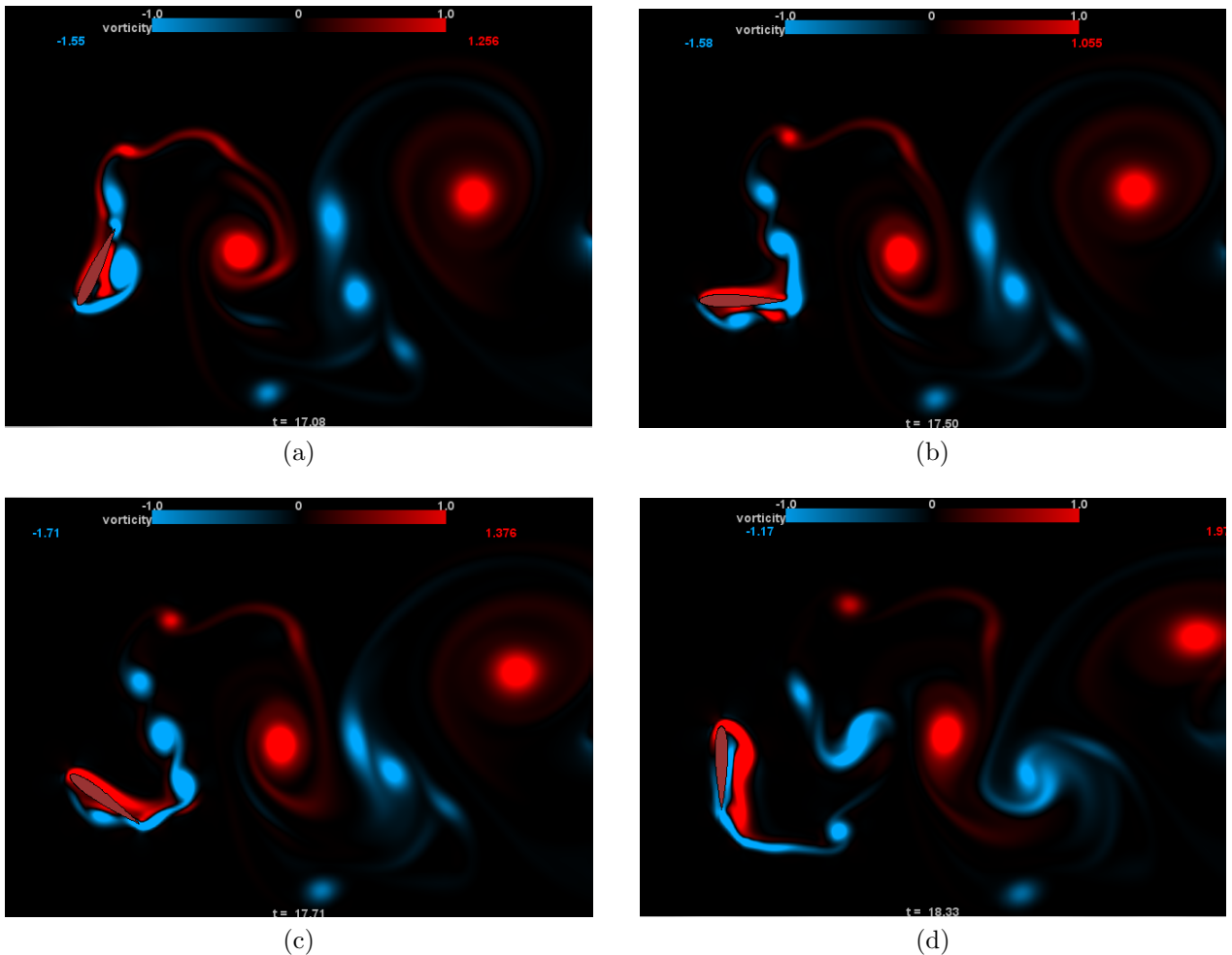


Figure C.40: $h_0/c = 0.5$, $St = 0.3$, $\theta_0 = 90^\circ$

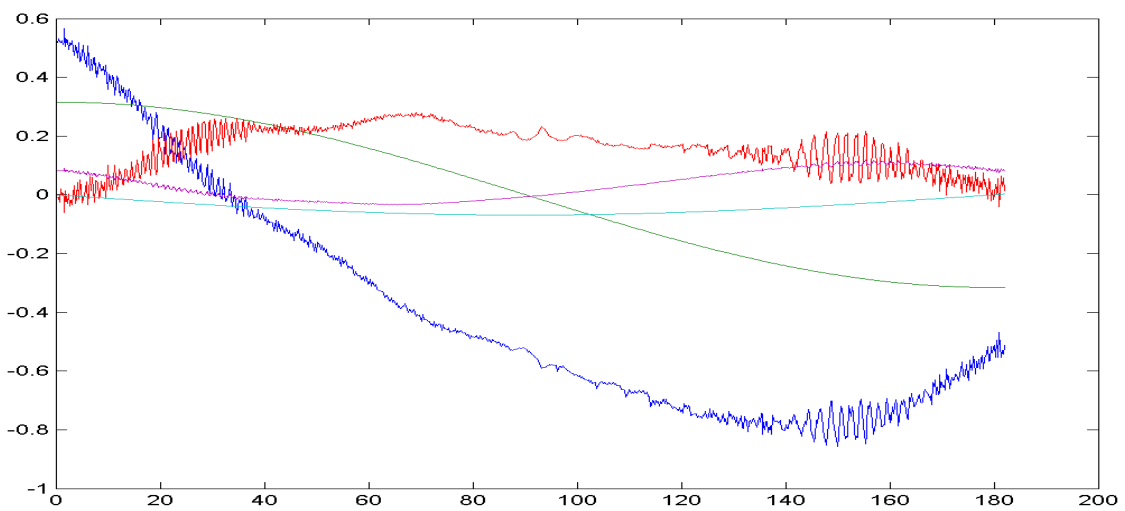
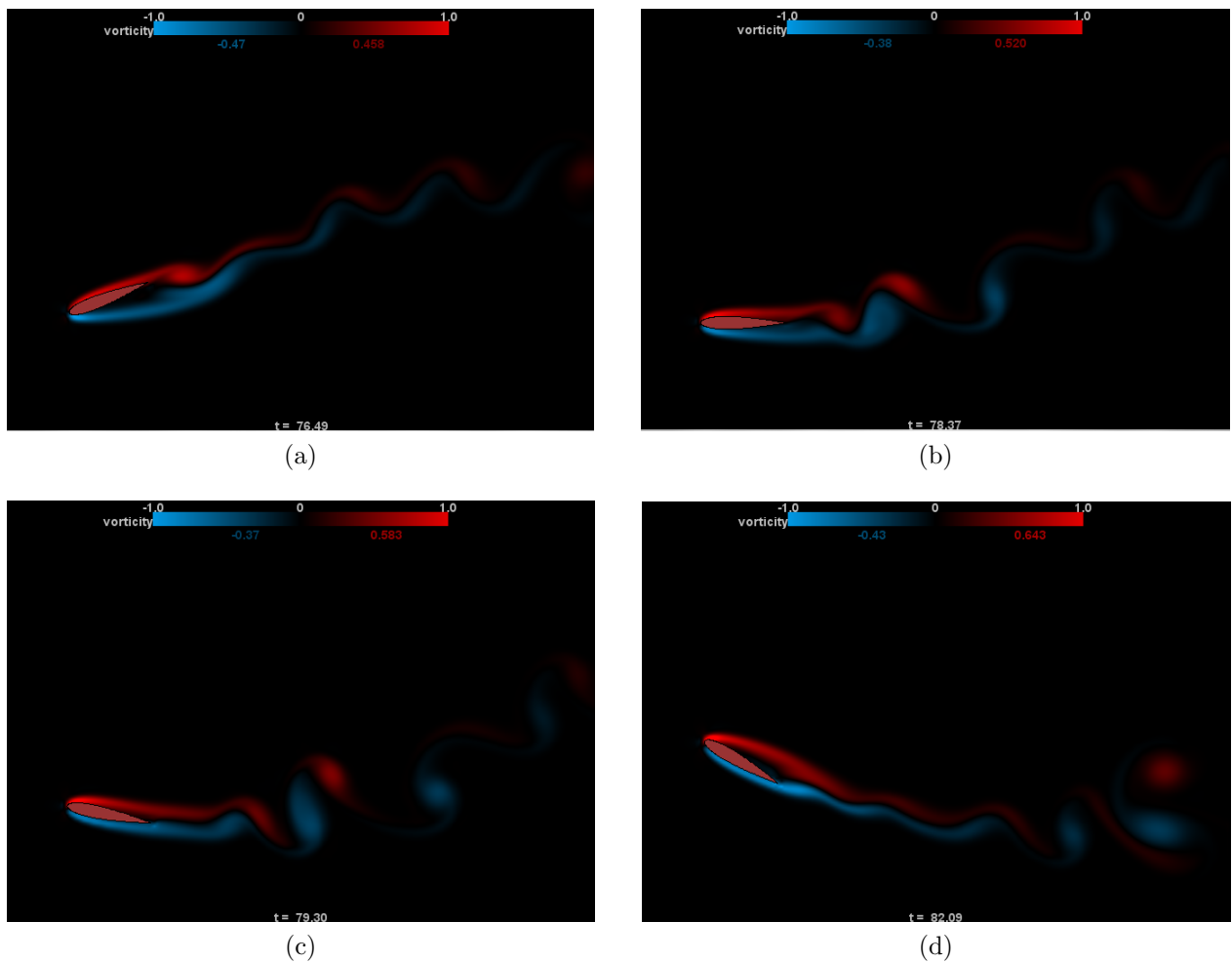


Figure C.41: $h_0/c = 0.75$, $St = 0.1$, $\theta_0 = 30^\circ$

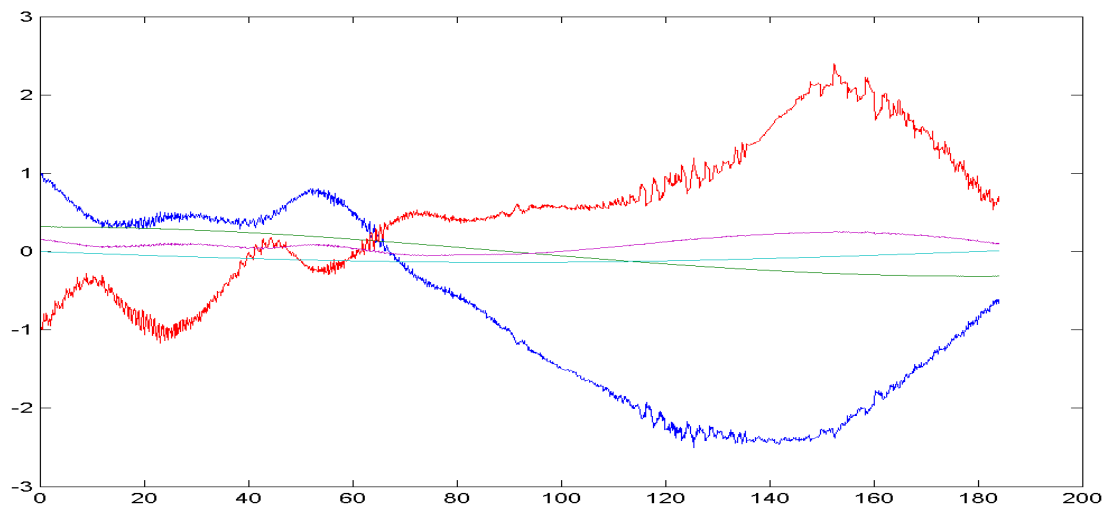
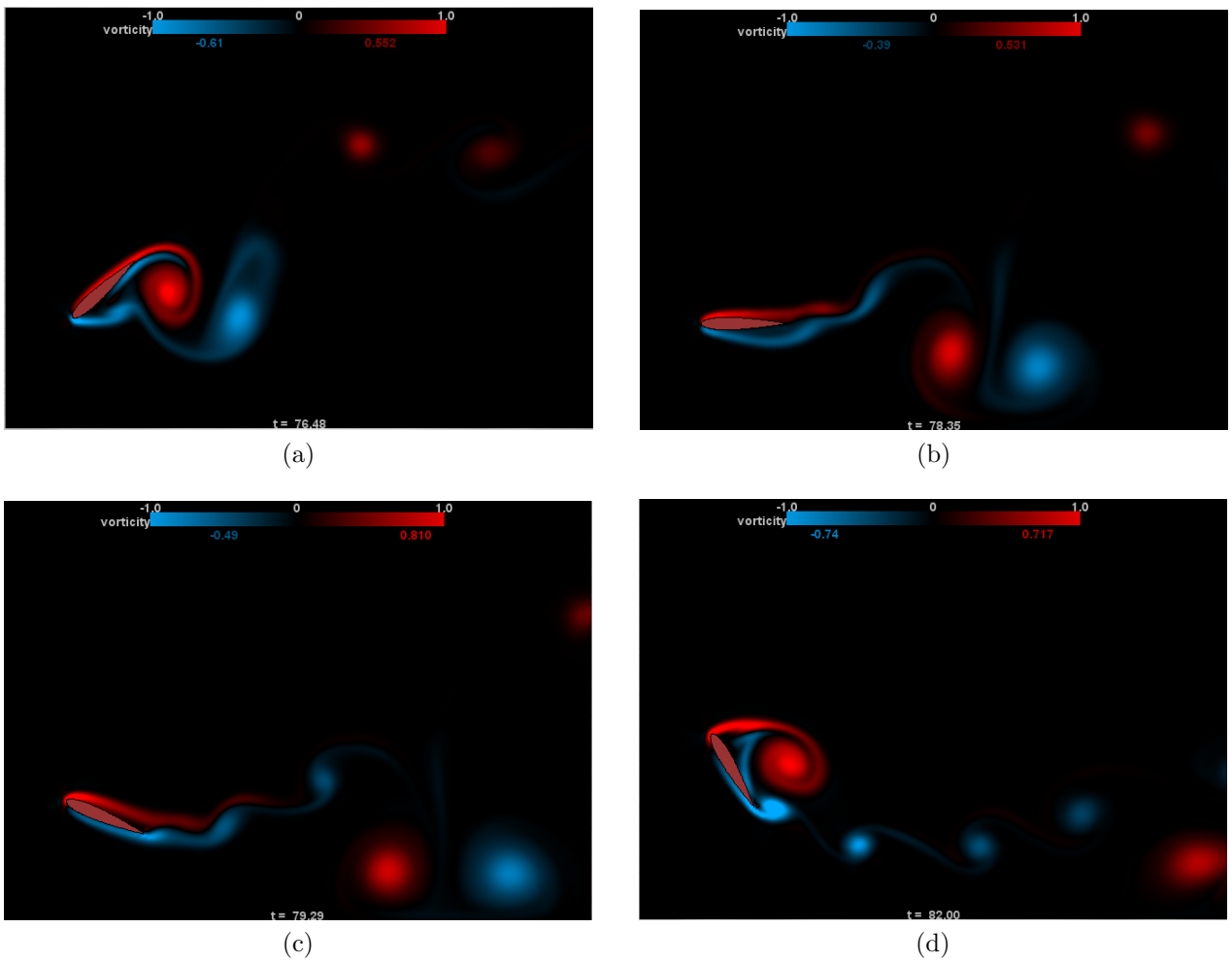


Figure C.42: $h_0/c = 0.75$, $St = 0.1$, $\theta_0 = 60^\circ$

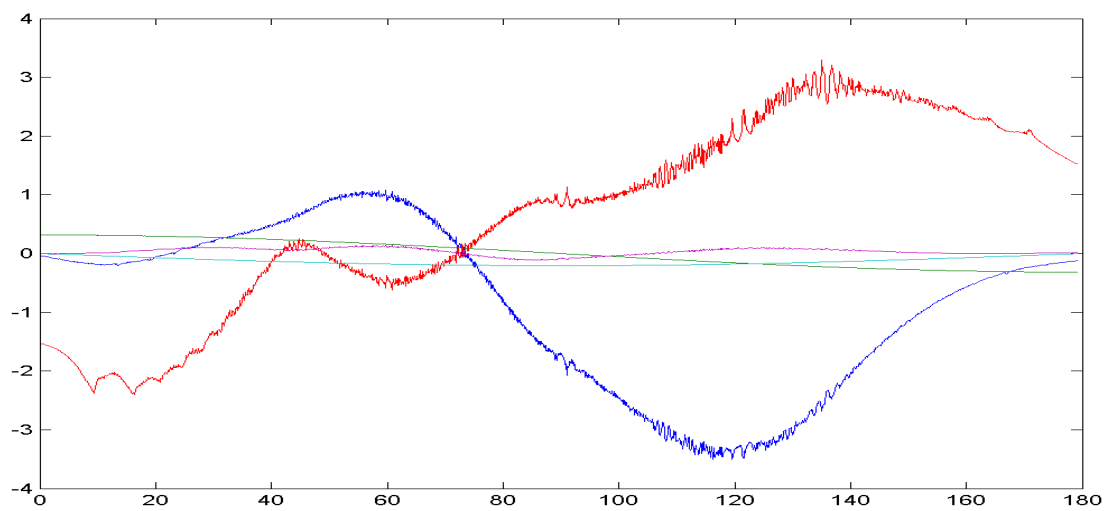
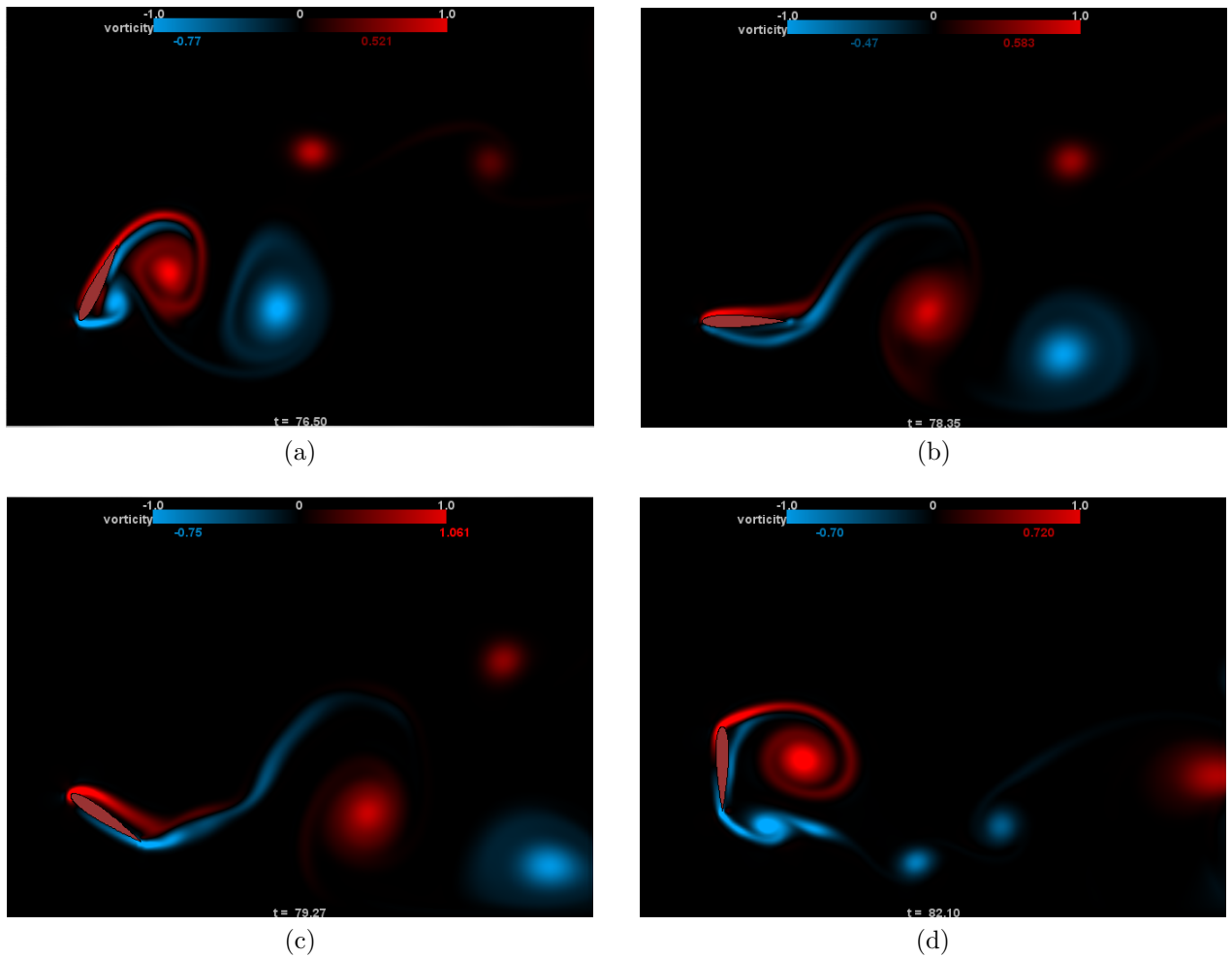


Figure C.43: $h_0/c = 0.75$, $St = 0.1$, $\theta_0 = 90^\circ$

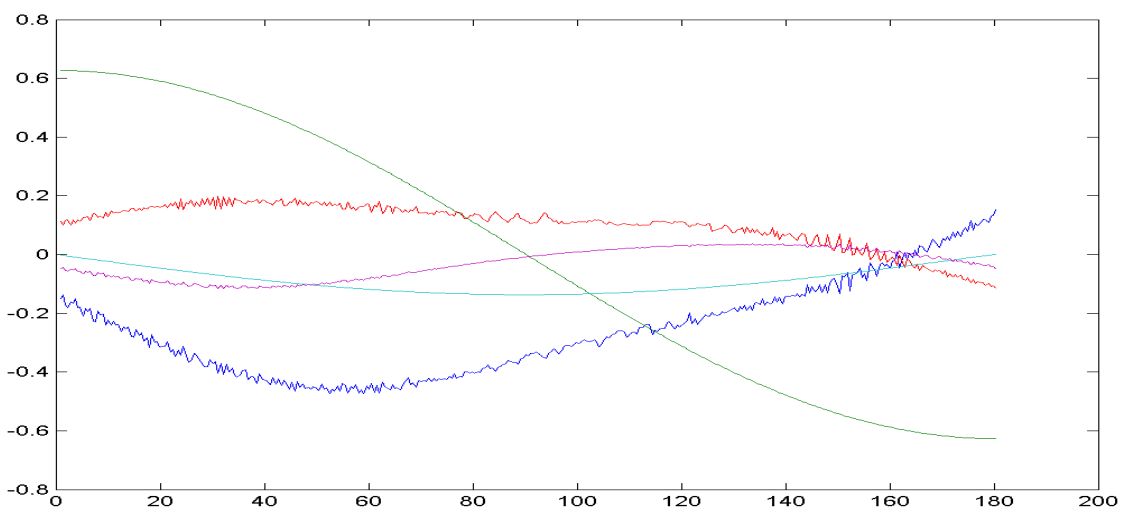
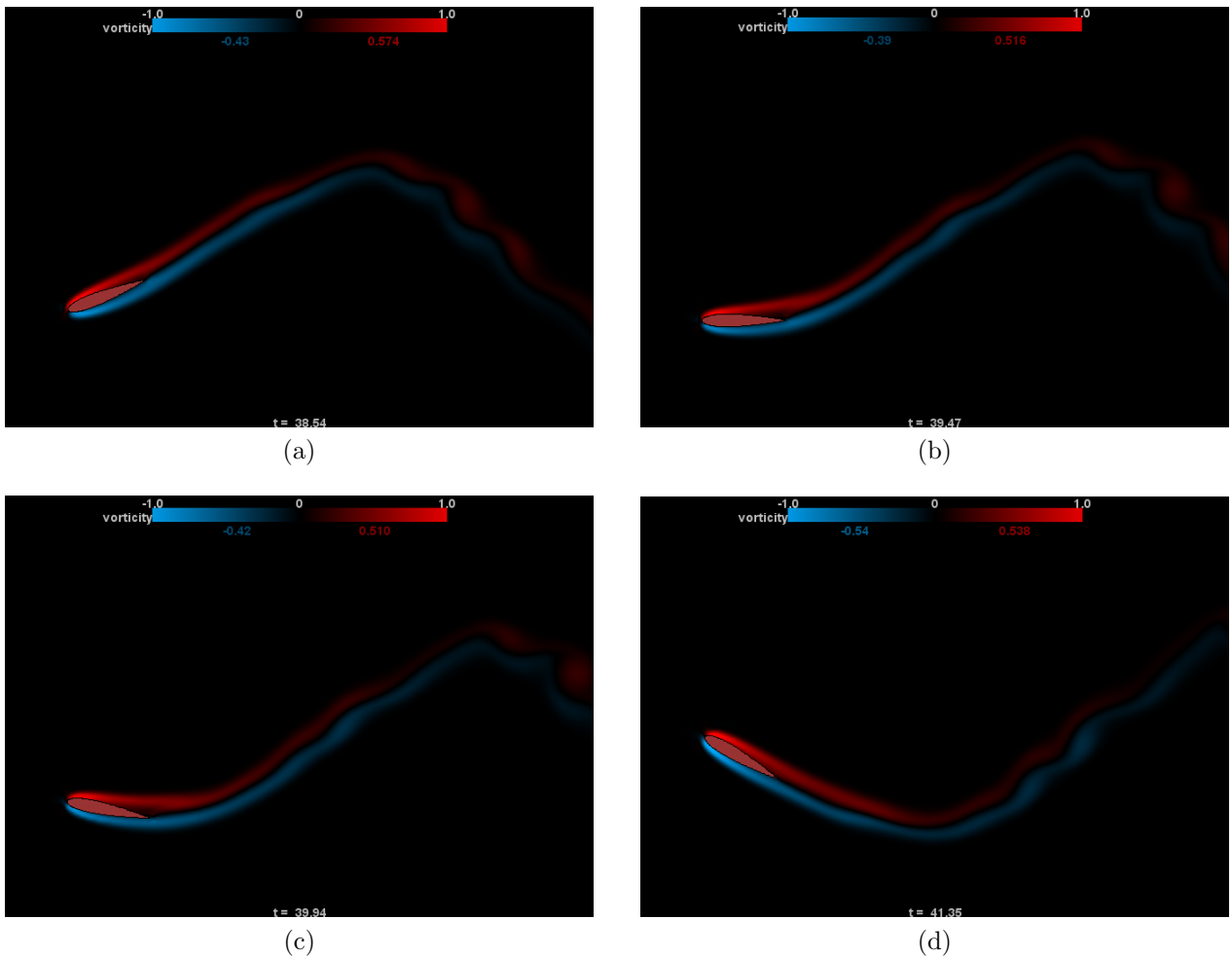


Figure C.44: $h_0/c = 0.75$, $St = 0.2$, $\theta_0 = 30^\circ$

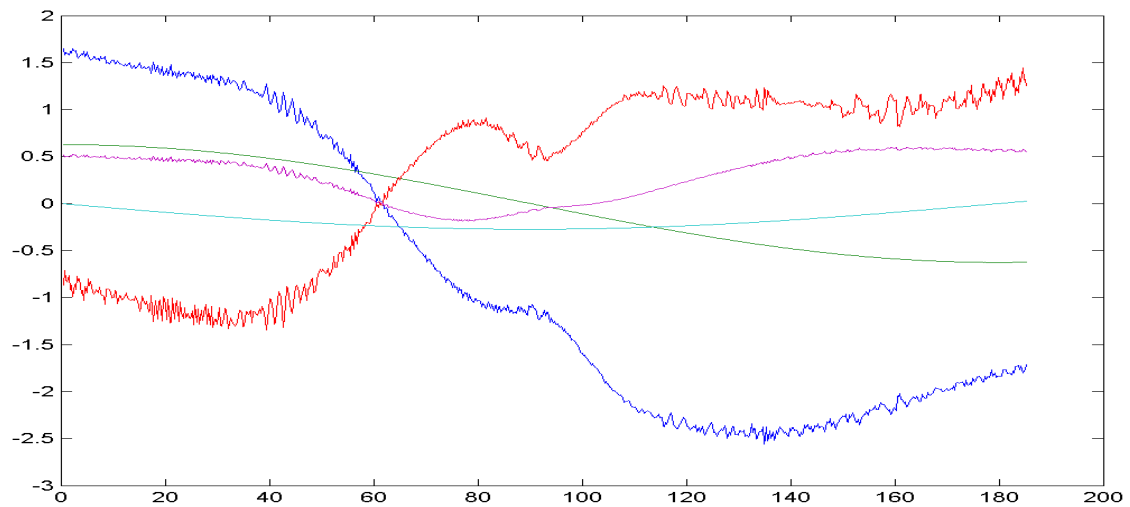
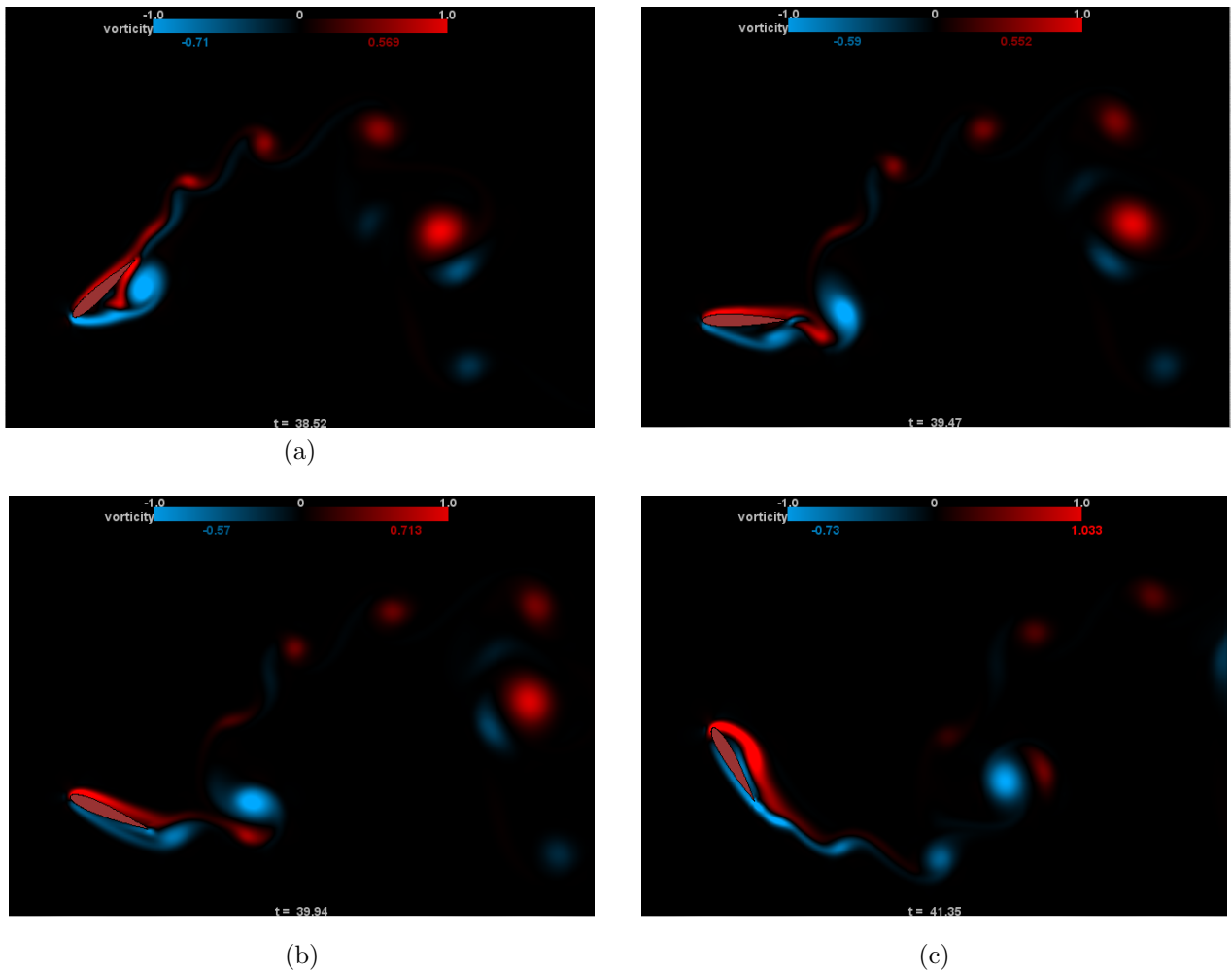


Figure C.45: $h_0/c = 0.75$, $St = 0.2$, $\theta_0 = 60^\circ$

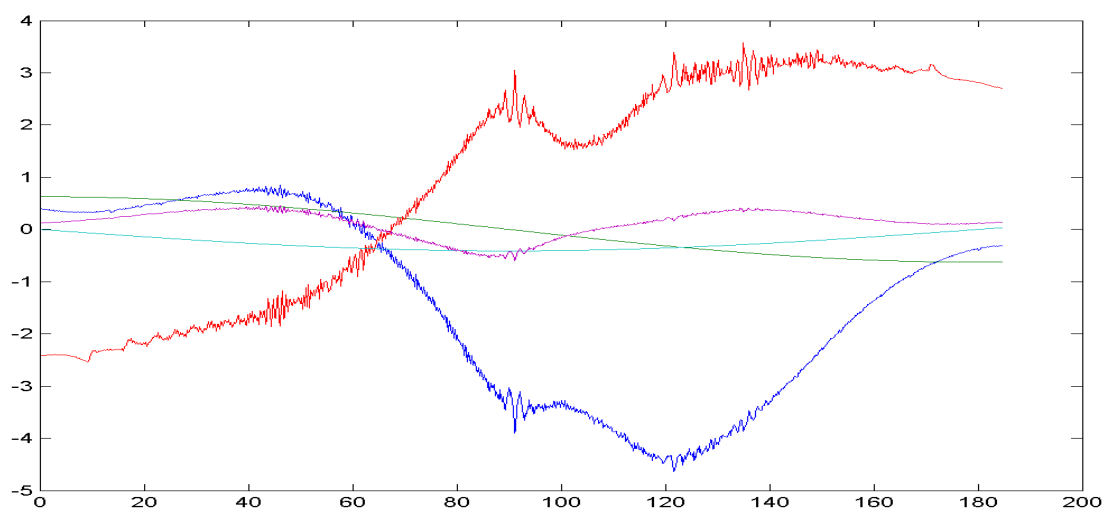
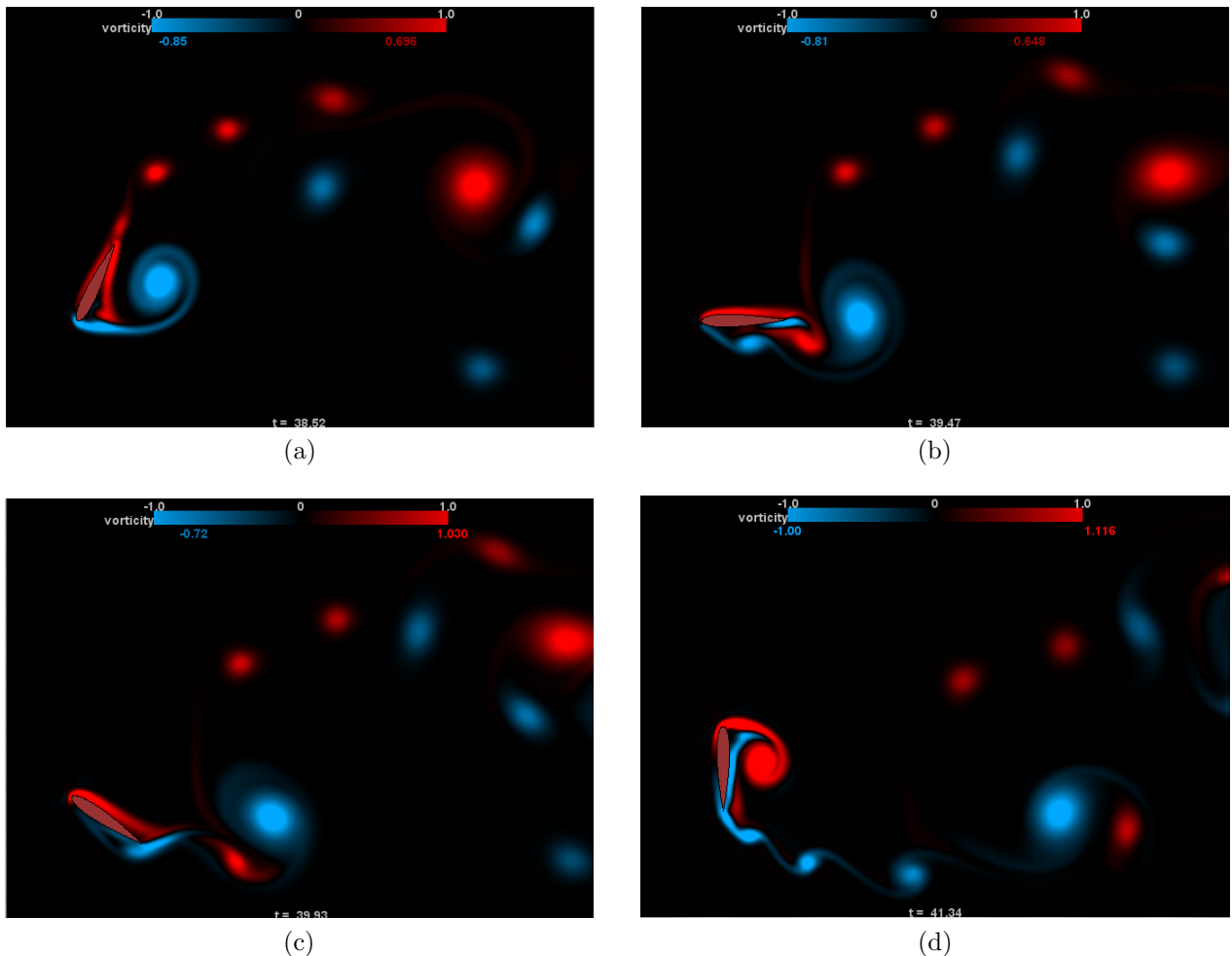


Figure C.46: $h_0/c = 0.75$, $St = 0.2$, $\theta_0 = 90^\circ$

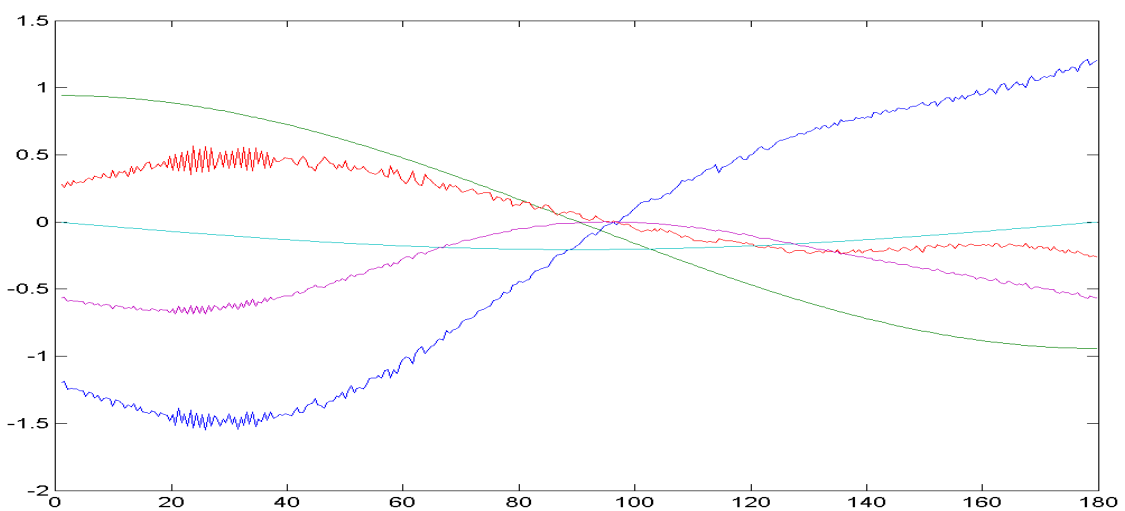
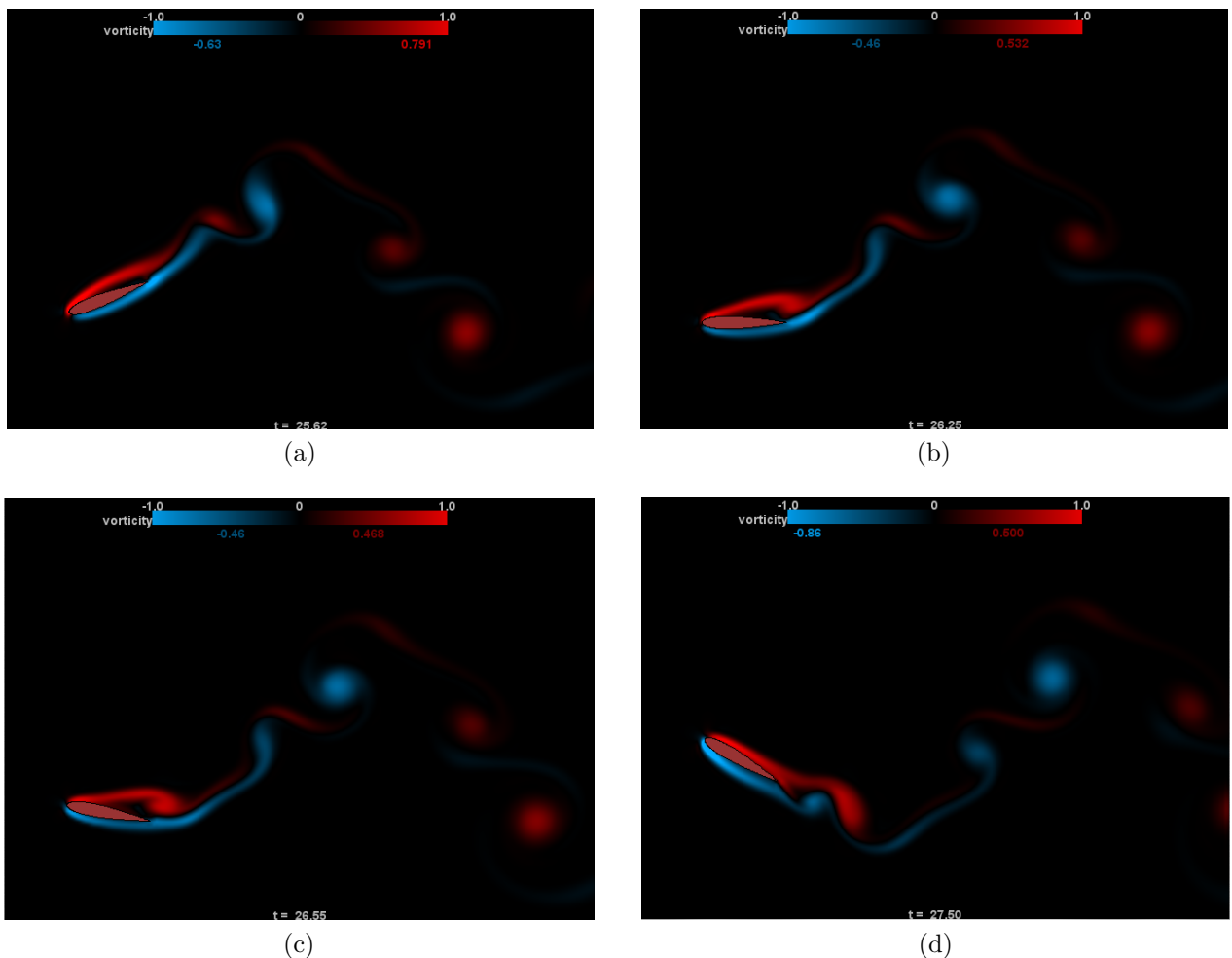


Figure C.47: $h_0/c = 0.75$, $St = 0.3$, $\theta_0 = 30^\circ$

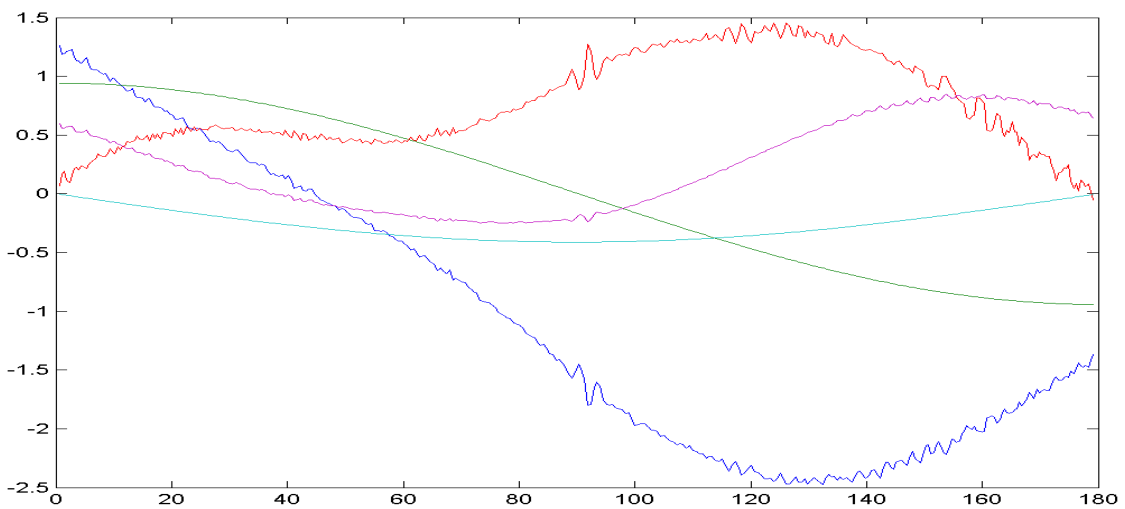
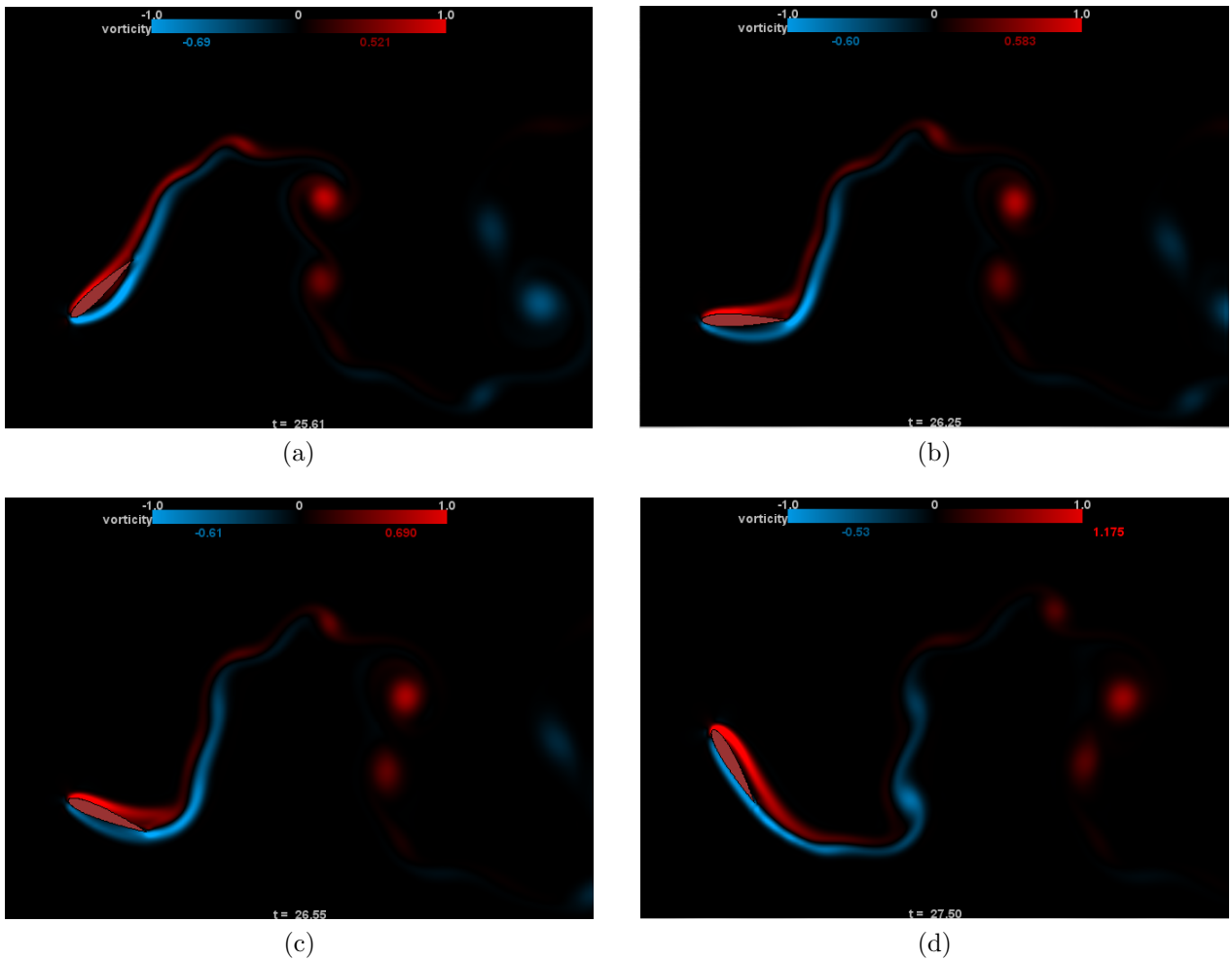


Figure C.48: $h_0/c = 0.75$, $St = 0.3$, $\theta_0 = 60^\circ$

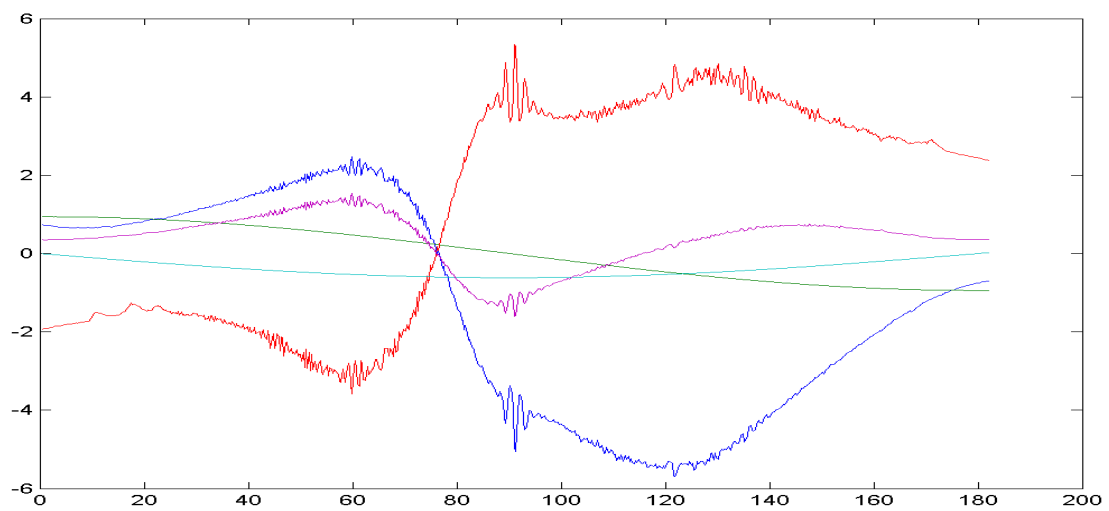
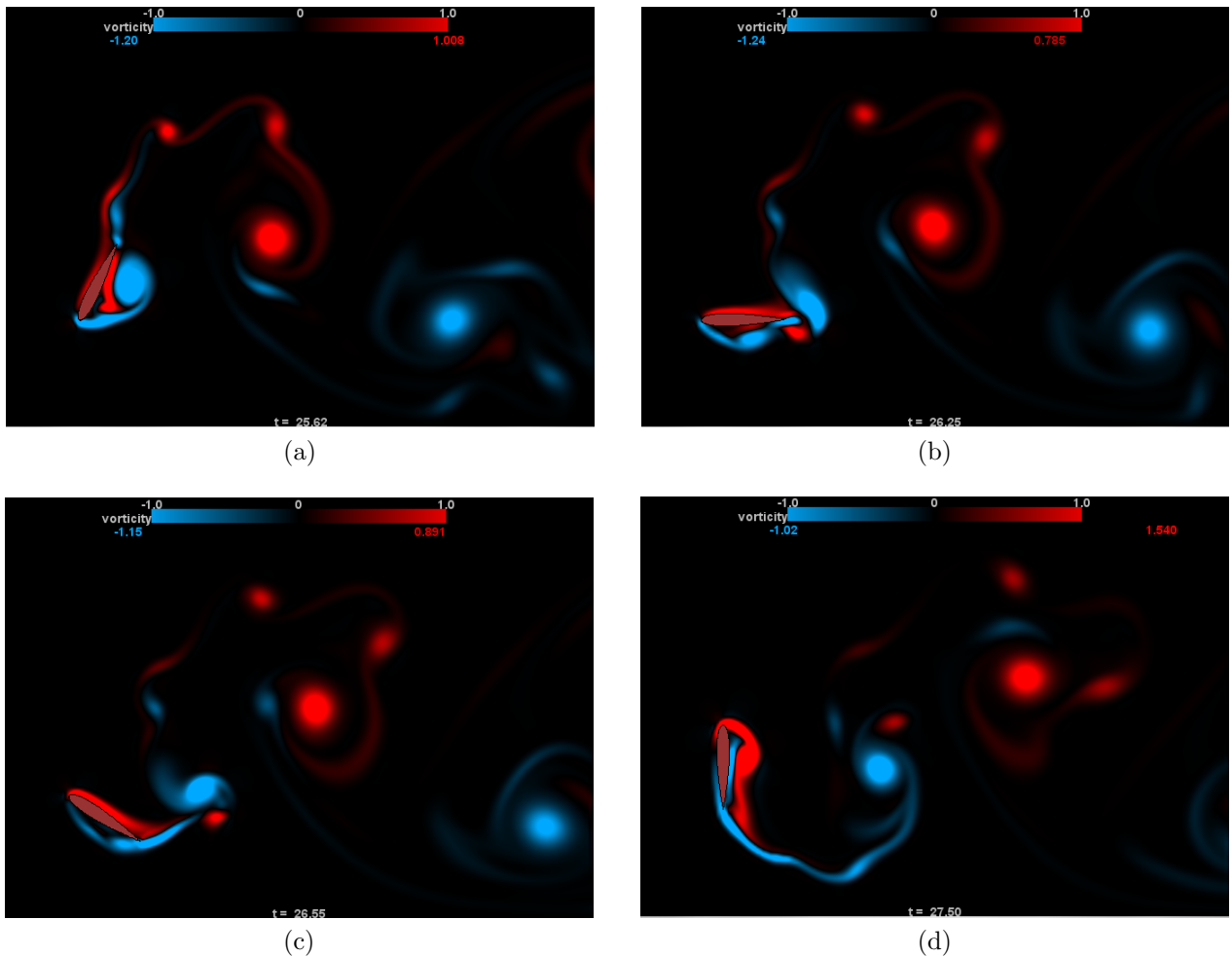


Figure C.49: $h_0/c = 0.75$, $St = 0.3$, $\theta_0 = 90^\circ$

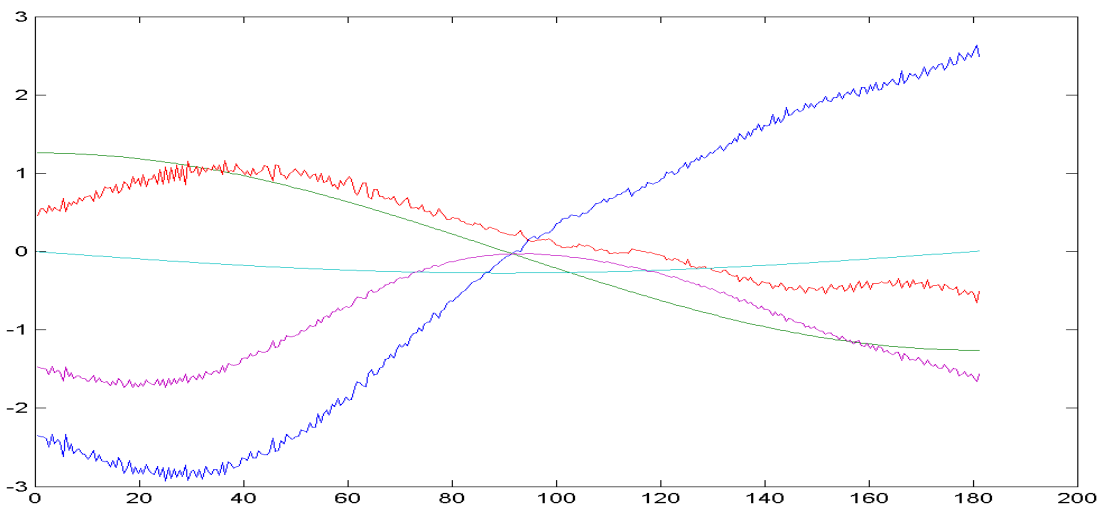
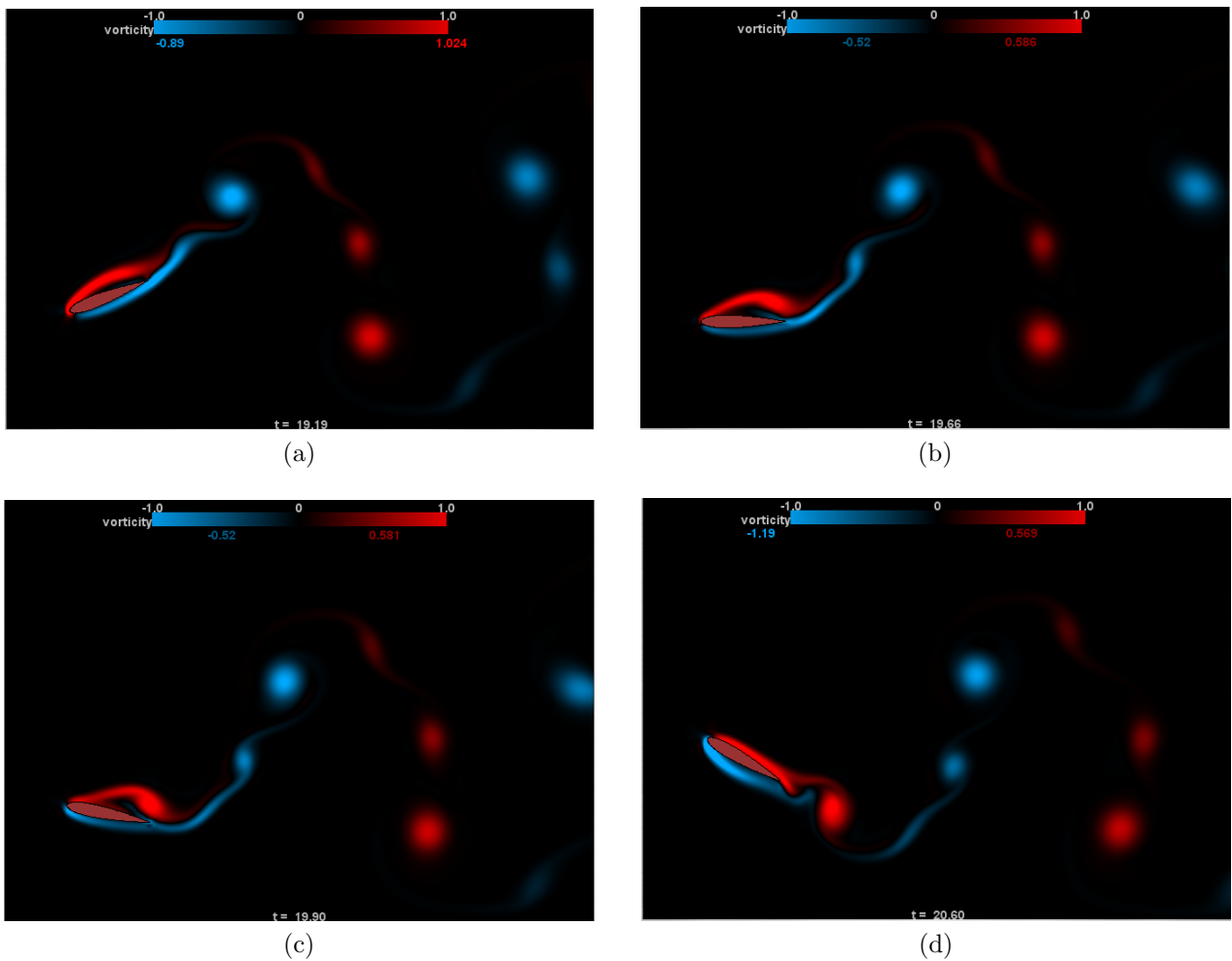


Figure C.50: $h_0/c = 0.75$, $St = 0.4$, $\theta_0 = 30^\circ$

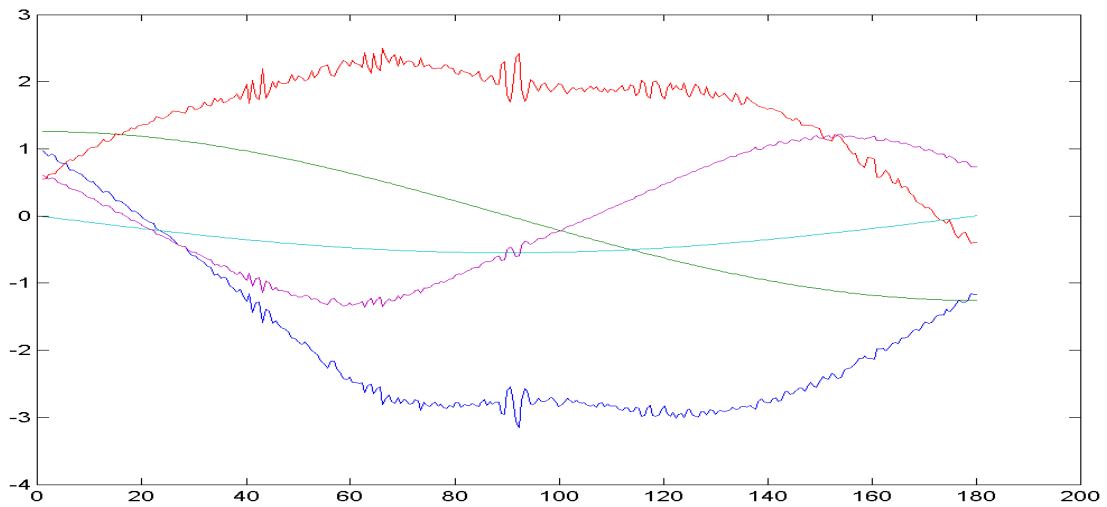
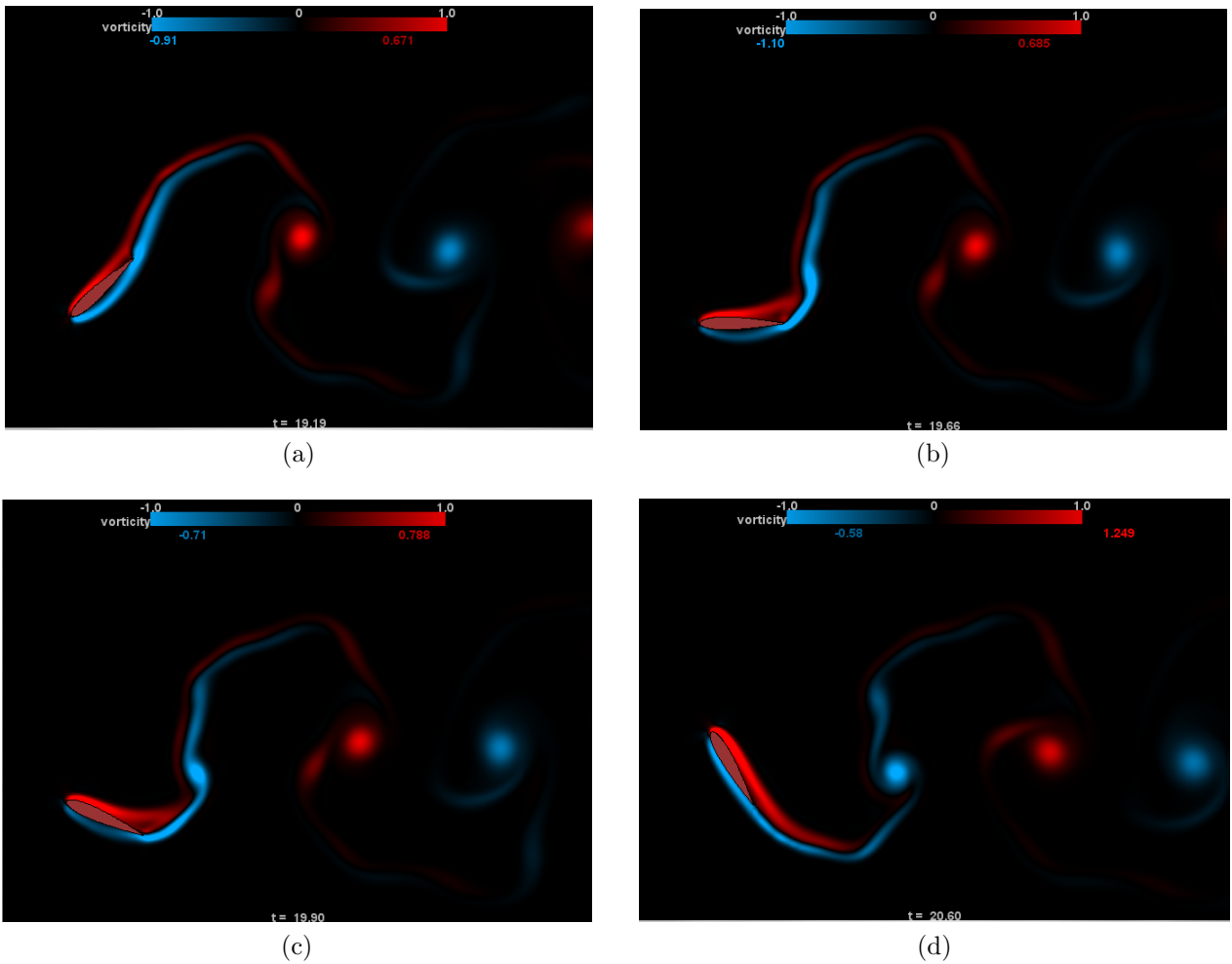


Figure C.51: $h_0/c = 0.75$, $St = 0.4$, $\theta_0 = 60^\circ$

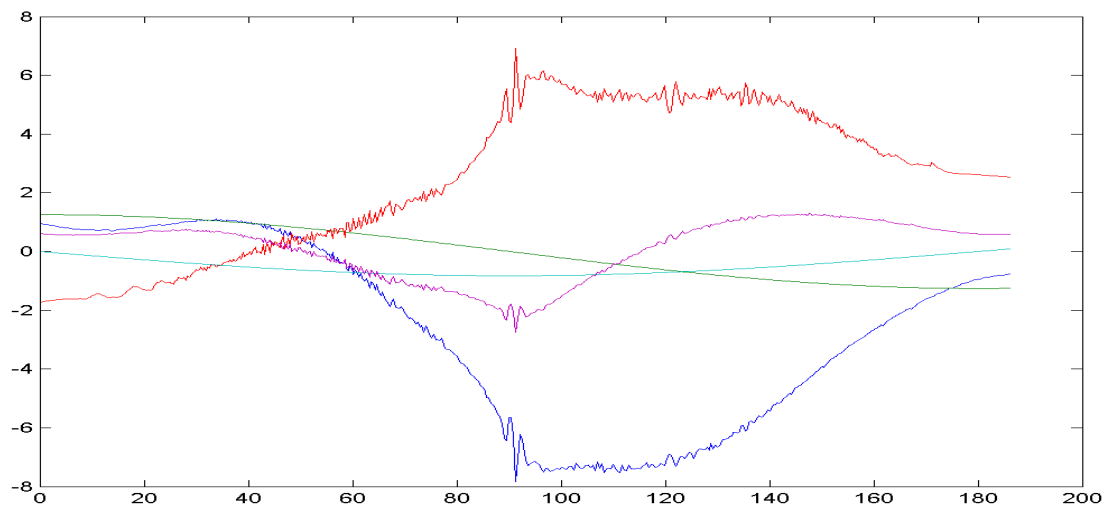
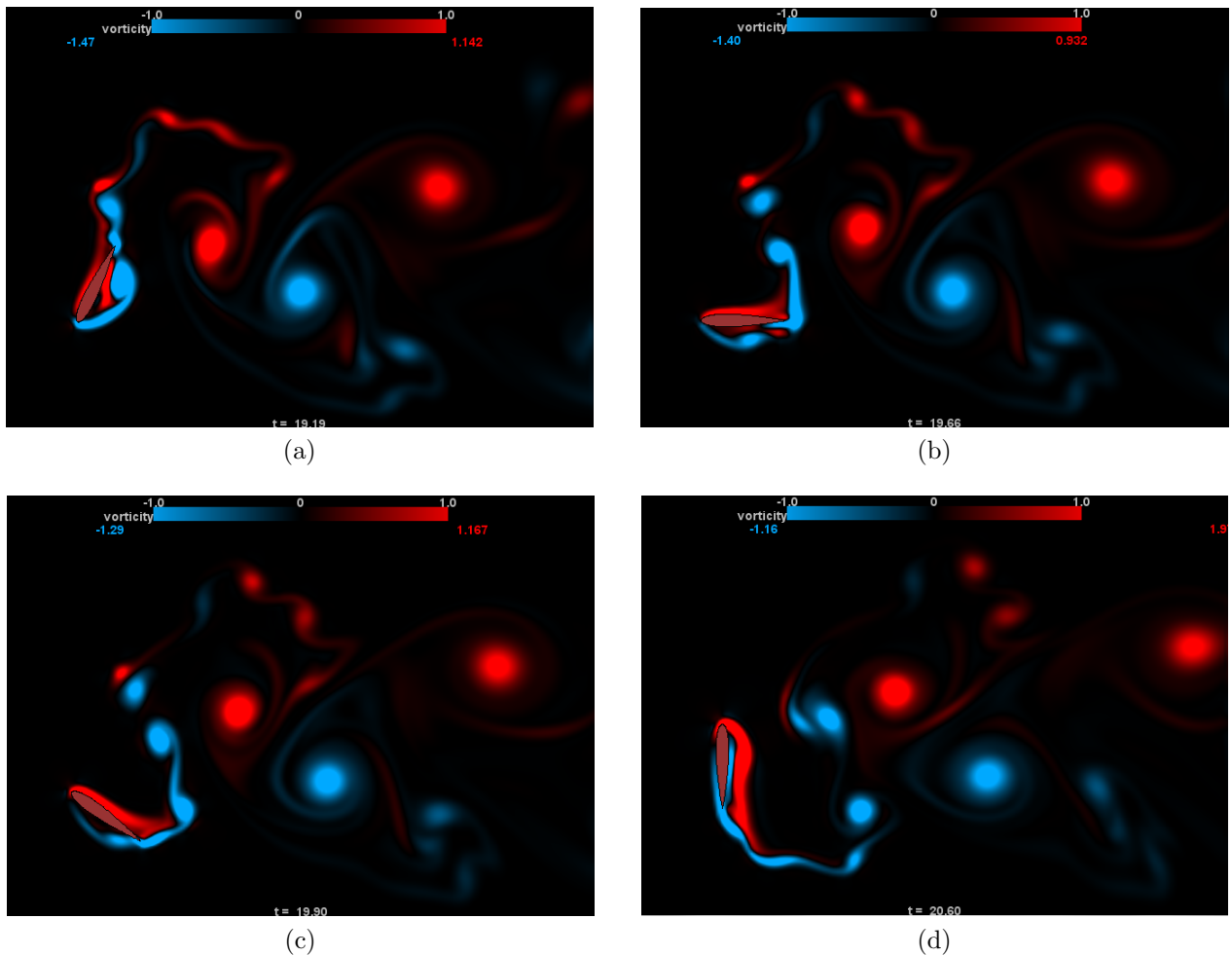


Figure C.52: $h_0/c = 0.75$, $St = 0.4$, $\theta_0 = 90^\circ$

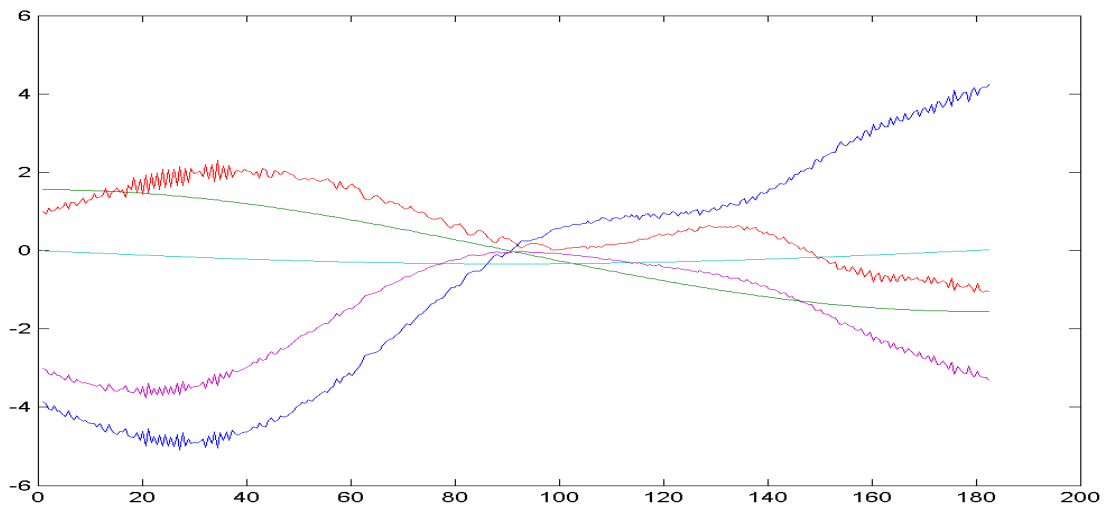
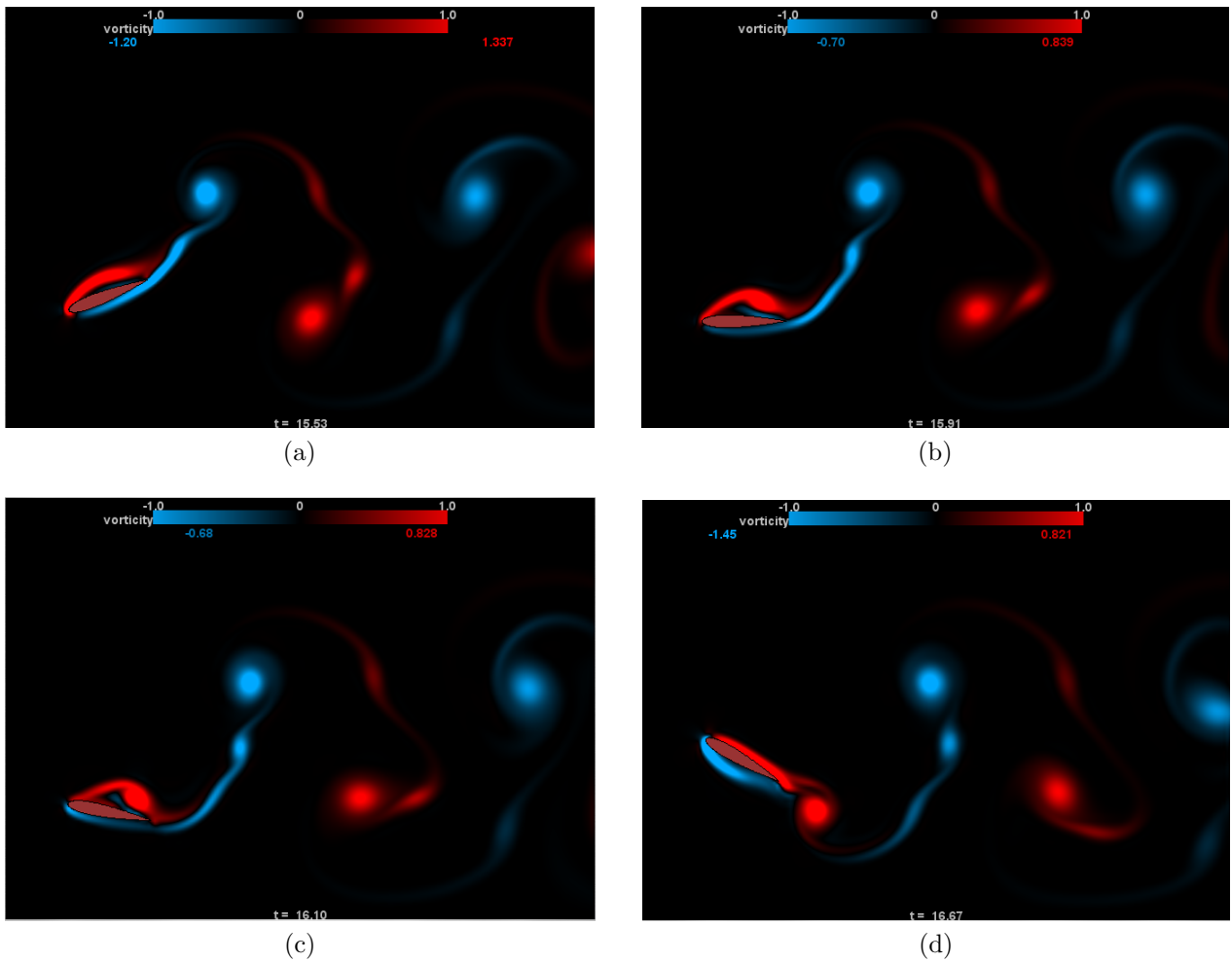


Figure C.53: $h_0/c = 0.75$, $St = 0.5$, $\theta_0 = 30^\circ$

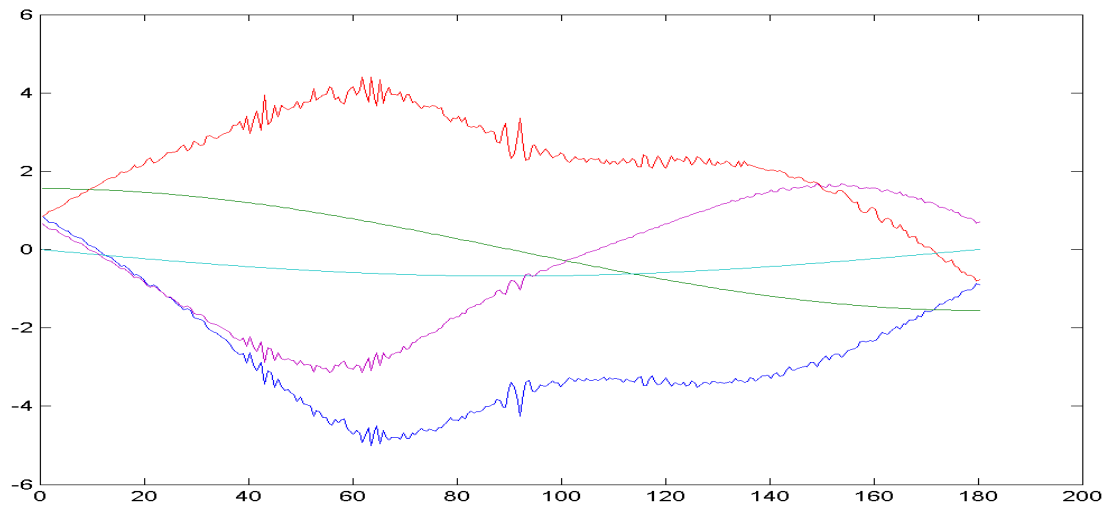
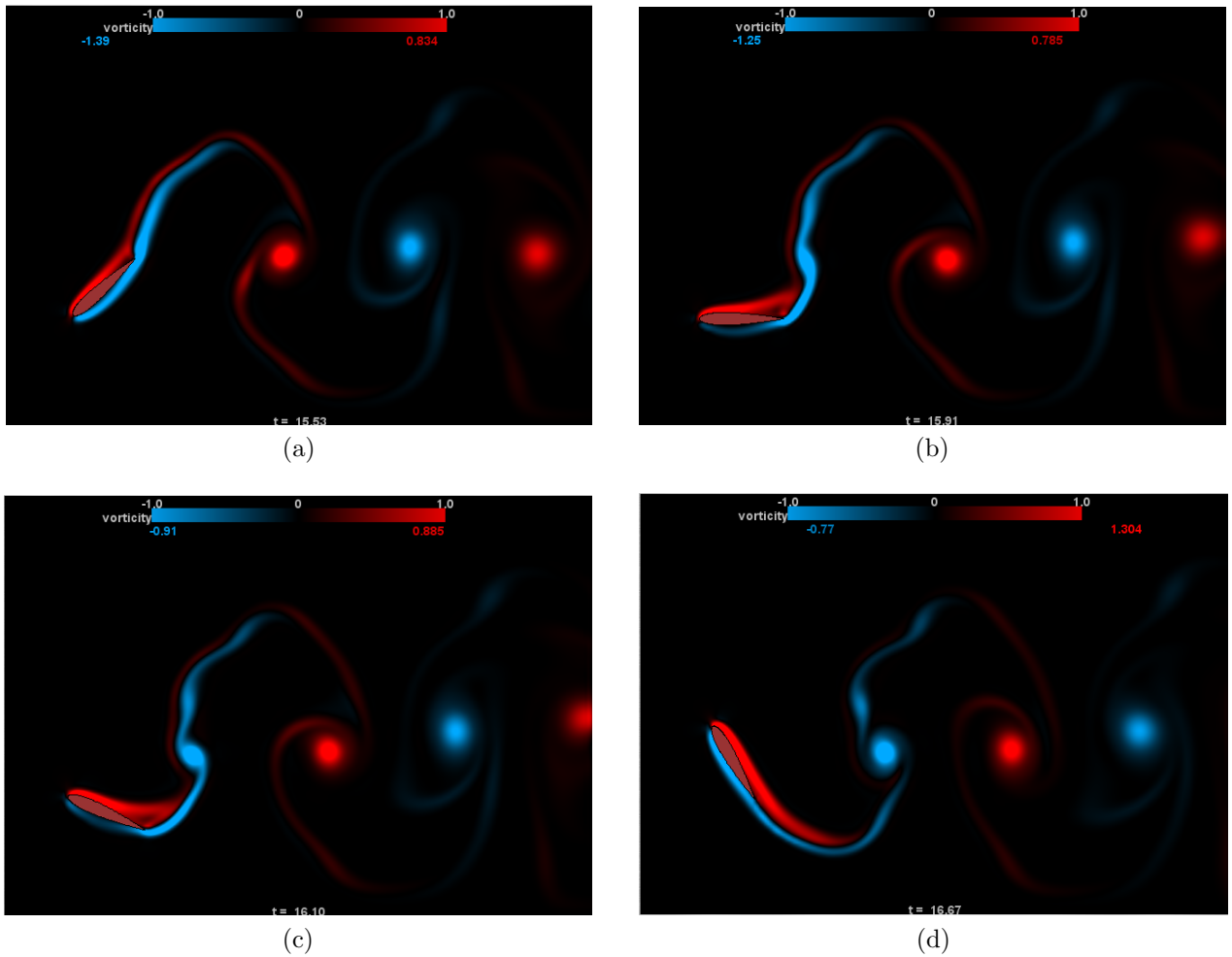


Figure C.54: $h_0/c = 0.75$, $St = 0.5$, $\theta_0 = 60^\circ$

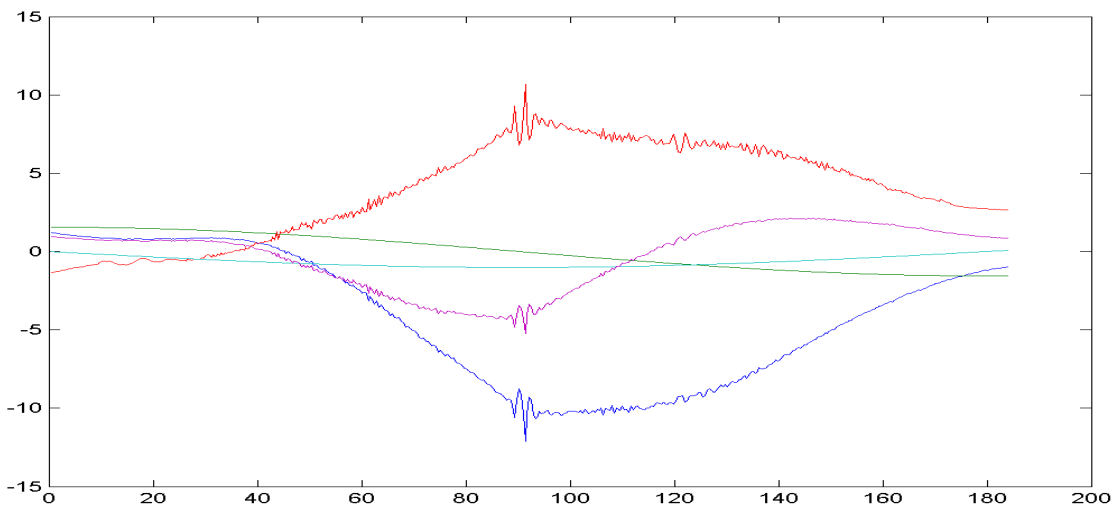
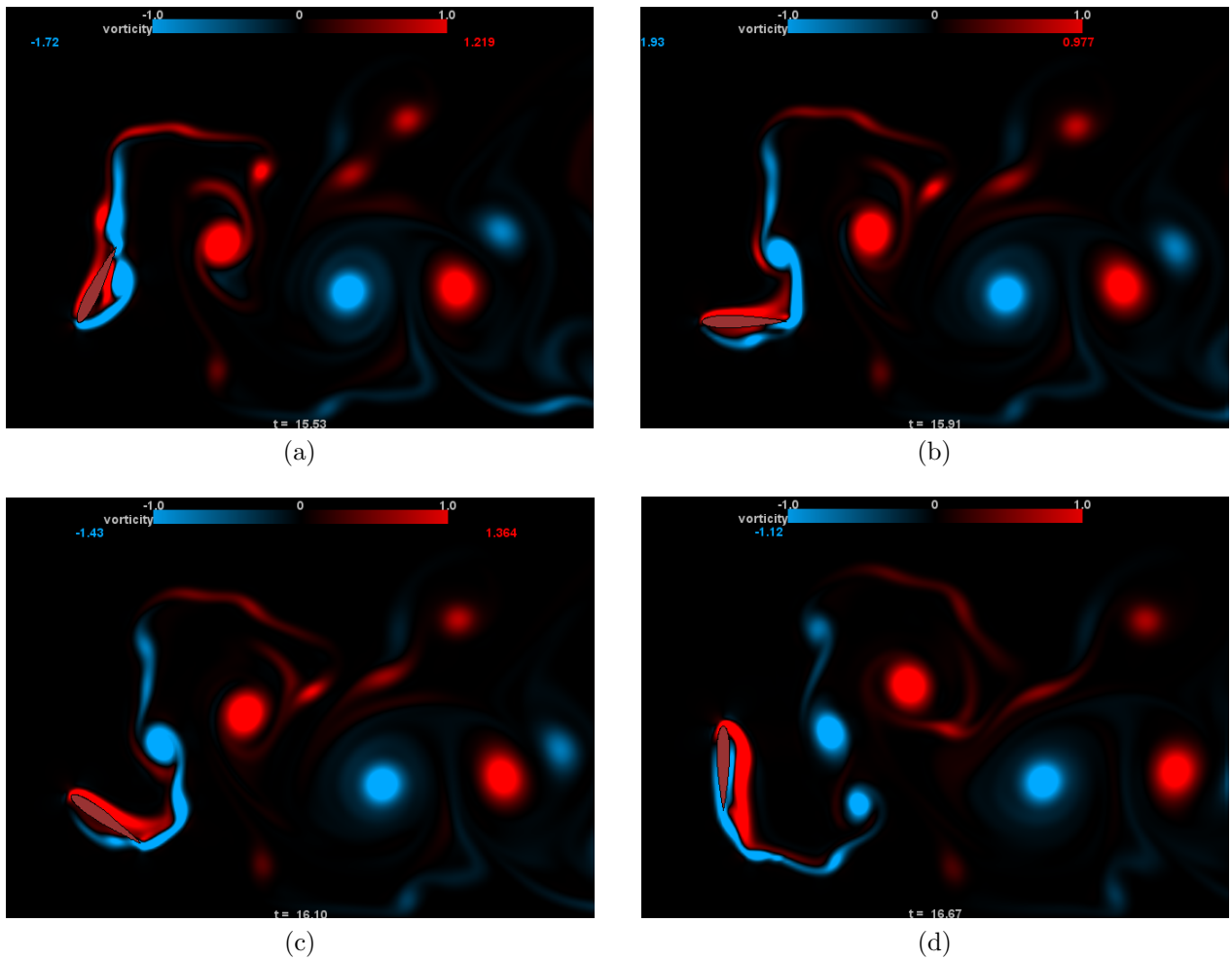


Figure C.55: $h_0/c = 0.75$, $St = 0.5$, $\theta_0 = 90^\circ$

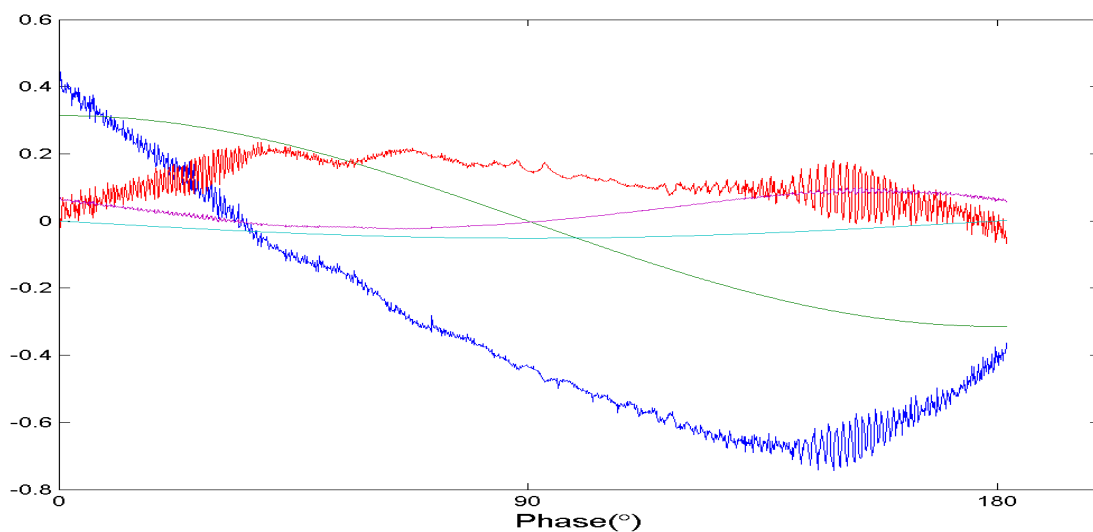
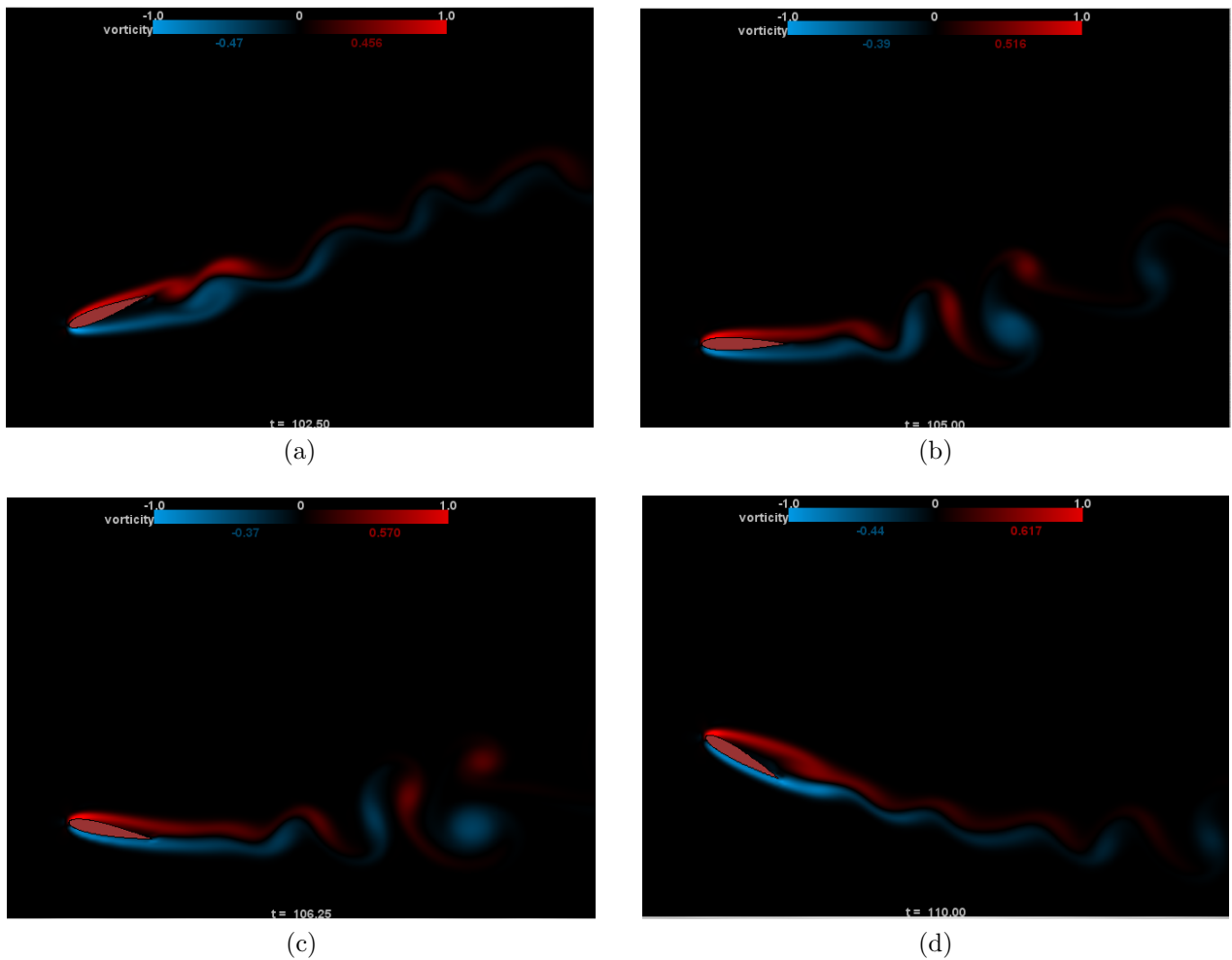


Figure C.56: $h_0/c = 1.0$, $St = 0.1$, $\theta_0 = 30^\circ$

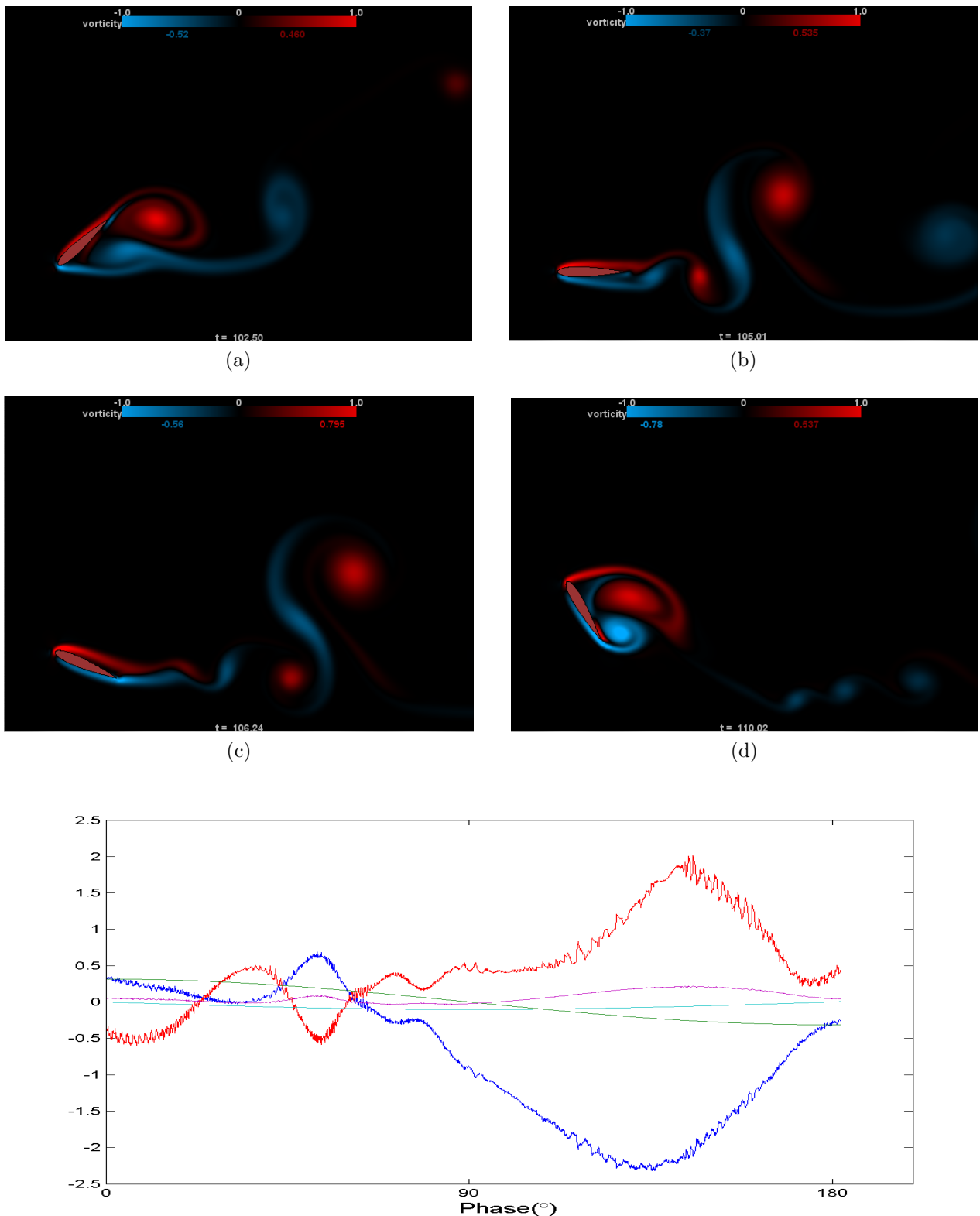


Figure C.57: $h_0/c = 1.0$, $St = 0.1$, $\theta_0 = 60^\circ$

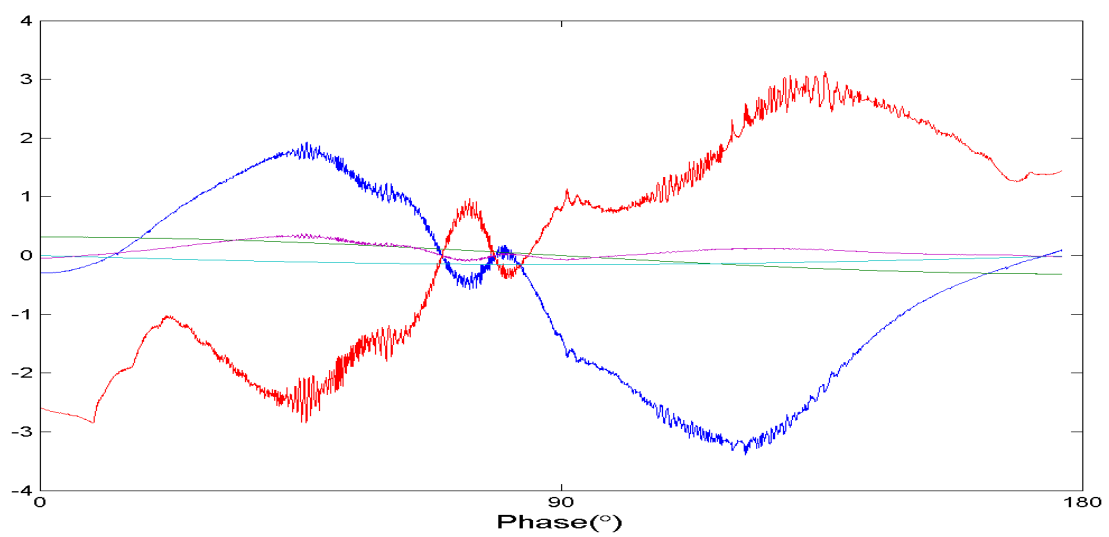
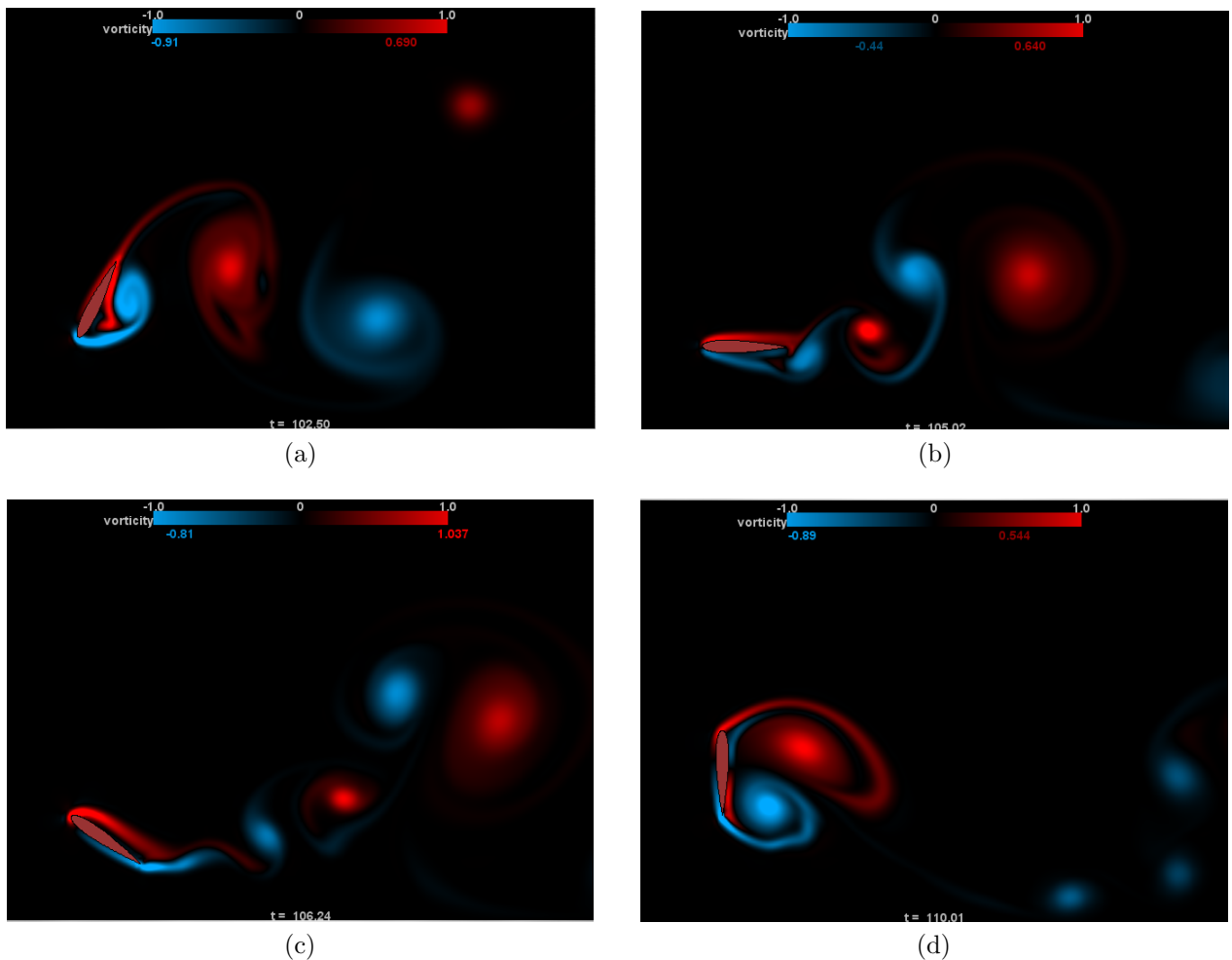


Figure C.58: $h_0/c = 1.0$, $St = 0.1$, $\theta_0 = 90^\circ$

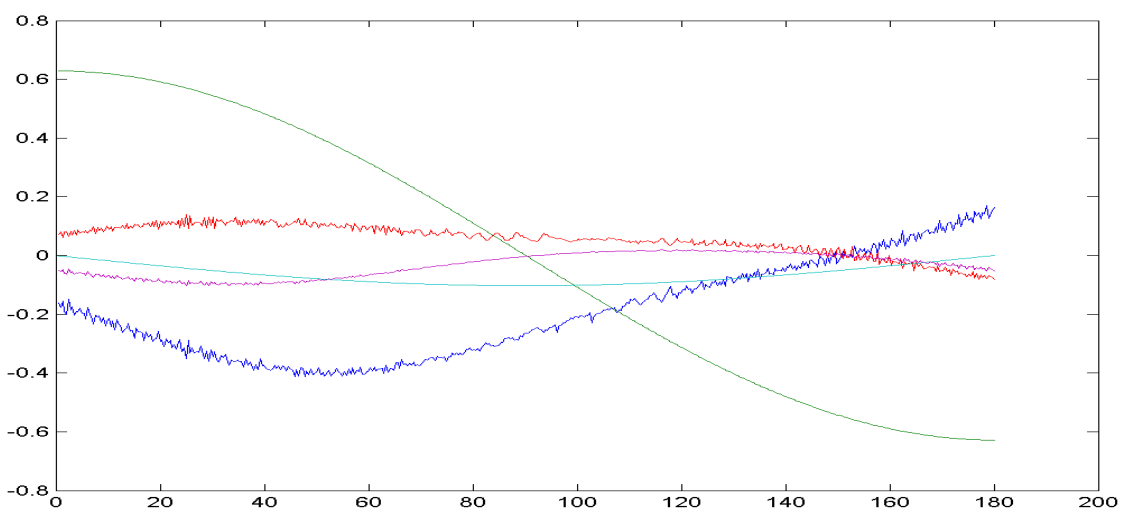
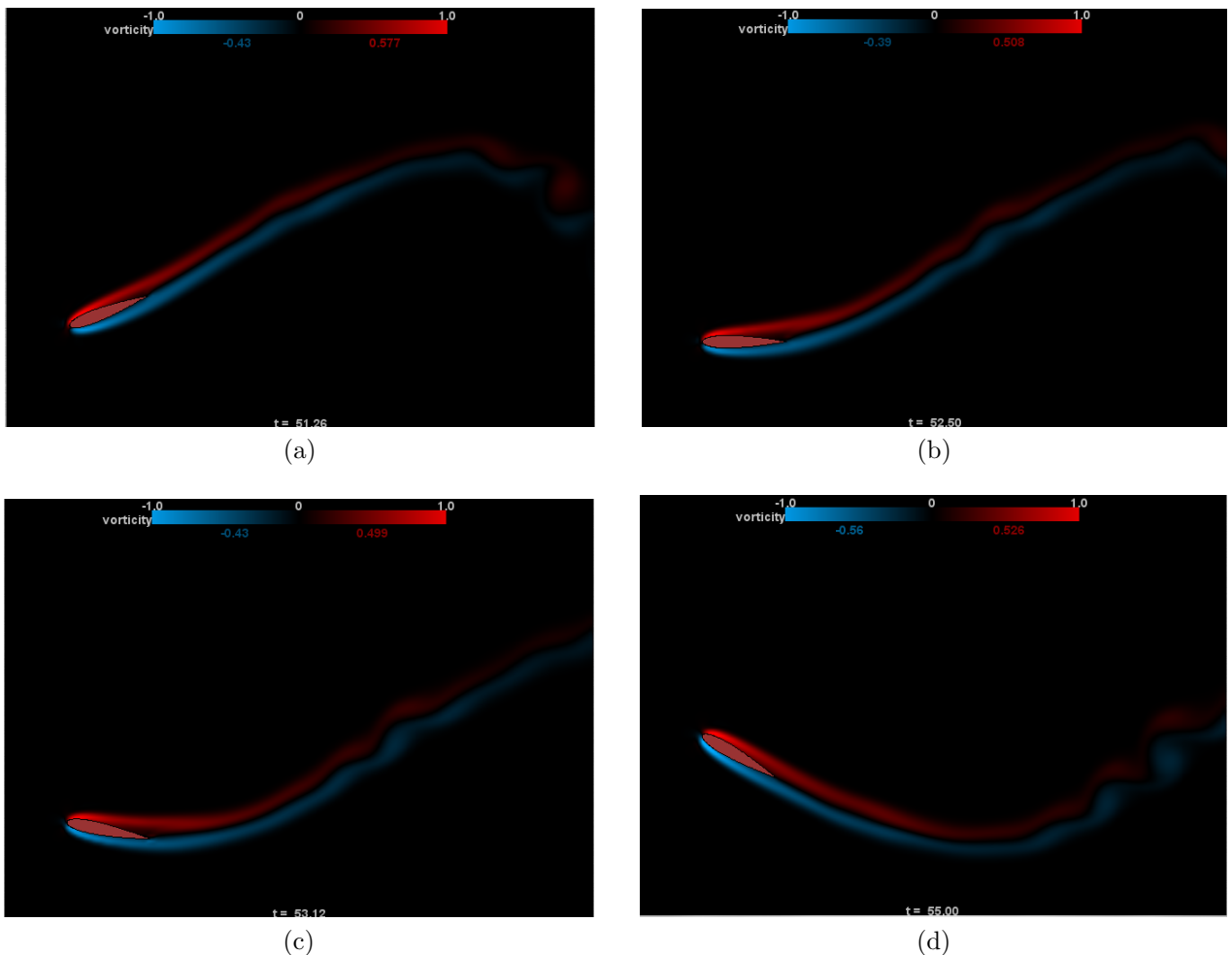


Figure C.59: $h_0/c = 1.0$, $St = 0.2$, $\theta_0 = 30^\circ$

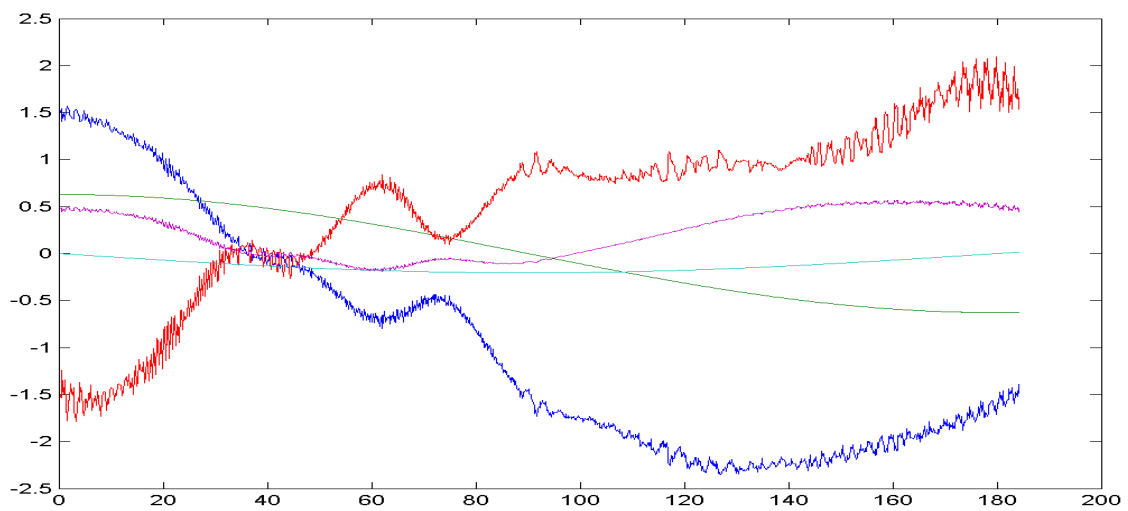
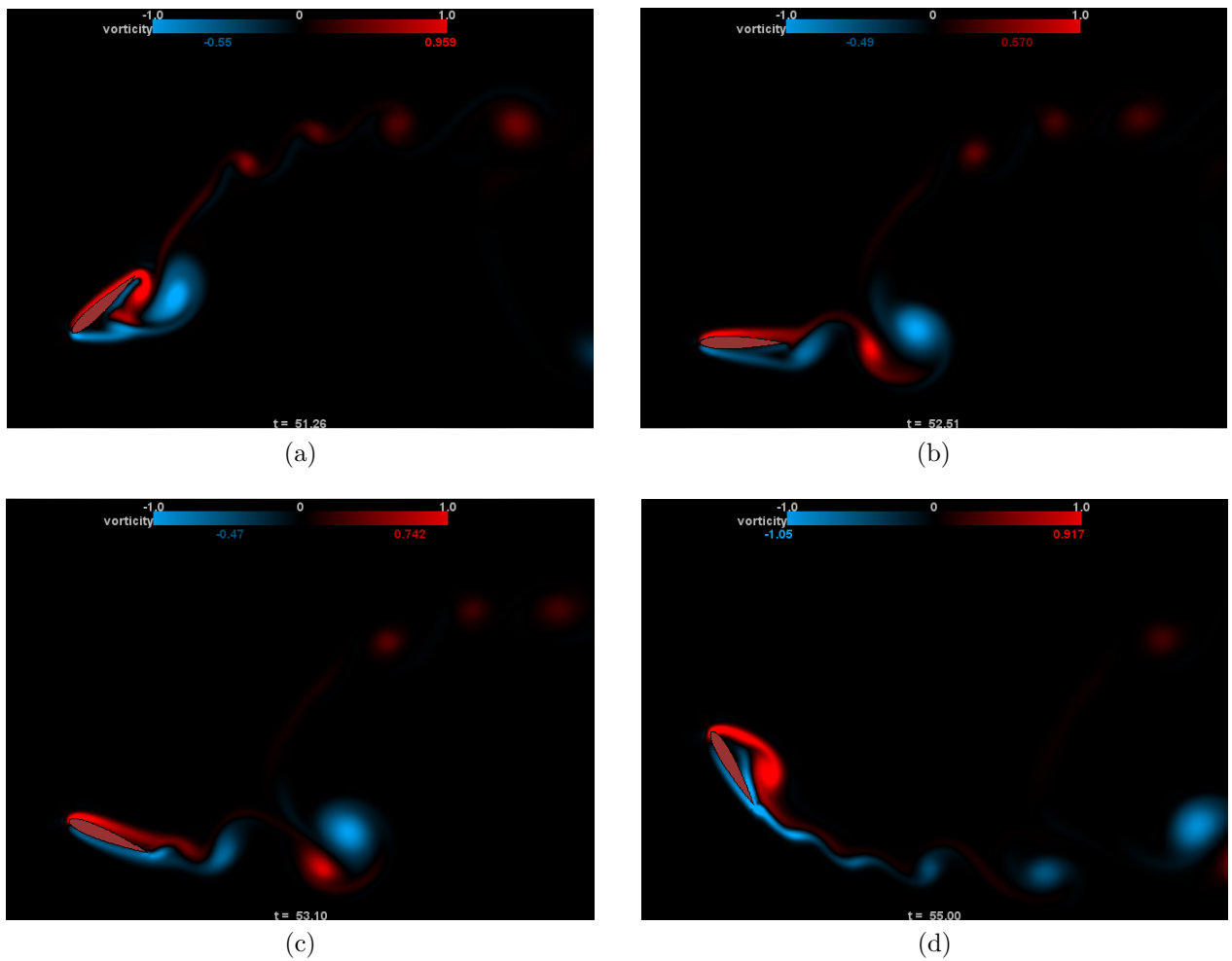


Figure C.60: $h_0/c = 1.0$, $St = 0.2$, $\theta_0 = 60^\circ$

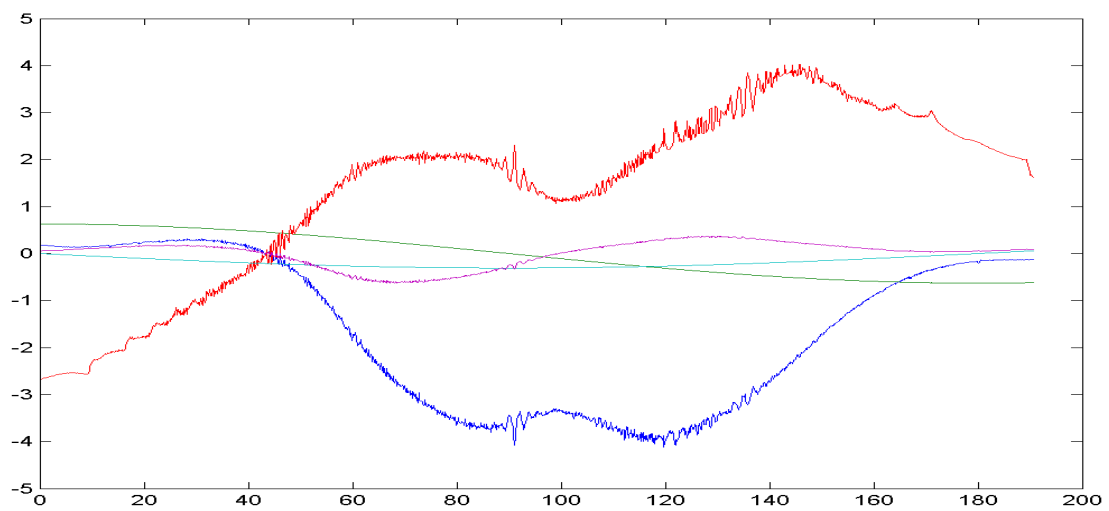
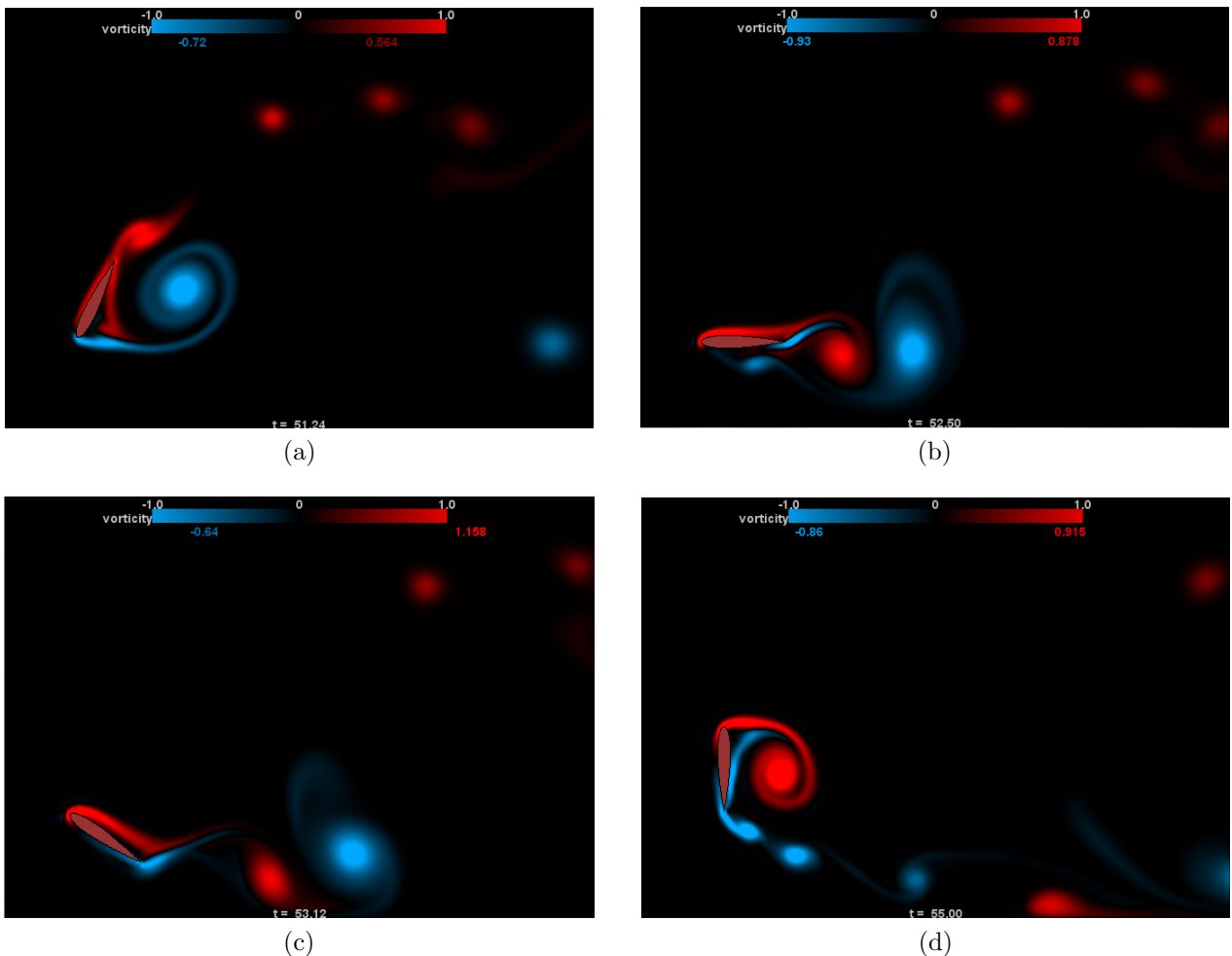


Figure C.61: $h_0/c = 1.0$, $St = 0.2$, $\theta_0 = 90^\circ$

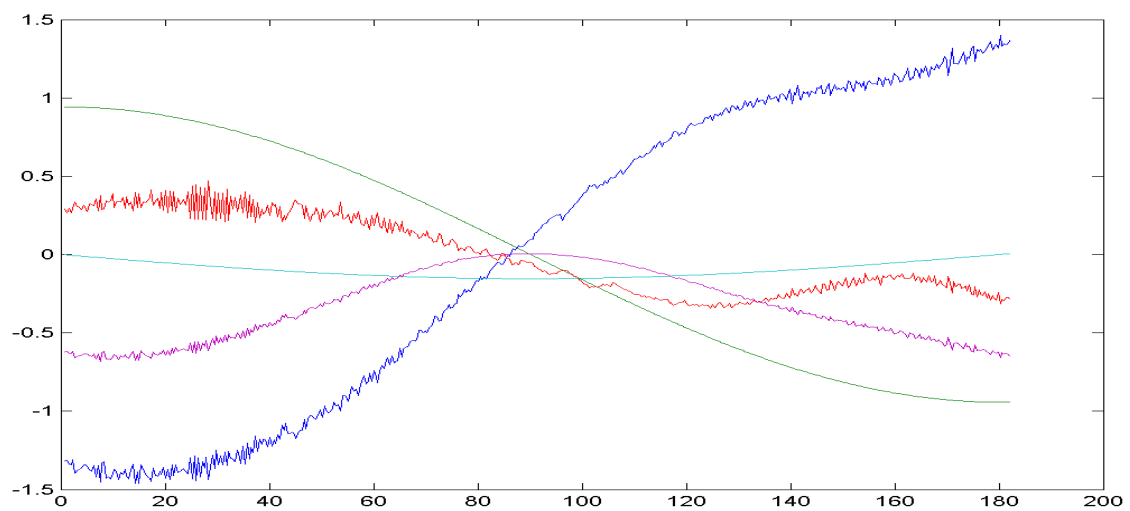
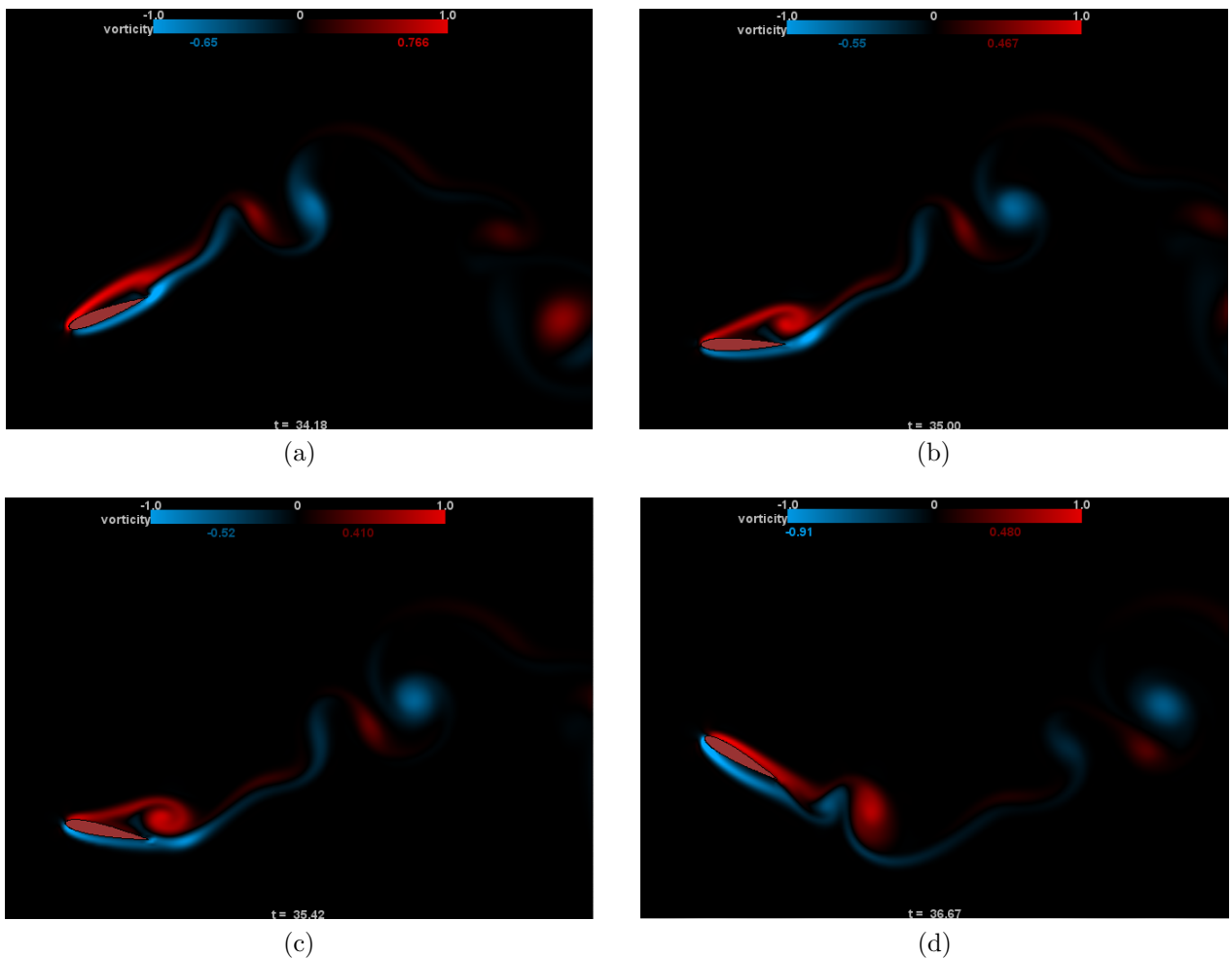


Figure C.62: $h_0/c = 1.0$, $St = 0.3$, $\theta_0 = 30^\circ$

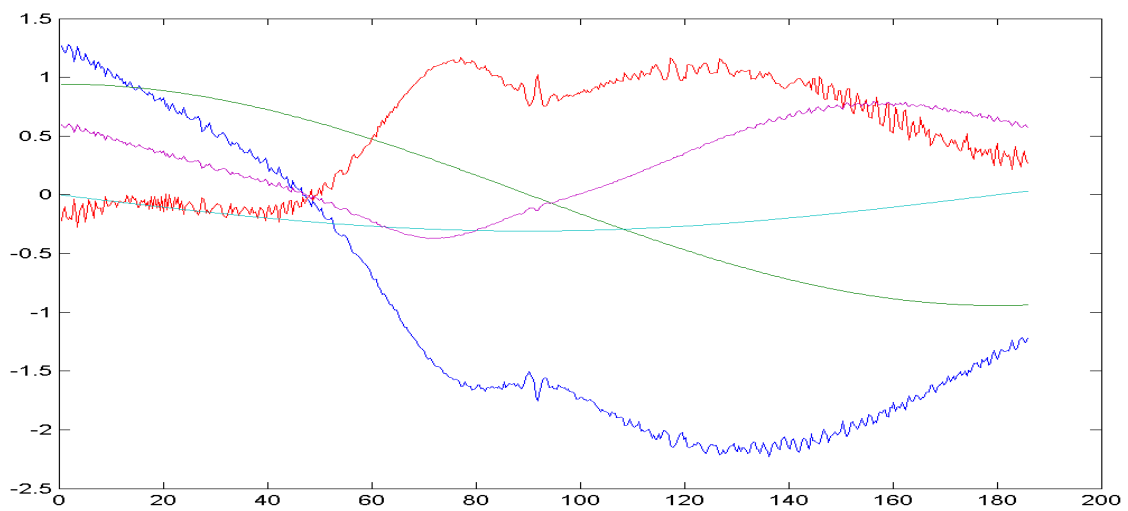
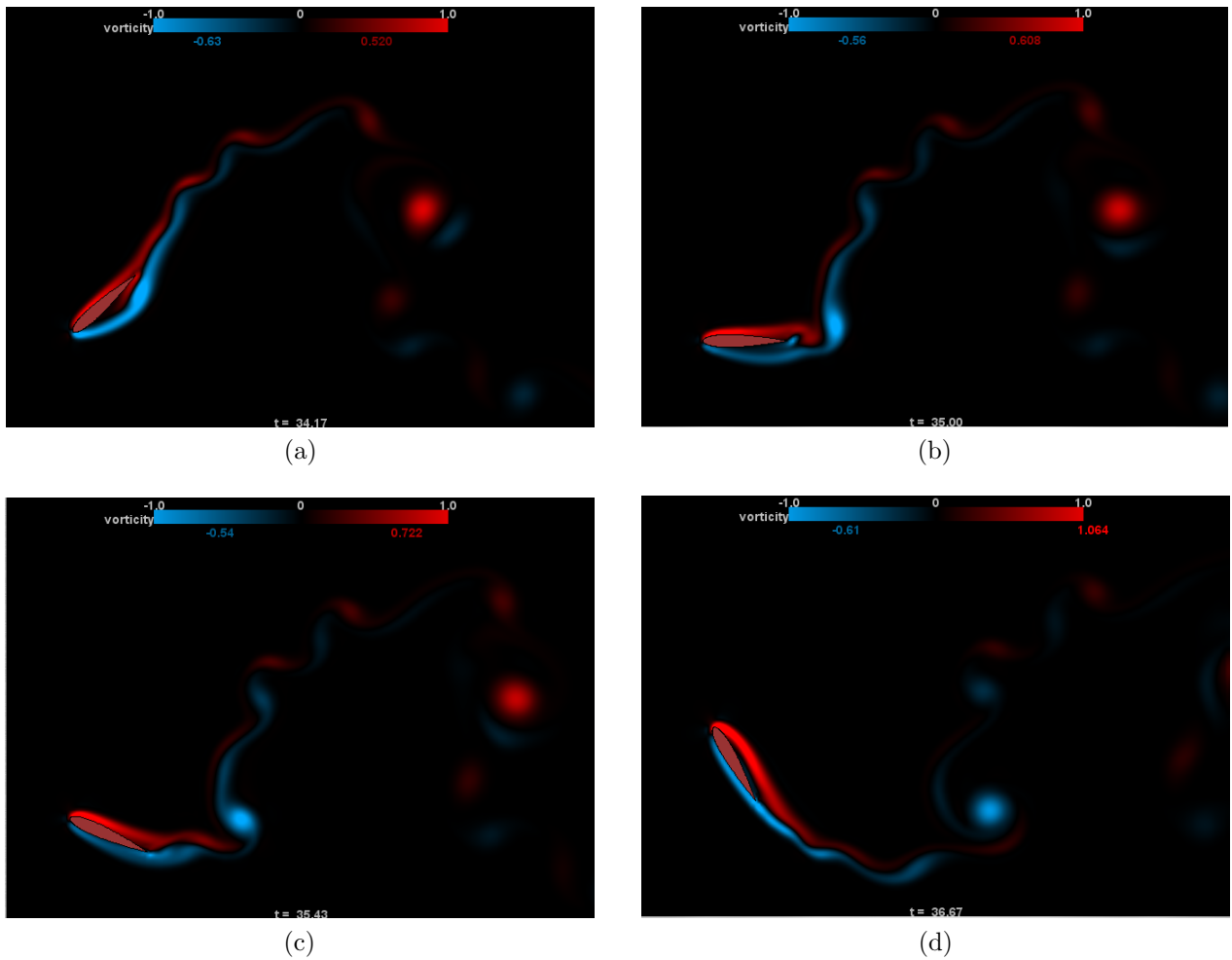


Figure C.63: $h_0/c = 1.0$, $St = 0.3$, $\theta_0 = 60^\circ$

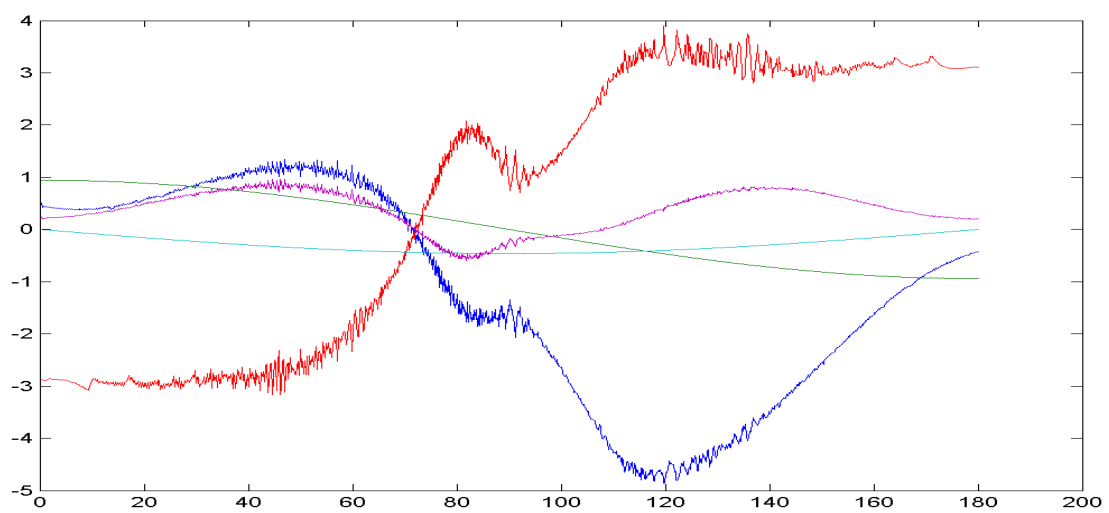
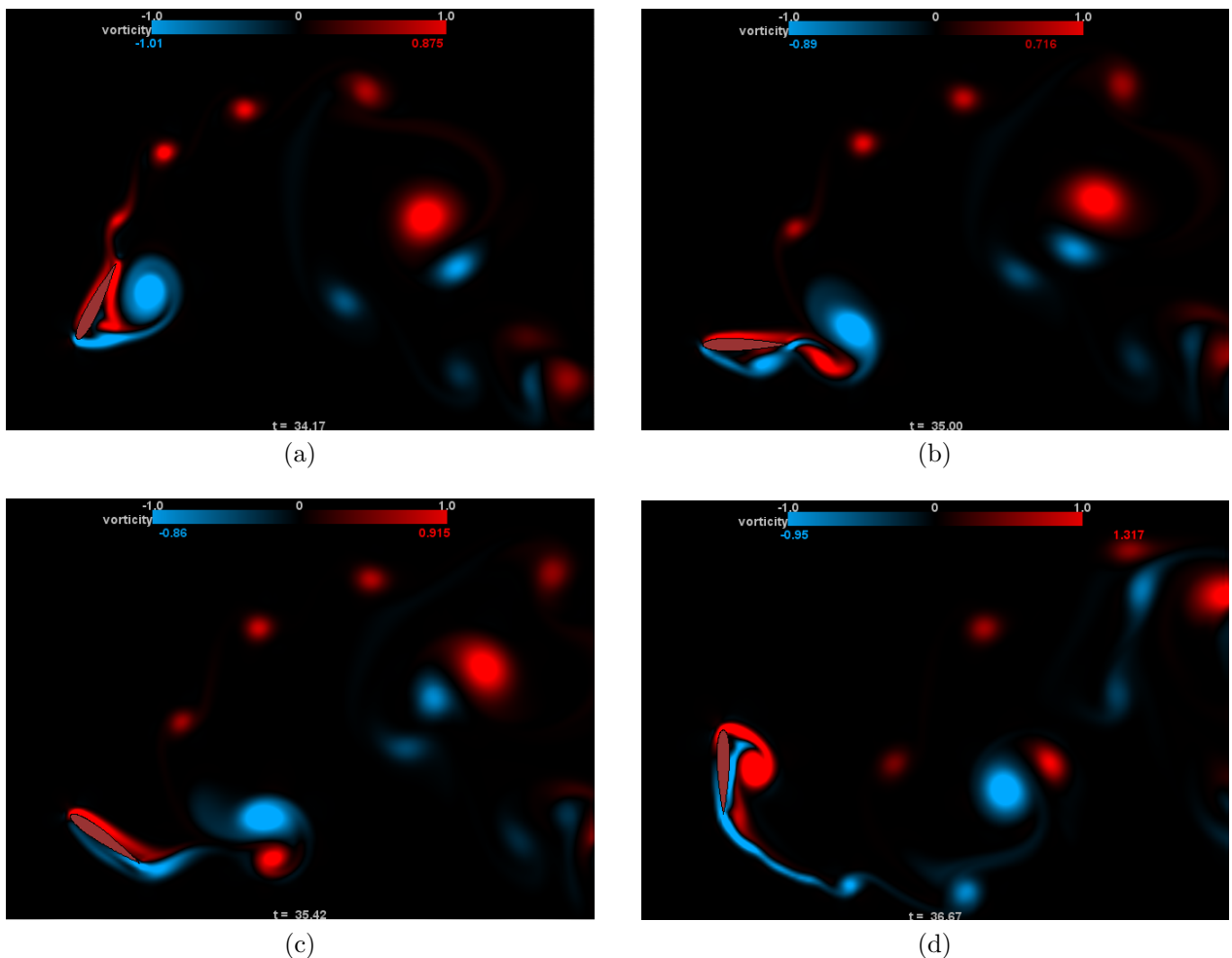


Figure C.64: $h_0/c = 1.0$, $St = 0.3$, $\theta_0 = 90^\circ$

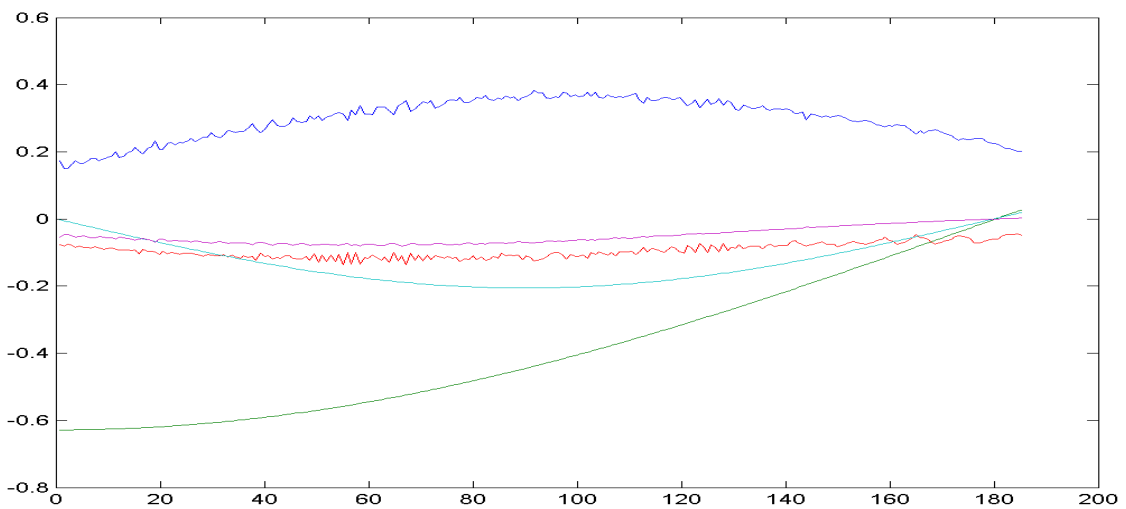
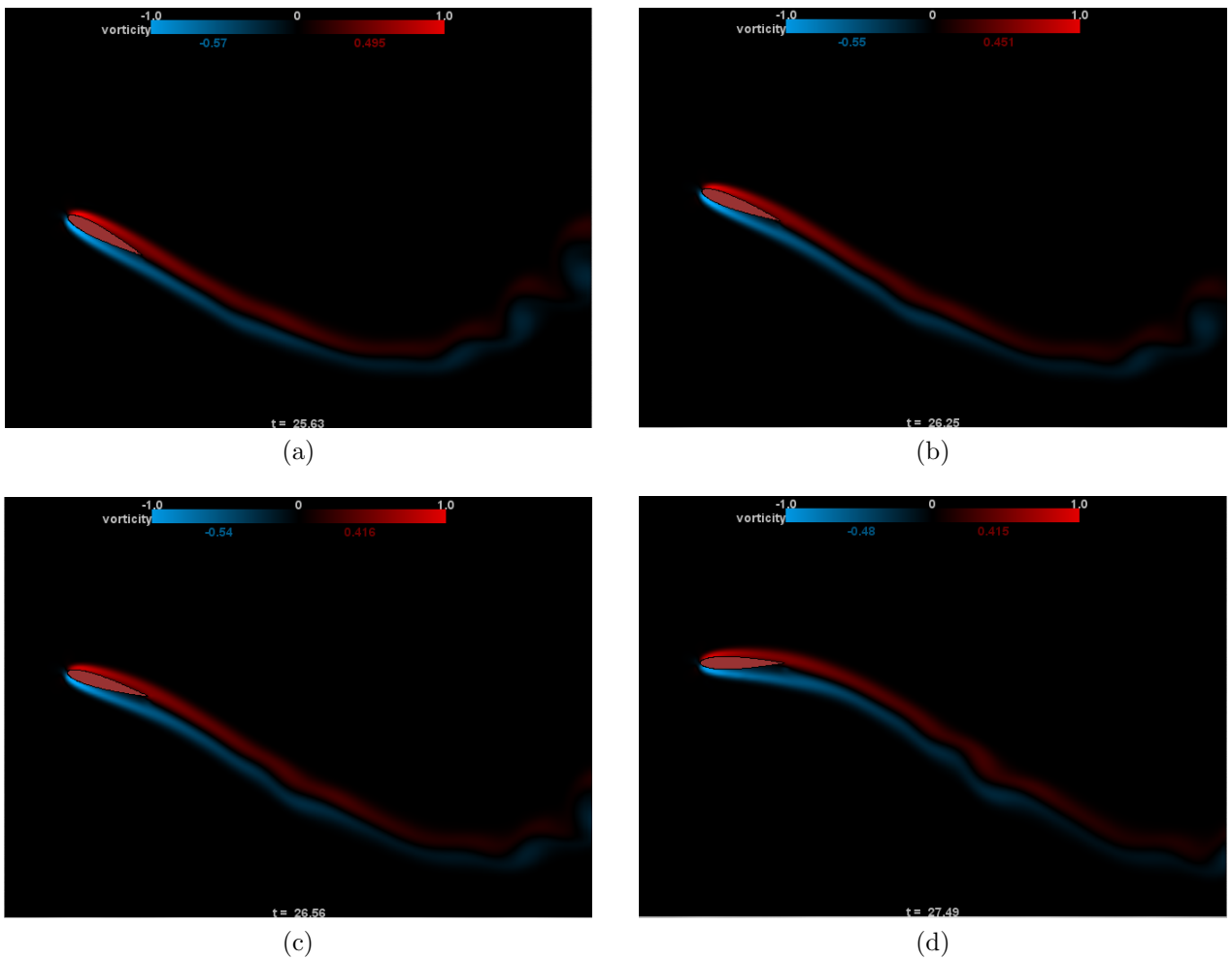


Figure C.65: $h_0/c = 1.0$, $St = 0.4$, $\theta_0 = 30^\circ$

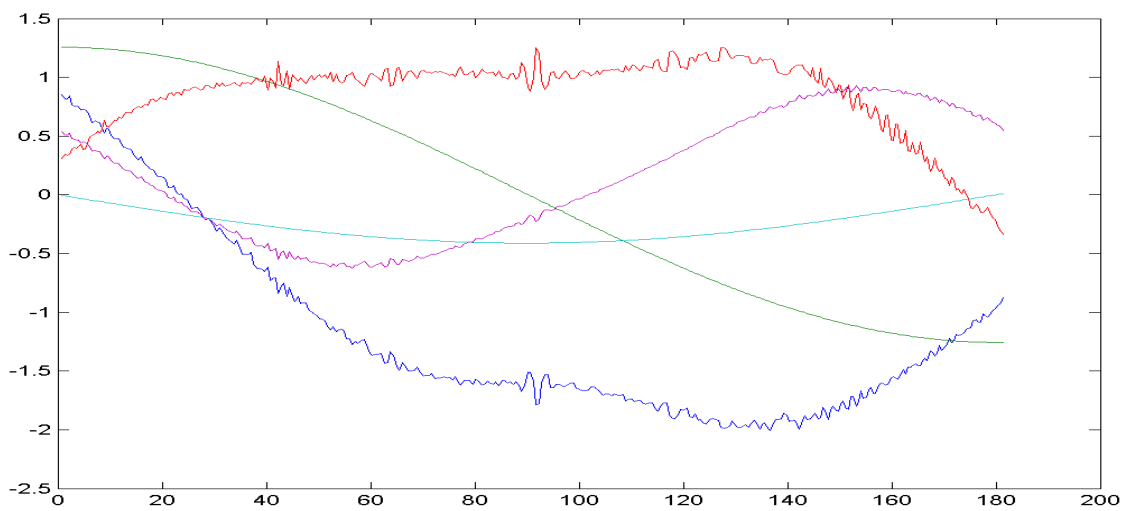
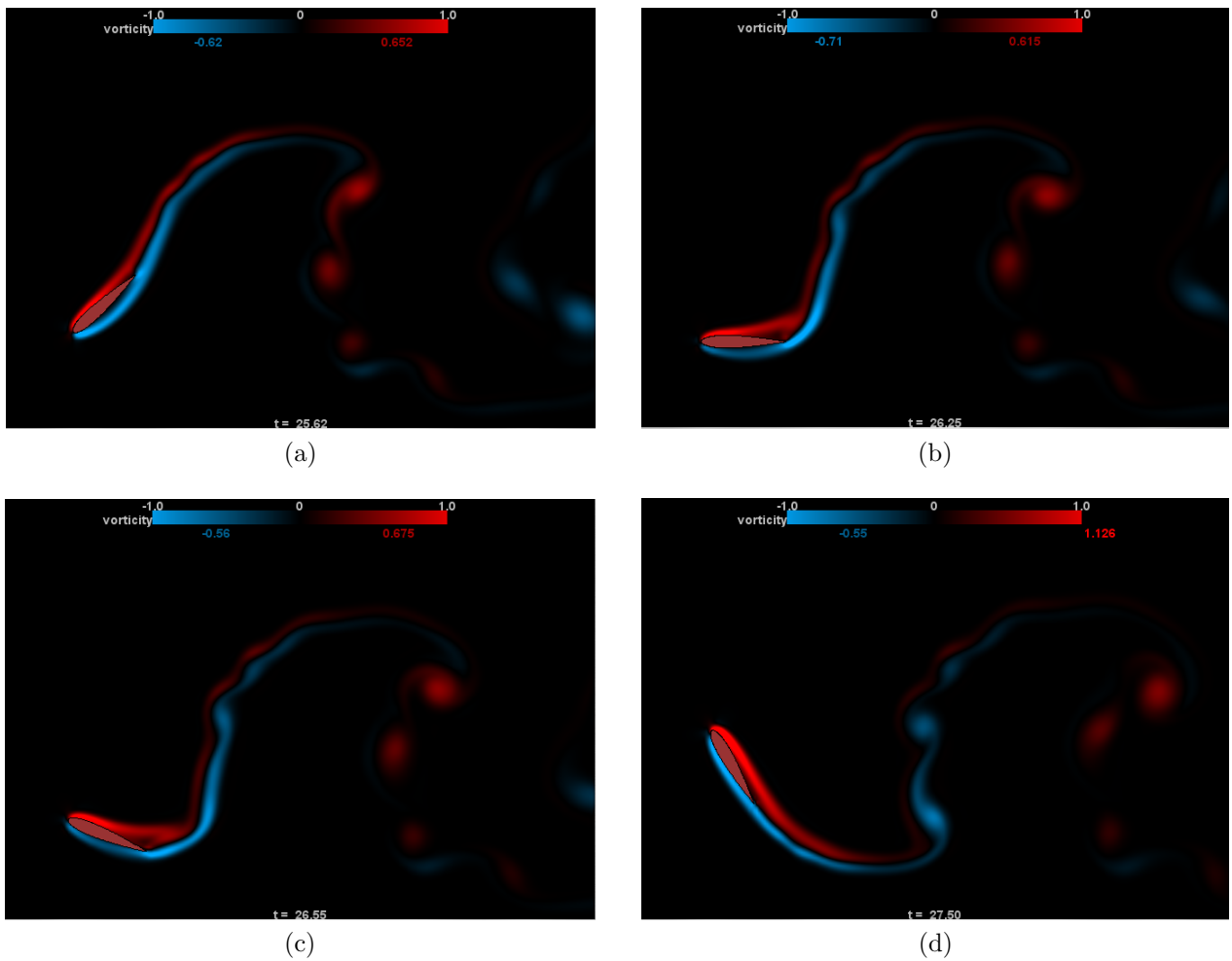


Figure C.66: $h_0/c = 1.0$, $St = 0.4$, $\theta_0 = 60^\circ$

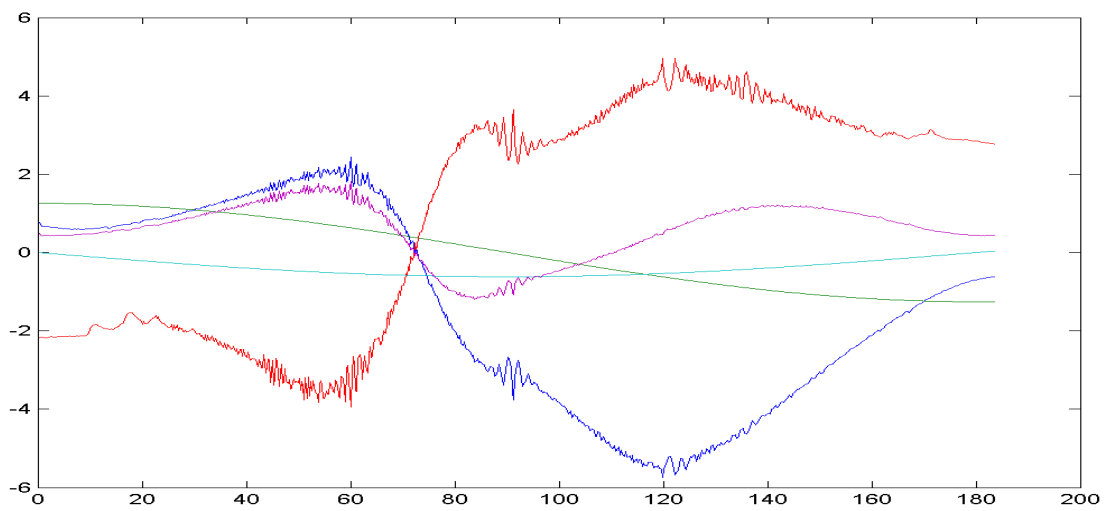
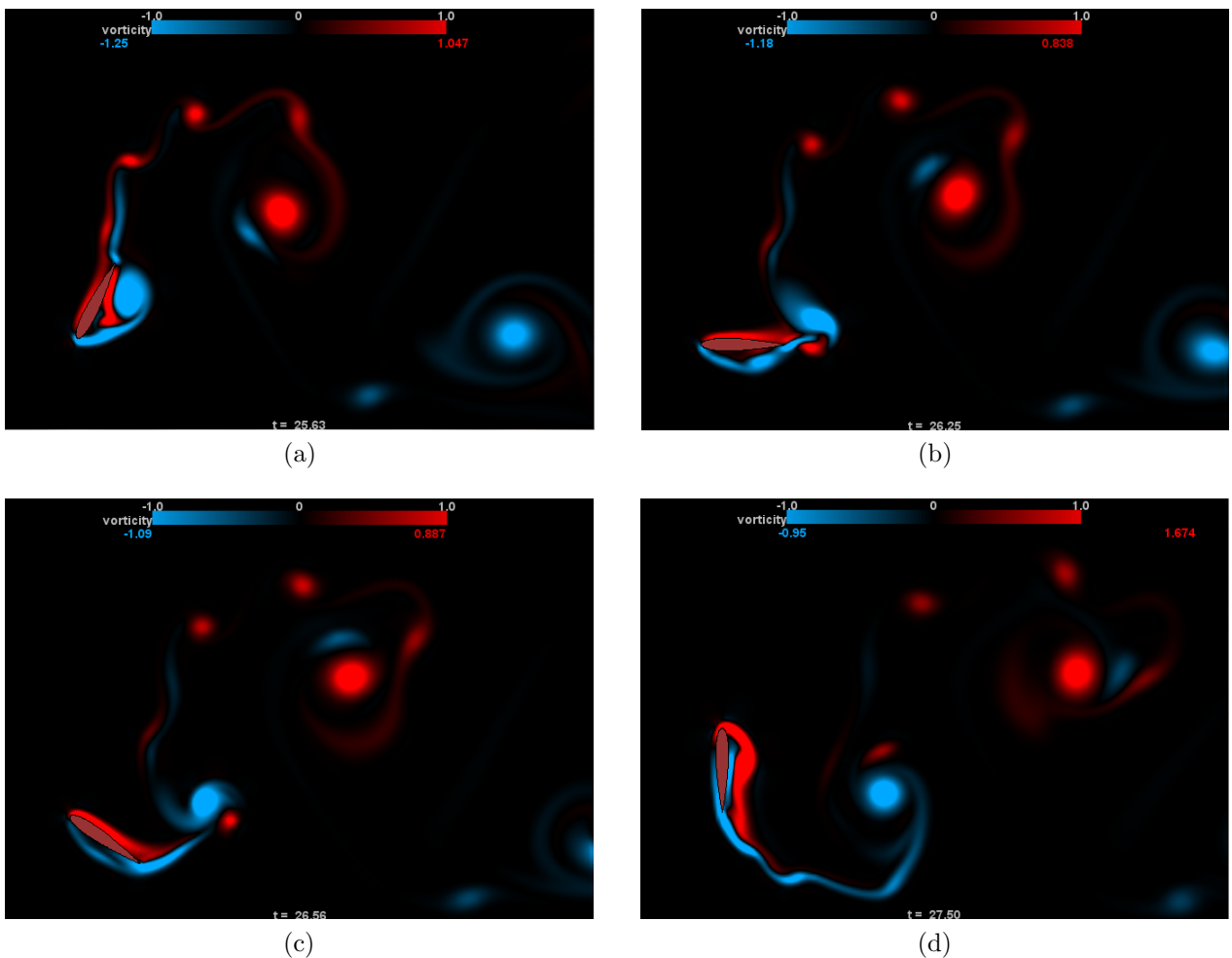


Figure C.67: $h_0/c = 1.0$, $St = 0.4$, $\theta_0 = 90^\circ$

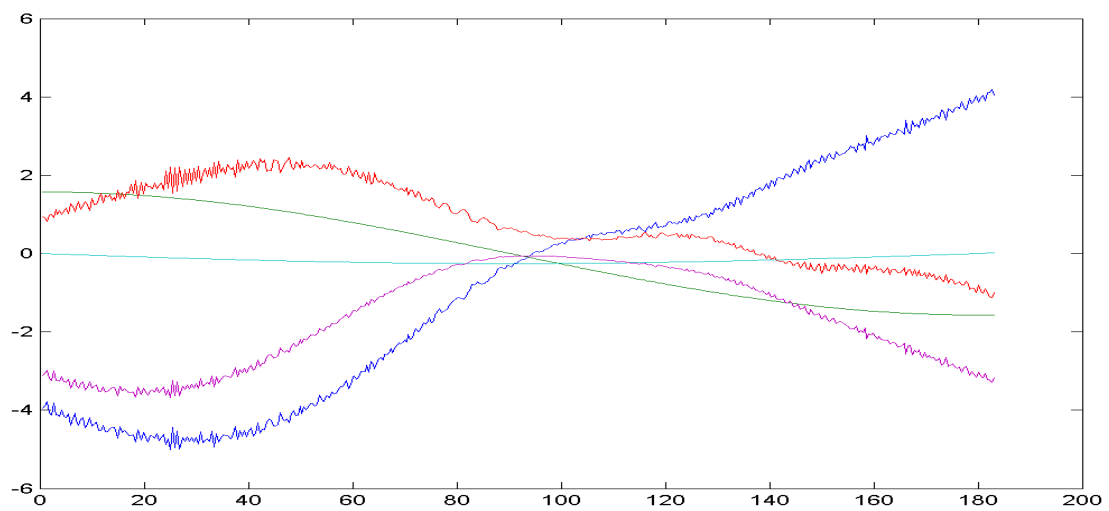
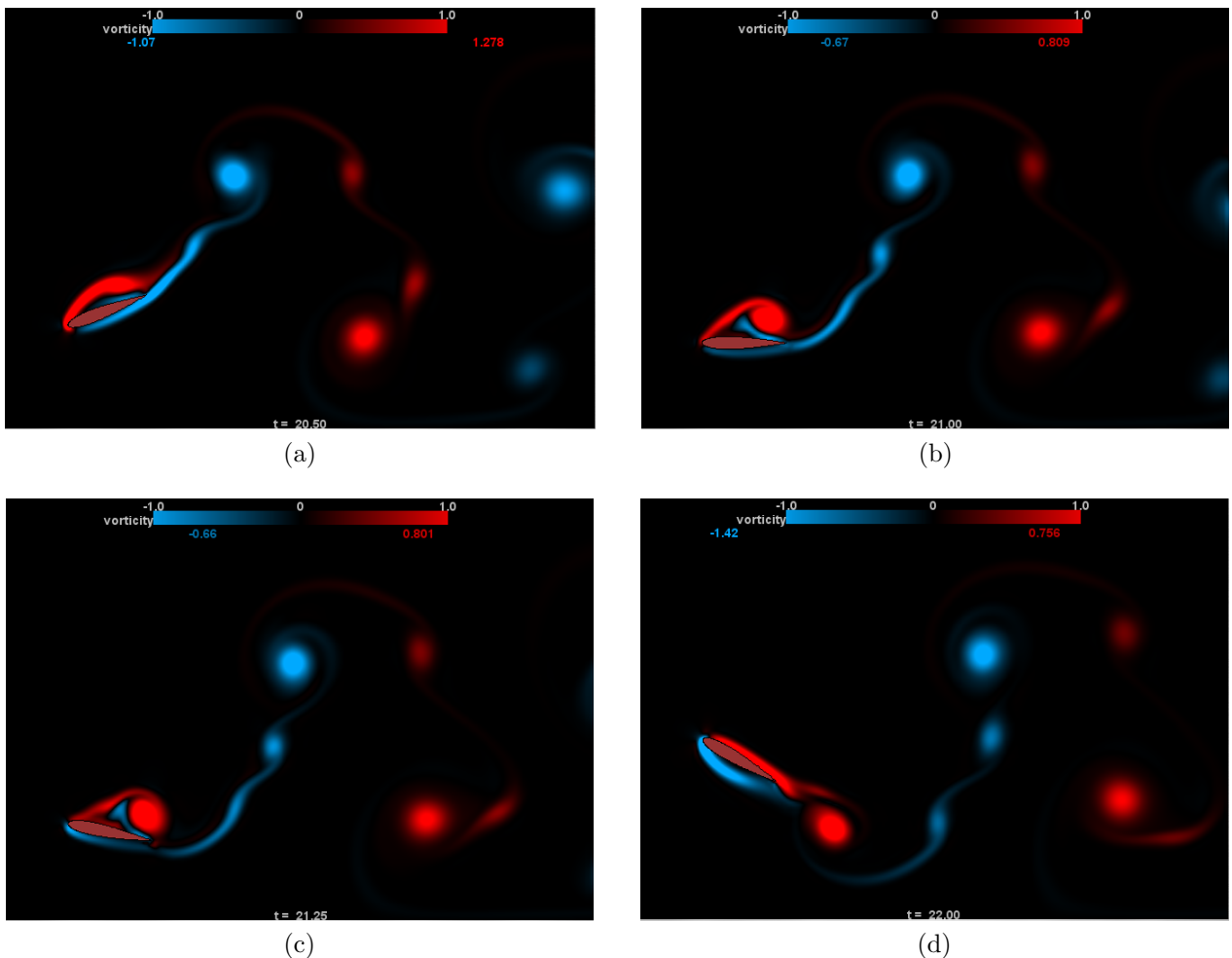


Figure C.68: $h_0/c = 1.0$, $St = 0.5$, $\theta_0 = 30^\circ$

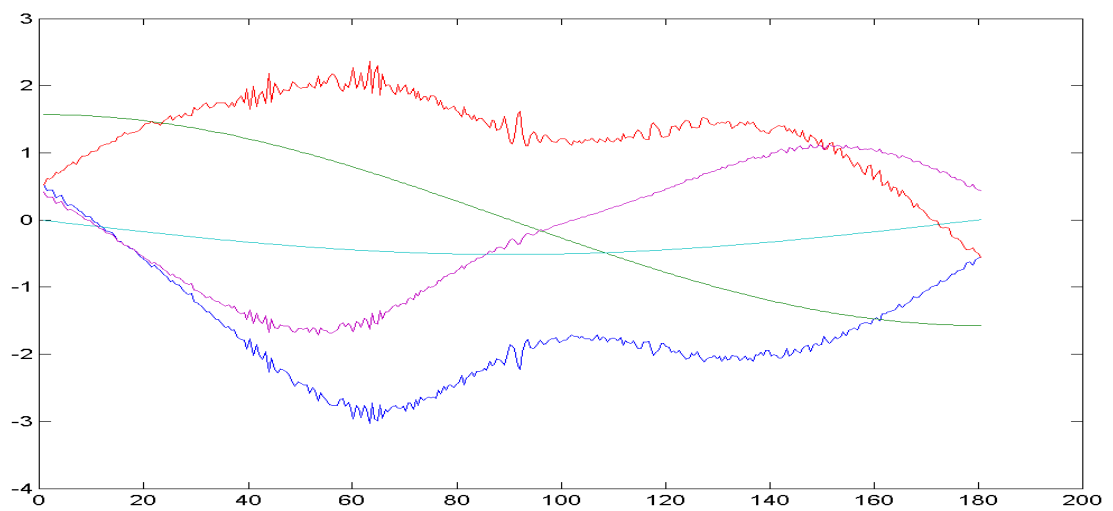
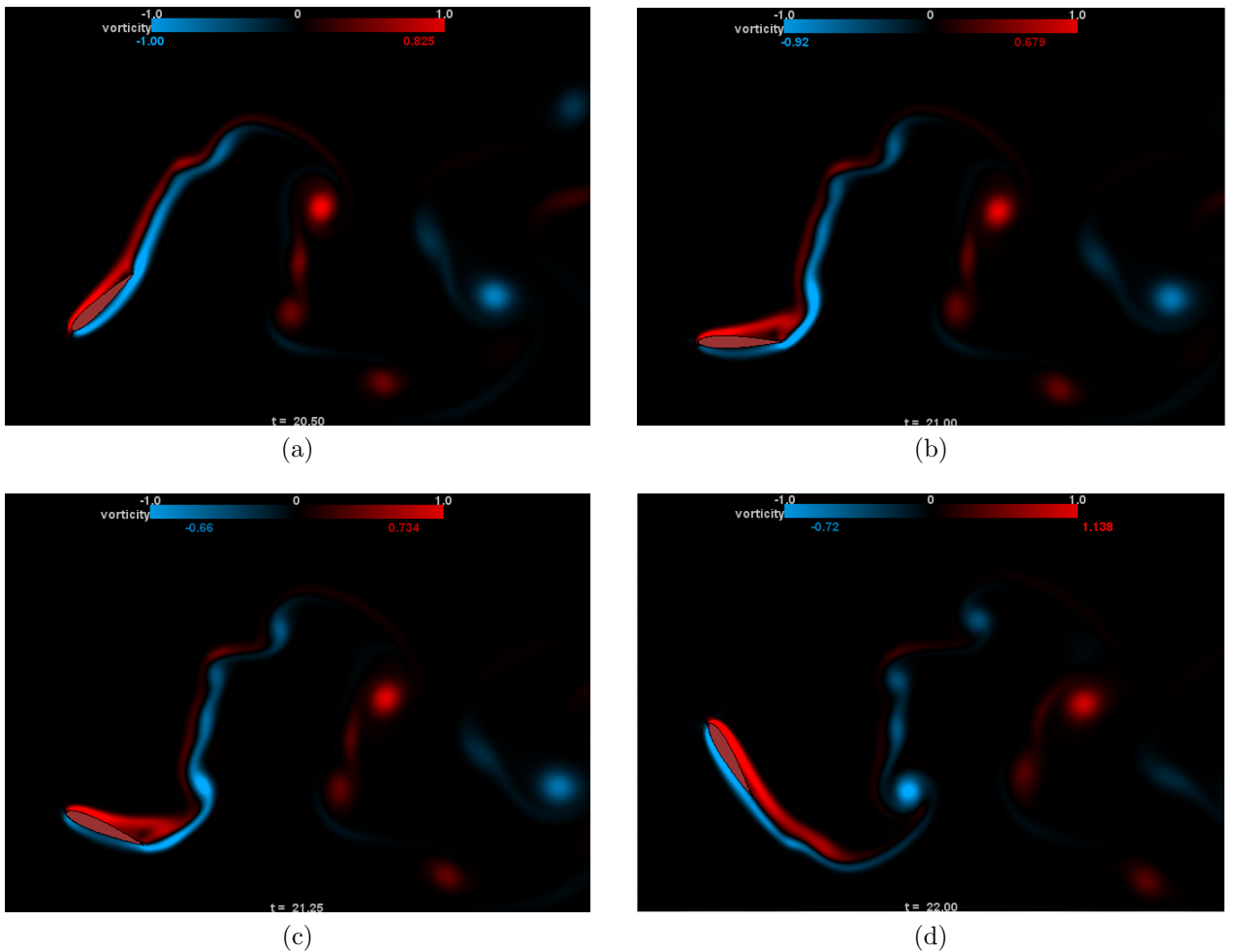


Figure C.69: $h_0/c = 1.0$, $St = 0.5$, $\theta_0 = 60^\circ$

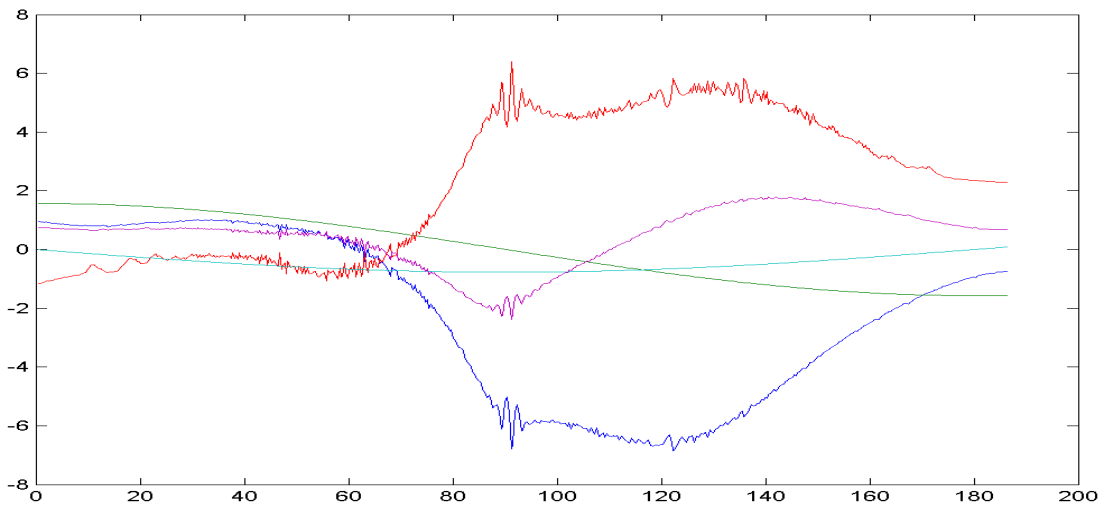
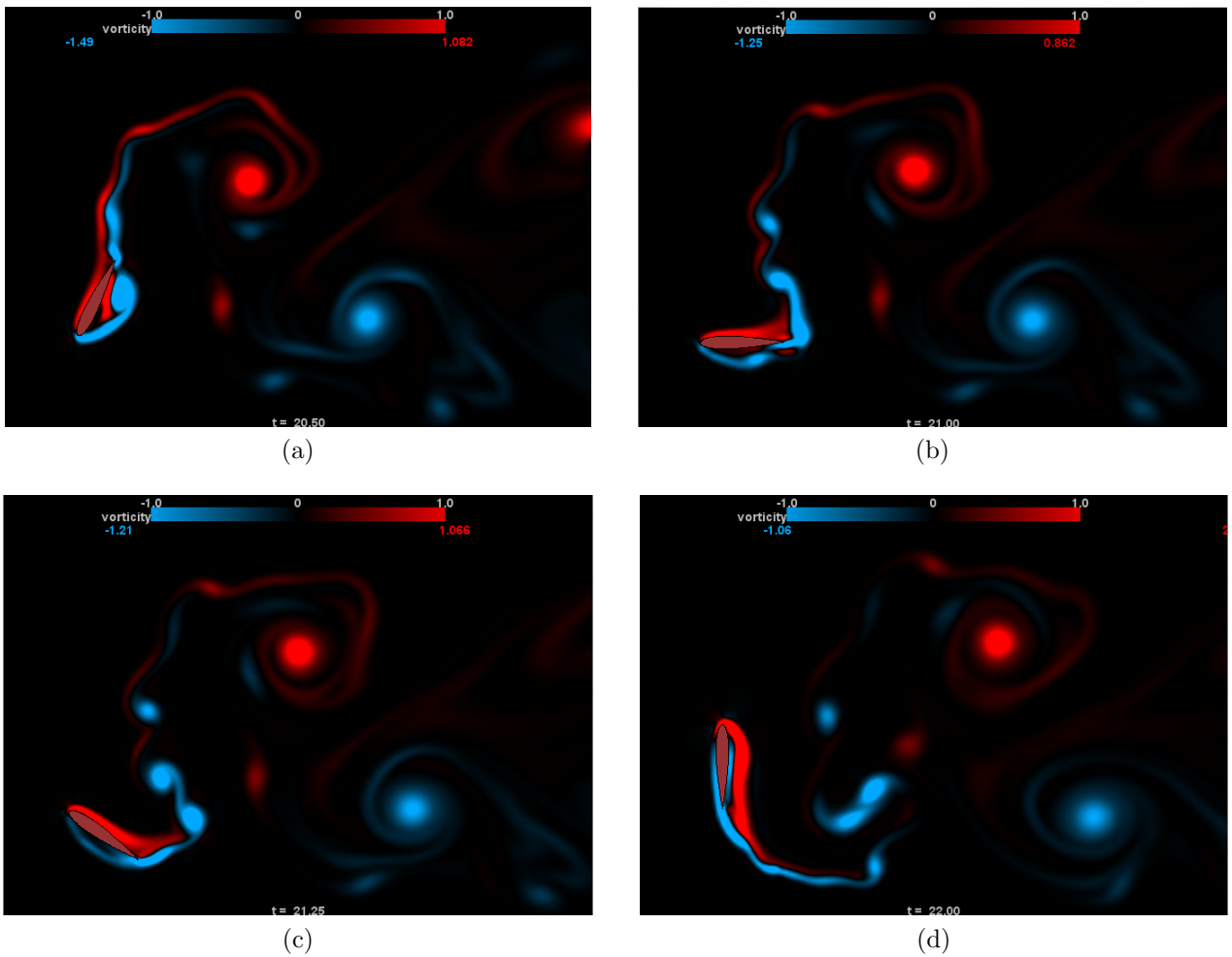


Figure C.70: $h_0/c = 1.0$, $St = 0.5$, $\theta_0 = 90^\circ$

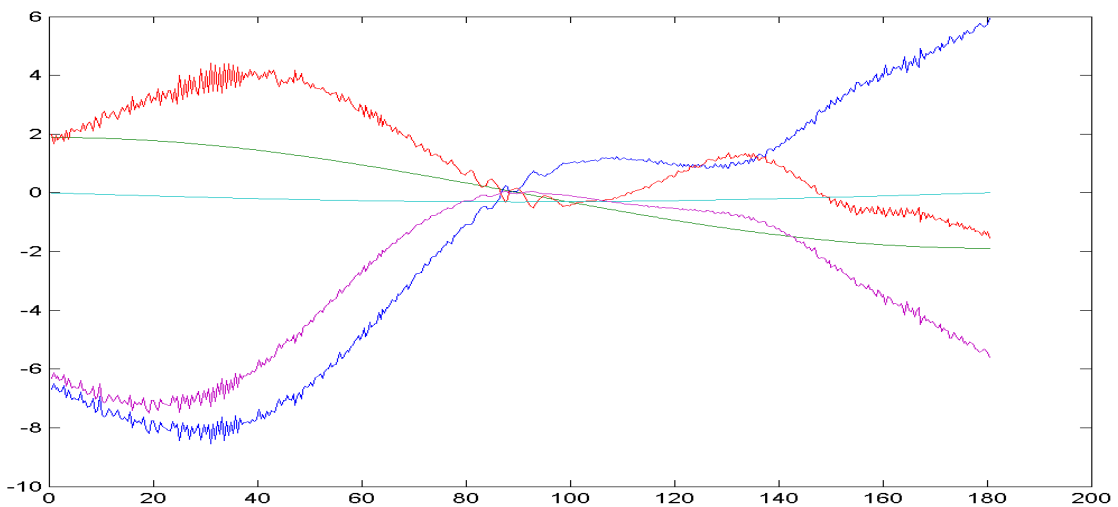
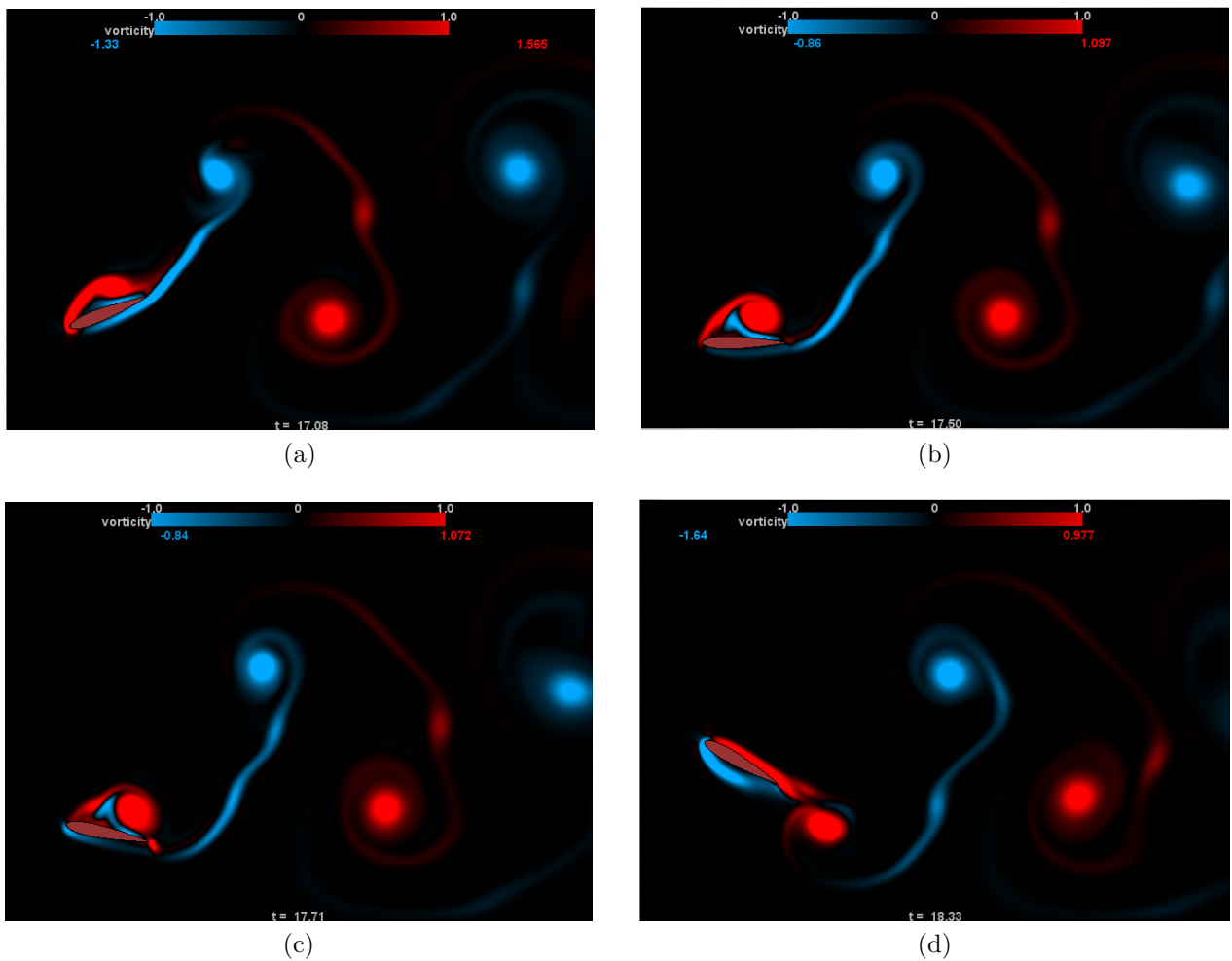


Figure C.71: $h_0/c = 1.0$, $St = 0.6$, $\theta_0 = 30^\circ$

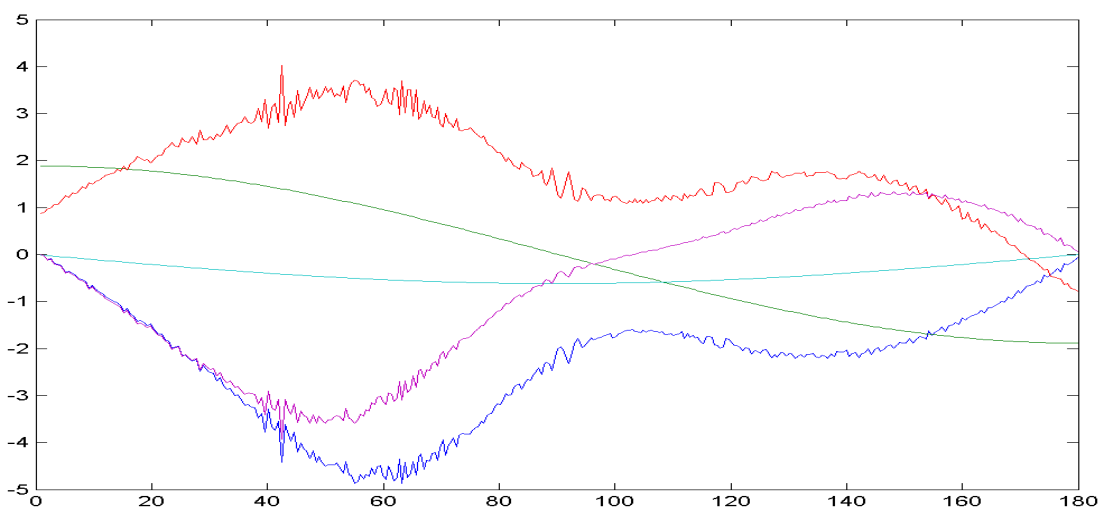
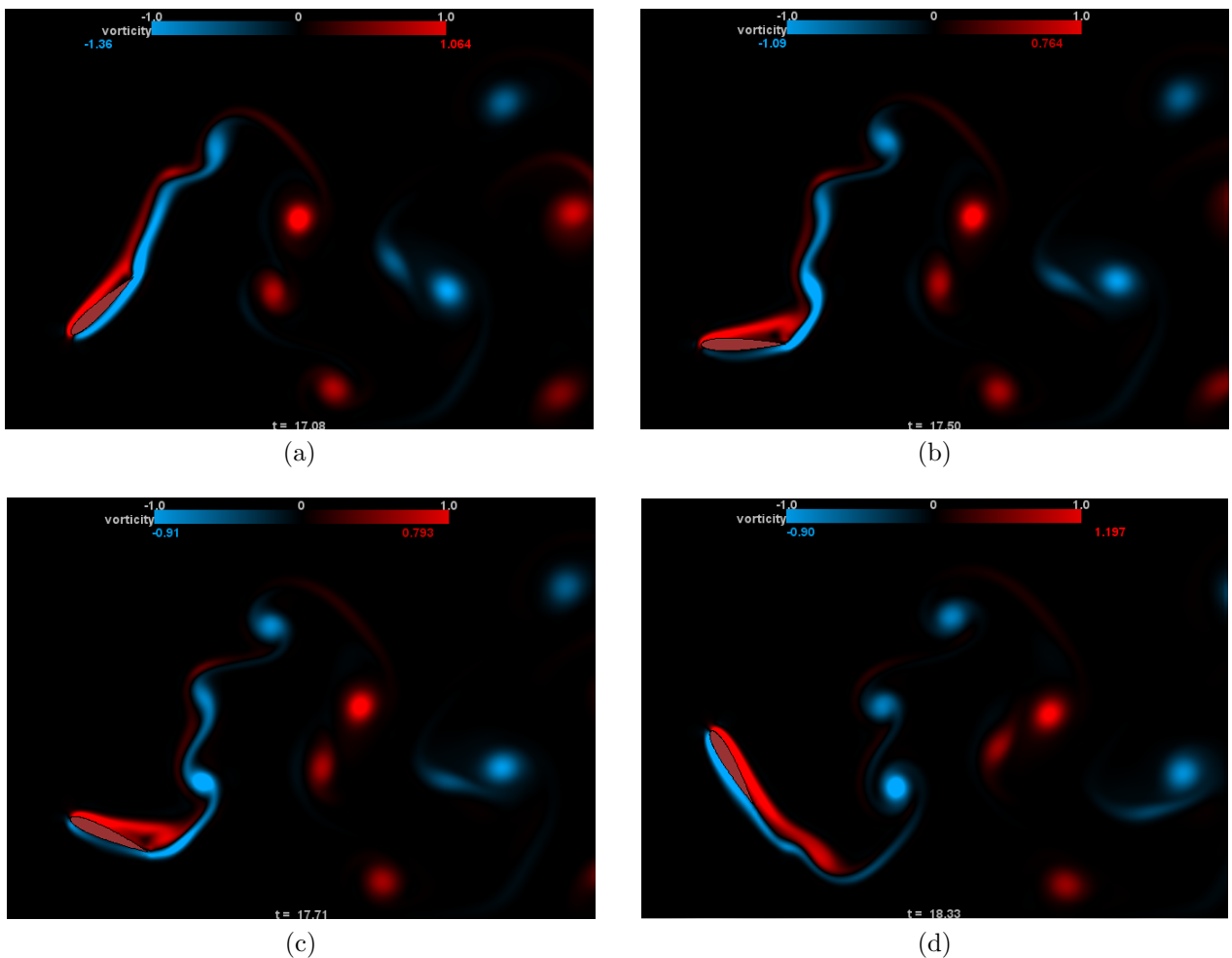


Figure C.72: $h_0/c = 1.0$, $St = 0.6$, $\theta_0 = 60^\circ$

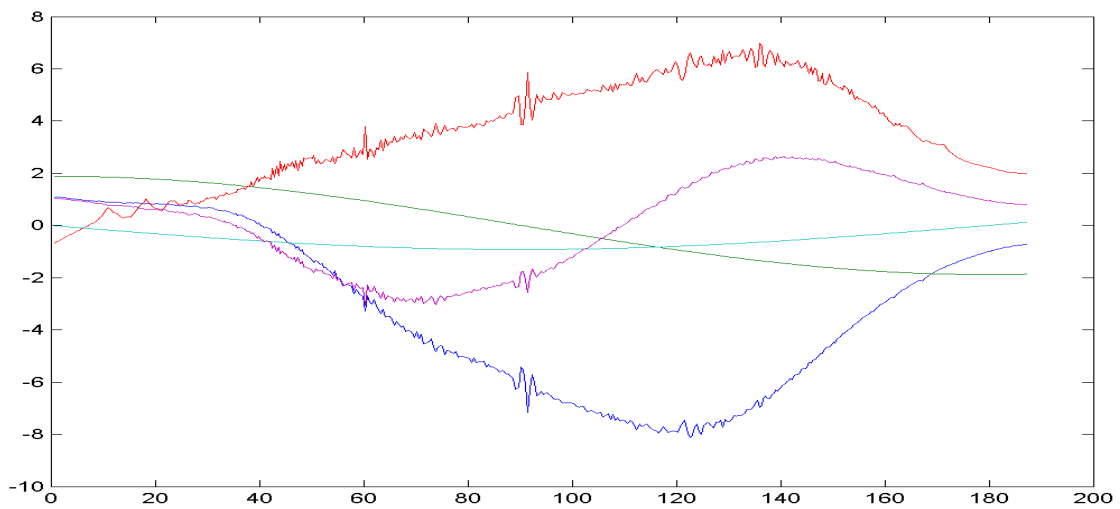
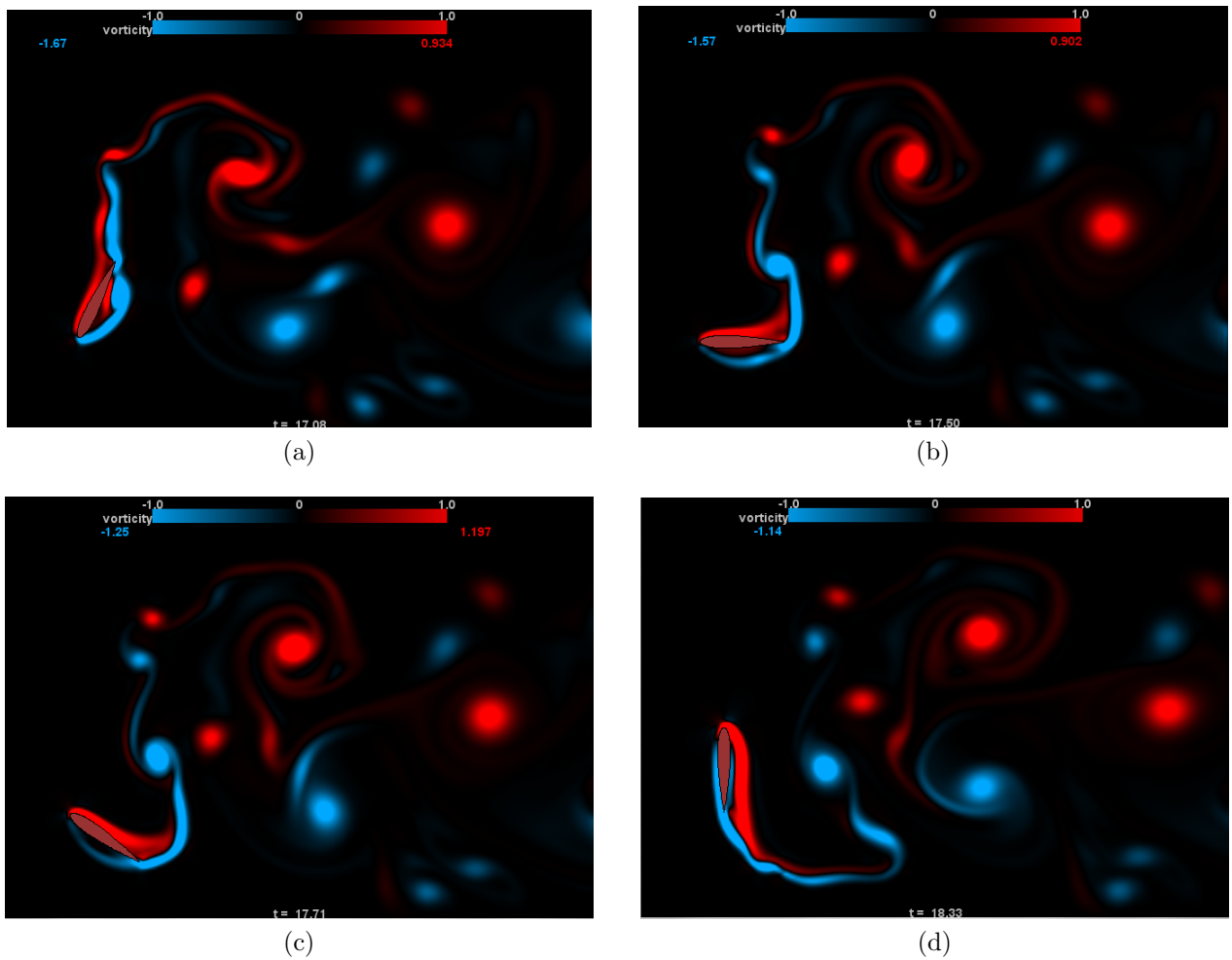


Figure C.73: $h_0/c = 1.0$, $St = 0.6$, $\theta_0 = 90^\circ$

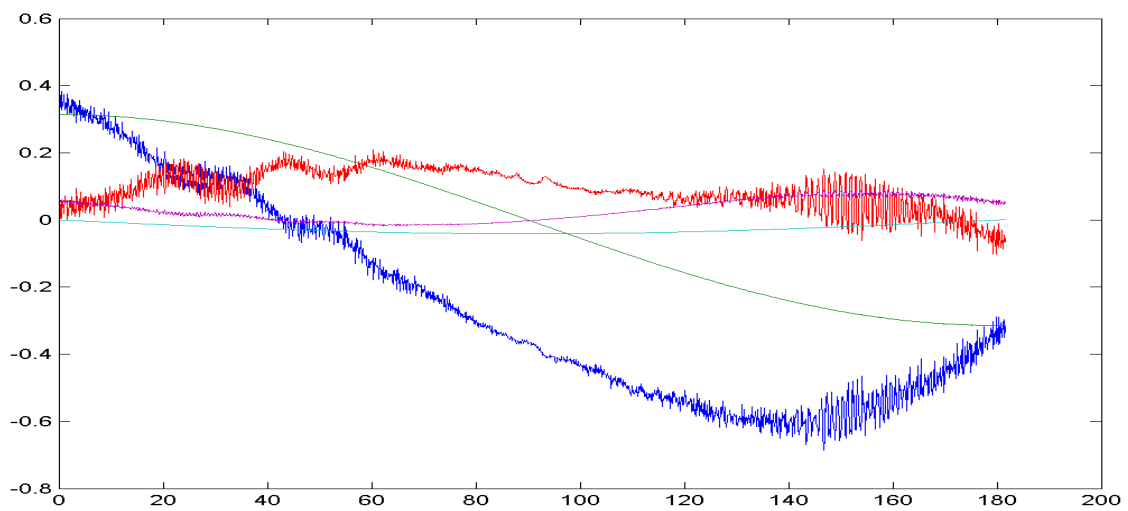
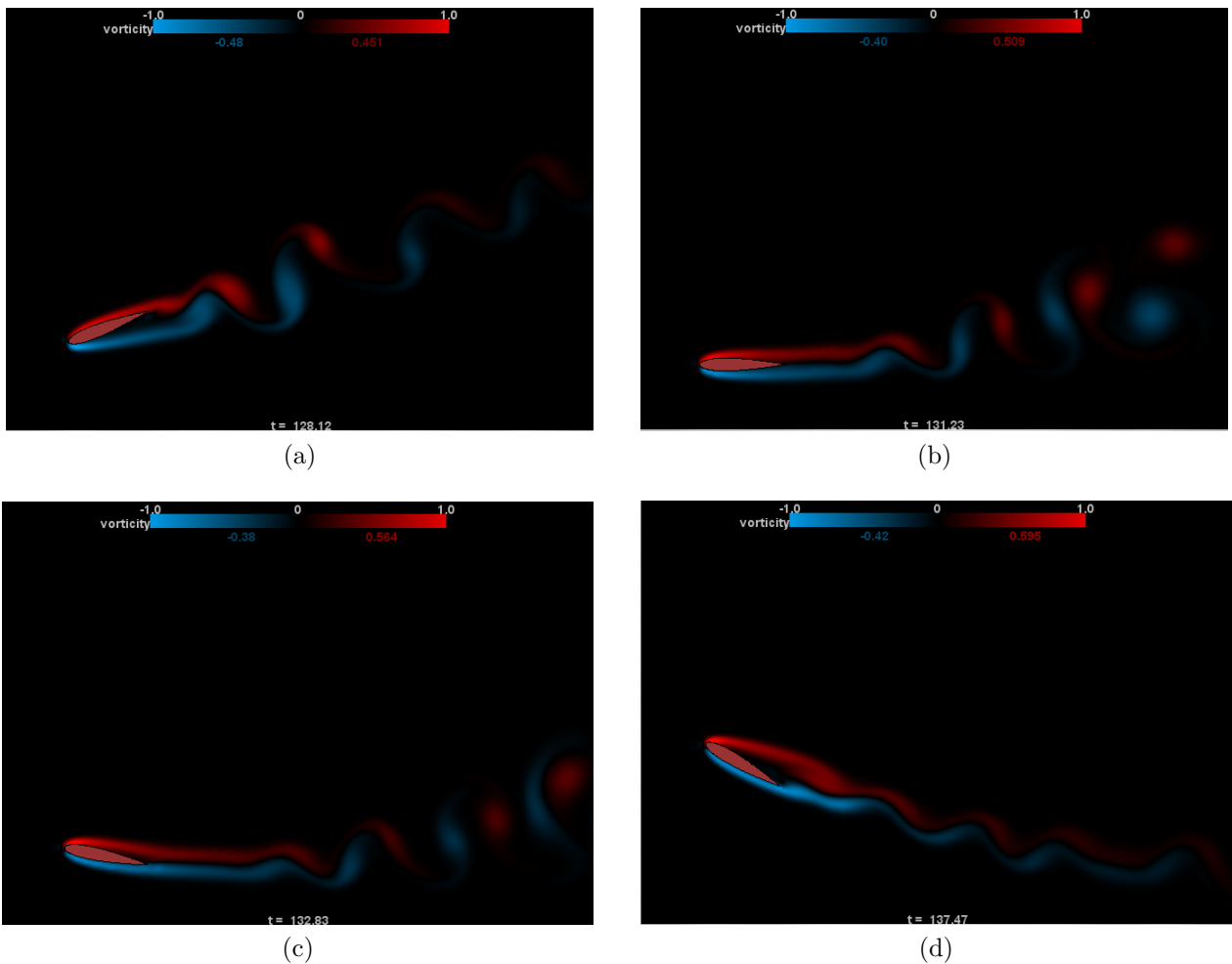


Figure C.74: $h_0/c = 1.25$, $St = 0.1$, $\theta_0 = 30^\circ$

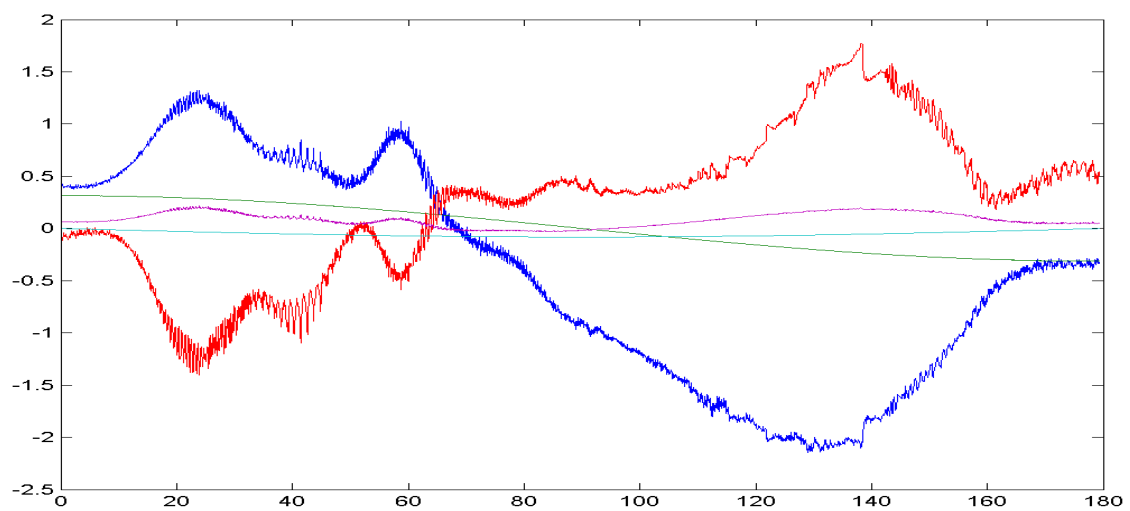
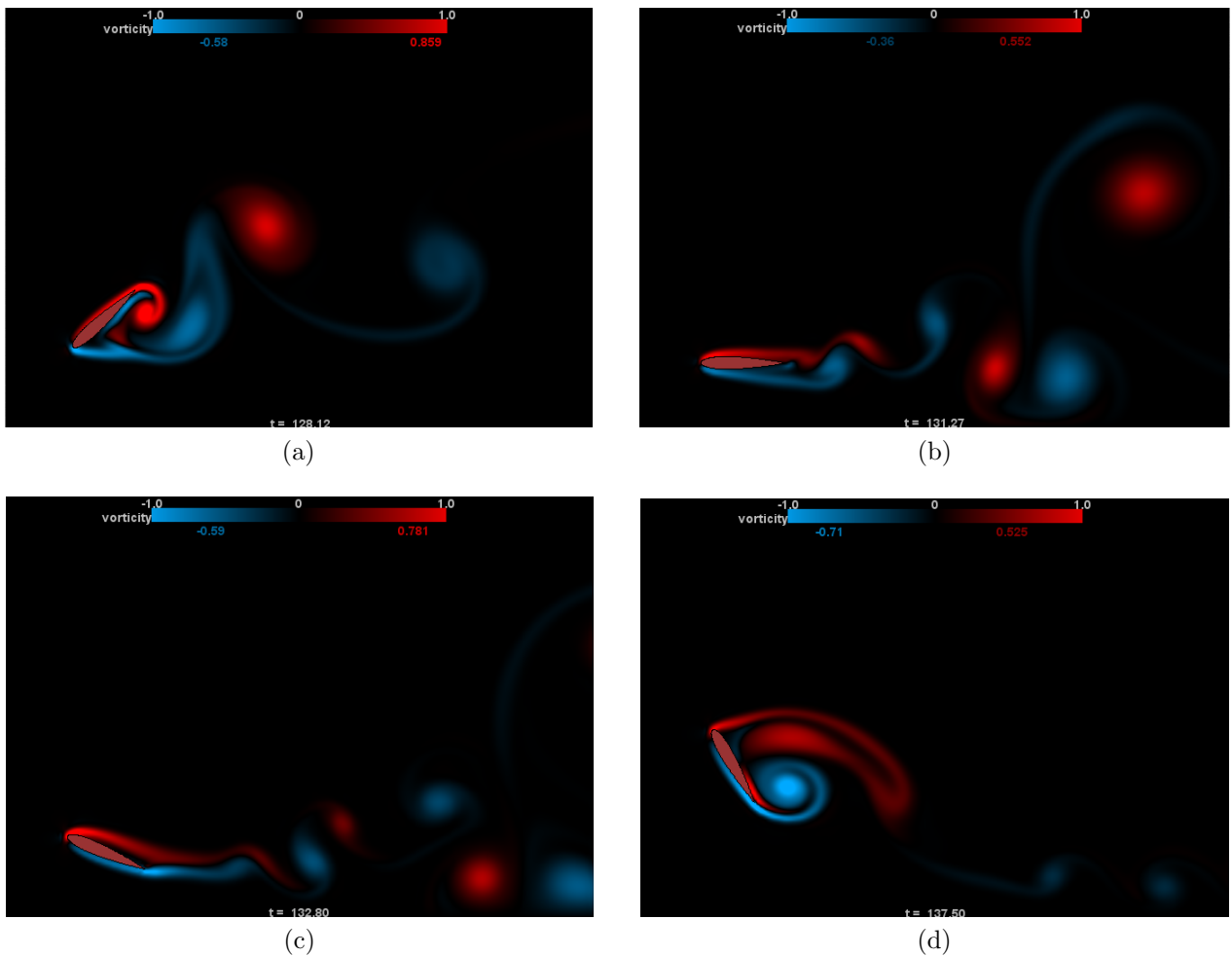


Figure C.75: $h_0/c = 1.25$, $St = 0.1$, $\theta_0 = 60^\circ$

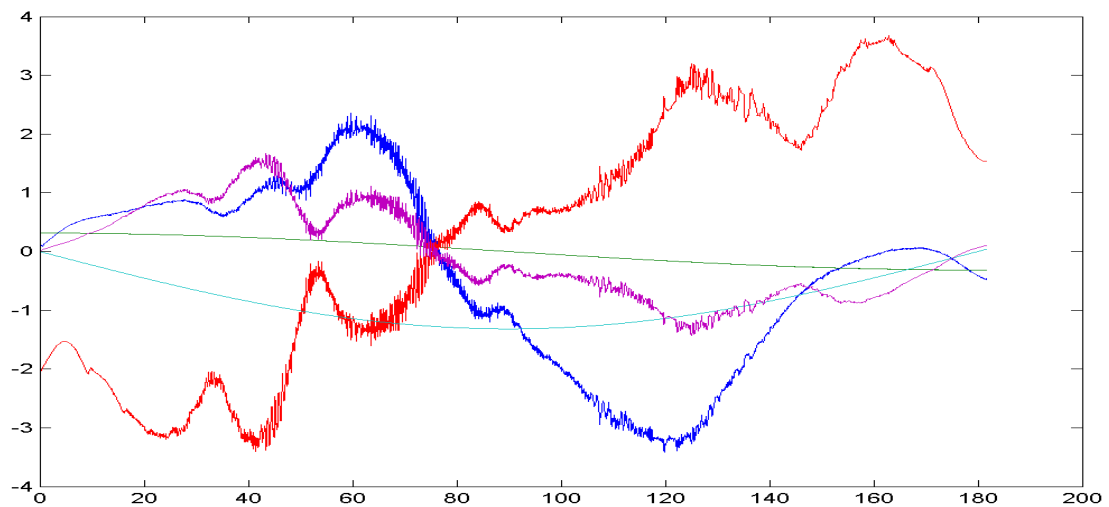
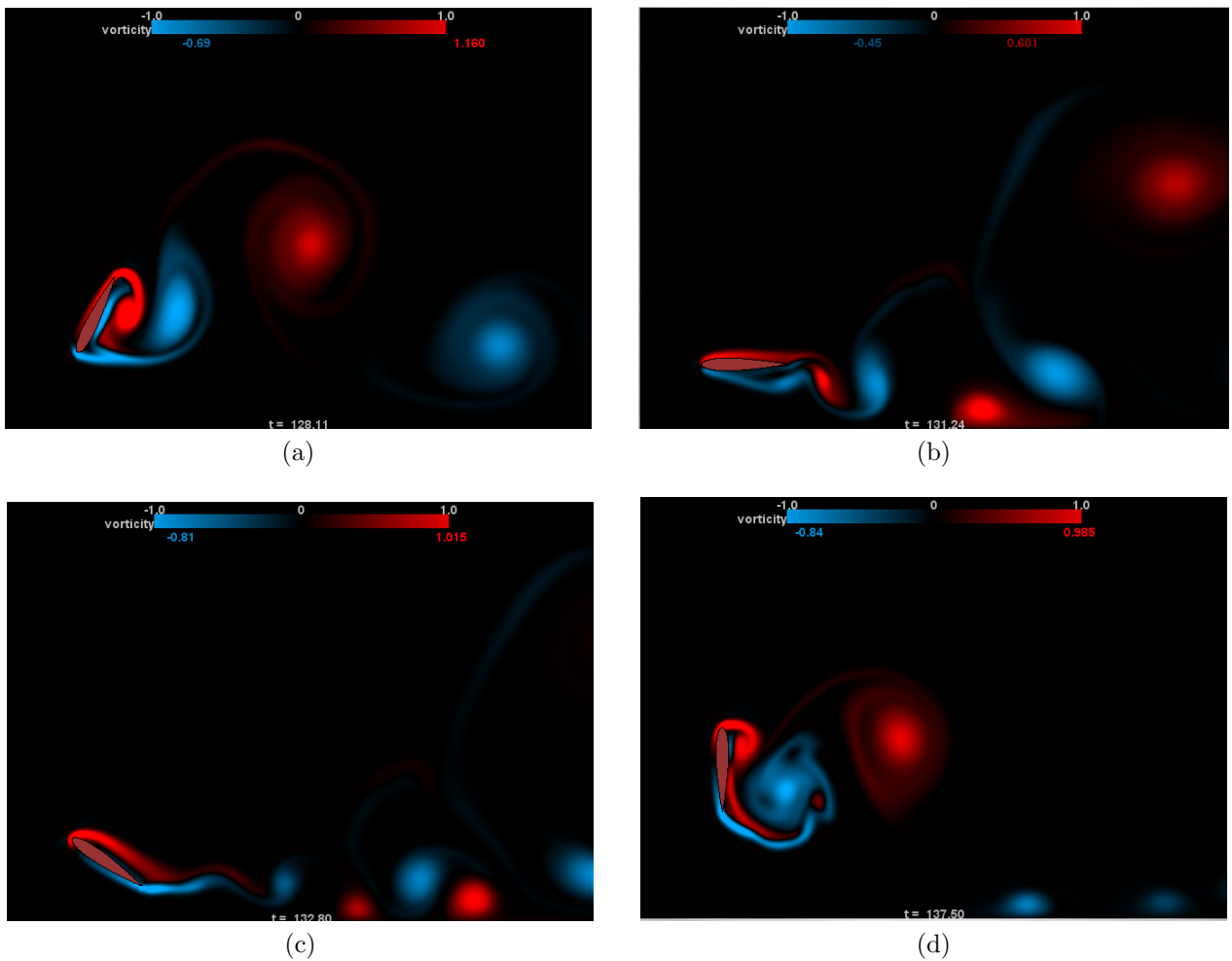


Figure C.76: $h_0/c = 1.25$, $St = 0.1$, $\theta_0 = 90^\circ$

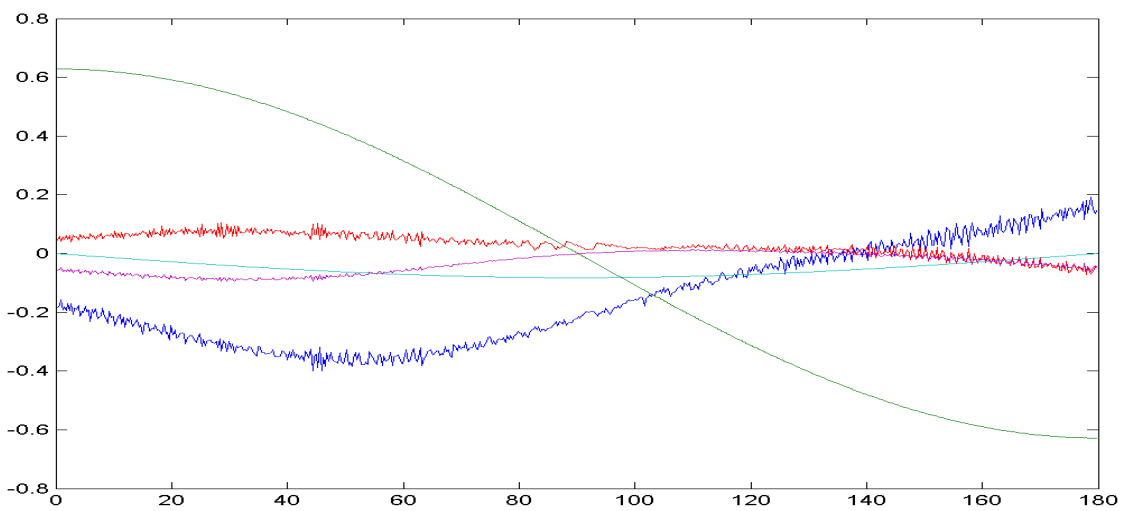
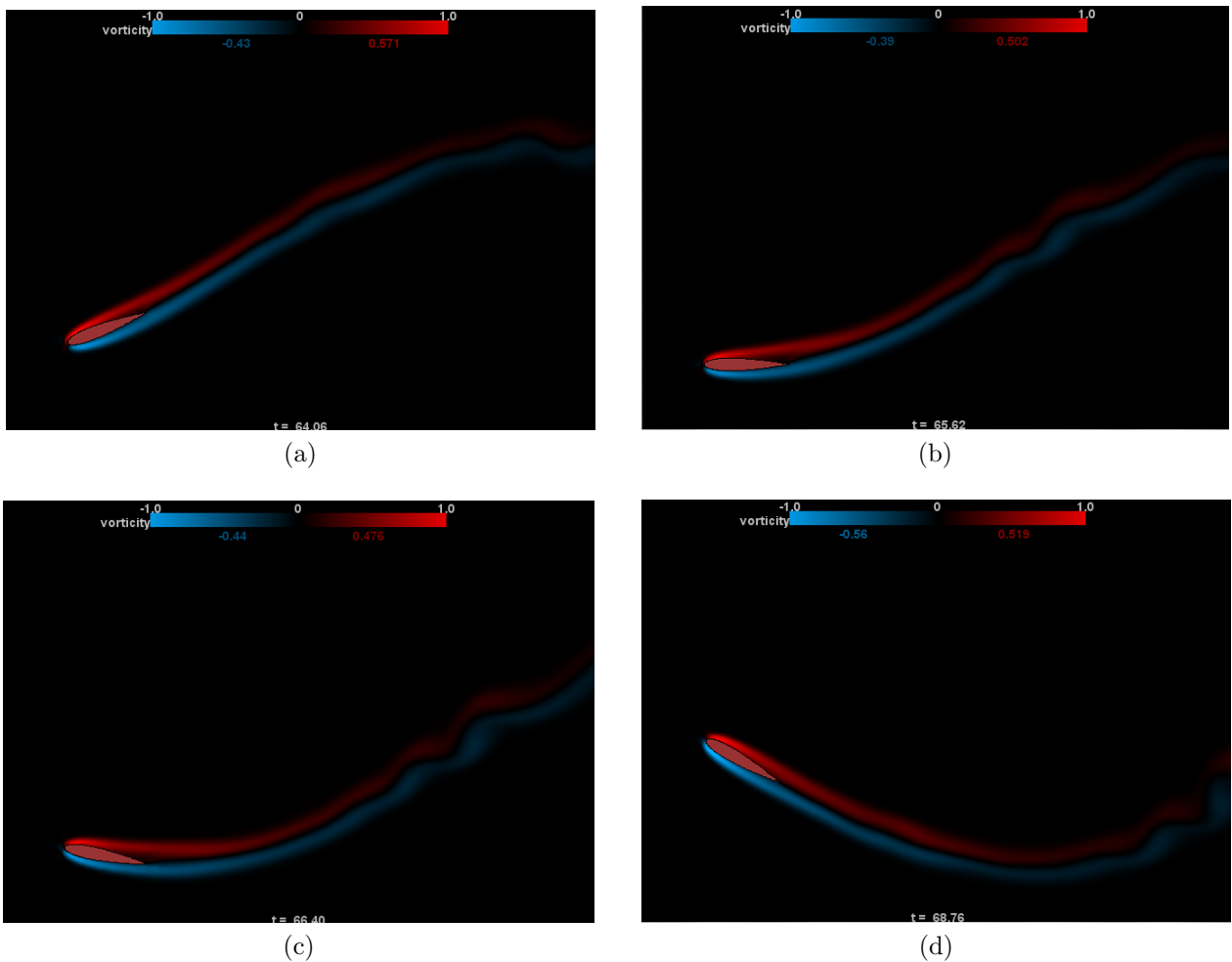


Figure C.77: $h_0/c = 1.25$, $St = 0.2$, $\theta_0 = 30^\circ$

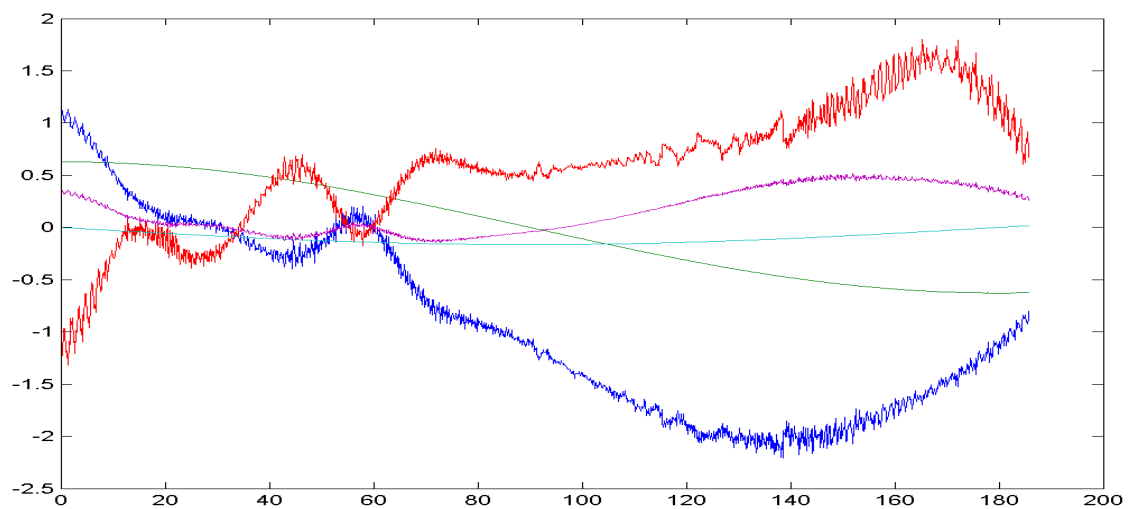
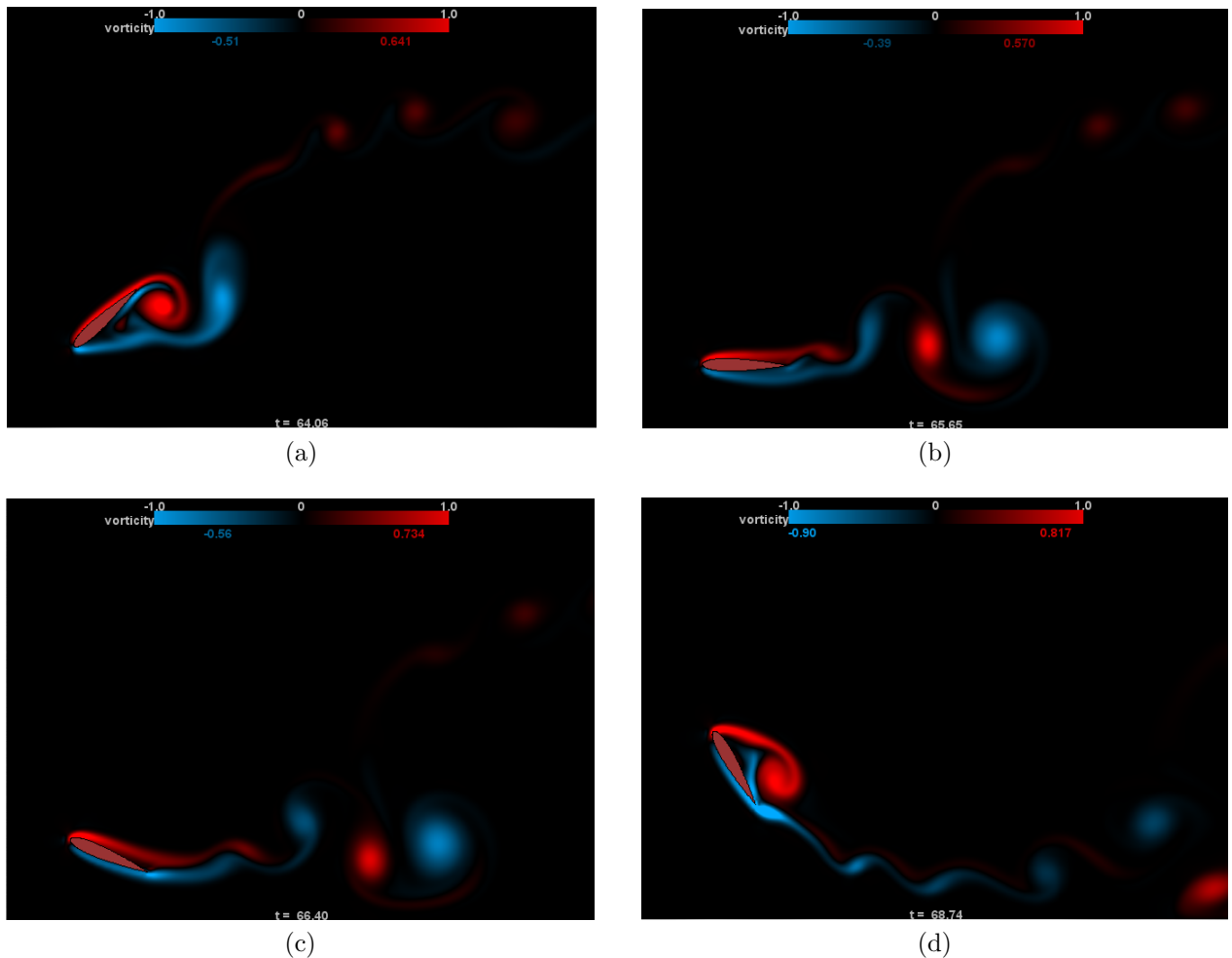


Figure C.78: $h_0/c = 1.25$, $St = 0.2$, $\theta_0 = 60^\circ$

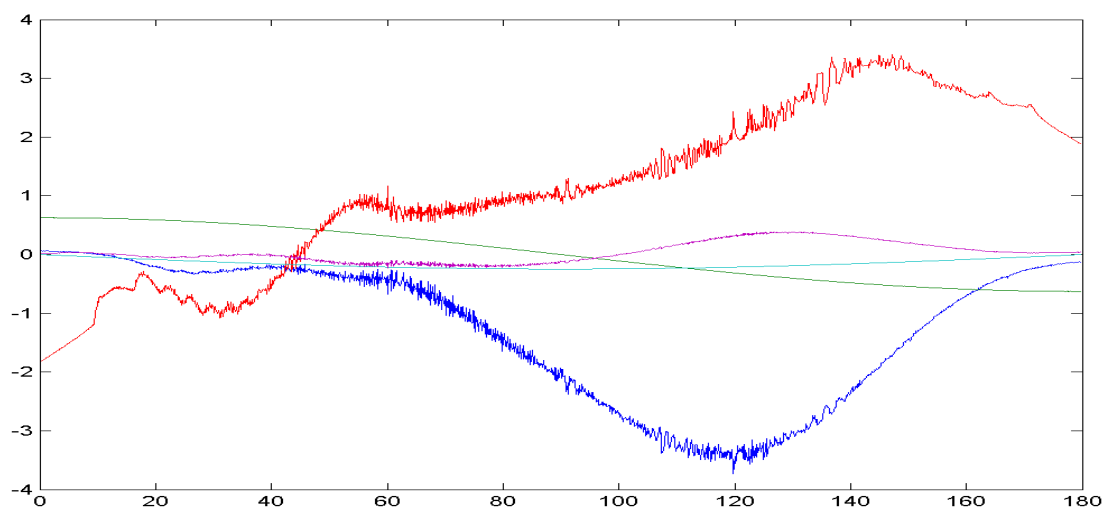
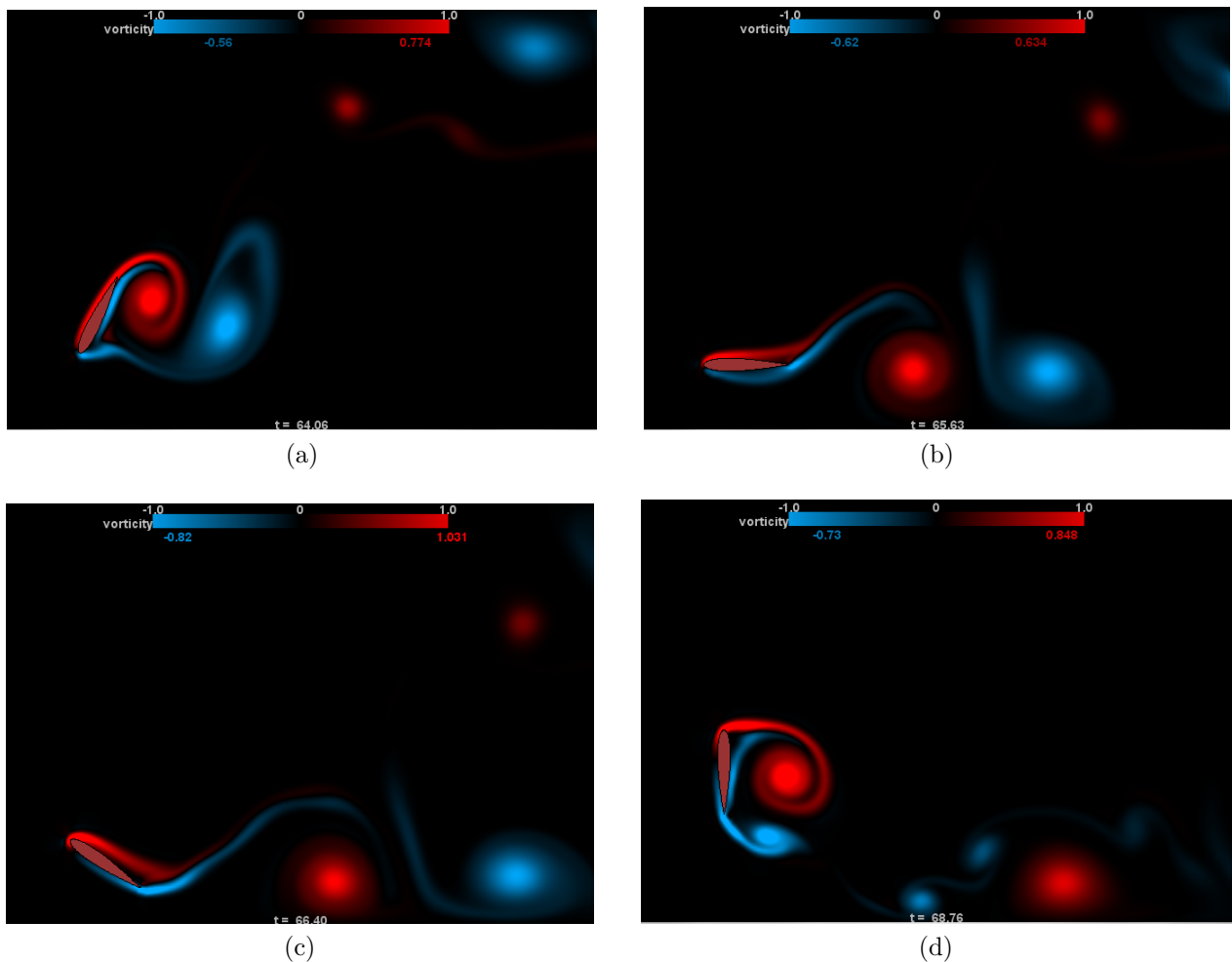


Figure C.79: $h_0/c = 1.25$, $St = 0.2$, $\theta_0 = 90^\circ$

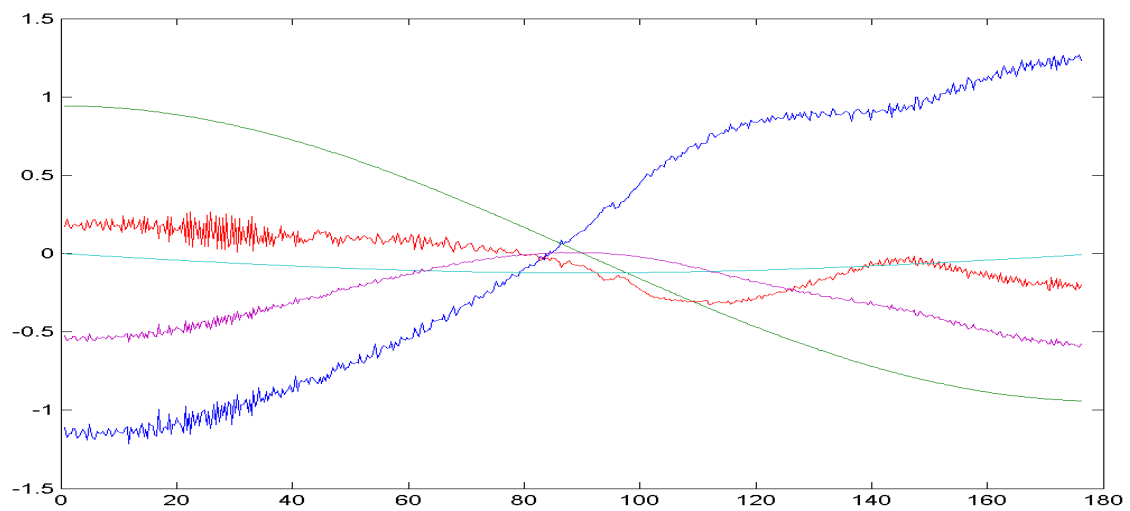
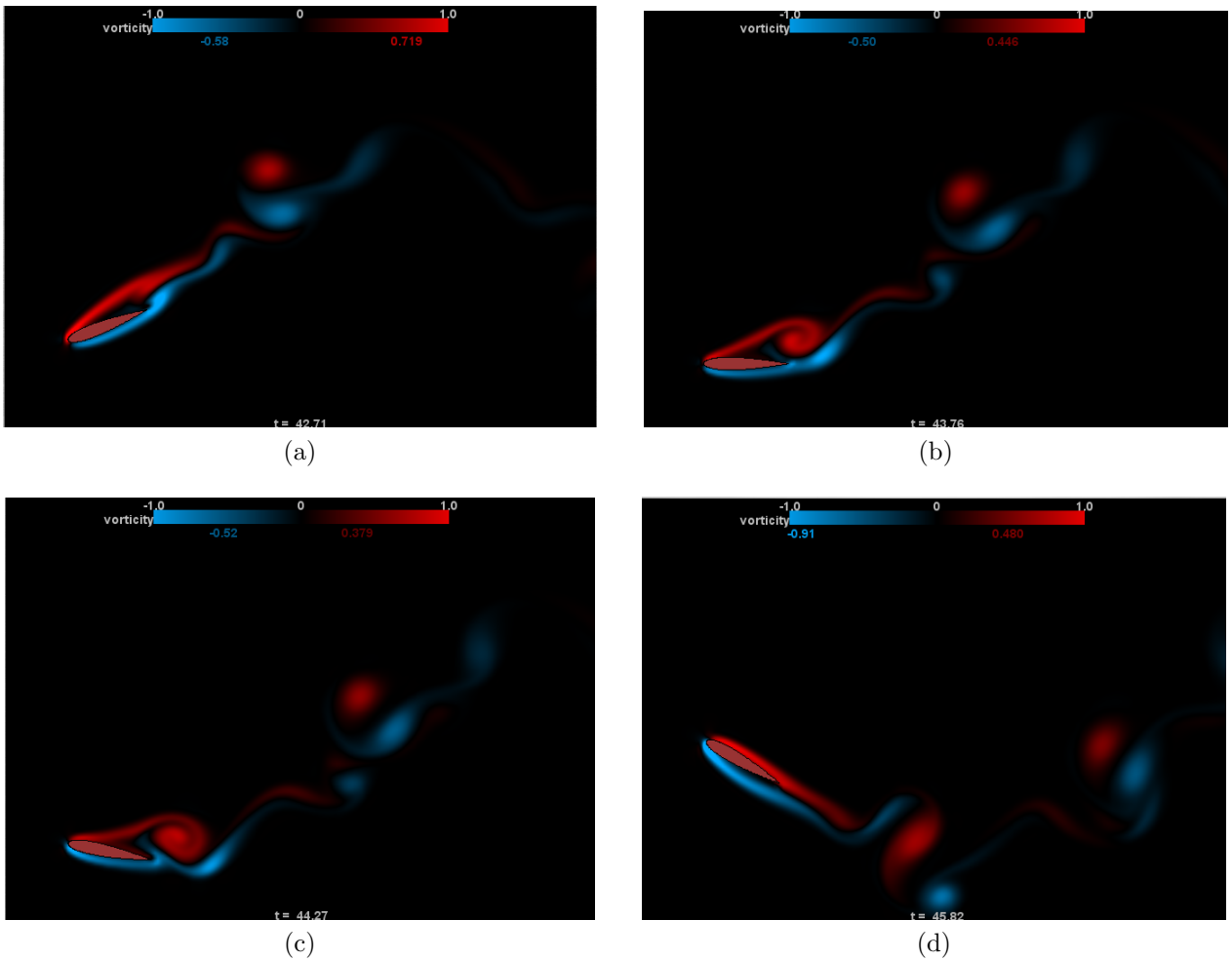


Figure C.80: $h_0/c = 1.25$, $St = 0.3$, $\theta_0 = 30^\circ$

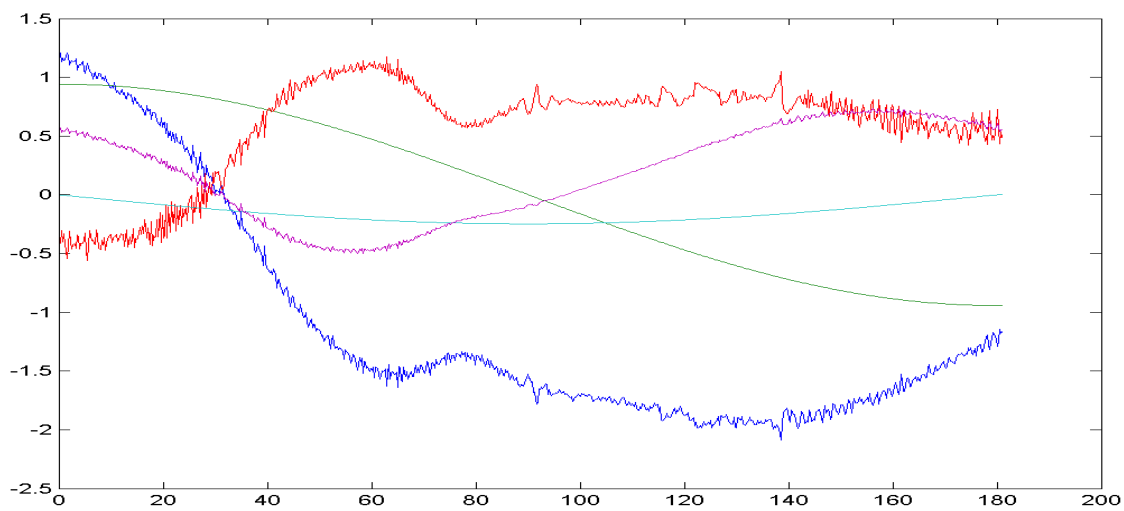
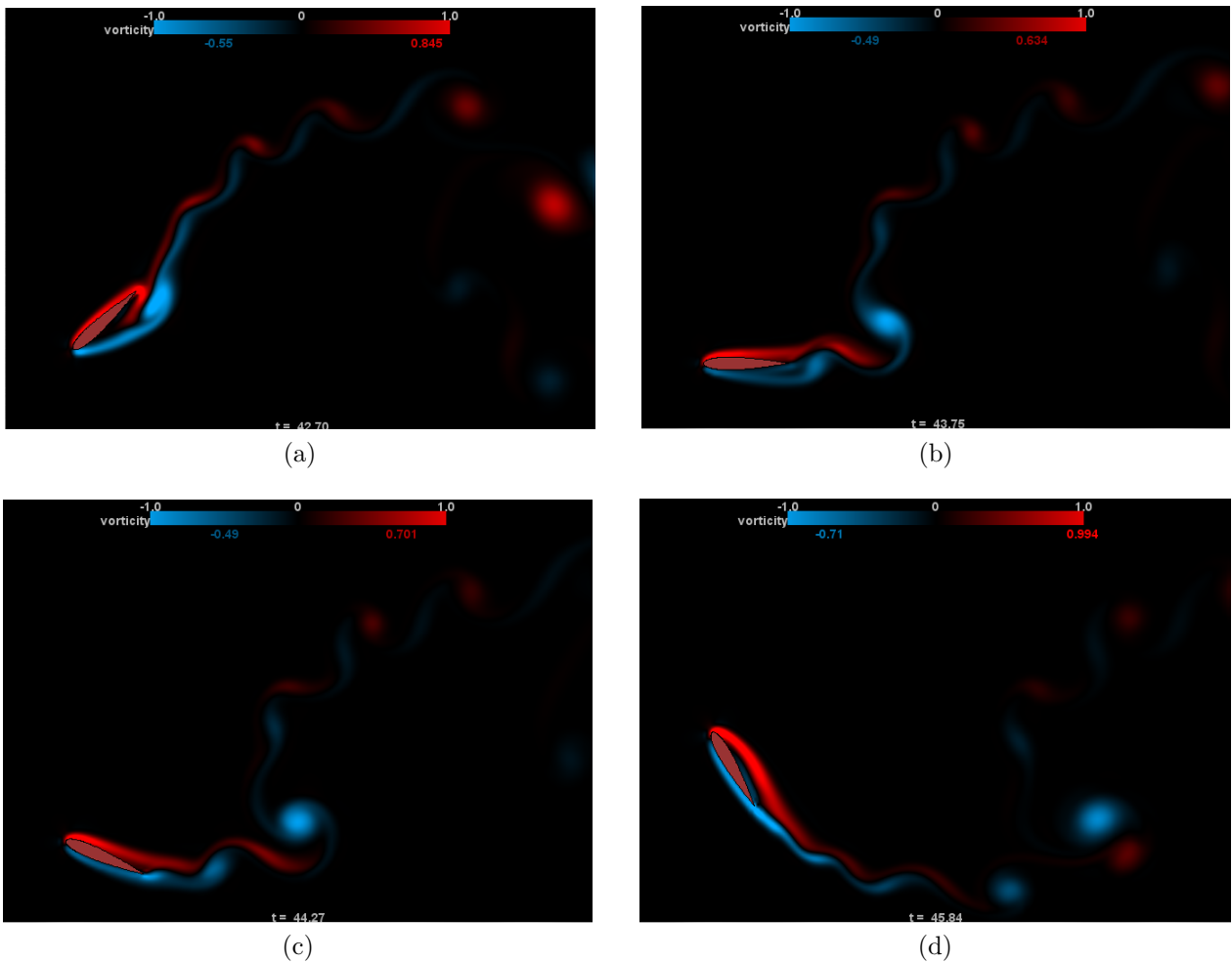


Figure C.81: $h_0/c = 1.25$, $St = 0.3$, $\theta_0 = 60^\circ$

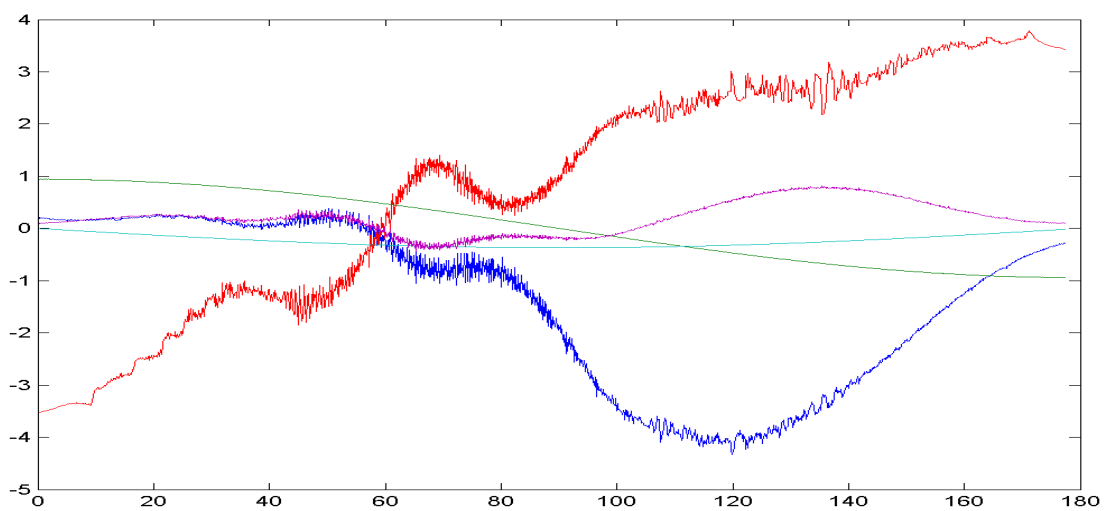
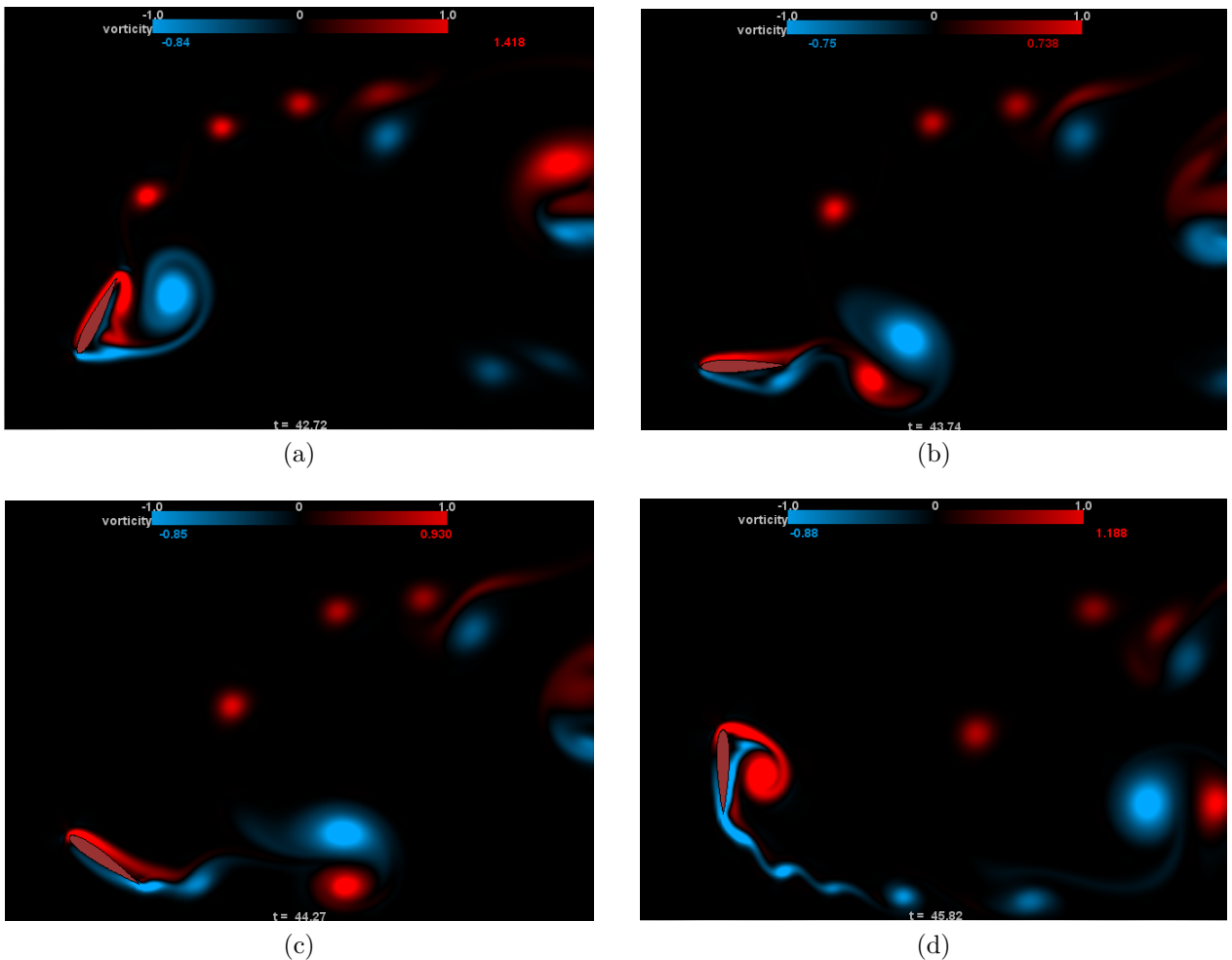


Figure C.82: $h_0/c = 1.25$, $St = 0.3$, $\theta_0 = 90^\circ$

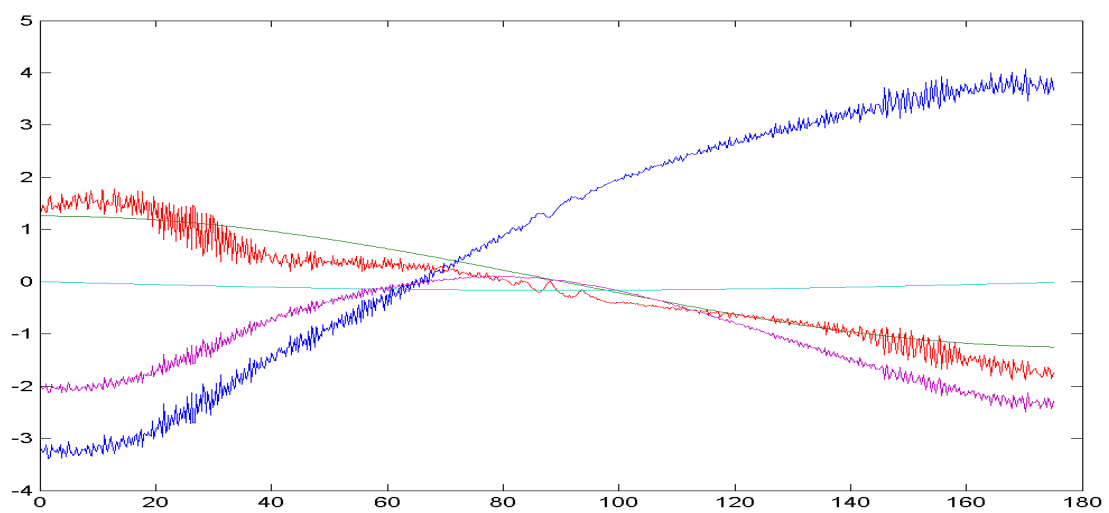
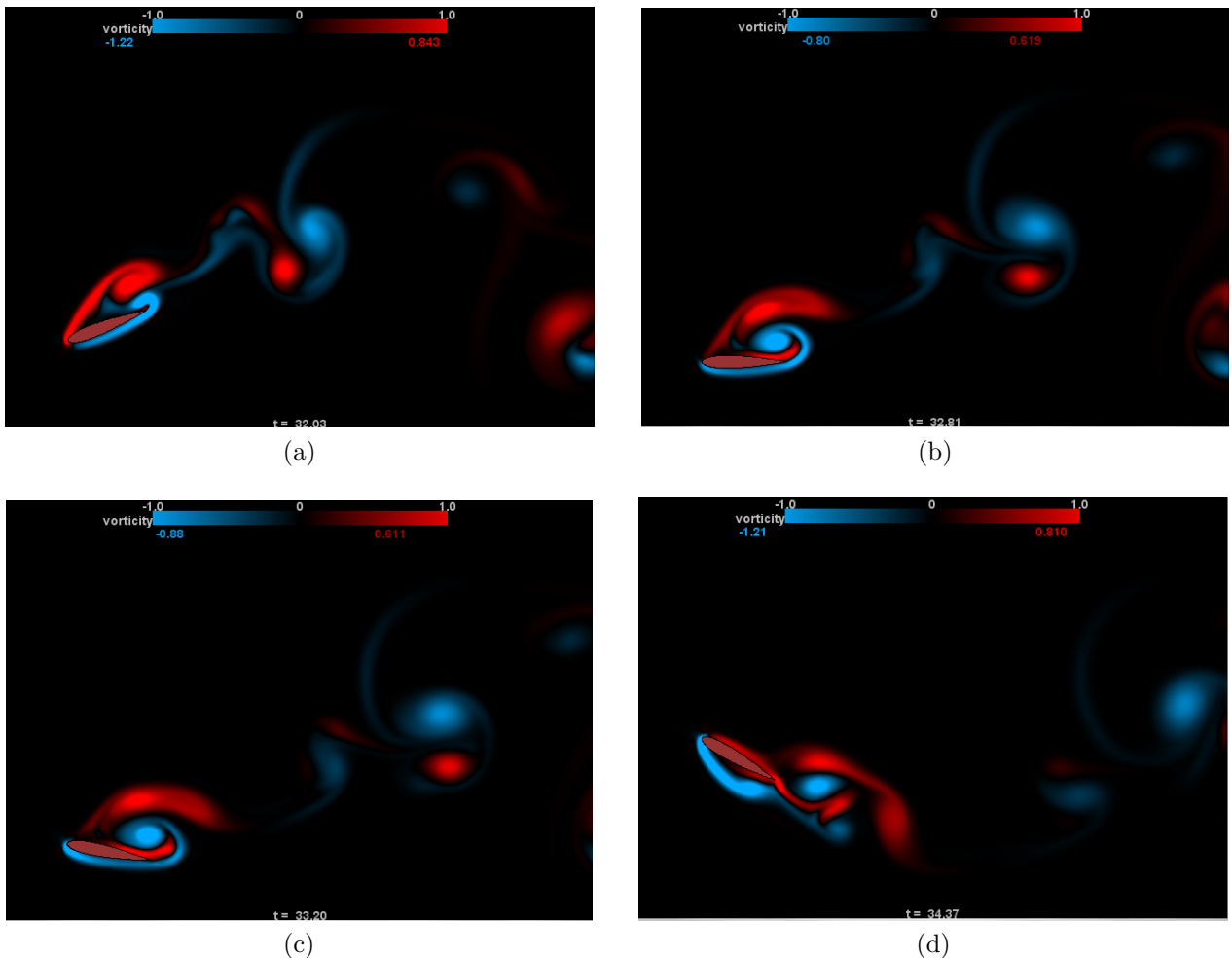


Figure C.83: $h_0/c = 1.25$, $St = 0.4$, $\theta_0 = 30^\circ$

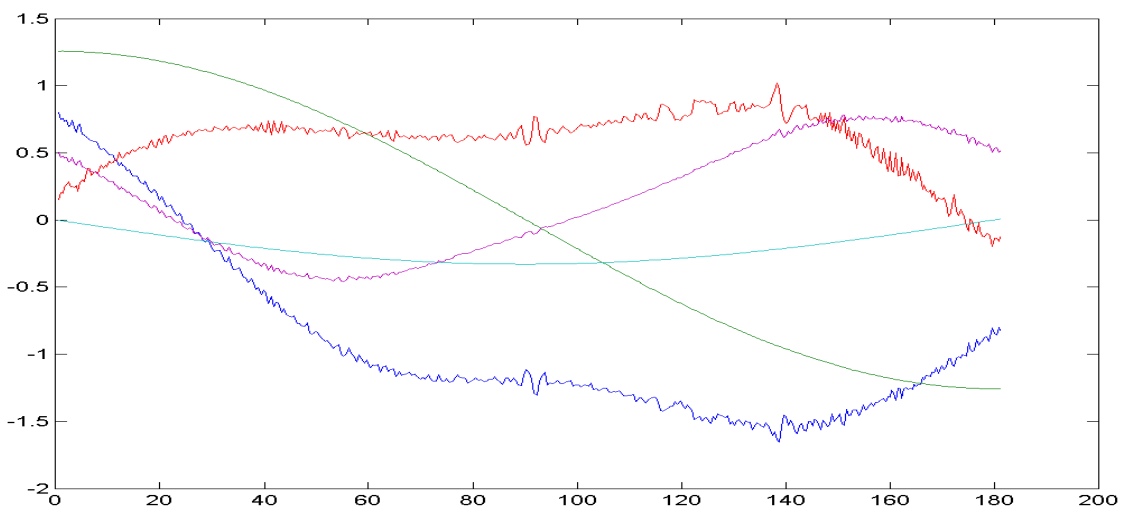
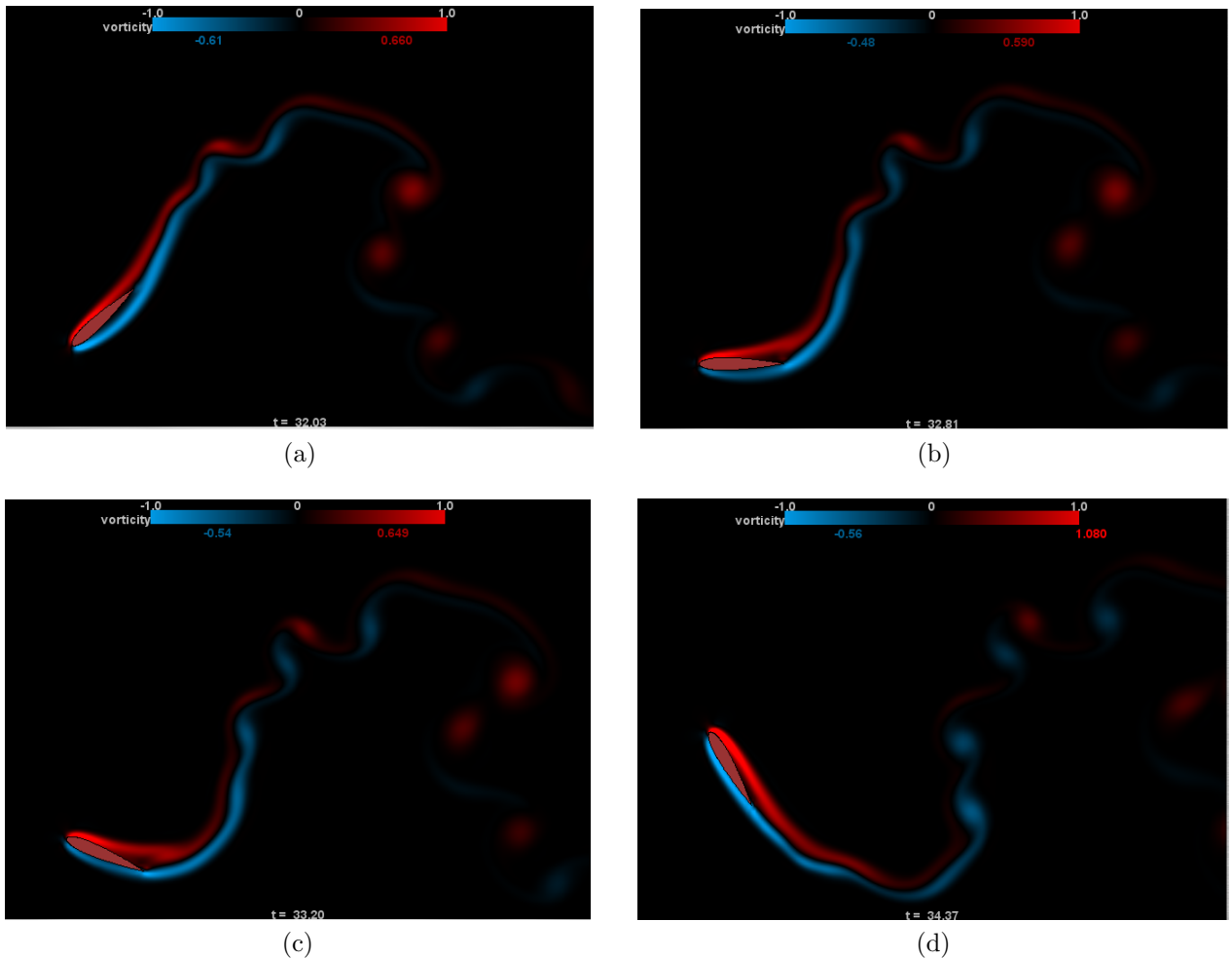


Figure C.84: $h_0/c = 1.25$, $St = 0.4$, $\theta_0 = 60^\circ$

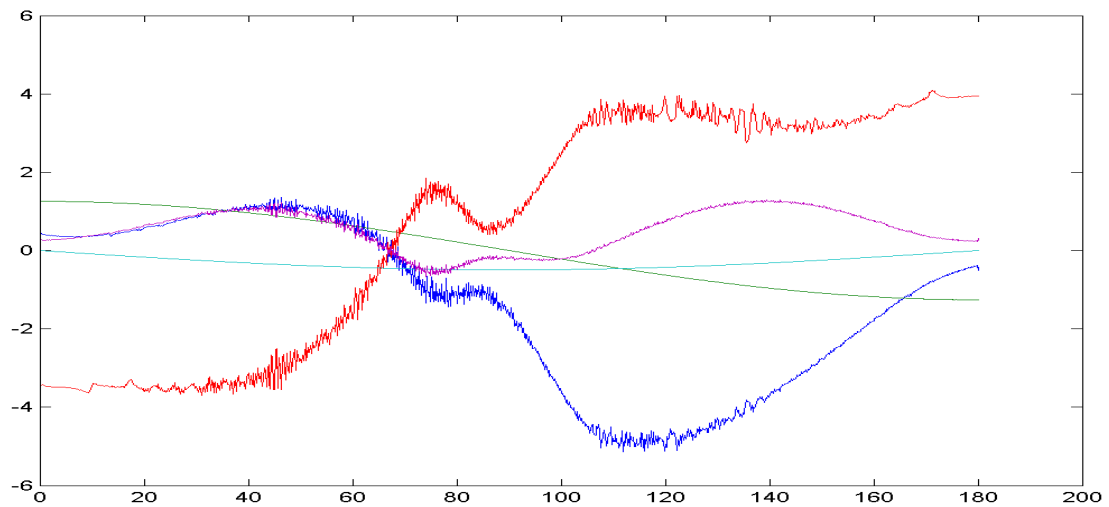
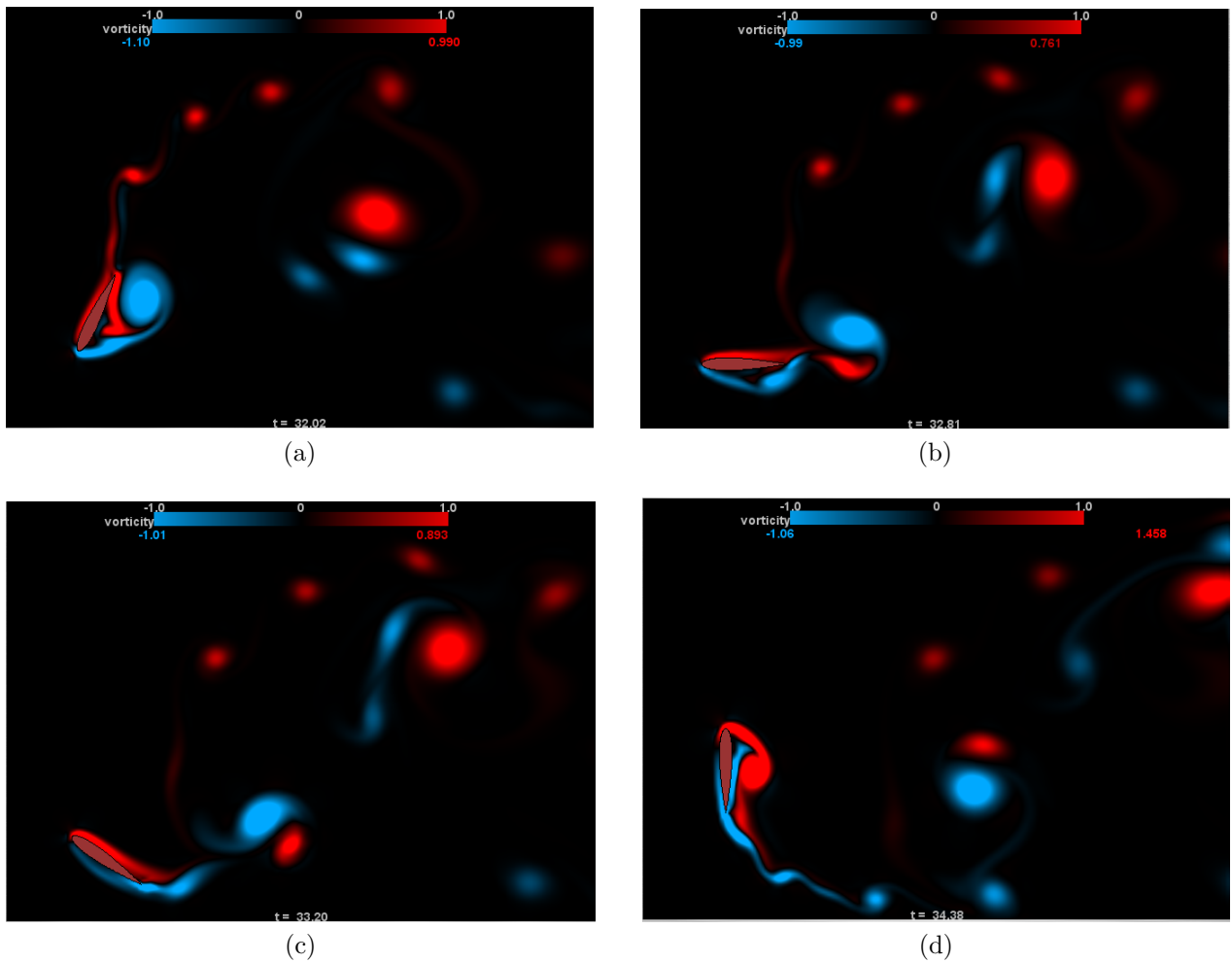


Figure C.85: $h_0/c = 1.25$, $St = 0.4$, $\theta_0 = 90^\circ$

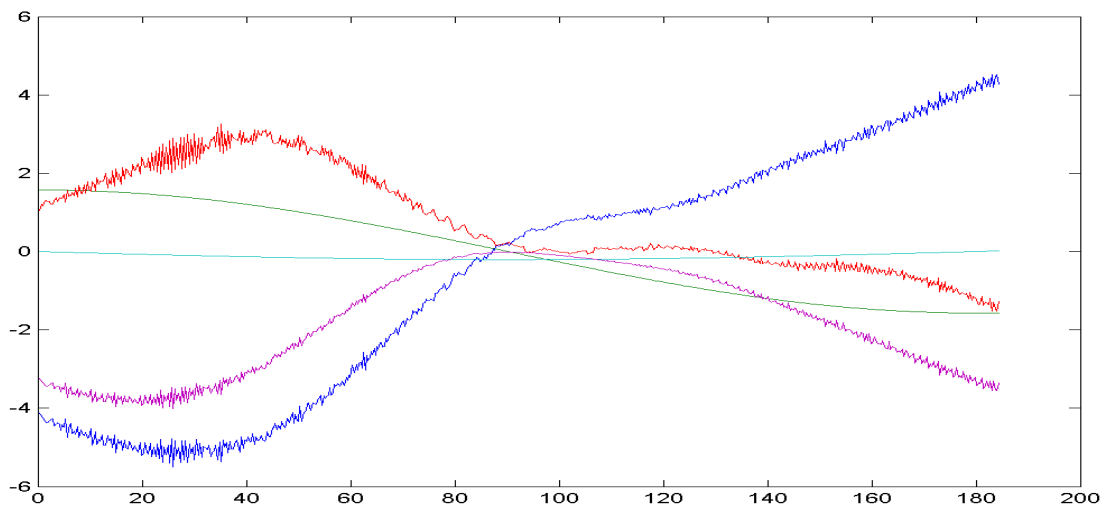
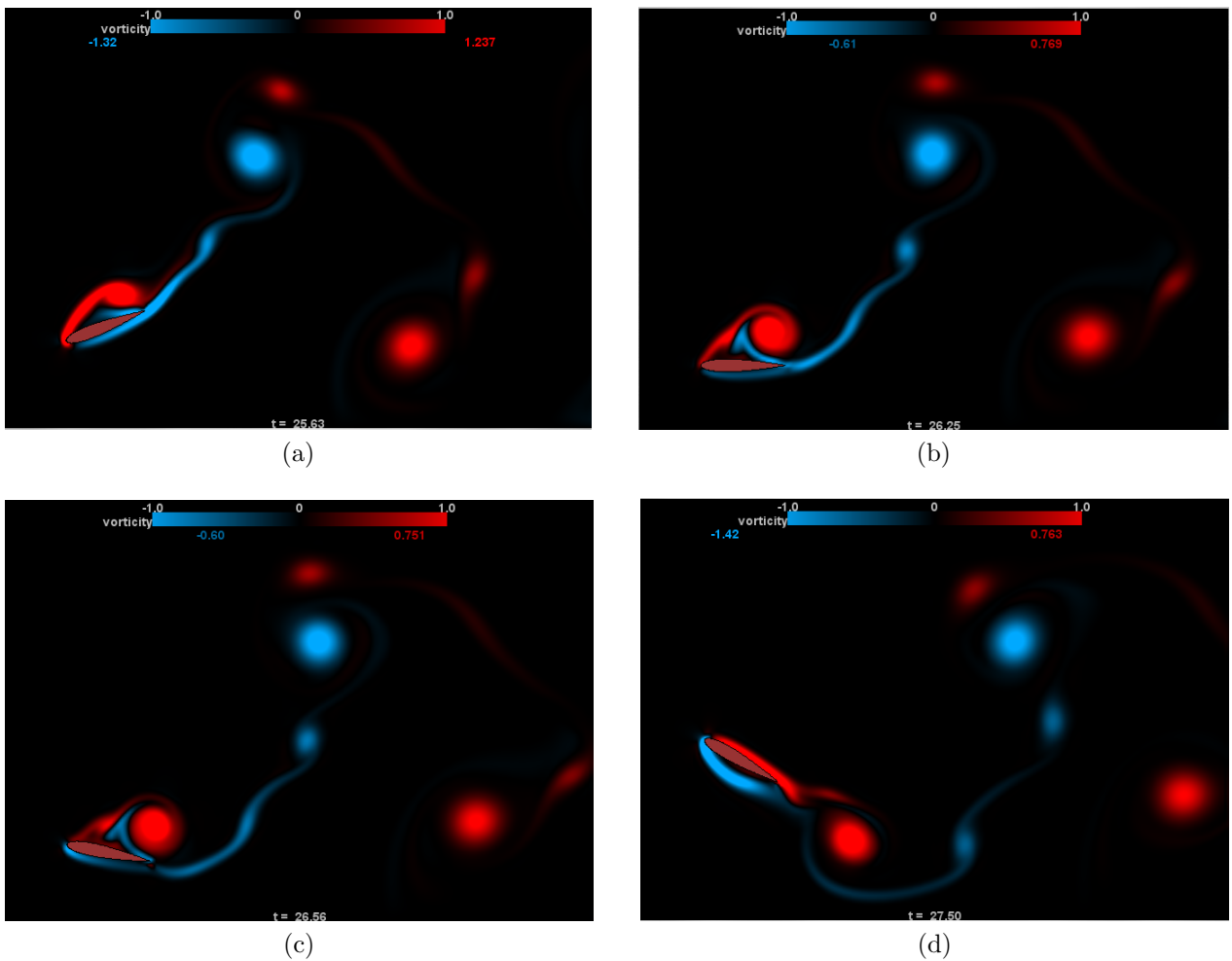


Figure C.86: $h_0/c = 1.25$, $St = 0.5$, $\theta_0 = 30^\circ$

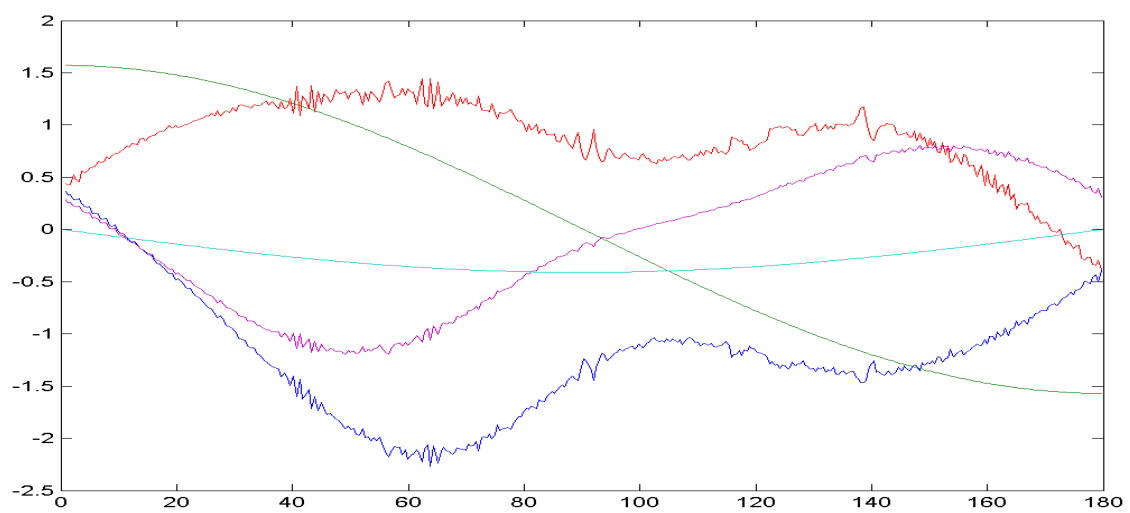
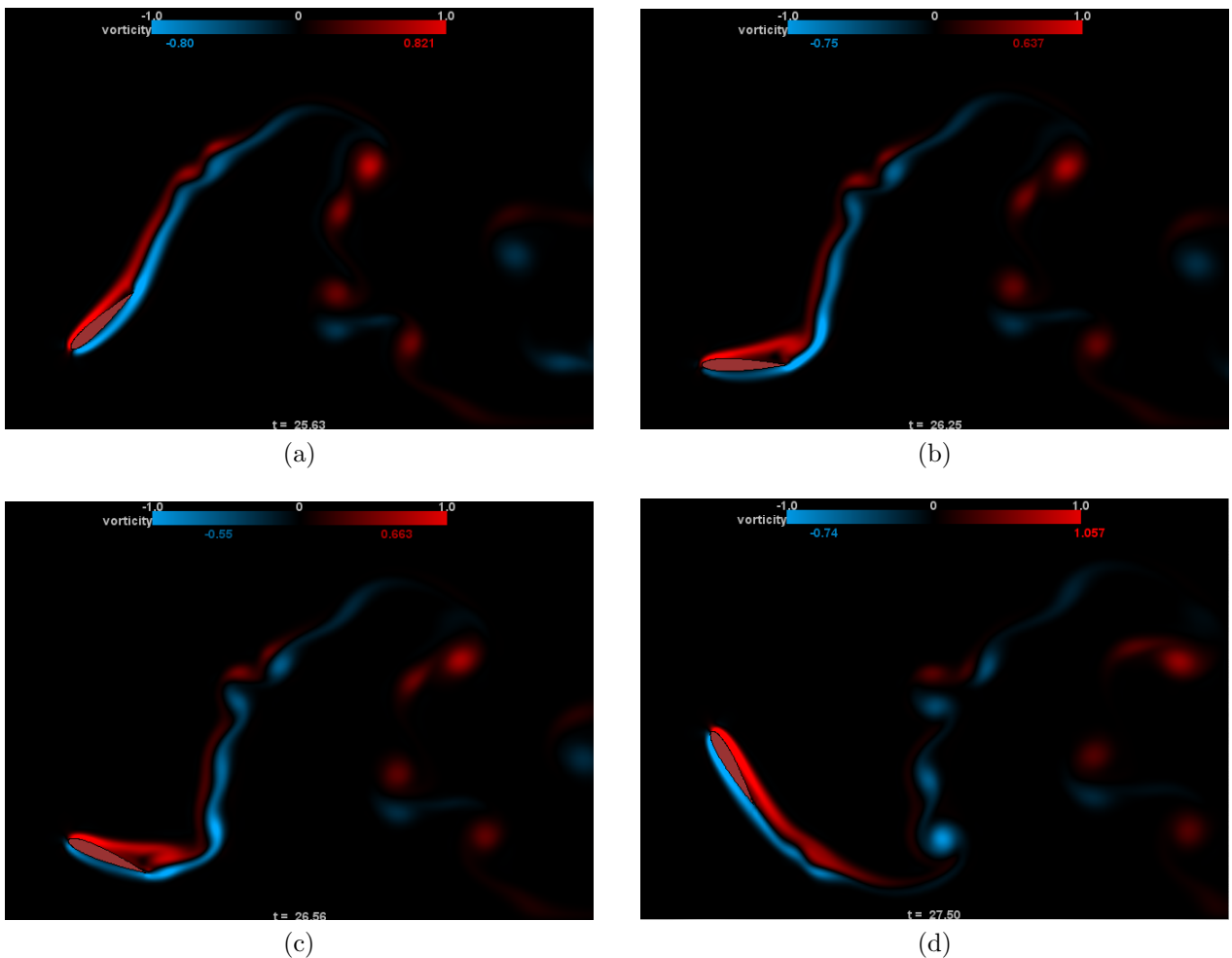


Figure C.87: $h_0/c = 1.25$, $St = 0.5$, $\theta_0 = 60^\circ$

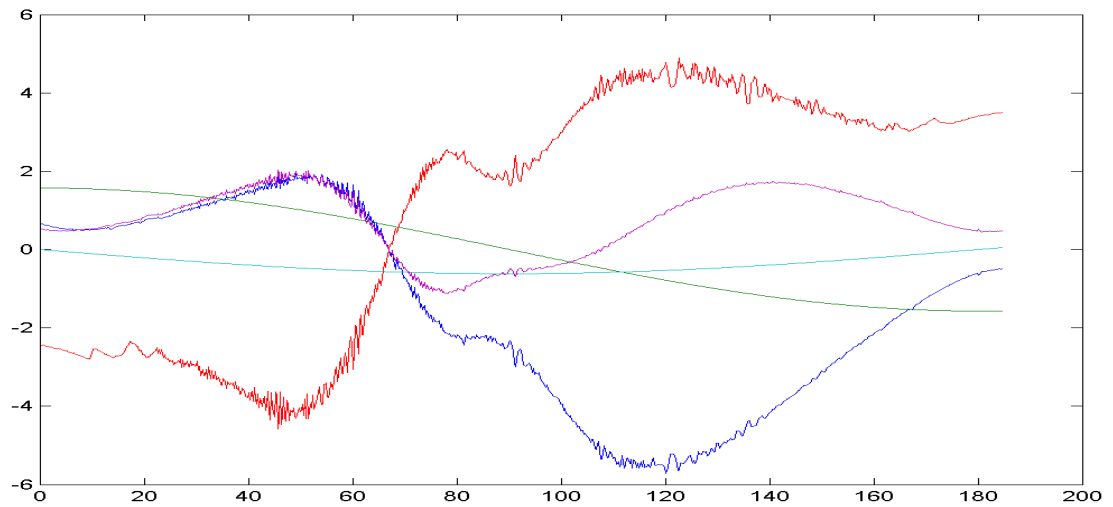
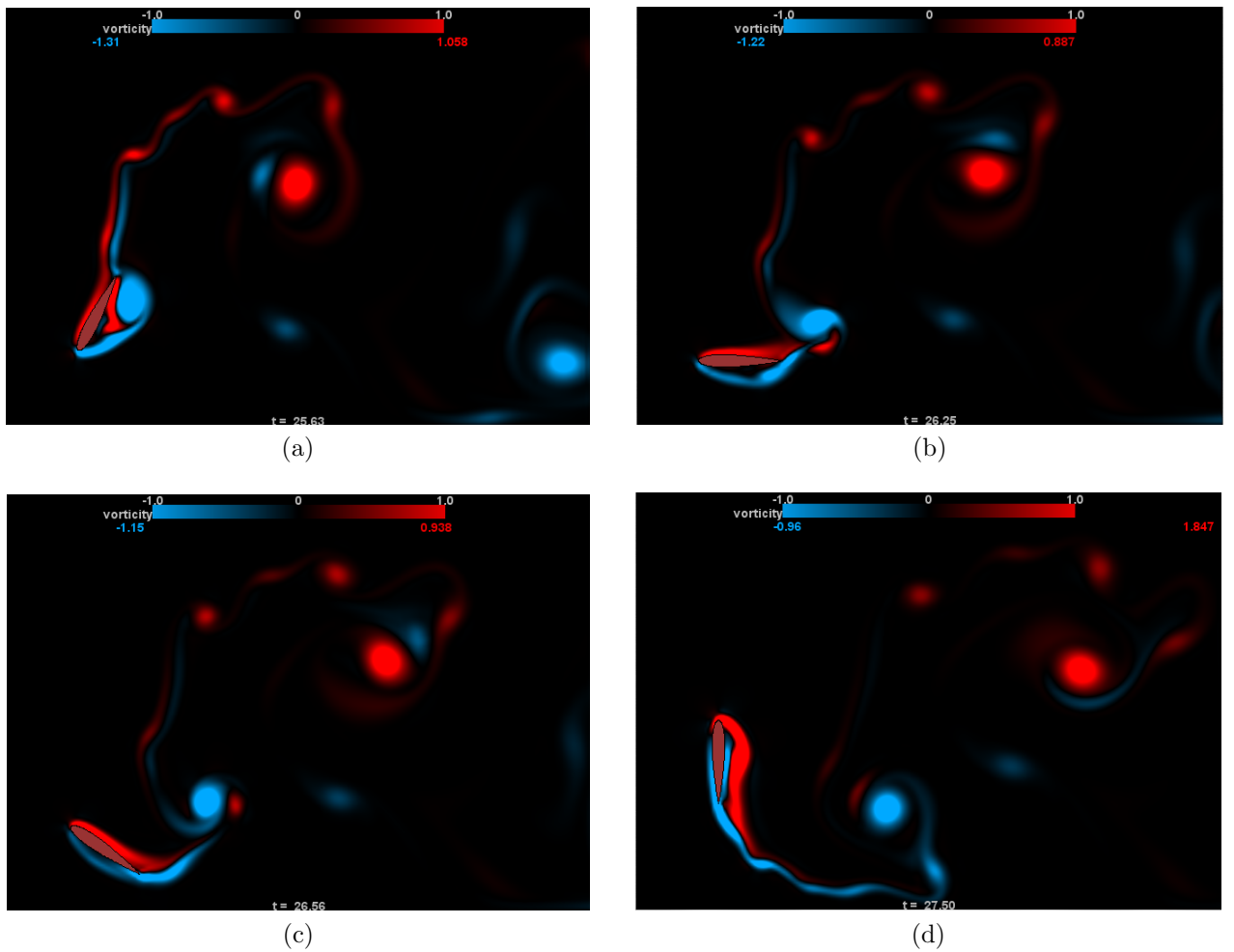


Figure C.88: $h_0/c = 1.25$, $St = 0.5$, $\theta_0 = 90^\circ$

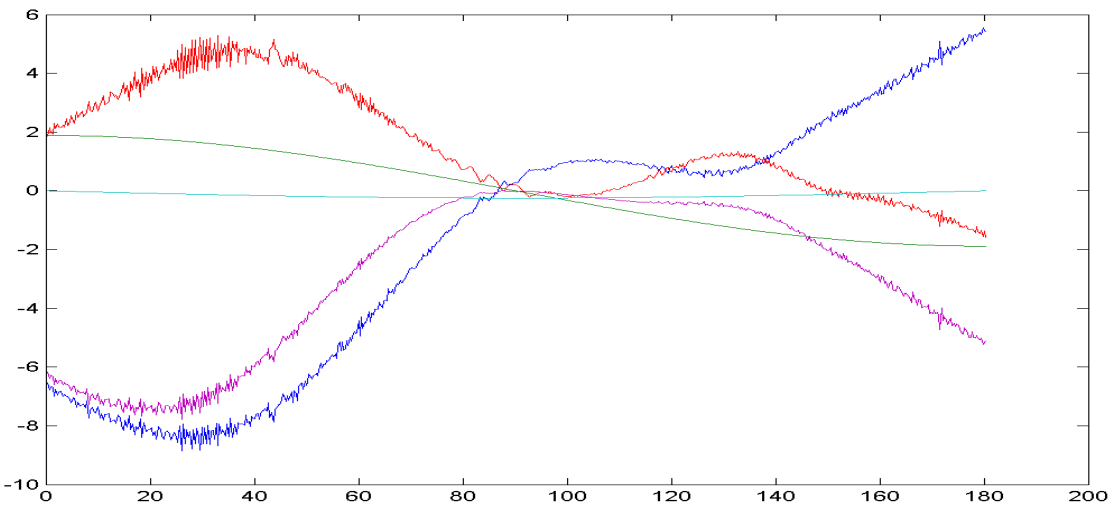
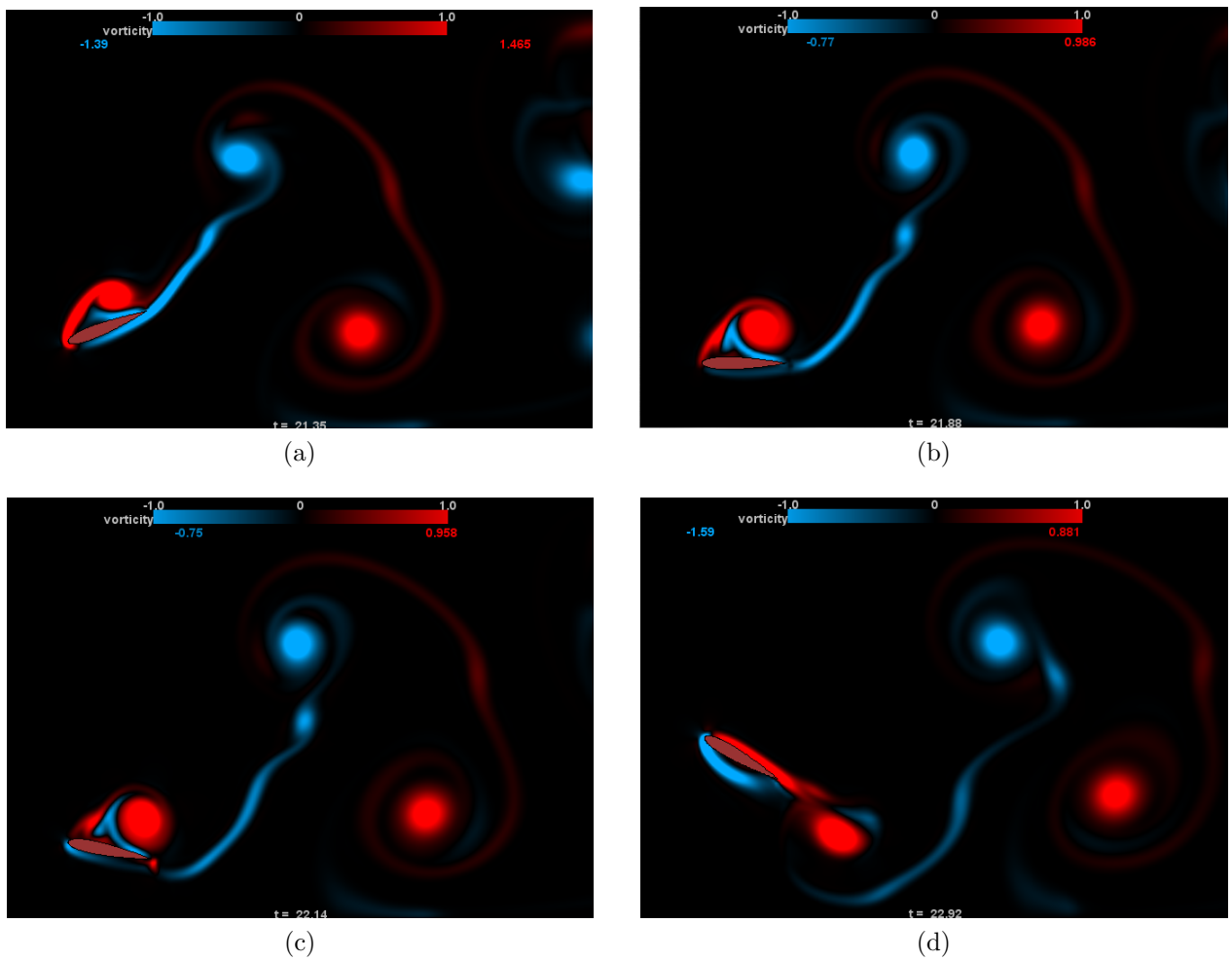


Figure C.89: $h_0/c = 1.25$, $St = 0.6$, $\theta_0 = 30^\circ$

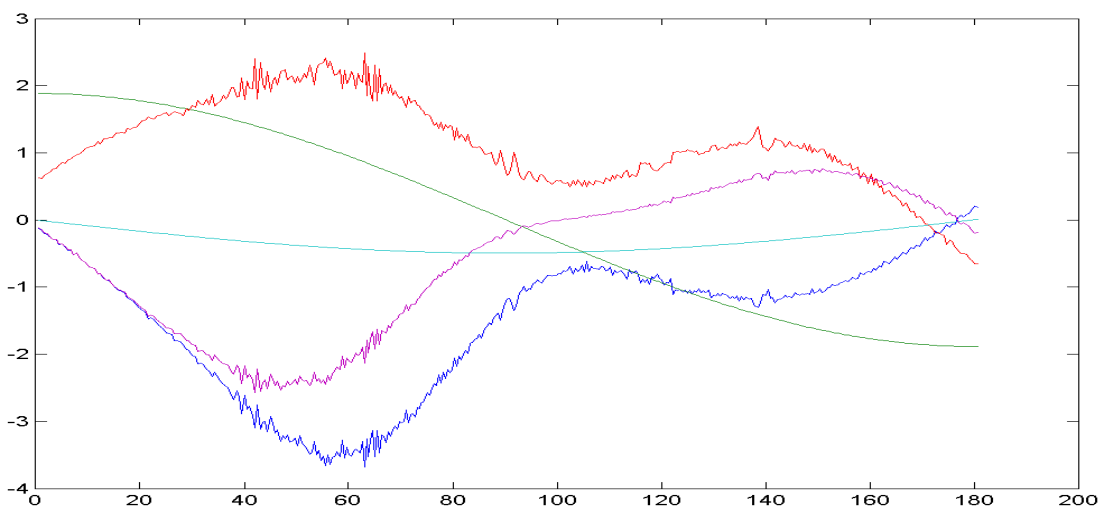
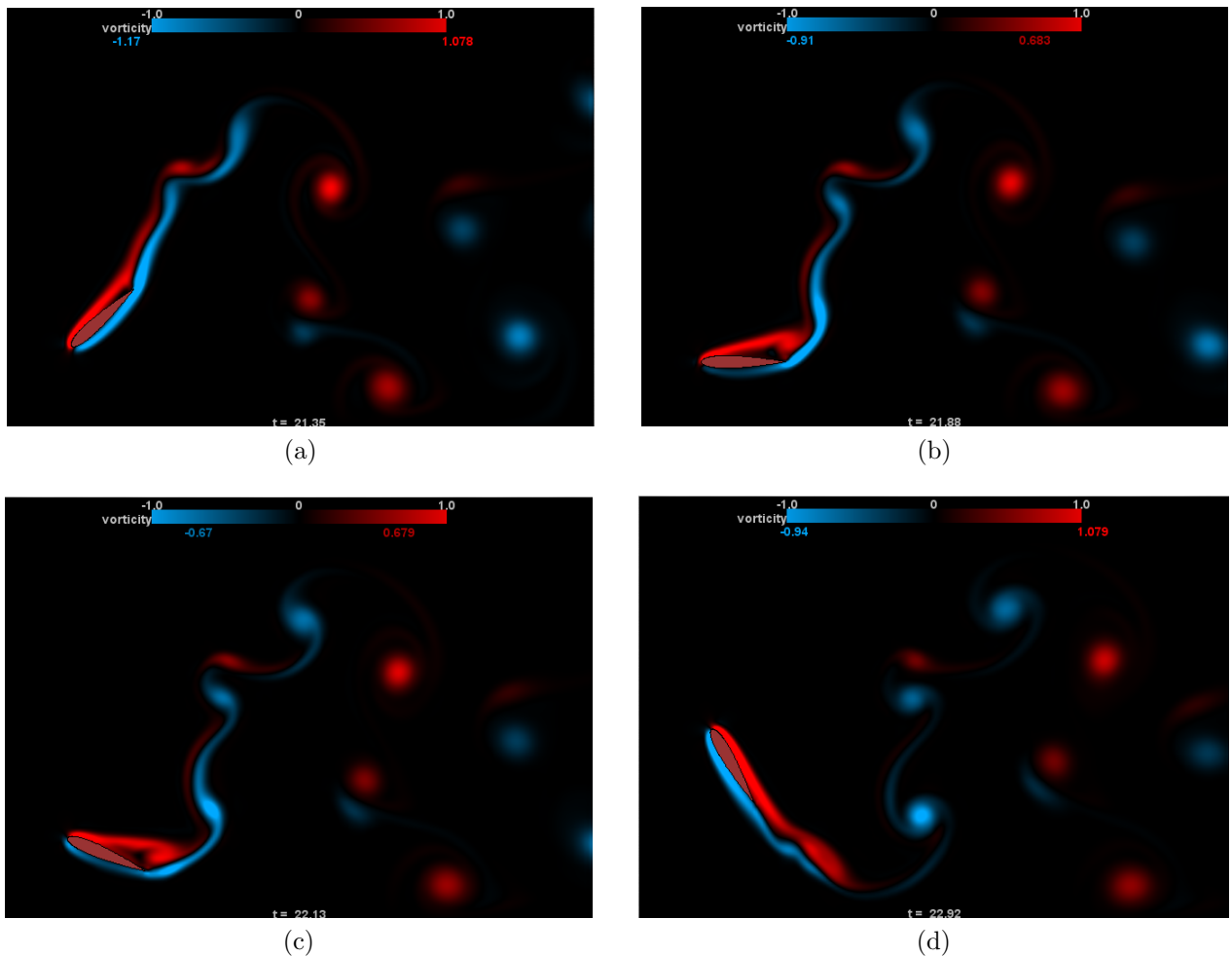


Figure C.90: $h_0/c = 1.25$, $St = 0.6$, $\theta_0 = 60^\circ$

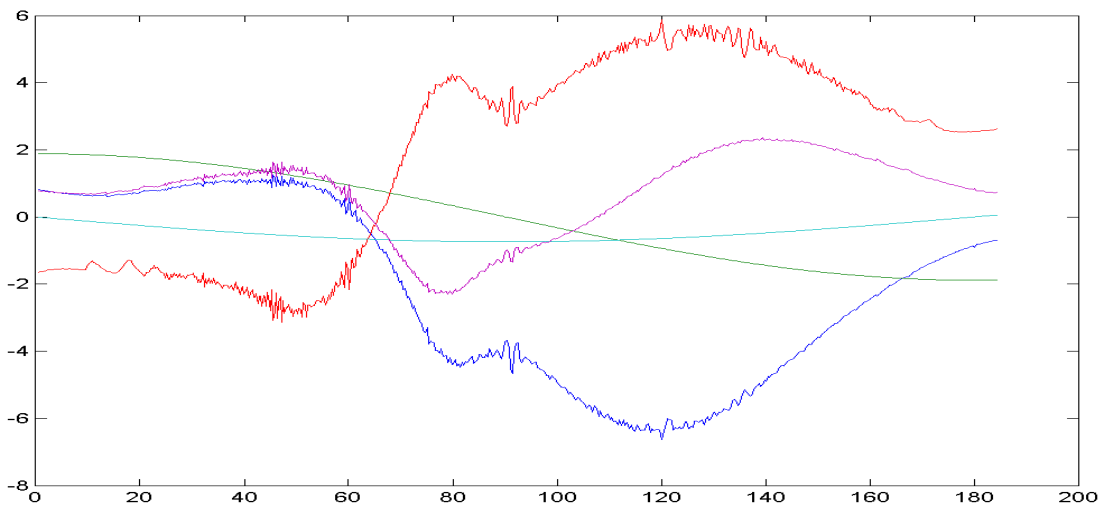
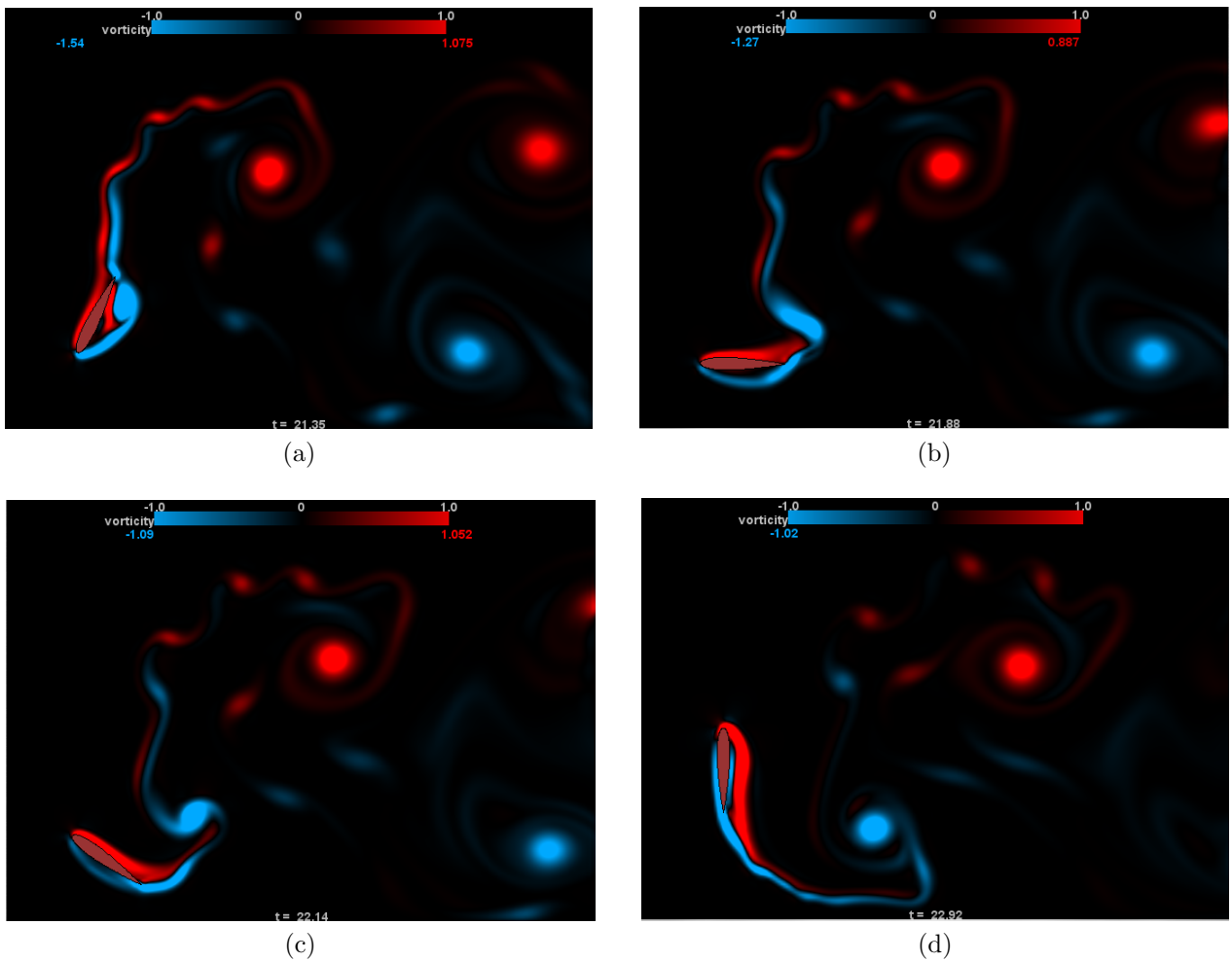


Figure C.91: $h_0/c = 1.25$, $St = 0.6$, $\theta_0 = 90^\circ$

APPENDIX D

Database

A database was created for a parameter space of 140 motion trajectories for easy access and future analysis. Sinusoidal pitch and heave motions were forced and alterations made in heave amplitude normalized by the chord length of the foil (h_0/c), pitch amplitude (θ_0), and Strouhal number (St). The parameter space is represented in Table 1 is copied below. All applicable combinations of this parameter space were simulated based on the ranges depicted in the efficiency plots. If continuing increases in the Strouhal number was leading to large magnitudes of negative efficiency, tests were not continued for that h_0/c as depicted by the "N/A" in the efficiency charts in Appendix A.

Parameter	Values
$\frac{h_0}{c}$	0.5 0.75 1.0 1.25
θ_0	30° 40° 50° 60° 70° 80° 90°
St	0.1 0.2 0.3 0.4 0.5 0.6

Table D.7: Simulation Parameter Space

Included in the database for each simulation are two dimensional pressure fields of the computational grid seen in the screen-shots of the foil and its wake in Appendix C. The pressure fields were binned based on the phase of the sinusoidal motion and averaged over 10 cycles of motion. The resulting pressure field available in the database is a ".mat" file of a three dimensional matrix of the horizontal axis of the grid, the vertical axis of the grid, and each degree of phase shown in a schematic in Figure D.92 below. Similarly formulated three dimensional matrices are also available in the database for the horizontal component of the velocity field and the vertical component of the velocity field.

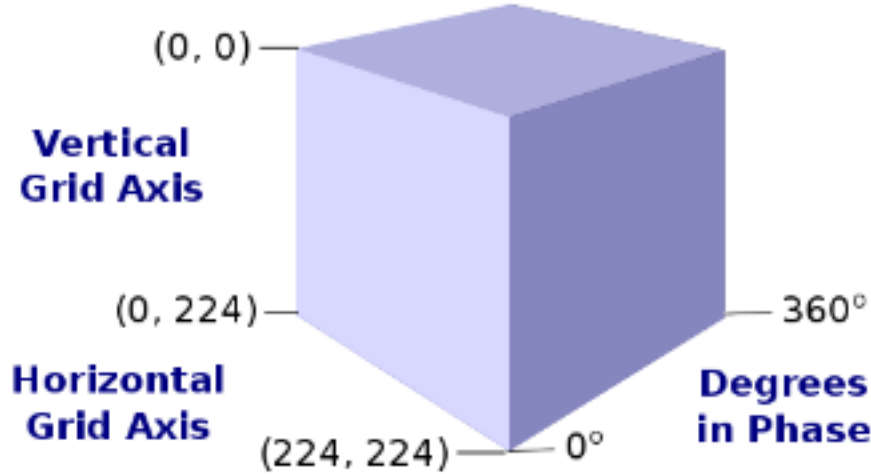


Figure D.92: Matrix format of pressure and velocity fields ".mat" files.

For each simulation, one cycle of motion was recorded in a video in order to see a good visual of the foil's wake pattern. Also, text files were saved including measured/calculated values at each time step for this recorded cycle outlined below in Table D.8

The Database is saved on a 3 Terabyte external hard drive formatted to both MAC OS and Windows software. It includes a "Database" folder and MATLAB ".m" files used in the creation of this thesis. The "Database" folder is the main folder containing four folders for each heave amplitude to chord length ratio. Each h_0/c folder holds separate folders for each St and θ_0 combination. For example these are denoted in the form "St01PS30" where "01" represents $St = 0.1$ and "30" represents $\theta_0 = 30^\circ$. A Representation of the folder set-up is outlined below:

- Database
- HeaveAmp05
- HeaveAmp075

Filenames (.txt)	Description
ForceY	Non-dimensional transverse force pointing from the body to the fluid. Multiply by $(1/2)*\rho*U^2*$ chord to get the coefficient of lift.
HeaveVel	Heave motion divided by time-step
DT	Time step in real time
CycTime	Total real time of overall simulation
AngAccel	Angular (pitch) acceleration
AngVel	Angular (pitch) velocity
FluidMoment	Non-Dimensional fluid moment on the foil based on integrated pressure. Multiply by $(1/2)*\rho*U^2*$ chord to get Coefficient of Moment.
Phase	Degree in phase. Calculated as follows:
Heave	Heave (transverse) motion measured at tail of the foil.
Attack	Angle of Attack calculated from pitch and heave motion using equation in Chapter 2.
Pitch	Pitch angle (degrees)
PressureMeasurements	Pressure measurements at 200 equally spaced locations around the foil starting at the nose and moving around it counter clockwise back to the nose again.
OrthCoordX	X coordinate for each of the 200 Pressure measurements around the foil with respect to the global coordinate system.
OrthCoordY.	Y coordinate for each of the 200 Pressure measurements around the foil with respect to the global coordinate system.
Centroid	X and Y coordinate of the centroid of the foil with respect to the global coordinate system.
SegLengths	Segment lengths that each of the 200 pressure measurements are centered about.
NX	X component of normal stress at each of the pressure measurement locations.
NY	Y component of normal stress at each of the pressure measurement locations.
Foil.mov (not .txt)	Movie of the foil motion and vorticity of the fluid over the sixth cycle.

Table D.8: Text files store extracted data for every timestep in the sixth cycle of motion.

- HeaveAmp1
- HeaveAmp125
 - St01PA30
 -
 - St06PA90

APPENDIX E

Laboratory Set-up

Listed below is the MATLAB file written to create the motion programs in the PMAC software format. Following the MATLAB code is an example of one of the sinusoidal motion programs for running the motors.

E.1 MATLAB Motion Program Writer

```
% Commands to Start file in Pewin
fprintf(fid,'CLOSE\n');
fprintf(fid,'END GATHER\n');
fprintf(fid,'DELETE GATHER\n');
fprintf(fid,'DELETE TRACE\n\n');

% Write the header with program information

fprintf(fid,'//*****\n');
fprintf(fid,'// prog 1 Homing Routine\n');

% Write the homing program routine

fprintf(fid,'\n\n//Homing Routine\n');
fprintf(fid,'open prog1\n');
fprintf(fid,'clear\n');
fprintf(fid,'// Homing Y-axis\n');
fprintf(fid,'I124=$020001      //reset I variable to turn off ...
    end limit disable just for homing\n');
fprintf(fid,'ta 25\n');
fprintf(fid,'ts 25\n');
```

```

fprintf(fid,'f 10\n');
fprintf(fid,'inc\n');
fprintf(fid,'While (m121 = 0)\n');    % Positive End Limit bit
fprintf(fid,'y +5\n');
fprintf(fid,'EndWhile\n');
fprintf(fid,'dwell 0\n');
fprintf(fid,'HOMEZ1\n');
fprintf(fid,'dwell 200\n');
fprintf(fid,'f 10\n');
fprintf(fid,'While (m120=1)      //While the home limit is not ...
           triggered\n');
fprintf(fid,'y - 4\n');
fprintf(fid,'EndWhile\n');
fprintf(fid,'dwell 0\n');
fprintf(fid,'HOMEZ1\n');
fprintf(fid,'I124=$000001      //reset I variable to trigger end ...
           limits\n');
fprintf(fid,'close\n\n');

fprintf(fid,'open prog2\n');
fprintf(fid,'clear\n');
fprintf(fid,' //Homing z-axis\n');
fprintf(fid,'I224=$020001\n');
fprintf(fid,'ta 25          // set acc time to 25 ms\n');
fprintf(fid,'ts 25          // set s-curve time to 25 ms\n');
fprintf(fid,'f 0.5          // set feed-rate to 0.5 ...
           units/s\n');
fprintf(fid,'inc          // incremental mode\n');
fprintf(fid,'dwell 0      // do not blend into next move\n');
fprintf(fid,'While (m220 = 0)\n');
fprintf(fid,' z + 0.001  \n');
fprintf(fid,' dwell 20  \n');

```

```

fprintf(fid, 'If (m262 !< -13000)\n');
fprintf(fid, 'While (m220 = 0)\n');
fprintf(fid, ' z - 0.001\n');
fprintf(fid, ' dwell 20 \n');
fprintf(fid, ' EndWhile \n');
fprintf(fid, ' EndIf \n');
fprintf(fid, ' EndWhile \n');
fprintf(fid, ' dwell 0 \n');
fprintf(fid,'HOMEZ2           // set encoder position to 0\n');
fprintf(fid,'I224=$000001\n');
fprintf(fid,'close\n\n');

fprintf(fid,'open prog3\n');
fprintf(fid,'clear\n');
fprintf(fid,'// Homing U-axis\n');
fprintf(fid,'I324=$020001\n');
fprintf(fid,'ta 500           // set acc time to 500 ms\n');
fprintf(fid,'ts 500           // set s-curve time to 500 ...
ms\n'); %this will determine your Jerk.
fprintf(fid,'f 0.05          // set feedrate to 1 ...
units/s\n'); %velocity in unit system defined for that ...
axis (mm/s)

fprintf(fid,'inc           // incremental mode\n');
fprintf(fid,'While (m322 = 0) // While Negative End Limit not ...
triggered\n'); %Negative End Limit bit
fprintf(fid,'u -15           // move U-axis specified distance\n');
fprintf(fid,'EndWhile\n');
fprintf(fid,'dwell 0           // do not blend into next ...
move\n');
fprintf(fid,'HOMEZ3           // set encoder position to ...
0\n'); %Move to limit switch and call that home.
fprintf(fid,'dwell 200         // wait 200 ms\n');

```

```

fprintf(fid,'f 0.05\n');
fprintf(fid,'u+100\n');
fprintf(fid,'dwell 0\n');
fprintf(fid,'HOMEZ3\n');
fprintf(fid,'I324=$000001\n');
fprintf(fid,'close\n\n');

fprintf(fid,'open prog4\n');
fprintf(fid,'clear\n');
fprintf(fid,'// Homing X-axis\n');
fprintf(fid,'I424=$020001      //reset I variable to turn off ...
    end limit disable just for homing\n');
fprintf(fid,'ta 25                  // set acc time to 25 ms\n');
fprintf(fid,'ts 25                  // set s-curve time to 25 ...
    ms\n');
fprintf(fid,'f 1                      // set feedrate to 1 ...
    units/s\n');
fprintf(fid,'inc                     // incremental mode\n');
fprintf(fid,'While (m421 = 0)    // Positive End Limit Bit\n'); ...
    % Positive End Limit bit
fprintf(fid,'x +5                  // move X-axis specified ...
    distance\n');           % While we are not at the limit switch, ...
    move axis
fprintf(fid,'EndWhile\n');
fprintf(fid,'dwell 0                  // do not blend into next ...
    move\n');
fprintf(fid,'HOMEZ4                  // set encoder position to 0\n');
fprintf(fid,'dwell 200                 // wait 200 ms\n');
fprintf(fid,'f 1                      // set feed-rate to 1\n');
fprintf(fid,'While (m420=1)    //While the home limit is not ...
    triggered\n');

```

```

fprintf(fid,'x -10                                // move 10 mm towards ...
Home\n');

fprintf(fid,'EndWhile\n');

fprintf(fid,'dwell 0                           // do not blend into next ...
move\n');

fprintf(fid,'HOMEZ4                         // set encoder position to ...
0\n'); %call this Home

fprintf(fid,'I424=$000001           //reset I variable to trigger ...
end limits\n');

fprintf(fid,'close\n\n\n');

counter=4; %labels each program a different program#
%U=0.3;          % m/s
U=300;           %mm/s

%chord = 0.0698;    %meters = 2.75 inches = 69.85 mm
chord = 69.85; %mm
psi = pi/2;

St = [0.15 0.2 0.3 0.4 0.5 0.6]; %Strouhal from 0.1 to 0.6 in ...
increments of 0.1

HeaveToChord = [0.5:0.25:1.25]; %heave to chord
H0 = HeaveToChord.*chord; %heave amplitude
theta0 = [30:10:90]; %pitch amp in degrees
theta0r = theta0*pi/180; %pitch amp in radians

%lengthTank = 3.6576; %length of tank 14 ft = 4.2m (input 12 ft ...
= 3.6576m)

lengthTank = 2500; % mm (towing length)
tRun = lengthTank/U; %time of run in seconds

```

```

%%%%%%%%%%%%%
%%%%%%%%%%%%%
for ha = H0(4)
for st = St(6)           %Change this by +1 when you change ...
the filename!!!!
for theta = theta0r

counter=counter+1; %start with prog5 (prog1 – prog4 is ...
homing)

num_points=200;          %number of timesteps

f = (st*U) / (2*ha);
T = 1/f;
Tms = T*1000;           %period in milliseconds
w=2*pi*f;

%*****
numloops = floor(tRun/T); % round(2/T); % + 2;      %(2/T) ...
is for the 2 second startup at beginning when motion ...
is not actually happening
timestep=(Tms/num_points);

t=0:timestep/1000:(T-(timestep/1000)); %time is in s

time_step=timestep; %time step is in ms

endtime=T*numloops;
towlength=U*endtime;

```

```

%*****%

```

```

hy = ha*sin(w.*t);
hyv = ha*w*cos(w.*t);
M = mean(hy);
HY = hy-M;

%Defining motions for all motors
yy = HY;      %Heave Motion
vy = hyv;      %Heave Velocity
y=diff(yy);   % Incremental heave motion

x=0;           %No Inline motion right now
vx=0;

ZZ = -theta.*sin(w.*t+psi);      %pitch motion (negative ...
                                because pitch direction was defined in CME oppositely)
vZ = -theta.*w.*cos(w.*t+psi);  %Angular velocity of the ...
                                z-axis
z=diff(ZZ);                  %Incremental pitch motion

uu=U.*t;                      %Tow position motion
vu=U.*ones(1,length(t));     %Tow Velocity
u=diff(uu);                  %Incremental Tow Motion

%%%%%
lead_in_time = 2;
twist_start_position = Z(1);
twist_lead_in_velocity = vZ(1); %radians / second

```

```

twist_lead_in_acceleration = ...

twist_lead_in_velocity/lead_in_time;

twist_lead_in_position = twist_start_position - 0.5 * ...
twist_lead_in_acceleration * lead_in_time ^ 2;

fprintf(fid,'//*****\n');
fprintf(fid,'open prog%2.0f\n',counter);
fprintf(fid,'clear\n');

% fprintf(fid,'I0315=32\n');      %abort/limit ...
deceleration rate

% fprintf(fid,'I0415=32\n');

% fprintf(fid,'I0115=32\n');

fprintf(fid,'linear           // set to linear ...'

positioning mode\n');

fprintf(fid,'abs           // absolute positioning ...'

mode\n');

fprintf(fid,'//Attention!!! Following points must be same ...'

as starting points of motion loop\n');

%fprintf(fid,'dwell 0\n\n');

fprintf(fid,'PVT %5.3f\n',lead_in_time*1000);

fprintf(fid,'    Z    %7.5f   :   %7.5f   Y    %7.5f   :   ...'

%7.5f   U    %7.5f   :   %7.5f ...'

\n',ZZ(1),0,YY(1),0,UU(1),0); % zeros for zero ...

velocities....15 instead of u(1) so we are beyond the ...

limit switch

fprintf(fid,'dwell 3000\n');

fprintf(fid,'p%li=%2.0f\n',2,numloops);

fprintf(fid,'PVT %5.3f\n',time_step);

fprintf(fid,'inc\n');

%fprintf(fid,'TM %5.3f\n', time_step/30);

%fprintf(fid,'TS %5.3f\n', time_step/25);

```

```

fprintf(fid,'cmd"endgather"\n');           %This ...
    Ends previous gathering

fprintf(fid,'cmd"delete gather"\n');
fprintf(fid,'cmd"define gather"\n');
fprintf(fid,'cmd"gather"\n');

fprintf(fid,'m7147 = 1\n');                %Data trigger: Used ...
    to line up time data with DAQ

fprintf(fid,'While (p%li>0)\n',2);      %p is a index for ...
    counting how many cycles of motion occurred. Begins at ...
    "numloops" and decreases by one every cycle

fprintf(fid,'    p%li=p%li-1\n',2,2);
fprintf(fid,'    // Attention!!! Last point must differ ...
    from first point!!!\n');

for j = 1:(length(t)-1)
    fprintf(fid,'Z    %7.5f    :    %7.5f    Y    %7.5f    :    ...
    %7.5f U    %7.5f    :    ...
    %7.5f\n',z(j),vz(j),y(j),vy(j),u(j),vu(j));
end

%     for j = 1:length(t)
%         fprintf(fid,'Z    %7.5f    :    %7.5f    Y    %7.5f    : ...
%    %7.5f    U+    %7.5f    :    %7.5f ...
%    \n',z(j),vz(j),y(j),vy(j),4.4,vu(j));
%
%     end

fprintf(fid,'EndWhile\n');

fprintf(fid,'dwell 5000\n');

fprintf(fid,'cmd"endgather"\n');  % end gathering of data

fprintf(fid,'m7147 = 0\n');        % turn off the bit ...
    indicating the motors are in motion

fprintf(fid,'ta 12000             // set acc time to 500 ...
    ms\n');

```

```

fprintf(fid,'ts 1000           // set s-curve time to ...
500 ms\n');
fprintf(fid,'f 0.5            // set feedrate to 1 ...
units/s\n');
fprintf(fid,'linear          // linear mode\n');
fprintf(fid,'abs              // absolute mode\n');
fprintf(fid,'dwell 0\n');
fprintf(fid,'z 0\n',theta); %Brings foil back to 0-degree ...
position before tow back
fprintf(fid,'dwell 0\n');
fprintf(fid,'inc             // incremental mode\n');
fprintf(fid,'U -%5.3f\n',towlength); %Incrementally ...
tow tank back to 0 position
fprintf(fid,'close\n\n\n');

end
end
fclose(fid); %Stop writing the programs

```

E.2 Example Motion Program

```
//*****  
open prog 5  
clear  
linear           // set to linear positioning mode  
abs              // absolute positioning mode  
//Attention!!! Following points must be same as starting points ...  
of motion loop  
PVT 2000.000  
Z   -0.52360   :   0.00000   Y   0.00000   :   0.00000   U   ...  
          0.00000   :   0.00000  
dwell 3000  
p2= 8  
PVT 4.851  
inc  
cmd"endgather"  
cmd"delete gather"  
cmd"define gather"  
cmd"gather"  
m7147 = 1  
While (p2>0)  
    p2=p2-1  
    // Attention!!! Last point must differ from first point!!!  
    Z   0.00026   :   -0.00000   Y   2.74255   :   565.48668 U   ...  
          1.45521   :   300.00000  
    Z   0.00077   :   0.10652   Y   2.73985   :   565.20764 U   ...  
          1.45521   :   300.00000  
    Z   0.00129   :   0.21293   Y   2.73443   :   564.37082 U   ...  
          1.45521   :   300.00000
```

Z	0.00180	:	0.31913	Y	2.72633	:	562.97703	U	...
	1.45521	:	300.00000						
Z	0.00232	:	0.42502	Y	2.71553	:	561.02765	U	...
	1.45521	:	300.00000						
Z	0.00283	:	0.53049	Y	2.70205	:	558.52460	U	...
	1.45521	:	300.00000						
Z	0.00334	:	0.63543	Y	2.68590	:	555.47035	U	...
	1.45521	:	300.00000						
Z	0.00384	:	0.73975	Y	2.66710	:	551.86793	U	...
	1.45521	:	300.00000						
Z	0.00434	:	0.84334	Y	2.64568	:	547.72087	U	...
	1.45521	:	300.00000						
Z	0.00484	:	0.94610	Y	2.62164	:	543.03329	U	...
	1.45521	:	300.00000						
Z	0.00533	:	1.04792	Y	2.59501	:	537.80979	U	...
	1.45521	:	300.00000						
Z	0.00581	:	1.14870	Y	2.56582	:	532.05554	U	...
	1.45521	:	300.00000						
Z	0.00629	:	1.24836	Y	2.53410	:	525.77622	U	...
	1.45521	:	300.00000						
Z	0.00677	:	1.34678	Y	2.49988	:	518.97801	U	...
	1.45521	:	300.00000						
Z	0.00724	:	1.44387	Y	2.46319	:	511.66764	U	...
	1.45521	:	300.00000						
Z	0.00770	:	1.53954	Y	2.42407	:	503.85232	U	...
	1.45521	:	300.00000						
Z	0.00815	:	1.63369	Y	2.38256	:	495.53975	U	...
	1.45521	:	300.00000						
Z	0.00859	:	1.72623	Y	2.33870	:	486.73815	U	...
	1.45521	:	300.00000						
Z	0.00903	:	1.81706	Y	2.29253	:	477.45619	U	...
	1.45521	:	300.00000						

Z	0.00946	:	1.90610	Y	2.24409	:	467.70305	U	...
	1.45521	:	300.00000						
Z	0.00988	:	1.99326	Y	2.19345	:	457.48833	U	...
	1.45521	:	300.00000						
Z	0.01028	:	2.07845	Y	2.14063	:	446.82213	U	...
	1.45521	:	300.00000						
Z	0.01068	:	2.16159	Y	2.08571	:	435.71497	U	...
	1.45521	:	300.00000						
Z	0.01107	:	2.24260	Y	2.02873	:	424.17782	U	...
	1.45521	:	300.00000						
Z	0.01145	:	2.32139	Y	1.96974	:	412.22205	U	...
	1.45521	:	300.00000						
Z	0.01181	:	2.39789	Y	1.90881	:	399.85946	U	...
	1.45521	:	300.00000						
Z	0.01217	:	2.47203	Y	1.84600	:	387.10227	U	...
	1.45521	:	300.00000						
Z	0.01251	:	2.54372	Y	1.78136	:	373.96305	U	...
	1.45521	:	300.00000						
Z	0.01284	:	2.61291	Y	1.71497	:	360.45477	U	...
	1.45521	:	300.00000						
Z	0.01315	:	2.67952	Y	1.64689	:	346.59077	U	...
	1.45521	:	300.00000						
Z	0.01346	:	2.74348	Y	1.57718	:	332.38473	U	...
	1.45521	:	300.00000						
Z	0.01375	:	2.80474	Y	1.50591	:	317.85066	U	...
	1.45521	:	300.00000						
Z	0.01402	:	2.86323	Y	1.43316	:	303.00291	U	...
	1.45521	:	300.00000						
Z	0.01429	:	2.91889	Y	1.35899	:	287.85614	U	...
	1.45521	:	300.00000						
Z	0.01454	:	2.97167	Y	1.28348	:	272.42528	U	...
	1.45521	:	300.00000						

Z	0.01477	:	3.02152	Y	1.20670	:	256.72558	U	...
	1.45521	:	300.00000						
Z	0.01499	:	3.06839	Y	1.12874	:	240.77252	U	...
	1.45521	:	300.00000						
Z	0.01520	:	3.11223	Y	1.04966	:	224.58184	U	...
	1.45521	:	300.00000						
Z	0.01539	:	3.15299	Y	0.96954	:	208.16953	U	...
	1.45521	:	300.00000						
Z	0.01556	:	3.19065	Y	0.88847	:	191.55178	U	...
	1.45521	:	300.00000						
Z	0.01572	:	3.22516	Y	0.80652	:	174.74499	U	...
	1.45521	:	300.00000						
Z	0.01587	:	3.25648	Y	0.72377	:	157.76575	U	...
	1.45521	:	300.00000						
Z	0.01599	:	3.28459	Y	0.64032	:	140.63082	U	...
	1.45521	:	300.00000						
Z	0.01611	:	3.30946	Y	0.55622	:	123.35710	U	...
	1.45521	:	300.00000						
Z	0.01620	:	3.33106	Y	0.47158	:	105.96164	U	...
	1.45521	:	300.00000						
Z	0.01628	:	3.34938	Y	0.38648	:	88.46161	U	1.45521 ...
		:	300.00000						
Z	0.01635	:	3.36439	Y	0.30099	:	70.87427	U	1.45521 ...
		:	300.00000						
Z	0.01640	:	3.37608	Y	0.21520	:	53.21700	U	1.45521 ...
		:	300.00000						
Z	0.01643	:	3.38444	Y	0.12921	:	35.50720	U	1.45521 ...
		:	300.00000						
Z	0.01645	:	3.38946	Y	0.04308	:	17.76237	U	1.45521 ...
		:	300.00000						
Z	0.01645	:	3.39113	Y	-0.04308	:	-0.00000	U	...
	1.45521	:	300.00000						

Z	0.01643	:	3.38946	Y	-0.12921	:	-17.76237	U	...
	1.45521	:	300.00000						
Z	0.01640	:	3.38444	Y	-0.21520	:	-35.50720	U	...
	1.45521	:	300.00000						
Z	0.01635	:	3.37608	Y	-0.30099	:	-53.21700	U	...
	1.45521	:	300.00000						
Z	0.01628	:	3.36439	Y	-0.38648	:	-70.87427	U	...
	1.45521	:	300.00000						
Z	0.01620	:	3.34938	Y	-0.47158	:	-88.46161	U	...
	1.45521	:	300.00000						
Z	0.01611	:	3.33106	Y	-0.55622	:	-105.96164	U	...
	1.45521	:	300.00000						
Z	0.01599	:	3.30946	Y	-0.64032	:	-123.35710	U	...
	1.45521	:	300.00000						
Z	0.01587	:	3.28459	Y	-0.72377	:	-140.63082	U	...
	1.45521	:	300.00000						
Z	0.01572	:	3.25648	Y	-0.80652	:	-157.76575	U	...
	1.45521	:	300.00000						
Z	0.01556	:	3.22516	Y	-0.88847	:	-174.74499	U	...
	1.45521	:	300.00000						
Z	0.01539	:	3.19065	Y	-0.96954	:	-191.55178	U	...
	1.45521	:	300.00000						
Z	0.01520	:	3.15299	Y	-1.04966	:	-208.16953	U	...
	1.45521	:	300.00000						
Z	0.01499	:	3.11223	Y	-1.12874	:	-224.58184	U	...
	1.45521	:	300.00000						
Z	0.01477	:	3.06839	Y	-1.20670	:	-240.77252	U	...
	1.45521	:	300.00000						
Z	0.01454	:	3.02152	Y	-1.28348	:	-256.72558	U	...
	1.45521	:	300.00000						
Z	0.01429	:	2.97167	Y	-1.35899	:	-272.42528	U	...
	1.45521	:	300.00000						

Z	0.01402	:	2.91889	Y	-1.43316	:	-287.85614	U	...
	1.45521	:	300.00000						
Z	0.01375	:	2.86323	Y	-1.50591	:	-303.00291	U	...
	1.45521	:	300.00000						
Z	0.01346	:	2.80474	Y	-1.57718	:	-317.85066	U	...
	1.45521	:	300.00000						
Z	0.01315	:	2.74348	Y	-1.64689	:	-332.38473	U	...
	1.45521	:	300.00000						
Z	0.01284	:	2.67952	Y	-1.71497	:	-346.59077	U	...
	1.45521	:	300.00000						
Z	0.01251	:	2.61291	Y	-1.78136	:	-360.45477	U	...
	1.45521	:	300.00000						
Z	0.01217	:	2.54372	Y	-1.84600	:	-373.96305	U	...
	1.45521	:	300.00000						
Z	0.01181	:	2.47203	Y	-1.90881	:	-387.10227	U	...
	1.45521	:	300.00000						
Z	0.01145	:	2.39789	Y	-1.96974	:	-399.85946	U	...
	1.45521	:	300.00000						
Z	0.01107	:	2.32139	Y	-2.02873	:	-412.22205	U	...
	1.45521	:	300.00000						
Z	0.01068	:	2.24260	Y	-2.08571	:	-424.17782	U	...
	1.45521	:	300.00000						
Z	0.01028	:	2.16159	Y	-2.14063	:	-435.71497	U	...
	1.45521	:	300.00000						
Z	0.00988	:	2.07845	Y	-2.19345	:	-446.82213	U	...
	1.45521	:	300.00000						
Z	0.00946	:	1.99326	Y	-2.24409	:	-457.48833	U	...
	1.45521	:	300.00000						
Z	0.00903	:	1.90610	Y	-2.29253	:	-467.70305	U	...
	1.45521	:	300.00000						
Z	0.00859	:	1.81706	Y	-2.33870	:	-477.45619	U	...
	1.45521	:	300.00000						

Z	0.00815	:	1.72623	Y	-2.38256	:	-486.73815	U	...
	1.45521	:	300.00000						
Z	0.00770	:	1.63369	Y	-2.42407	:	-495.53975	U	...
	1.45521	:	300.00000						
Z	0.00724	:	1.53954	Y	-2.46319	:	-503.85232	U	...
	1.45521	:	300.00000						
Z	0.00677	:	1.44387	Y	-2.49988	:	-511.66764	U	...
	1.45521	:	300.00000						
Z	0.00629	:	1.34678	Y	-2.53410	:	-518.97801	U	...
	1.45521	:	300.00000						
Z	0.00581	:	1.24836	Y	-2.56582	:	-525.77622	U	...
	1.45521	:	300.00000						
Z	0.00533	:	1.14870	Y	-2.59501	:	-532.05554	U	...
	1.45521	:	300.00000						
Z	0.00484	:	1.04792	Y	-2.62164	:	-537.80979	U	...
	1.45521	:	300.00000						
Z	0.00434	:	0.94610	Y	-2.64568	:	-543.03329	U	...
	1.45521	:	300.00000						
Z	0.00384	:	0.84334	Y	-2.66710	:	-547.72087	U	...
	1.45521	:	300.00000						
Z	0.00334	:	0.73975	Y	-2.68590	:	-551.86793	U	...
	1.45521	:	300.00000						
Z	0.00283	:	0.63543	Y	-2.70205	:	-555.47035	U	...
	1.45521	:	300.00000						
Z	0.00232	:	0.53049	Y	-2.71553	:	-558.52460	U	...
	1.45521	:	300.00000						
Z	0.00180	:	0.42502	Y	-2.72633	:	-561.02765	U	...
	1.45521	:	300.00000						
Z	0.00129	:	0.31913	Y	-2.73443	:	-562.97703	U	...
	1.45521	:	300.00000						
Z	0.00077	:	0.21293	Y	-2.73985	:	-564.37082	U	...
	1.45521	:	300.00000						

Z	0.00026	:	0.10652	Y	-2.74255	:	-565.20764	U	...
	1.45521	:	300.00000						
Z	-0.00026	:	0.00000	Y	-2.74255	:	-565.48668	U	...
	1.45521	:	300.00000						
Z	-0.00077	:	-0.10652	Y	-2.73985	:	-565.20764	U	...
	1.45521	:	300.00000						
Z	-0.00129	:	-0.21293	Y	-2.73443	:	-564.37082	U	...
	1.45521	:	300.00000						
Z	-0.00180	:	-0.31913	Y	-2.72633	:	-562.97703	U	...
	1.45521	:	300.00000						
Z	-0.00232	:	-0.42502	Y	-2.71553	:	-561.02765	U	...
	1.45521	:	300.00000						
Z	-0.00283	:	-0.53049	Y	-2.70205	:	-558.52460	U	...
	1.45521	:	300.00000						
Z	-0.00334	:	-0.63543	Y	-2.68590	:	-555.47035	U	...
	1.45521	:	300.00000						
Z	-0.00384	:	-0.73975	Y	-2.66710	:	-551.86793	U	...
	1.45521	:	300.00000						
Z	-0.00434	:	-0.84334	Y	-2.64568	:	-547.72087	U	...
	1.45521	:	300.00000						
Z	-0.00484	:	-0.94610	Y	-2.62164	:	-543.03329	U	...
	1.45521	:	300.00000						
Z	-0.00533	:	-1.04792	Y	-2.59501	:	-537.80979	U	...
	1.45521	:	300.00000						
Z	-0.00581	:	-1.14870	Y	-2.56582	:	-532.05554	U	...
	1.45521	:	300.00000						
Z	-0.00629	:	-1.24836	Y	-2.53410	:	-525.77622	U	...
	1.45521	:	300.00000						
Z	-0.00677	:	-1.34678	Y	-2.49988	:	-518.97801	U	...
	1.45521	:	300.00000						
Z	-0.00724	:	-1.44387	Y	-2.46319	:	-511.66764	U	...
	1.45521	:	300.00000						

Z	-0.00770	:	-1.53954	Y	-2.42407	:	-503.85232	U	...
	1.45521	:	300.00000						
Z	-0.00815	:	-1.63369	Y	-2.38256	:	-495.53975	U	...
	1.45521	:	300.00000						
Z	-0.00859	:	-1.72623	Y	-2.33870	:	-486.73815	U	...
	1.45521	:	300.00000						
Z	-0.00903	:	-1.81706	Y	-2.29253	:	-477.45619	U	...
	1.45521	:	300.00000						
Z	-0.00946	:	-1.90610	Y	-2.24409	:	-467.70305	U	...
	1.45521	:	300.00000						
Z	-0.00988	:	-1.99326	Y	-2.19345	:	-457.48833	U	...
	1.45521	:	300.00000						
Z	-0.01028	:	-2.07845	Y	-2.14063	:	-446.82213	U	...
	1.45521	:	300.00000						
Z	-0.01068	:	-2.16159	Y	-2.08571	:	-435.71497	U	...
	1.45521	:	300.00000						
Z	-0.01107	:	-2.24260	Y	-2.02873	:	-424.17782	U	...
	1.45521	:	300.00000						
Z	-0.01145	:	-2.32139	Y	-1.96974	:	-412.22205	U	...
	1.45521	:	300.00000						
Z	-0.01181	:	-2.39789	Y	-1.90881	:	-399.85946	U	...
	1.45521	:	300.00000						
Z	-0.01217	:	-2.47203	Y	-1.84600	:	-387.10227	U	...
	1.45521	:	300.00000						
Z	-0.01251	:	-2.54372	Y	-1.78136	:	-373.96305	U	...
	1.45521	:	300.00000						
Z	-0.01284	:	-2.61291	Y	-1.71497	:	-360.45477	U	...
	1.45521	:	300.00000						
Z	-0.01315	:	-2.67952	Y	-1.64689	:	-346.59077	U	...
	1.45521	:	300.00000						
Z	-0.01346	:	-2.74348	Y	-1.57718	:	-332.38473	U	...
	1.45521	:	300.00000						

Z	-0.01375	:	-2.80474	Y	-1.50591	:	-317.85066	U	...
	1.45521	:	300.00000						
Z	-0.01402	:	-2.86323	Y	-1.43316	:	-303.00291	U	...
	1.45521	:	300.00000						
Z	-0.01429	:	-2.91889	Y	-1.35899	:	-287.85614	U	...
	1.45521	:	300.00000						
Z	-0.01454	:	-2.97167	Y	-1.28348	:	-272.42528	U	...
	1.45521	:	300.00000						
Z	-0.01477	:	-3.02152	Y	-1.20670	:	-256.72558	U	...
	1.45521	:	300.00000						
Z	-0.01499	:	-3.06839	Y	-1.12874	:	-240.77252	U	...
	1.45521	:	300.00000						
Z	-0.01520	:	-3.11223	Y	-1.04966	:	-224.58184	U	...
	1.45521	:	300.00000						
Z	-0.01539	:	-3.15299	Y	-0.96954	:	-208.16953	U	...
	1.45521	:	300.00000						
Z	-0.01556	:	-3.19065	Y	-0.88847	:	-191.55178	U	...
	1.45521	:	300.00000						
Z	-0.01572	:	-3.22516	Y	-0.80652	:	-174.74499	U	...
	1.45521	:	300.00000						
Z	-0.01587	:	-3.25648	Y	-0.72377	:	-157.76575	U	...
	1.45521	:	300.00000						
Z	-0.01599	:	-3.28459	Y	-0.64032	:	-140.63082	U	...
	1.45521	:	300.00000						
Z	-0.01611	:	-3.30946	Y	-0.55622	:	-123.35710	U	...
	1.45521	:	300.00000						
Z	-0.01620	:	-3.33106	Y	-0.47158	:	-105.96164	U	...
	1.45521	:	300.00000						
Z	-0.01628	:	-3.34938	Y	-0.38648	:	-88.46161	U	...
	1.45521	:	300.00000						
Z	-0.01635	:	-3.36439	Y	-0.30099	:	-70.87427	U	...
	1.45521	:	300.00000						

Z	-0.01640	:	-3.37608	Y	-0.21520	:	-53.21700	U	...
	1.45521	:	300.00000						
Z	-0.01643	:	-3.38444	Y	-0.12921	:	-35.50720	U	...
	1.45521	:	300.00000						
Z	-0.01645	:	-3.38946	Y	-0.04308	:	-17.76237	U	...
	1.45521	:	300.00000						
Z	-0.01645	:	-3.39113	Y	0.04308	:	-0.00000	U	...
	1.45521	:	300.00000						
Z	-0.01643	:	-3.38946	Y	0.12921	:	17.76237	U	...
	1.45521	:	300.00000						
Z	-0.01640	:	-3.38444	Y	0.21520	:	35.50720	U	...
	1.45521	:	300.00000						
Z	-0.01635	:	-3.37608	Y	0.30099	:	53.21700	U	...
	1.45521	:	300.00000						
Z	-0.01628	:	-3.36439	Y	0.38648	:	70.87427	U	...
	1.45521	:	300.00000						
Z	-0.01620	:	-3.34938	Y	0.47158	:	88.46161	U	...
	1.45521	:	300.00000						
Z	-0.01611	:	-3.33106	Y	0.55622	:	105.96164	U	...
	1.45521	:	300.00000						
Z	-0.01599	:	-3.30946	Y	0.64032	:	123.35710	U	...
	1.45521	:	300.00000						
Z	-0.01587	:	-3.28459	Y	0.72377	:	140.63082	U	...
	1.45521	:	300.00000						
Z	-0.01572	:	-3.25648	Y	0.80652	:	157.76575	U	...
	1.45521	:	300.00000						
Z	-0.01556	:	-3.22516	Y	0.88847	:	174.74499	U	...
	1.45521	:	300.00000						
Z	-0.01539	:	-3.19065	Y	0.96954	:	191.55178	U	...
	1.45521	:	300.00000						
Z	-0.01520	:	-3.15299	Y	1.04966	:	208.16953	U	...
	1.45521	:	300.00000						

Z	-0.01499	:	-3.11223	Y	1.12874	:	224.58184	U	...
	1.45521	:	300.00000						
Z	-0.01477	:	-3.06839	Y	1.20670	:	240.77252	U	...
	1.45521	:	300.00000						
Z	-0.01454	:	-3.02152	Y	1.28348	:	256.72558	U	...
	1.45521	:	300.00000						
Z	-0.01429	:	-2.97167	Y	1.35899	:	272.42528	U	...
	1.45521	:	300.00000						
Z	-0.01402	:	-2.91889	Y	1.43316	:	287.85614	U	...
	1.45521	:	300.00000						
Z	-0.01375	:	-2.86323	Y	1.50591	:	303.00291	U	...
	1.45521	:	300.00000						
Z	-0.01346	:	-2.80474	Y	1.57718	:	317.85066	U	...
	1.45521	:	300.00000						
Z	-0.01315	:	-2.74348	Y	1.64689	:	332.38473	U	...
	1.45521	:	300.00000						
Z	-0.01284	:	-2.67952	Y	1.71497	:	346.59077	U	...
	1.45521	:	300.00000						
Z	-0.01251	:	-2.61291	Y	1.78136	:	360.45477	U	...
	1.45521	:	300.00000						
Z	-0.01217	:	-2.54372	Y	1.84600	:	373.96305	U	...
	1.45521	:	300.00000						
Z	-0.01181	:	-2.47203	Y	1.90881	:	387.10227	U	...
	1.45521	:	300.00000						
Z	-0.01145	:	-2.39789	Y	1.96974	:	399.85946	U	...
	1.45521	:	300.00000						
Z	-0.01107	:	-2.32139	Y	2.02873	:	412.22205	U	...
	1.45521	:	300.00000						
Z	-0.01068	:	-2.24260	Y	2.08571	:	424.17782	U	...
	1.45521	:	300.00000						
Z	-0.01028	:	-2.16159	Y	2.14063	:	435.71497	U	...
	1.45521	:	300.00000						

Z	-0.00988	:	-2.07845	Y	2.19345	:	446.82213	U	...
	1.45521	:	300.00000						
Z	-0.00946	:	-1.99326	Y	2.24409	:	457.48833	U	...
	1.45521	:	300.00000						
Z	-0.00903	:	-1.90610	Y	2.29253	:	467.70305	U	...
	1.45521	:	300.00000						
Z	-0.00859	:	-1.81706	Y	2.33870	:	477.45619	U	...
	1.45521	:	300.00000						
Z	-0.00815	:	-1.72623	Y	2.38256	:	486.73815	U	...
	1.45521	:	300.00000						
Z	-0.00770	:	-1.63369	Y	2.42407	:	495.53975	U	...
	1.45521	:	300.00000						
Z	-0.00724	:	-1.53954	Y	2.46319	:	503.85232	U	...
	1.45521	:	300.00000						
Z	-0.00677	:	-1.44387	Y	2.49988	:	511.66764	U	...
	1.45521	:	300.00000						
Z	-0.00629	:	-1.34678	Y	2.53410	:	518.97801	U	...
	1.45521	:	300.00000						
Z	-0.00581	:	-1.24836	Y	2.56582	:	525.77622	U	...
	1.45521	:	300.00000						
Z	-0.00533	:	-1.14870	Y	2.59501	:	532.05554	U	...
	1.45521	:	300.00000						
Z	-0.00484	:	-1.04792	Y	2.62164	:	537.80979	U	...
	1.45521	:	300.00000						
Z	-0.00434	:	-0.94610	Y	2.64568	:	543.03329	U	...
	1.45521	:	300.00000						
Z	-0.00384	:	-0.84334	Y	2.66710	:	547.72087	U	...
	1.45521	:	300.00000						
Z	-0.00334	:	-0.73975	Y	2.68590	:	551.86793	U	...
	1.45521	:	300.00000						
Z	-0.00283	:	-0.63543	Y	2.70205	:	555.47035	U	...
	1.45521	:	300.00000						

```

Z -0.00232 : -0.53049 Y 2.71553 : 558.52460 U ...
1.45521 : 300.00000

Z -0.00180 : -0.42502 Y 2.72633 : 561.02765 U ...
1.45521 : 300.00000

Z -0.00129 : -0.31913 Y 2.73443 : 562.97703 U ...
1.45521 : 300.00000

Z -0.00077 : -0.21293 Y 2.73985 : 564.37082 U ...
1.45521 : 300.00000

EndWhile

dwell 5000

cmd"endgather"

m7147 = 0

ta 12000           // set acc time to 500 ms
ts 1000            // set s-curve time to 500 ms
f 0.5              // set feedrate to 1 units/s
linear             // linear mode
abs                // absolute mode
dwell 0
Z 0
dwell 0
inc                // incremental mode
U -2328.333
close

```

BIBLIOGRAPHY

- “Bp statistical review of world energy,” June 2012. [Online]. Available: <http://www.bp.com/statisticalreview>
- Abdulsadda, A. and Tan, X., “An artificial lateral line system using ipmc sensor arrays,” *International Journal of Smart and Nano Materials*, vol. 3, no. 3, September 2012.
- Bernitsas, M., “Vivace: A new concept in generation of clean and renewable energy from fluid flow,” *Journal of Offshore Mechanics and Arctic Engineering*, vol. 130, no. 041101, November 2008.
- BP, “Bp energy outlook 2030,” <http://www.bp.com/>, January 2012.
- Chen, J., Engel, J., Chen, N., Pandya, S., Coombs, S., and Liu, C., “Artificial lateral line and hydrodynamic object tracking,” *Micro Electro Mechanical Systems*, pp. 694–697, 2006.
- Coombs, S. and Netten, S., *Fish Biomechanics*, R.E. Shadwick, G., Ed. Academic Press, January 2006, vol. 23.
- Department of Trade and Industry, “Stingray tidal stream energy device - phase 3,” Engineering Business LTD, UK, Tech. Rep. T/06/00230/00/REP URN 05/864, 2005.
- Fernandez, V. I., Maertens, A., Yaul, F. M., Dahl, J., Lang, J. H., and Triantafylou, M. S., “Lateral-line inspired sensor arrays for navigation and object identification,” *Marine Technology Society Journal*, vol. 45, no. 4, pp. 130–146, July/August 2011.
- Groot, C. and Margolis, L., *Pacific salmon life histories*. UBC Press, 1991.
- Grue, J., Mo, A., and Palm, E., “Propulsion of a foil moving in water waves,” *Journal of Fluid Mechanics Digital Archive*, vol. 186, pp. 393–417, 2006.
- Isshiki, H. and Murakami, M., “A theory of wave devouring propulsion. iv: a comparison between theory and experiment in case of a passive-type hydrofoil propulsor.” *Journal of Society of Naval Architects of Japan*, vol. 156, pp. 102–114, 1984.
- Jha, A. “Making waves: Uk firm harnesses power of the sea ... in portugal.”
- Kinsey, T., Dumas, G., Lalande, G., Ruel, J., Mehut, A., Viarouge, P., Lemay, J., and Jean, Y., “Prototype testing of hydrokinetic turbine based on oscillating hydrofoils,” *Renewable Energy*, vol. 36, pp. 1710–1718, November 2011.

- Kloos, G., Gonzalez, C., and Finnigan, T., “The biostream tidal current energy converter,” in *Proceedings of the 8th European Wave and Tidal Energy Conference*. Uppsala, Sweden: BioPower Systems Pty Ltd, 2009, pp. 426 – 434.
- Krieg, M., Klein, P., Hodgkinson, R., and Mohseni, K., “A hybrid class underwater vehicle: Bioinspired propulsion, embedded system, and acoustic communication and localization system,” *Marine Technology Society Journal*, vol. 45, no. 4, pp. 153–164, Jul/Aug 2011.
- Liao, J. C., Beal, D. N., Lauder, G. V., and Triantafyllou, M. S., “Fish exploiting vortices decrease muscle activity,” *Science*, vol. 302, pp. 1566–1569, November 2003.
- Licht, S., Wibawa, M., Hover, F., and Triantafyllou, M., “In-line motion causes high thrust and efficiency in flapping foils that use power downstroke,” *The Journal of Experimental Biology*, vol. 613, pp. 63–71, September 2009.
- Licht, S., Hover, F., and Triantafyllou, M., “Design of a flapping foil underwater vehicle.”
- McKinney, W. and DeLaurier, J., “The wingmill: An oscillating-wing windmill,” *Journal of Energy*, vol. 5, pp. 109–115, 1981.
- NASA. “Center of pressure.” [Online]. Available: <http://www.grc.nasa.gov/www/k-12/airplane/cp.html>
- Paish, M., “Can 1mw tidal systems compete with off-shore wind?: An analysis of the opportunities and challenges associated with scaling up,” in *4th International Conference on Ocean Energy*. Dublin: Pulse Tidal ltd; The Electric Works, October 2012.
- Simpson, B. J., “Experimental studies of flapping foils for energy extraction,” Master’s thesis, Massachusetts Institute of Technology, Cambridge, MA, September 2009.
- Webb, J., *Encyclopedia of Fish Physiology: From Genome to Environment*, 1st ed., Farrell, A. P., Ed. Academic Press, July 2011.
- Webb, J., “Morphological diversity, development, and evolution of the mechanosensory lateral line system,” 2012.
- Weymouth, G. and Yue, D. K., “Boundary data immersion method for cartesian-grid simulations of fluid-body interaction problems,” *Journal of Computational Physics*, vol. 230, pp. 6233–6247, April 2011.
- Xu, Y., Ren, Z., and Mohseni, K., “Lateral line inspired pressure feedforward for autonomous underwater vehicle control,” ser. Workshop on Robotics for Environmental Monitoring, August 2012.

- Yang, Y., Chen, N., Tucker, C., Pandya, S., Jones, D., and Liu, C., “Biomimetic flow sensing using artificial lateral lines,” *ASME Conference Proceedings*, vol. 43025, pp. 1331–1338, 2007.
- Zhu, Q. and Peng, Z., “Mode coupling and flow energy harvesting by a flapping foil,” *Physics of Fluids*, vol. 21, no. 033601, 2009.
- Zhu, Q., “Optimal frequency for flow energy harvesting of a flapping foil,” *Journal of Fluid Mechanics*, vol. 675, pp. 495–517, March 2011.